

Affinity-Modulation Drug Delivery Using Thermosensitive Elastin-Like Polypeptide Block  
Copolymers

by

Andrew J. Simnick

Department of Biomedical Engineering  
Duke University

Date: \_\_\_\_\_

Approved:

\_\_\_\_\_  
Ashutosh Chilkoti, Ph.D., Supervisor

\_\_\_\_\_  
Mark W. Dewhirst, Ph.D., D.V.M.

\_\_\_\_\_  
Kam W. Leong, Ph.D.

\_\_\_\_\_  
George A. Truskey, Ph.D.

\_\_\_\_\_  
Christopher D. Kontos, M.D.

Dissertation submitted in partial fulfillment of  
the requirements for the degree of Doctor of Philosophy  
in the Department of  
Biomedical Engineering in the Graduate School  
of Duke University

2010

ABSTRACT

Affinity-Modulation Drug Delivery Using Thermosensitive Elastin-Like Polypeptide Block

Copolymers

by

Andrew J. Simnick

Department of Biomedical Engineering  
Duke University

Date: \_\_\_\_\_

Approved:

\_\_\_\_\_  
Ashutosh Chilkoti, Ph.D., Supervisor

\_\_\_\_\_  
Mark W. Dewhirst, Ph.D., D.V.M.

\_\_\_\_\_  
Kam W. Leong, Ph.D.

\_\_\_\_\_  
George A. Truskey, Ph.D.

\_\_\_\_\_  
Christopher D. Kontos, M.D.

Dissertation submitted in partial fulfillment of  
the requirements for the degree of Doctor of Philosophy  
in the Department of  
Biomedical Engineering in the Graduate School  
of Duke University

2010

Copyright by  
Andrew Joseph Simnick  
2010

## Abstract

Antivascular targeting is a promising strategy for tumor therapy. This strategy overcomes many of the transport barriers and has shown efficacy in many preclinical models, but targeting epitopes on tumor vasculature can also promote accumulation in healthy tissues. We used Elastin-like Polypeptide (ELP) to form block copolymers (BCs) consisting of two separate ELP blocks seamlessly fused at the genetic level. ELPBCs self-assemble into spherical micelles at a critical micelle temperature (CMT), allowing external control over monovalent unimer and multivalent micelle forms. We hypothesized that thermal self-assembly could trigger specific binding of ligand-ELPBC to target receptors via the multivalency effect as a method to spatially restrict high-avidity interactions. We termed this approach *Dynamic Affinity Modulation* (DAM). The objectives of this study were to design, identify, and evaluate protein-based drug carriers that specifically bind to target receptors through static or dynamic multivalent ligand presentation.

ELPBCs were modified to include a low-affinity GRGDS or GNGRG ligand and a unique conjugation site for hydrophobic compounds. This addition did not disrupt micelle self-assembly and facilitated thermally-controlled multivalency. The ability of ligand-ELPBC to specifically interact with isolated  $\alpha v \beta 3$  or CD13 was tested using an *in vitro* binding assay incorporating an engineered cell line. RGD-ELPBC promoted specific receptor binding in response to multivalent presentation but NGR-ELPBC did not. Enhanced binding with multivalent presentation was also observed only with constructs exhibiting CMT < body temperature. This study establishes proof-of-principle of DAM, but ELPBC requires thermal optimization for use with applied hyperthermia. Static affinity targeting of fluorescent ligand-ELPBC was then analyzed *in vivo* using intravital microscopy (IM), immunohistochemistry (IHC), and custom image processing algorithms. IM showed increased accumulation of NGR-ELPBC in tumor tissue relative to normal tissue while RGD-ELPBC and non-ligand ELPBC did not, and IHC verified these observations. This study

shows (1) multivalent NGR presentation is suitable for static multivalent targeting of tumors and tumor vasculature, (2) multivalent RGD presentation may be suitable for DAM with thermal optimization, and (3) ELPBC micelles may selectively target proteins at the tumor margin.

## **Dedication**

To Clarence Simnick, Darlene Rea, and Dr. Rosemarie Carroll

Abstract .....	iv
List of Tables .....	xv
List of Figures.....	xvi
Acknowledgements .....	xix
1 Affinity Modulation Drug Targeting: Strategy, Benefits, and Challenges .....	1
1.1 Cancer .....	1
1.1.1 Neoplastic Development .....	1
1.1.2 Phenotypic Differences in Primary Tumors .....	3
1.1.2.1 Interstitial pH .....	3
1.1.2.2 Interstitial Fluid Pressure .....	4
1.1.2.3 Endothelial Cells .....	5
1.2 Cancer Therapy: Strategies and Challenges .....	6
1.2.1 Systemic Chemotherapy .....	7
1.2.1.1 Small-Molecule Chemotherapeutics .....	7
1.2.1.2 Polymeric Delivery of Chemotherapeutics .....	8
1.2.1.3 Peptide-Based Drug Delivery.....	10
1.2.1.4 Stimulus-Responsive Polymers .....	10
1.2.2 Antiangiogenic/Antivascular Therapy .....	11
1.2.2.1 Targeted Small Molecule Therapeutics .....	11
1.2.2.2 High-Affinity Macromolecules .....	12
1.2.3 Hyperthermia .....	12
1.2.3.1 Clinical Hyperthermia.....	13
1.2.3.2 Physiological Effects of Hyperthermia .....	13
1.2.3.3 Thermally-Responsive Drug Carriers .....	15

1.3 Ligand-Receptor Binding .....	16
1.3.1 Thermodynamic Overview.....	16
1.3.2 Multivalency Effect.....	17
1.3.3 Examples of Ligand-Receptor Systems for Tumor Therapy .....	18
1.3.3.1 $\alpha\text{v}\beta\text{3}$ Integrin – RGD .....	19
1.3.3.2 CD13 – NGR.....	20
1.3.3.3 Limitations of Multivalent Targeting Strategies .....	21
1.4 Elastin-Like Polypeptide .....	21
1.4.1 ELP Drug Delivery Applications .....	22
1.4.2 Elastin-Like Polypeptide Block Copolymers.....	23
1.5 Affinity-Modulation Targeting.....	24
1.5.1 Overview.....	24
1.5.2 Specific Aims .....	26
1.5.2.1 Specific Aim 1 – Design of Self-Assembling Block Copolymers for Affinity-Modulated Targeting .....	26
1.5.2.2 Specific Aim 2 – Identification of Conditions for Multivalent Interaction and Constructs Capable of Affinity-Modulation.....	26
1.5.2.3 Specific Aim 3 – <i>In Vivo</i> Characterization of ELP Block Copolymers in Both Tumor and Normal tissues .....	27
1.5.3 Potential Difficulties .....	27
2 Fluorescence Characterization of Elastin-Like Polypeptide Block Copolymers .....	28
2.1 Introduction.....	29
2.1.1 Critical Micelle Concentration.....	29
2.1.2 Micelle Core Rigidity.....	30
2.1.3 Fluorescence Probes .....	30
2.1.3.1 Pyrene.....	30



2.1.3.2 PC <sub>3</sub> P .....	31
2.2 Materials and Methods .....	32
2.2.1 Thermal Control of Fluorescence Spectrophotometer .....	32
2.2.2 Determination of Critical Micelle Concentration of ELPBC .....	33
2.2.2.1 Sample Preparation .....	33
2.2.2.2 Data Acquisition and Analysis.....	33
2.2.3. Evaluation of Microviscosity .....	34
2.2.3.1 Sample Preparation .....	34
2.2.3.2 Data Acquisition and Analysis.....	34
2.3. Results and Discussion .....	35
2.3.1 Thermally-Controlled Fluorescence Spectrophotometry.....	35
2.3.2 Critical Micelle Concentration of Elastin-Like Polypeptide Block Copolymers .....	36
2.3.3 Evaluation of Microstructure of Micelle Core Versus Aggregate.....	39
2.4 Significance .....	43
3 Generation and Evaluation of Ligand-Functionalized Elastin-like Polypeptide Block Copolymer .....	45
3.1 Introduction .....	45
3.1.1 ELP Block Copolymer Modification .....	46
3.1.1.1 Construct Design .....	46
3.1.1.2 Ligand Selection .....	47
3.1.1.3 Vector Design .....	48
3.1.1.4 ELPBC Expression, Purification, and Functionalization .....	48
3.1.2 Dynamic Light Scattering .....	49
3.2 Materials and Methods .....	50
3.2.1 Vector Design and Generation .....	50

3.2.2 Library Generation.....	51
3.2.3 ELPBC Purification.....	51
3.2.4 Fluorophore Conjugation.....	52
3.2.5 Dynamic Light Scattering Measurements.....	52
3.3. Results and Discussion.....	53
3.3.1 Generation of RGD-, NGR-, and Non-Ligand ELPBC Gene Library.....	53
3.3.2 Expression of Functionalized ELPBCs.....	54
3.3.3 Evaluation of ELPBC Thermal Self-Assembly.....	55
3.3.3.1 Effects of Ligand and Conjugate on Hydrodynamic Radius.....	56
3.3.3.2 Effects of Ligand and Conjugate on Critical Micelle Temperature.....	58
3.3.3.3 Effects of Ligand and Conjugate on Coordination Number and Ligand Density ..	60
3.4 Significance.....	61
4 Development of a Cell Line with Controllable Cell Receptor Expression for Cell-Binding Assay.....	62
4.1 Introduction.....	62
4.1.1. Ligand-Receptor Binding Assays.....	63
4.1.1.1 Thermodynamic Assays.....	63
4.1.1.2 Surface-Based Assays.....	64
4.1.1.3 Cell-Based Assays.....	65
4.1.2 Universal Binding Assay Design.....	67
4.1.2.1 K562 Erythroleukemia.....	67
4.1.2.2 Tetracycline-Responsive Plasmid System.....	68
4.1.3 Flow Cytometry.....	69
4.1.4 Retroviral Infection Strategy.....	69
4.2 Materials and methods.....	71

4.2.1 Cell Culture .....	71
4.2.2 Gene Construction.....	71
4.2.3 Lipid-Based Transformation .....	72
4.2.4 Retroviral Infection.....	72
4.2.5 Luciferase Assay .....	73
4.2.6 Semi-Quantitative RT-PCR .....	74
4.2.7 Antibody Staining.....	74
4.2.8 Flow Cytometry Analysis .....	75
4.2.9 Confocal Microscopy .....	75
4.3 Results and Discussion .....	75
4.3.1 Evaluation of Retroviral Infection.....	76
4.3.2 Regulation of Bulk Protein Expression.....	77
4.3.3 Plasmid Generation .....	79
4.3.4 Titration of a Monomeric Cell Surface Receptor .....	80
4.3.5 Titration of a Dimeric Cell Surface Receptor .....	84
4.4 Significance .....	87
5 Evaluation of Dynamic Affinity Modulation Using Elastin-Like Polypeptide Block Copolymers..	89
5.1 Introduction .....	89
5.1.1 K562 Binding Assay .....	90
5.2 Materials and Methods .....	91
5.2.1 Cell Culture.....	91
5.2.2 Cell Uptake .....	92
5.2.3 Flow Cytometry Analysis .....	92
5.2.4 Confocal Imaging.....	92

5.3 Results and Discussion .....	93
5.3.1 Evaluation of RGD-ELPBC Constructs with Constant Overexpression .....	93
5.3.1.1 Effects of Monovalent RGD Presentation on Cell Uptake .....	93
5.3.1.2 Effects of Micelle Self-Assembly on Non-Specific Cell Uptake .....	94
5.3.1.3 Effects of Multivalent RGD Presentation on Specific Cell Uptake .....	95
5.3.1.4 Effects of Nanoscale RGD Presentation on Specific Cell Uptake .....	99
5.3.2 Evaluation of NGR-ELPBC Constructs with Constant Overexpression .....	100
5.3.2.1 Effects of Monovalent NGR Presentation on Cell Uptake .....	101
5.3.2.2 Effects of Micelle Self-Assembly on Nonspecific Uptake by Doxycycline-Responsive Cells .....	101
5.3.2.3 Effects of Micelle Self-Assembly on Nonspecific Uptake by Doxycycline-Responsive Cells .....	102
5.3.2.4 Receptor Codependence for <i>In Vitro</i> NGR Uptake.....	105
5.4 Significance .....	107
6 Evaluation of <i>In Vivo</i> Multivalent Targeting Using ELP Block Copolymers .....	108
6.1 Introduction .....	108
6.1.1 Intravital Microscopy.....	109
6.1.1.1 Laser-Scanning Confocal Microscopy .....	110
6.1.1.2 Dorsal Fold Window Chamber Model .....	111
6.1.1.3 Imaging Fluorescence Compounds Within the Vasculature.....	112
6.1.1.4 Image Processing .....	113
6.1.2 Immunohistochemistry .....	113
6.2 Materials and Methods .....	114
6.2.1 CMT Measurement in Serum .....	114
6.2.2 ELPBC-Doxorubicin Conjugation .....	114

6.2.3 Dose Preparation.....	115
6.2.4 Dorsal Fold Window Chamber Surgery.....	115
6.2.5 Confocal Imaging Procedure.....	116
6.2.5.1 ELPBC-AlexaFluor488.....	116
6.2.5.2 ELPBC-Doxorubicin.....	117
6.2.6 Image Analysis.....	117
6.2.6.1 MATLAB Functions.....	117
6.2.6.2 Data Processing Routine.....	118
6.2.7 Immunohistochemistry.....	119
6.2.7.1 Dose administration.....	119
6.2.7.2 Imaging and Staining Protocol.....	120
6.2.7.3 Colocalization Analysis.....	120
6.3 Results and Discussion.....	121
6.3.1 Construct Selection.....	121
6.3.2 Self-Assembly in Serum.....	121
6.3.3 Analysis of RGD-, NGR-, and Non-Ligand ELP-64/90 Accumulation Using the Dorsal Fold Window Chamber Model.....	125
6.3.3.1 Development of Automated Mask Generation.....	125
6.3.3.2 Effects of Multivalent Ligand Presentation on Tumor Spatial Distribution.....	128
6.3.3.3 Effects of Multivalent Ligand Presentation on Vascular Clearance.....	131
6.3.3.4 Effects of Multivalent Ligand Presentation on Tumor and Normal Tissue Accumulation.....	133
6.3.3.5 Effects of Multivalent Ligand Presentation on Extravasation Distance.....	136
6.3.4 Analysis of RGD-, NGR-, and Non-Ligand ELP-64/90 Cell Localization Using Immunohistochemistry.....	138
6.3.5 Evaluating Potential for Delivery of Doxorubicin Using ELPBC.....	143

6.3.5.1 Effects of Doxorubicin Conjugation on ELPBC Self-Assembly.....	143
6.3.5.2 Evaluation of Doxorubicin-Functionalized Constructs Using the Dorsal Fold Window Chamber.....	145
6.4 Significance .....	148
7 Affinity-Modulation Drug Delivery: Conclusions and Future Directions .....	150
7.1 Conclusions .....	150
7.2 Future Directions .....	151
7.2.1 Development of ELP2-ELP4 Block Copolymers for Targeted Drug Delivery .....	151
7.2.1.1 NGR-ELPBC .....	151
7.2.1.2 RGD-ELPBC .....	152
7.2.1.3 Non-Ligand ELPBC.....	155
7.2.2 Protocols Applicable to Outside Study .....	156
7.2.2.1 Fluorescence-Based Characterization of Thermosensitive ELPBCs .....	156
7.2.2.2 K562 Cell Testing Platform .....	157
7.2.2.3 Intravital Antibody Staining .....	158
7.2.3 Additional Paths of Study .....	160
7.2.3.1 “Living” Predictive Model for ELPBC generation .....	160
7.2.3.2 Evaluation of the Effects of Endotoxin on Multivalent Targeting .....	161
References.....	164
Biography.....	182

## List of Tables

Table 1: Description of requirements for static and dynamic affinity modulation.....	28
Table 2: CMC of micelle-forming ELPBCs.....	39
Table 3: Description of constructs developed for affinity targeting studies.....	54
Table 4: transition temperatures of 10 $\mu$ M functionalized ELPBC in PBS. ....	58
Table 5: Overview of the effects of modification on the CMT and Z of ELPBCs. ....	59
Table 6: Examples of active/control cell lines for testing $\alpha$ v $\beta$ 3 and CD13 ligand-receptor binding <i>in vitro</i> .....	66
Table 7: Results of NGR-mediated uptake studies with different cell lines. ....	106
Table 8: MATLAB functions used for image analysis .....	118
Table 9: MATLAB scripts used for image analysis .....	118
Table 10: Self-assembly parameters of ELPBC-Dox constructs. ....	144
Table 11: List of proteins with potential affinity for transitioned ELPBC .....	156

## List of Figures

Figure 1: Role of angiogenesis in tumor development. ....	2
Figure 2: Example of phenotypic differences between normal vessels and tumor vessels. ....	4
Figure 3: Schematic of multivalent targeting using low-affinity peptide ligands.....	19
Figure 4: Diagram of ELP2/ELP4 block copolymer.. ....	23
Figure 5: ELP block copolymers that form micelles in response to heat. ....	24
Figure 6: Schematic of dynamic affinity modulation using functionalized ELPBCs. ....	25
Figure 7: Structures and spectra of pyrene and 1,3-bis(1-pyrenyl)propane. ....	32
Figure 8: Block diagram of fluorescence spectroscopy data acquisition. ....	35
Figure 9: Example of temperature-independent CMC calculation using pyrene spectra as a function of temperature. ....	36
Figure 10: Determination of CMC of ELPBCs using fluorescence spectroscopy. ....	37
Figure 11: Evaluation of ELPBC rigidity using fluorescence spectroscopy. ....	40
Figure 12: Comparison of micelle viscosity to aggregate viscosity. ....	42
Figure 13: Diagram of modified ELPBC. ....	46
Figure 14: Structure of RGD and NGR tripeptide ligands. ....	47
Figure 15: Gene cassettes for creation of custom vectors for ELPBC library generation. ....	50
Figure 16: SDS-PAGE of purified and modified ELPBC. ....	55
Figure 17: Hydrodynamic radius ( $R_h$ ) of 10 $\mu$ M ELPBC-AlexaFluor488 solutions as a function of temperature. ....	57
Figure 18: Schematic of tetracycline-responsive expression system. ....	68
Figure 19: Diagram of flow cytometry data acquisition and processing. ....	70
Figure 20: GFP expression in K562 cells infected with retrovirus and selected with puromycin... ..	77
Figure 21: Dose-response curves of luciferase expression in wild-type and modified K562 cells in response to doxycycline. ....	78



Figure 22: Synthesis of genes for use with tetracycline-responsive system. ....	79
Figure 23: (A) K562-Tet-On-APN and (B) K562-Tet-On- $\beta$ 3 response to increasing doxycycline concentration.....	81
Figure 24: Confocal microscopy images of K562-Tet-On-CD13 stained with FITC-WM15 Ab following incubation with doxycycline.....	82
Figure 25: Gel electrophoresis results following RT-PCR testing for $\beta$ 3 expression.....	86
Figure 26: $\alpha\beta$ 3 expression on K562- $\alpha\beta$ 3 cells.....	91
Figure 27: Flow cytometry histograms of K562-WT and K562/ $\alpha\beta$ 3 cells following incubation with ELPBC constructs at temperatures below and above the CMT. ....	94
Figure 28: Quantitative effects of multivalent RGD presentation on specific cellular uptake. ....	96
Figure 29: Confocal fluorescence images of K562/ $\alpha\beta$ 3 cells following incubation with 10 $\mu$ M of RGD-ELPBC (green).....	98
Figure 30: Size of RGD-ELP-150 as a function of temperature. ....	99
Figure 31: Uptake of RGD-ELP-150 constructs by K562 and K562/ $\alpha\beta$ 3 cells.....	100
Figure 32: Flow cytometry histograms of K562-Tet-On-CD13 cells incubated with ELPBC constructs at temperatures below and above the CMT. ....	102
Figure 33: Quantitative effects of multivalent NGR presentation on specific cellular uptake. ....	103
Figure 34: Uptake of NGR-ELP-150 constructs by both CD13+ and CD13- K562-Tet-On-CD13 cells. ....	105
Figure 35: Schematic of confocal microscopy. ....	111
Figure 36: Overview of intravital microscopy using the dorsal fold window chamber model.....	112
Figure 37: Flow chart illustrating image processing routine for accumulation and extravasation analysis using the dorsal fold window chamber model.....	119
Figure 38: Turbidity profiles of 10 $\mu$ M ELPBC-AlexaFluor488 solutions in serum.....	123
Figure 39: Turbidity profiles of 5 $\mu$ M ELPBC-AlexaFluor488 solutions in serum.....	124
Figure 40: Effects of threshold selection on mask generation and data calculation.....	126
Figure 41: Schematic of automated mask generation algorithm. ....	128

Figure 42: Example spatial distribution of ELP-64/90 within the tumor 45 min following systemic administration.....	130
Figure 43: Spatial distribution of RGD-ELP-64/90 within the tumor 45 min following systemic administration.....	130
Figure 44: Spatial distribution of NGR-ELP-64/90 within the tumor 45 min following systemic administration.....	131
Figure 45: Vascular concentration of ELPBC as a function of time in both tumor and normal vasculature.....	133
Figure 46: Extravascular concentration of ELPBC as a function of time in both tumor and normal vasculature.....	135
Figure 47: Penetration distance of ELP-64/90, RGD-ELP-64/90, and NGR-ELP-64/90 micelles. ....	137
Figure 48: Immunohistochemistry images of tumor tissue following administration of ELPBC (green).....	140
Figure 49: Immunohistochemistry images of normal muscle tissue following administration of ELPBC. ....	141
Figure 50: Colocalization of ELPBC with endothelial cells and perivascular nuclei. ....	142
Figure 51: Hydrodynamic radius of non-ligand-, RGD-, and NGR-ELP-64/90-Dox constructs as a function of temperature. ....	144
Figure 52: Confocal images of ELP-64/90-Dox and FITC-Dextran in tumor vasculature.....	147
Figure 53: Confocal images of 100 $\mu$ M non-ligand, RGD-, and NGR-ELP-64/90-Dox constructs in FaDu tumors using the dorsal fold window chamber.....	148
Figure 54: Confocal images of C26 cells incubated with free Dox, ELP-OregonGreen, or ELP-Dox nanoparticles.....	153
Figure 55: Neutrophil localization in tumor vasculature.....	159
Figure 56: Confocal images of RGD-ELP-64/90 and NGR-ELP-64/90 in presence of endotoxin. ....	162

## Acknowledgements

In graduate school, one quickly realizes that the bridge to success is built on support from others. Thankfully, many have helped along the way to making this work a success.

I thank Dr. Ashutosh Chilkoti for providing the opportunity to attend Duke University, providing the vision of this exciting project, and trusting my ability to perform in area of study vastly different from my prior experience. I hope that this effort has lived up to expectations. My dissertation committee, Dr. Christopher Kontos, Dr. Mark Dewhirst, Dr. Kam Leong, and Dr. George Truskey, has provided a surplus of valuable recommendation and support. Their scientific input greatly broadened the scope and relevance of this work, and their technical expertise made many of these experiments possible. Our main collaborator at UNC-Chapel Hill, Dr. Rihe Liu, was also very generous in his assistance of overcoming some of the largest technical hurdles.

The mentorship and expertise provided by my peers and coworkers was also integral in my professional and personal development. I thank Dr. Matthew Dreher for taking me under his wing and introducing me to life at Duke, Dr. Alex Valencia for generously accepting a Blue Devil into the lab and providing technical and cultural insight, and Dr. Wenge Liu for being a patient, helpful, and dangerous teacher. Maureen Upton, Bryce and Anjul Davis, Jeffrey Lamack, Luke McSpadden, Nima Badie, Rob Kirkton, Mohammed Shamji, Charles Anamelechi, Vadim Polikov, Ryan Hill, Sarah MacEwan, Jonathan McDaniel, Matt Novak, Kathy Barbour, and Marcus Henderson have all been fantastic departmental colleagues, and Robert Ducker, Elizabeth Nelson, Nathan Jenness, and Jeffrey Coles all made CBIMMS an ideal working environment. Additionally, Joseph Farfel, Varun Marupadi, Balint Otvos, Aurelia D'Antonio, Matt Irvin, Kenny Morton, Vito Mecca, Jeff Rogers, Josh Stohl, Marshall Thompson, and Marc Frahm all reminded me that life is still interesting outside of biomedical engineering and that success can take many

different forms. And Bonnie Lai deserves special thanks for doing the impossible and convincing me that everything works out for the best.

My family deserves the greatest recognition of all. My parents, Richard and Nancy Simnick, and my grandparents, Lottie Rea and Mary Simnick, have all been unyielding in their support. The work ethic, perseverance, and respect for achievement they instilled in me at a young age are the sole reasons this dissertation exists. While growing up may have taken longer than expected, they can now take pride in having a doctor in the family.

# **1 Affinity Modulation Drug Targeting: Strategy, Benefits, and Challenges**

## **1.1 Cancer**

Cancer is a disease marked by unregulated cellular growth caused by genetic mutation resulting from random alteration or environmental cues. Cancer results in approximately 560,000 annual deaths and total cost of \$219.2 billion [1], making it the second largest cause of death in the United States. Cancer begins with disruption of normal homeostatic mechanisms balancing cell growth and apoptosis. This balance is regulated by two gene types, oncogenes and tumor suppressor genes. Oncogenes produce factors that trigger cell division [2] while tumor suppressor genes regulate cell growth by triggering apoptosis in response to disruption in DNA [3; 4]. Mutations in oncogenes lead to uncontrolled cell growth, while mutations in tumor suppressor genes “switch off” ability to regulate this growth. This creates a positive feedback loop for neoplastic development. Combinations of mutations in these gene types lead to cancer [2], although it is not known exactly which combination(s) of mutations will cause malignancy. While accumulation of defects may take place over years, neoplastic growth following transformation occurs rapidly.

### **1.1.1 Neoplastic Development**

The typical stages of neoplastic development are described in Fig. 1. As the neoplasm develops following its dormant stage, it begins to outstrip available local nutrients and oxygen, resulting in local hypoxia. This necessitates delivery of additional nutrients via systemic circulation. Thus, angiogenesis, the development of new blood vessels, is required for continued neoplastic growth [5]. While tumors can switch to an angiogenic state through a number of processes, vascularization of avascular neoplasms is common. This process is stimulated by autocrine and paracrine factors released from the tumor [6]. Similar to oncogenesis, angiogenesis is controlled by the balance of positive [7; 8] and negative factors [9; 10].

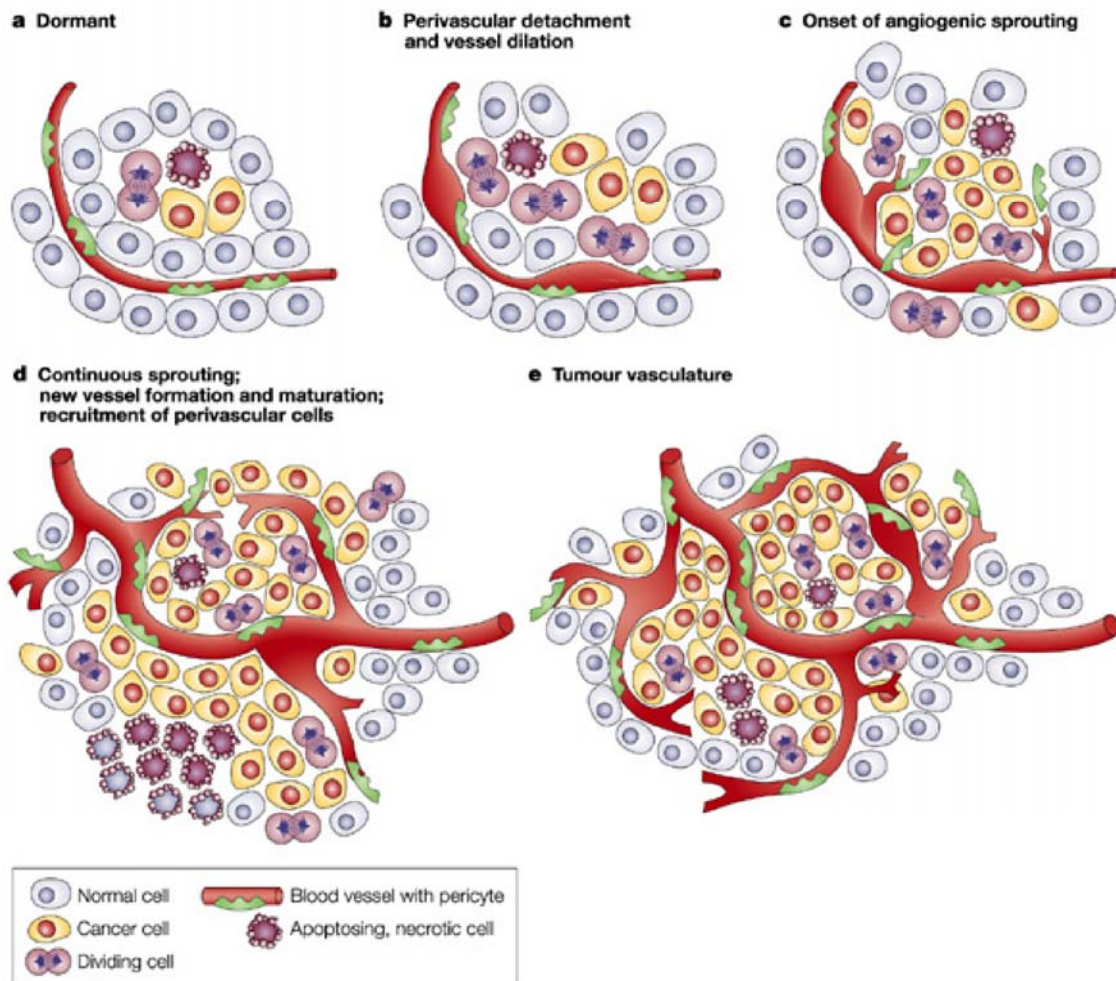


**Figure 1: Role of angiogenesis in tumor development. (a) The developing neoplasm will remain dormant (b) until rearrangement of normal vessels (c) and onset of angiogenesis. (d) Vessels will continue to develop and provide nutrients to the developing neoplasm. (e) The persistent vascular rearrangement leads to an irregular network throughout the growing tumor. Reprinted by permission from Macmillan Publishers Ltd: Nature Reviews Cancer, Bergers, G. and Benjamin, L.E., *Tumorigenesis and the angiogenic switch*. 3(6): 401-410. copyright 2003.**

Positive factors promote angiogenesis and vessel maintenance such as vascular endothelial growth factor (VEGF) and angiopoietin-1 (ANG1), respectively. VEGF is secreted following transcription by hypoxia-induced factor (HIF) in hypoxic regions [11; 12] and ANG-1 is expressed constitutively by associated pericytes [13; 14]. Negative factors cause vessel disruption and restrict vascularization such as angiopoietin-2 (ANG2) secreted by tumor cells. A balance

between positive and negative factors regulates tumor development [15]. The balance tipping towards positive factors signals the “angiogenic switch” and continued growth. At this point, the angiogenic phenotype of the neoplasm appears and vascular growth dominates due to a surplus of VEGF and other positive factors [16]. Elevated levels of VEGF cause persistent remodeling and growth of blood vessels within the tumor region, while a shift in the balance towards ANG1 and away from ANG2 via pericyte recruitment results in maintenance of the growing tumor vasculature rather than regression of tumor vasculature [17-19].

Primary tumors may become metastatic as cancerous cells break from the primary neoplasm and embed themselves in different regions throughout the body such as the lung or brain. Additionally, metastatic tumors can be difficult to detect and lead to problems even with removal of the primary tumor. While the focus of this work is therapy targeting the primary tumor, we also must take metastatic potential into account. Recent studies have shown that different targeted tumor treatment strategies will kill tumor cells expressing the targeting moiety but leave more aggressive cells to repopulate the neoplasm. In addition to neoplastic growth and angiogenesis, metastatic potential must be reduced to sufficiently address and control cancer.

### **1.1.2 Phenotypic Differences in Primary Tumors**

Excess VEGF, ANG1, and ANG2 promotes continuous remodeling of tumor vasculature, causing it to be erratic and incomplete [20]. Thus, tumor vasculature is characterized by chaotic structure and leakiness compared to normal vessels [21] (Fig. 2). The heterogeneous and leaky tumor vessel coverage [22] in conjunction with differences in tumor cell behavior leads to physiological differences in tumor tissue versus normal tissue such as lowered pH, high interstitial fluid pressure (IFP), and altered protein expression on endothelial cell surfaces.

#### **1.1.2.1 Interstitial pH**

Incomplete and erratic vascular organization within the tumor region causes low perfusion of tumor tissues and further increased hypoxia [20]. This directly leads to increased HIF expression followed by upregulation of positive growth factors, creating a positive feedback cycle

promoting growth and angiogenesis. Despite angiogenesis, the tumor retains the hypoxic regions yet maintains high metabolic rates, leading to an increase in anaerobic respiration and

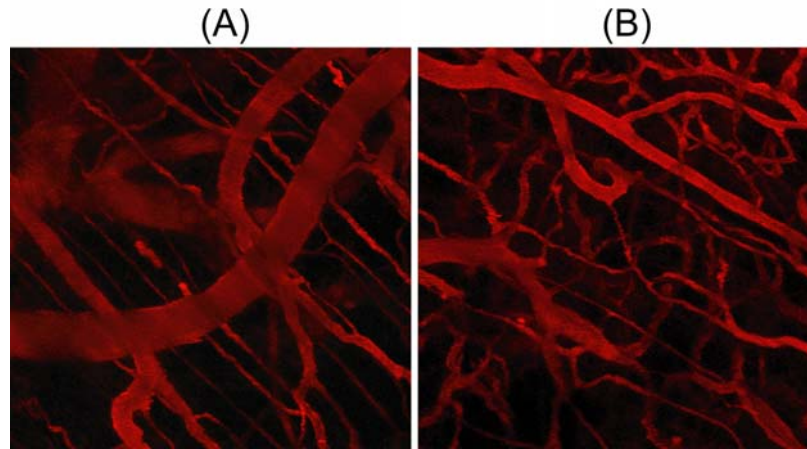


**Figure 2: Example of phenotypic differences between normal vessels and tumor vessels. (A) Normal vessels are straight, larger, ordered and (B) tumor vessels are tortuous, small, and irregular.**

lactic acid and  $\text{CO}_2$ . This increased lactic acid production is in addition to the increased ability of tumor cells to produce lactic acid even in the presence of oxygen [23]. The buildup of lactic acid in the extracellular space lowers the extracellular pH within the tumor. Furthermore, excess  $\text{CO}_2$  generated by the tumor cell is hydrated to  $\text{HCO}_3^-$  through carbonic anhydrase, an enzyme upregulated by hypoxia [24; 25]. These combine to create an overall acidic extracellular environment within the tumor with a range of  $\text{pH} = 5.8 - 7.6$  in malignant human tumors [26]. This is supported by the correlation between mean  $\text{pO}_2$  and interstitial pH averaged over the tumor [27]. However, the pH gradient does not necessarily correlate with  $\text{pO}_2$  on a per-vessel basis [28]. This pH gradient has relevance to tumor therapy either as a target or a barrier. While many groups have targeted proteins implicated in tumor acidification [29] or designed pH-sensitive carriers to exploit this physiological difference [30; 31], pH can also have a deleterious effect on common therapeutics or peptide ligands with moieties sensitive to slight changes in pH.

### **1.1.2.2 Interstitial Fluid Pressure**

The leakiness of incomplete vessels allows convective fluid flow from the vessel into the tumor at the periphery [32]. Since tumors lack a functional lymphatic system to clear this fluid



[33], the IFP towards the center of the tumor [34] increases as a result. The IFP reaches a maximum at the center of the tumor and drops sharply near the tumor edge, promoting outward fluid flow [35]. There is also minimal convective flow at the tumor center [35] due to balancing of vascular fluid pressure (VFP) and IFP. This leads to diffusion as the dominant force for transport of molecules into the tumor at the center. While small molecules can enter the tumor via diffusion at the tumor center, these molecules are also rapidly cleared from the tumor region via diffusion and convection [36]. Alternatively, the lack of convective flow at the tumor center prevents substantial extravasation of macromolecules from central vasculature due to low diffusion coefficients of high MW constructs. Though the high permeability and low convection allows retention of macromolecules through the enhanced permeability and retention (EPR) effect [37], the low penetration distance greatly reduces the effect of macromolecular drug delivery for intratumoral drug delivery [38]. Additionally, high permeability and low IFP at the tumor periphery does allow for extravasation of macromolecular constructs at the tumor margin through convective transport, but outward fluid flow from the tumor reduces retention in this region [32]. The high IFP serves as a formidable barrier for tumor therapy. These observed transport behaviors caused by IFP reduce the efficacy of macromolecular drug delivery strategies by reducing drug exposure at tumor cells far from the vasculature.

### **1.1.2.3 Endothelial Cells**

Angiogenic tumor vasculature exhibits several phenotypic differences due to the consistently high levels of VEGF and prolonged remodeling of tumor blood vessels. This rapid vessel turnover makes the endothelial cells more susceptible to agents targeting cells with high rates of mitosis. The presence of VEGF causes tumor vasculature to exhibit similar characteristics to normal angiogenic vessels and thus upregulate complexes implicated with angiogenesis such as Tie-2 [39; 40],  $\alpha\beta 3$  integrin [41], MMP-2/9 [42; 43], and CD13 [44], all of which generate a phenotypic difference between tumor vessels and normal vessels. The endothelium is also fenestrated in areas with high VEGF levels [45; 46], making tumor vessels

more permeable to therapeutic compounds [37]. These differences in endothelial cells can all be manipulated for drug delivery using both active and passive delivery strategies.

## ***1.2 Cancer Therapy: Strategies and Challenges***

The majority of cancer patients that undergo therapy receive a combination of surgery, external beam radiation, and chemotherapy. Each of the approaches has positive and negative tradeoffs, the importance of which vary depending on the tumor type and stage of progression. Surgery, the most direct approach, is a highly successful method for tumors that are physically accessible and exhibit clearly defined margins that results in complete removal of pathological tissue. However, surgery can be challenging, ineffective, or even debilitating for deep tissue tumors such as glioblastoma, metastatic tumors, or other invasive tumors that cannot be removed without significant disruption to surrounding healthy tissue [47; 48]. Additionally, surgery is limited to visible primary tumors and not useful for removing micrometastases, increasing potential for offsite tumor growth.

External beam radiation is a complimentary non-invasive method for inaccessible tumors and infiltrating tumors. External beam radiation is employed to confer a lethal dose of gamma radiation to rapidly-dividing tumor cells via x-rays. It also can target cells at the tumor margin. This commonly-used method is highly successful in promoting tumor shrinkage and can facilitate surgical resection of the tumor. However, external beam radiation is rarely used by itself as repeated application of this method is hampered by the high doses of radiation used. Adverse side effects are common as the dose delivered to tumor tissue can confer lethal effects to healthy proliferating cells, especially with high-voltage x-rays used for deep-tissue targeting. In order to combat this off-site cytotoxicity, improvements have been made to better localize radiation to the tumor site such as intensity modulation [49] or image-guiding [50]. Additionally, this localized approach is less useful for off-site targeting of metastases due to a limited area of exposure.

Chemotherapy involves the administration of cytotoxic chemical agents to selectively disrupt the tumor either by selectively killing tumor cells or tumor vasculature. While

chemotherapeutics can be administered either as a systemic bolus injection or as a local depot proximal to the tumor, the vast majority of chemotherapeutics are administered systemically. Thus, the remainder of this section will focus on systemic chemotherapy for tumor therapy.

### **1.2.1 Systemic Chemotherapy**

The goal of systemic chemotherapy is to deliver cytotoxic compounds from the vascular compartment to the intracellular sites on pathogenic tumor cells while minimizing exposure to healthy tissues. Although the concept is simple, there are numerous transport barriers preventing this. For the compound to reach the tumor, it must traverse through the vessel wall, penetrate into the interstitium towards tumor cells, traverse the tumor cell membrane, and reach the intracellular site of action [51]. Furthermore, physiological differences in the tumor restrict these steps such as high IFP and long diffusion distances, making this complex transport situation even more challenging [35].

Both small-molecule chemotherapeutics and macromolecular drug carriers have been used to target tumor cells, and each has advantages and disadvantages given these transport barriers. Small-molecule therapeutics have the advantages of rapid diffusion, significant tumor penetration, and cell uptake at the tumor site but the disadvantages of short plasma half-life, fast tumor clearance, and significant accumulation in healthy tissues. Conversely, macromolecular therapeutics have the advantages of long plasma half-life, slow tumor clearance, and low accumulation in healthy tissues but the disadvantages of slow diffusion, minimal tumor penetration, and low cell uptake. Thus, a successful vehicle for tumor drug delivery should incorporate as many of the advantages of each class of therapeutics as possible.

#### **1.2.1.1 Small-Molecule Chemotherapeutics**

Small molecule chemotherapeutics are cytotoxic agents that preferentially target replicating cells, including those within the tumor. Most drugs in this class are hydrophobic, cyclic compounds that disrupt replicating cells by damaging DNA (e.g. alkylating agents such as Cisplatin) [52], disrupting DNA replication (Camptothecin) [53], modifying microtubule formation

(e.g. taxanes such as Paclitaxel) [54; 55], inhibiting cell cycle progression [56], or intercalating with DNA strands (Doxorubicin) [57]. Additionally, other small molecule therapeutics such as specific inhibitors (Cilengitide) [58; 59] or vascular disrupting agents (Combrestatin) [60] show specific binding to the tumor and tumor vasculature. Typically, a combination of these drugs is used to exploit different mechanisms, preventing selection of tumor cells resistant to a particular pathway and reducing the potential for drug resistance.

Typically, small-molecule therapeutics are administered systemically. This permits delivery to both vascularized primary tumors and sites of metastases. Their low molecular weight (MW) will allow diffusion from the vessels in the central tumor regions, and the small size will allow rapid intracellular uptake likely through facilitated diffusion. However, this approach is fraught with challenges. First, small-molecule therapeutics delivered systemically are quickly cleared from the bloodstream resulting in low plasma half-life. Second, these agents distribute throughout the body and affect normal tissues along with cancer cells such as cardiac, gastrointestinal, and bone marrow tissue [61; 62]. Third, some tumors exhibit multidrug resistance through (1) raised expression of P-glycoprotein to pump small molecules from the intracellular space [63] or (2) low radio- or chemosensitivity [64]. Fourth, tumor cells exist in different points of the cell cycle, conferring heterogeneous sensitivity to a specific chemotherapeutic. Fifth, angiogenic vasculature promotes incomplete tumor coverage [65] and high interstitial fluid pressure, leading to heterogeneous drug distribution, low penetration distance into the tumor [33; 35; 51; 66] and rapid clearance of chemotherapeutics from the tumor due to outward fluid flow. These all lower the effectivity of a chemotherapeutic dose.

#### **1.2.1.2 Polymeric Delivery of Chemotherapeutics**

Polymers have recently gained attention as macromolecular carriers capable of improving chemotherapeutic delivery to tumors [67; 68]. Polymer conjugates for drug delivery are typically large hydrophilic molecules linked to a therapeutic agent that (a) improve the solubility over other formulations, (b) increase plasma half-life, (c) reduce toxicity, (d) evade multidrug

resistance, and (e) add functionality [67; 69-71]. These conjugates can target tumors either “passively” through the EPR effect or “actively” through a triggered stimulus or affinity towards the site of therapy [68; 72-74]. All of these attributes have led to higher anticancer efficiency for passively targeted polymer conjugates compared to free drug [68; 72; 75-78].

Block copolymers represent a second-generation carrier that consists of at least two blocks with differing polarity [79; 80]. These block copolymers can self-assemble into high MW nanoparticles through hydrophobic intra- and intermolecular interaction [81]. Self-assembly occurs when polarity differences between the two blocks, along with other factors such as charge density, pH, and salt concentration [82; 83], generate a balance between intramolecular and intermolecular repulsive and attractive forces. This balance leads to phase separation [84] through partitioning of the hydrophobic and hydrophilic blocks. Under the correct conditions, phase separation leads to self-assembly of nanoscale polymer structures such as vesicles [85] and micelles.

Polymeric micelles have received great attention as potential carriers for hydrophobic drugs or genes [72; 76; 86-89]. The dense hydrophobic core encapsulates hydrophobic compounds, increasing the solubility of these compounds in an aqueous environment, while the diffuse hydrated corona shields the drugs through an extended layer [76]. Polymeric micelles typically have a critical micelle concentration (CMC) lower than surfactant micelles, allowing for self-assembly at concentrations relevant for drug delivery [90]. Micelles also retain the other advantages of polymeric delivery such as prolonged plasma half-life and increased accumulation through the EPR effect [91] with additional benefits such as higher drug loading through both covalent and non-covalent interaction. The size of a typical micelle ( $R_h < 100$  nm) also allows it to evade scavenging through the reticuloendothelial system, providing further potential of increased plasma half-life [92]. Furthermore, the predictable self-assembly behavior allows for incorporation of functional groups in the corona that range from passive groups such as PEG [72; 88; 93] to active groups such as targeting ligands [75; 94; 95] or cell-penetrating peptides [96]. However,

this high MW also leads to short penetration distances and poor spatial distribution, supporting the use of polymeric micelles for targeting regions proximal to the blood vessel [38].

### **1.2.1.3 Peptide-Based Drug Delivery**

Recent advances in peptide-based polymer design have led to the use of polypeptides as high MW carriers for anticancer therapy. There are several inherent advantages to using polypeptides as opposed to other synthetic polymers. First, polypeptides comprised of natural amino acids are more likely to maintain biocompatibility throughout the degradation process, breaking down into metabolites excreted through normal pathways rather than synthetic monomers [97]. Second, genetically encoded peptides exhibit precise MW and sequence uniformity, both of which affect pharmacokinetics, transport, biodistribution, and degradation [98-100]. Third, moieties such as short targeting peptide segments or unique conjugation sites can be incorporated at the genetic level at predetermined locations along the peptide chain [101; 102]. Fourth, amphiphilic polypeptides can be used to encapsulate drugs in self-assembling structures such as micelles and vesicles similar to those made from synthetic polymers [101; 103; 104], exhibiting similar functionality with the additional benefits described above. Fifth, peptides with defined sequences can be used to create more complicated secondary structures via self-assembly, some of which show potential for drug delivery applications [105].

### **1.2.1.4 Stimulus-Responsive Polymers**

Stimulus-responsive polymers have been designed to improve drug accumulation in specific regions within the body. These carriers respond to environmental or external cues to optimize carrier properties or activity for its current environment. Control over carrier activity is embedded within the “smart” polymer and controlled either by internal or external stimuli. Internal stimuli are based physiological differences between tumor and normal tissues such as pH [106], while external stimuli such as applied heat [107-110] typically promote changes in the carrier in order to direct its behavior. This sensitivity to stimuli is incorporated through polymer composition [111-114]. Carrier manipulation in response to either endogenous or exogenous stimuli allows

optimization of transport characteristics in each stage or incorporation of triggered functionality, helping to get drug to the tumor more efficiently.

## **1.2.2 Antiangiogenic/Antivascular Therapy**

An alternative strategy to deliver compounds directly to tumor cells is manipulation of tumor blood vessels [115]. Angiogenic vessels are an attractive target as they support tumor growth [116], generate many of the transport barriers such as high IFP [33], and contribute to tumor heterogeneity by promoting uneven perfusion and hypoxic regions [117]. Thus, attacking these vessels will restrict tumor growth as well as reduce the barriers restricting drug delivery to individual tumor cells. While many strategies have been introduced for restricting angiogenesis such as slowing tumor angiogenesis through inhibitors [118] or improving drug delivery to the tumor by reorganizing the vessels [119], our focus is antivascular therapy by selectively killing endothelial cells in the tumor region [120]. Experimental data shows that disruption of one endothelial cell can result in cytotoxicity of 1000 tumor cells [121], and luminal accessibility of tumor endothelial cells represents a significant transport advantage. Angiogenic tumor vessels are also an attractive target from a physiological perspective due to compositional homogeneity between tumors, upregulation of angiogenic markers, and reduced multidrug resistance [122]. Thus, endothelial cells are a more feasible target than individual tumor cells due to ease of transport and ability to target different receptors.

### **1.2.2.1 Targeted Small Molecule Therapeutics**

A key to antivascular targeting is preferentially localizing the drug to the vasculature. Small-molecule therapeutics with effects on microtubule formation selectively restrict cell division in proliferating endothelial cells in angiogenic vessels [54; 123] while others show affinity for upregulated markers and receptors in tumor vasculature such as the  $\alpha\beta3$  integrin [60]. These methods have shown great success in murine models with significant effects on tumor regression [124]. Some of these drugs have also led to off-site toxicity similar to untargeted small molecule

therapeutics [125]. Difficulties in localizing small molecule drug to either the vasculature or the tumor region itself has led to development of secondary vessel targeting methods.

### **1.2.2.2 High-Affinity Macromolecules**

As previously described, macromolecules are useful for systemic drug delivery. Macromolecules either with inherent or engineered affinity for biological markers can be used to specifically target angiogenic vessels. Targeting vessels incorporating high-affinity macromolecules such as antibodies, homopolymers, micelles, and liposomes has proven effective in improving localization and improving tumor control [126-128]. The main difficulty in targeting tumor vasculature is the ubiquity of these targets; those upregulated within tumor vessels are also present in angiogenic normal vasculature with low basal levels of expression. A carrier with low affinity for its target ( $K_d > 10^{-6} \text{ M}^{-1}$ ) may not specifically bind within the tumor [129], but a carrier with high affinity for its target may also preferentially accumulate in regions with low receptor expression. This can lead to accumulation in healthy vessels and presents a tradeoff between affinity and specificity. To circumvent this limitation, the ideal carrier for vascular targeting should restrict its activity to the tumor vasculature and remain inactive in normal circulation.

### **1.2.3 Hyperthermia**

Applied heat, or hyperthermia, has been identified as a adjunct method for cancer therapy. Hyperthermia has been associated with promoting cytotoxicity [130] and enhancing radio- and chemosensitivity within tumor tissue [131-133]. Additionally, hyperthermia has been associated with improved tumor oxygenation, macromolecular extravasation, and improved cellular uptake through activation of the heat shock proteins [134-138]. All of these effects make it a desirable adjunct method of cancer therapy. As a result, much work has been done to establish applied hyperthermia as a clinically-relevant technique. Recent studies have investigated combination treatment strategies combining chemotherapy and hyperthermia for different tumor types such as skin, breast, brain, bladder, head and neck, and cervical cancers [139] while others



have aimed towards developing different drug carriers for use in tandem with applied hyperthermia.

### **1.2.3.2 Physiological Effects of Hyperthermia**

Typical human cells have a breaking point at 43.5°C with cell death increasing 2-fold per degree over this temperature and decreasing 2-4-fold per degree below this temperature [140; 141]. Based on this, localized hyperthermia can be separated into low-temperature hyperthermia (39 – 42 °C), high-temperature hyperthermia (43 – 45 °C), and thermal ablation (47 – 50 °C) [142], each resulting in different physiological effects. This section will focus primarily on low- and high-temperature hyperthermia.

Low hyperthermia does not promote noticeable changes, affect cell death, or promote vascular shutdown at  $T < 42$  °C, but it can affect the cytotoxicity of different therapeutic compounds [137; 143; 144]. Low hyperthermia has also been associated with improved blood flow and oxygenation, and further studies have shown secondary effects such as an increased immune response [135]. T-cell and NK cell activation [145], upregulation of proteins such as TNF- $\alpha$  or L-selectin [146], and recruitment of macrophages, lymphocytes, and granulocytes [147] promotes immune cell migration and autologous cytotoxicity. Conversely, high temperature hyperthermia confers direct cytotoxicity as its primary physiological effect. There will also be greater activation of heat shock proteins at these temperatures, leading to both increased cellular uptake and lower multidrug resistance. However, this is accompanied by an increase in thermotolerance. There also is disruption of endothelial cells on angiogenic vessels leading to increased pore formation and permeability [148]. While this can promote antitumor effects in the short term, it can also lead to development of hypoxic regions, increased acidosis, and lower pH within the tumor.

The physiological response in each temperature range must be taken into account when choosing the proper regime for a particular treatment strategy. Each of these ranges has different advantages and disadvantages based on the desired therapeutic effect. For example,

combination antivasular therapy for accessible tumors benefits from low-temperature hyperthermia (39 – 41 °C) as low temperatures can be applied for times over 1 hour and lower temperature reduces risk of thermotolerance [131]. Strategies utilizing heat as an external stimulus may also benefit from low-temperature hyperthermia due to retention of normal tumor physiology. Conversely, localized hyperthermia targeting tumor cells may improve with high-hyperthermia ( $T < 43.5$  °C) due to vascular disruption, short-term increased permeability, improved cellular uptake [149], and induced cytotoxicity away from the blood vessels [149-151].

### **1.2.3.1 Clinical Application of Hyperthermia**

There are important considerations relevant to clinical hyperthermia application in addition to the physiological effects. First, localized, regional, or whole-body hyperthermia is chosen based on the specific treatment strategy and the target tissue [143]. Localized hyperthermia targets only the primary tumor and minimizes heating to surrounding normal tissues; regional hyperthermia targets larger regions of the body such as large internal cavities or entire limbs; and whole-body hyperthermia is used to heat the entire body and is useful for highly metastatic tumors [152].

Second, a heating method must be selected to selectively heat the selected tissue region. The two main technologies currently used to heat tumors, RF arrays and ultrasound, are both based on electromagnetic radiation. RF waves and ultrasound are used both for superficial tumors < 4 cm deep and deeper tissues > 5 cm deep [142]. RF arrays are simpler to operate and can heat a wider region, but ultrasound provides the advantage of tissue penetration and image guiding for specific regional heating. Newer technologies such as highly-focused ultrasound are in development for thermal ablation in deeper tissues [153] and may be useful for milder hyperthermia application. These techniques typically incorporate some form of thermometry to provide thermal feedback. Direct measurement using topical sensors on the skin or invasive sensors implanted into the tumor allows for temperature monitoring and correlation of heating to treatment outcome . Noninvasive thermometry, typically performed using MRI, provides similar

information but does so in a 3D fashion, allowing for greater control and observation of temperature throughout the tumor during a heating time course [154-156].

Third, there are other practical limitations based on physiological restrictions. One limitation is the heterogenous composition of tissue within the tumor region. As different tumor types will heat at different rates, it is challenging to reach a steady-state temperature throughout the entire tumor within a specific temperature window. This is especially true for deeper tumors due to EM absorption by different tissue layers in the path of the wave. Another limitation is the presence of unheated blood flowing through the tumor. Large, turbulent vessels can act as a heat sink due to rapid blood flow near the heated mass [157]. This may result in imperfect heating of the tumor even in a steady-state condition. One strategy for counteracting this effect is targeting the tumor margin to heat the blood flowing into the tumor. This can reduce the heat sink effect and thermal heterogeneity, but this may also cause varying effects to normal tissue surrounding the tumor depending on the heating strategy. A third limitation is patient comfort. In many cases, the time of hyperthermia application and the power of the applied wave is limited not by tissue considerations but rather patient tolerance, especially a concern for tumors situated near bone. There also can be development of superficial burns from the technique, but these occur in a small number of patients in clinical trials.

### **1.2.3.3 Thermally-Responsive Drug Carriers**

Systemic drug carriers with a built-in thermal response have been developed for use with hyperthermia. For example, thermally-sensitive liposomes have been developed to melt at temperatures associated with low-temperature hyperthermia [108; 158]. At normothermic conditions, these liposomes exhibit high plasma half-life and remain intact within the vasculature [150]. With localized hyperthermia, the liposomes melt and release their payload within the tumor. This allows for greater penetration distance of the small molecule compared to the liposome as well as greater uptake and antitumor activity. Other stimulus-responsive compounds for systemic therapy include polymers and polypeptides that exhibit an inverse phase transition at a specific

transition temperature ( $T_t$ ); at  $T > T_t$ , these constructs transform from a soluble state to an insoluble state. Carriers that exhibit a  $T_t$  from 37 °C – 42 °C such as the synthetic polymer pNIPAAm and the recombinant polypeptide Elastin-like Polypeptide (ELP) [110; 159; 160] have been shown to improve tumor accumulation 2-fold in response to heat [161]. ELP will be described in further detail in section 1.4.

## **1.3 Ligand-Receptor Binding**

### **1.3.1 Thermodynamic Overview**

Ligand-receptor binding facilitates molecular recognition of biological targets, and important processes such as antibody-antigen binding, remote cell signaling, protein transcription, and cell adhesion all depend on specific ligand-receptor binding [162]. Binding ability is defined either by the affinity constant,  $K$ , or the dissociation constant,  $K_d$ . These two values are reciprocals of each other and both are used to describe the strength of a particular interaction. A lower  $K_d$  represents a stronger interaction while a higher  $K_d$  represents a weaker interaction. Most naturally-occurring specific interactions occur in the nanomolar range (i.e. antibody-antigen interaction [163]) but can decrease to femtomolar range (i.e. biotin-avidin [164]). While there is not a universal  $K_d$  representing the cutoff between passive and active macromolecules, previous work has shown that antibodies show specific binding behaviors at  $K_d > 10^{-6}$  [129].

$K_d$  is directly related to the change in Gibbs free energy following binding:

$$\Delta G = -RT \ln\left(\frac{1}{K_d}\right) = \Delta H - T\Delta S \quad (1.1)$$

where  $K_d$  represents the association constant,  $R$  represents the ideal gas constant,  $T$  represents temperature,  $\Delta H$  is the change in enthalpy, and  $\Delta S$  is the change in entropy. When  $\Delta G < 0$ , the binding event will result in a lower energy state and becomes favorable. Based on this relation, either a decrease in enthalpy or an increase change in entropy will favor ligand-receptor interaction.  $H$  will decrease through additional non-covalent interactions, favoring the reaction. However,  $S$  will typically decrease when binding events restrict degrees of freedom. Thus, while

strong non-covalent interactions will promote a spontaneous binding event, a decrease in entropy can offset this interaction. This is seen in the increase in binding affinity of constrained versus flexible ligands [165]. This codependence on both enthalpic and entropic contributions requires both be taken into account when designing a ligand for receptor-mediated targeting. Additionally,  $K_d$  for a given reaction is temperature-dependent due to entropic contributions.

### 1.3.2 Multivalency Effect

At its simplest definition, the multivalency effect is the increase in avidity resulting from the simultaneous interaction of multiple ligands with multiple receptors [162; 166]. This effect has been observed empirically for many different ligand-receptor pairs [167-169] and is useful for transforming low-affinity monovalent ligands into high-avidity multivalent constructs capable of targeting specific receptors (Fig. 3). The multivalency effect is most pronounced with constructs exhibiting an increased number of accessible ligands binding to a surface with receptor overexpression.

Despite the wide acceptance of this phenomenon, the thermodynamic explanation of multivalency is debated in the literature. One proposed explanation relates the increase in overall avidity to the affinity of the individual ligand-receptor interactions [162]. The free energy of a monovalent interaction can be described as:

$$\Delta G = -RT \ln(K) \quad (1.2)$$

where  $K$  represents the association constant,  $R$  represents the ideal gas constant, and  $T$  represents temperature. Based on this relation, the free energy of a multivalent interaction can be described as:

$$\Delta G_{multi} = -RT \ln(K_{multi}) = -RT \ln\left(\frac{K_{mono}}{\alpha N}\right) \quad (1.3)$$

where  $K_{multi}$  is the avidity constant,  $K_{mono}$  is the affinity constant,  $N$  is the number of simultaneous ligand-receptor interactions, and  $\alpha$  is cooperativity. By rearranging these equations, we can

describe the theoretical avidity of a particle based on the number of accessible ligands according to the equation:

$$K_{multi} = (K_{mono})^{\alpha N} \quad (1.4)$$

In this model, the avidity of a multivalent interaction increases by the power of the number of individual ligand-receptor interactions. A different model approaches multivalency not as a cumulative effect of individual interactions but rather as a single interaction between the multivalent particle and the functionalized surface [166]. In this model, the multivalent interaction is defined by “functional affinity” and defined by the ratio of free and bound receptor:

$$K_{avidity} = \frac{[R_o] - [R]}{[R][L]} = \frac{1}{IC_{50}} \quad (1.5)$$

where  $R_o$  is the total concentration of receptor,  $R$  is the amount of free receptor, and  $L$  is the amount of free ligand. At a given temperature,  $K_{avidity}$  is the reciprocal of  $IC_{50}$ , the concentration at which 50% of receptors are occupied. This relation describes the empirical behavior similar to monovalent binding, but the equation does not describe the differences in monovalent affinity and multivalent avidity. One aspect of the multivalency effect not explicitly described by either of these models is geometric restriction. For a multivalent construct to exhibit this effect, the multivalent construct must be sufficiently large to permit multiple attached ligands to interact simultaneously with receptors. While rational design of multivalent constructs can incorporate selection of tether lengths and particle diameter based on ideal calculations, it is difficult to predict the exact behavior of constructs given the stochastic nature of polymer lengths in solution. Given the uncertainty of both the thermodynamic model and geometric parameters, many constructs used for multivalent interactions require empirical evaluation even with precise rational design.

### 1.3.3 Examples of Ligand-Receptor Systems for Tumor Therapy

Multivalency is of great interest in the design of “smart” materials as it has also been used as a method to create high-avidity inhibitors [170; 171] and targeted nanoparticles for biomedical applications [167; 169; 172; 173]. While countless ligand-receptor systems have been

identified for use in therapeutic targeting applications, we are focusing on two specific pairs associated with angiogenic vasculature: (1)  $\alpha\beta3$  integrin – RGD tripeptide [174] and (2) CD13 receptor – NGR tripeptide [44].

### 1.3.3.1 $\alpha\beta3$ Integrin – RGD

First, the  $\alpha\beta3$  integrin is a dimeric,  $\text{Ca}^{2+}$ -dependent cell receptor associated with vitronectin adhesion and associated cell signaling pathways [175]. This well-studied receptor has been identified as a requirement for angiogenesis [41; 176] although this claim has recently been debated in the literature [177]. Regardless of its role, this receptor is downregulated in normal vasculature but upregulated in tumor vasculature [178], making it an attractive target for

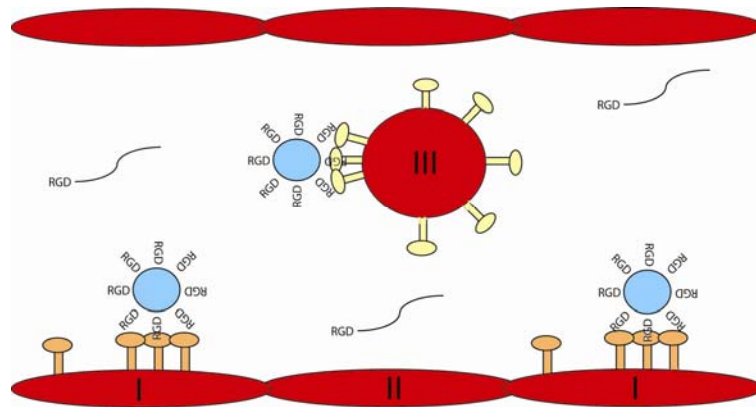


**Figure 3: Schematic of multivalent targeting using low-affinity peptide ligands. Monovalent ligand presentation does not promote specific interaction, but multivalent presentation can promote specific interaction with endothelial cells expressing the cognate receptor (I) compared to other endothelial cells not expressing these receptors (II). This high avidity can also promote binding to different receptors on healthy cells in the bloodstream (III) or other areas of angiogenesis, leading to offsite binding.**

antivascular therapy. While monoclonal antibodies targeting  $\alpha\beta3$  in tumor vasculature have been successful both clinically and commercially [179], another common approach for targeting is through the RGD tripeptide. This ligand, derived from a sequence found in the 3<sup>rd</sup> loop of fibronectin [180], exhibits low affinity in monovalent, linear form ( $K_d > 10^{-6}$ ) [165]. Researchers have attempted to circumvent this difficulty by increasing the affinity and specificity of the carrier for the  $\alpha\beta3$  integrin by forcing cyclic conformation of different sizes [165], using the multivalent

effect with liposomes [94] or micelles [181; 182], or re-engineering the tripeptide with different flanking residues [183].

Previous clinical trials involving RGD have been unsuccessful [184], and while the exact reasons for these failures is unknown [185], one reason may be promiscuous binding as RGD and its derivatives exhibit affinity for other integrins including  $\alpha 5\beta 1$ ,  $\alpha v\beta 5$ , and  $gpIIb\beta 3$  [180; 186]. Thus, the increase in affinity may facilitate binding to healthy tissues expressing basal levels of  $\alpha v\beta 3$  or other integrins, reducing the effectiveness of the  $\alpha v\beta 3$ -RGD interaction for specific targeting of tumor vasculature. Despite these recent challenges, integrin targeting through the RGD ligand remains a promising strategy for tumor targeting [187].

#### **1.3.3.2 CD13 – NGR**

CD13, identical to Aminopeptidase-N [188], is a Zn-mediated metalloprotease associated with many functions such as enzymatic reactions, cell signaling, viral entry, endocytosis, and cell adhesion [189]. It is a homodimer [190] that is expressed on the plasma membrane of angiogenic endothelial cells [44], myeloid cells at most stages of their development (neutrophils, monocytes/macrophages, etc) [191] and immature lymphoid cells. It also circulates in the plasma in soluble, active form (sCD13) at a higher concentration in cancer patients [192; 193]. This protein exists as two isoforms with a different one associated with angiogenic tumor vessels [128]. While the exact role of the CD13 isoform in normal tissues is unclear, the isoform present in tumors has gained attention as a possible site for vascular targeting due to affinity towards the NGR tripeptide [128]. NGR shows low affinity for CD13 in linear form, but high affinity/avidity for CD13 in both cyclic (cNGR) [128] and multivalent forms [194; 195]. While NGR has not been investigated as thoroughly as RGD, it is unclear if these carriers interact with CD13 expressed on healthy blood cells or sCD13 [128] and if these interactions can lead to systemic toxicity [196].

Similar to  $\alpha v\beta 3$ , targeting CD13 high avidity constructs may be beneficial within tumor vasculature but harmful outside of it. However, uncertainty regarding the binding mechanism



between NGR and CD13 mitigates some of this risk. Initially, NGR was thought to interact directly with CD13 on angiogenic vasculature and receptor-positive tumor cells to promote specific accumulation [44]. However, there has been recent debate over the mechanism of NGR accumulation within tumor vasculature due to recent evidence that CD13 can convert NGR into an intermediate termed *iso*-DGR with affinity for  $\alpha v\beta 3$  [197]. This potentially allows NGR to target vessels in a fashion similar to a prodrug and explains the reduction in off-site targeting despite widespread CD13 expression. Regardless of the mechanism, use of the NGR-CD13 ligand-receptor pair has shown improved specificity for the tumor *in vivo* [127; 198] and represents another promising system for multivalent targeting of tumor vasculature.

### **1.3.3.3 Limitations of Multivalent Targeting Strategies**

Despite the push to develop carriers with maximum affinity/avidity as a method to specifically target tumor vasculature, this strategy is somewhat limited. First, carriers specific for tumor-associated antigens with  $K_d < 10^{-7}$  M will show enhanced tumor accumulation over passive carriers with maximum accumulation occurring at  $K_d < 10^{-9}$  M [129]. Since the widely-used high-affinity cyclic RGD and NGR already exhibit the ability to specifically bind to their cognate receptor, raising the affinity through the multivalency effect will likely not increase specific accumulation any further. Second, high affinity constructs may bind to regions with basal levels of receptor expression and increase the risk of systemic toxicity through offsite accumulation. Third, high particle avidity for antigens located along the endothelium creates a binding site barrier, further preventing penetration into the tumor. This tradeoff limits the use of targeted tumor carriers to receptors proximal to the vasculature and not directly to tumor cells. While multivalent strategies show promise, more advancement is needed to overcome these limitations for translational success.

## **1.4 Elastin-Like Polypeptide**

ELP is a rationally-designed, genetically-encoded recombinant protein derived from mammalian tropoelastin [199]. It consists of the repeat pentapeptide unit Val-Pro-Gly-Xaa-Gly

where Xaa, the guest residue, is any amino acid besides proline. ELP solutions exhibit an inverse phase transition temperature ( $T_t$ ); it is soluble at  $T < T_t$  and insoluble at  $T > T_t$ . The  $T_t$  is based on guest residue composition and affected by molecular weight (MW), concentration, and solution ionic strength. These parameters can be tuned at the genetic level by alteration of guest residue composition or MW through the design process termed recursive directional ligation (RDL) [200]. ELP is expressed at high volumes in *E. coli* and is easily purified using non-chromatographic methods with inverse transition cycling (ITC) [201].

Precise composition, strict sequence requirements, and predictability of effects on  $T_t$  facilitate rational ELP design at the gene level. A good starting point for the design of ELPs comes from the studies of Urry and co-workers, who quantified the effects of each of the guest residues on transition temperature by determining the free energy change involved in the transition of ELPs containing a single guest residue [114; 199]. These studies clearly illustrated the effects of hydrophobicity on the  $T_t$  of an ELP and have facilitated the rational design of many different ELP constructs.

### **1.4.1 ELP Drug Delivery Applications**

ELPs have shown great potential as systemic drug carriers for tumor drug delivery in both normothermic and hyperthermic approaches [101; 102; 160; 202; 203]. For normothermic application, ELP retains the advantages of hydrophilic polymers for systemic tumor therapy. Their high and precise MW, controlled composition, monodispersity, and polypeptide backbone promotes longer plasma half-life, predictable biodistribution and pharmacokinetics, and biocompatibility. In treatment regimes in a preclinical mouse model, a single dose of ELP nanoparticles loaded with Doxorubicin (Dox) showed complete tumor regression at a dose below the upper toxicity limit of Dox (20 mg/kg) [202]. The LCST is also retained in serum [110], allowing for external control over the state of ELP and unique applications for tumor therapy using hyperthermia treatment. For example, applied hyperthermia will lead to formation of aggregates within the tumor and enhance tumor accumulation of ELP [105]. These aggregates formed in

vessels at  $T > LCST$ , leading to a 2 - 3 fold increase in accumulation. Cycling of the temperature and reversible ELP aggregation can further increase accumulation in the tumor due to an increase in local concentration and subsequent increase in vessel flux [160; 161]. Despite this increase, high MW ELP aggregate remains in the vascular and perivascular regions following the thermal transition, implying that thermally-dependent ELP constructs are best suited for targeting tumor vasculature.

### 1.4.2 Elastin-Like Polypeptide Block Copolymers

ELPs with different LCSTs can be fused seamlessly at the genetic level and coexpressed as ELP diblock copolymers (ELPBC) [204]. We have constructed ELP[V<sub>1</sub>A<sub>8</sub>G<sub>7</sub>]/ELP[V<sub>5</sub>] (ELP2/ELP4) block copolymers that form spherical micelles between 33 - 40°C with hydrodynamic radius ( $R_h$ ) between 25 - 35 nm [101] (Fig. 4). These constructs provide an advantage over other polymeric micelles [72; 88] and thermoresponsive block copolymers [205; 206] due to its single-step synthesis, aqueous purification, biocompatible nature, exact composition from the genetic backbone, and precise MW of each block. Each of the ELP blocks

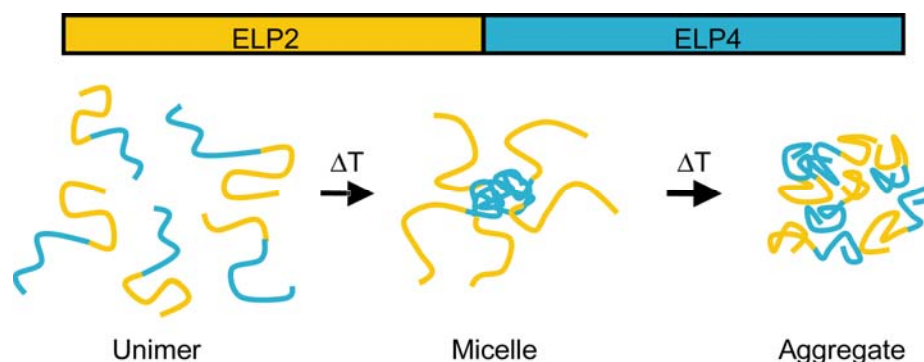


**Figure 4: Diagram of ELP2/ELP4 Block Copolymer. At  $T < CMT$ , both ELP blocks are hydrophilic and the ELPBC persists as soluble unimer. At  $CMT < T < T_t$ , ELP4 will become hydrophobic but ELP2 will be hydrophilic, resulting in nanoscale micelle formation. At  $T > T_t$ , both blocks will become hydrophobic resulting in microscale aggregate formation.**

forming the block copolymer will transition independently. At temperatures below the LCST of both blocks, ELPBCs are in soluble unimer form. At temperatures between the LCST of the two blocks, ELPBC will self-assemble into monodisperse spherical micelles. At temperatures above the LCST of both blocks, ELPBC will form micron-sized aggregates similar to homopolymeric

ELP. If the hydrophilic-to-hydrophobic MW segment ratio is .5 to 2, then the ELPBC will form stable micelles at temperatures between the two LCSTs [101] (Fig. 5). The temperature at which self-assembly occurs controlled both by the composition and MW of the hydrophobic block as well as the concentration of ELPBC in solution. The addition of exogenous amino acids or low MW compounds may also affect this self-assembly due to changes in coronal charge or core hydrophobicity [207; 208].

ELP Block Copolymers		Segment Ratio
ELP2-64	ELP4-120	.5
ELP2-64	ELP4-90	.66
ELP2-64	ELP4-60	1.0
ELP2-96	ELP4-60	1.5
ELP2-128	ELP4-60	2.0

**Figure 5: ELP block copolymers that form micelles in response to heat. Each ELPBC exhibits a different hydrophilic-to-hydrophobic segment ratio between .5 – 2.0.**

## ***1.5 Affinity-Modulation Targeting***

### **1.5.1 Overview**

Both the successes and side effects associated with antivasular targeting support the need for a carrier that interacts with tumor vasculature but remains inert in healthy tissues. To accomplish this, we have devised a strategy termed Dynamic Affinity Modulation (DAM) which combines ELPBC, hyperthermia, and the multivalency effect to spatially restrict carrier activity to the tumor vasculature while limiting interaction with normal vasculature. In this strategy, a low-affinity ligand is first attached to the hydrophilic block at the genetic level. This ligand-ELPBC persists as a monovalent unimer at low temperatures and self-assembles into a multivalent micelle at high temperatures (Fig. 6). The temperature threshold at which this transition occurs is the critical micelle temperature (CMT), and hyperthermia can adjust the temperature of the tumor region above and below the CMT. By triggering self-assembly of the ligand-ELPBC using applied hyperthermia, the binding activity of the ligand-ELPBC can be restricted through the multivalency

effect and effectively turned “on” and “off” reversibly with applied heat. This approach intends to harness the benefits of vascular targeting and polymeric drug delivery with ligand-functionalized, high-avidity micelles in the tumor and low-affinity polymeric drug delivery in healthy vasculature.

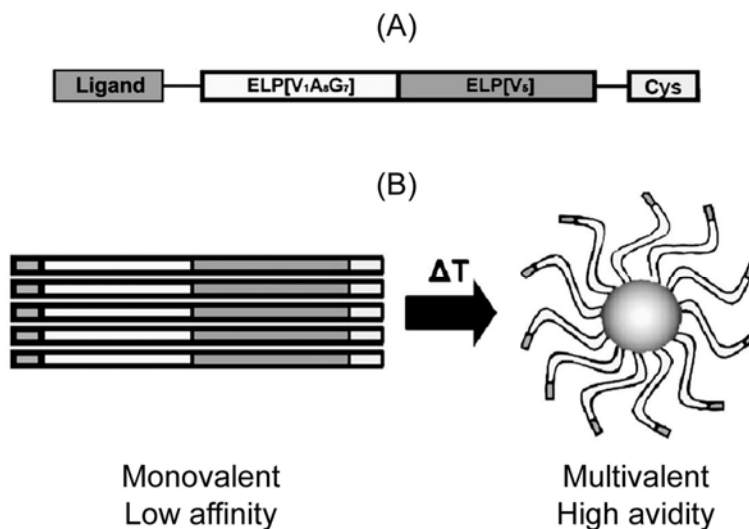


**Figure 6: Schematic of dynamic affinity modulation using functionalized ELPBCs. (A) Existing ELPBCs are modified at the gene level to incorporate a low-affinity ligand at the hydrophilic terminus and a unique binding site at the hydrophobic terminus. (B) The hydrophobic block will become insoluble at temperatures above the CMT causing self-assembly into micelles. These micelles will protect hydrophobic compounds in the core and present multiple copies of the low-affinity ligand on the corona, creating a high-avidity state according to the multivalency effect. Reproduced in part with permission from ACS Nano, submitted for publication.**

The unique properties of ELPBC permit the design of carriers for DAM. First, the genetic backbone of ELP ensures monodispersity, composition, and molecular weight (MW), all important parameters for design of macromolecular drug carriers. Second, ELP can be coexpressed with additional fusion proteins or terminal residues [209] for incorporation of peptide ligands or unique conjugation sites with minimal disruption to thermal transition behavior. Third, ligand-ELP constructs can be purified using inverse transition cycling (ITC), a non-chromatographic method permitting one-step synthesis of ligand-ELPBC at the benchtop with quantities suitable for high-throughput analysis [201]. Fourth, and most importantly, the exquisite sequence control exhibited by the ELP ensures that each construct has exactly one binding ligand located directly at the

hydrophilic terminus without additional synthesis, a distinct advantage over synthetic block copolymers.

## **1.5.2 Specific Aims**

This study incorporates three broad specific aims, each representing a different stage along the development cycle of ligand-ELPBC. Completion of the three provided sufficient information to: (1) determine if DAM using ELPBC is a realistic strategy for vascular targeting, (2) evaluate the parameters of the ELPBC design which facilitate specific interaction both *in vitro* and *in vivo*, and (3) propose modifications to the ELPBC design to improve the long-term outlook for realistic application of the affinity-modulations strategy.

### **1.5.2.1 Specific Aim 1 – Design of Self-Assembling Block Copolymers for Affinity-Modulated Targeting**

In Specific Aim 1 (SA1), we hypothesized that ELPBC retained its thermosensitive self-assembly properties (A) at concentrations relevant to drug delivery and (B) following addition of peptide and synthetic conjugate. First, we further evaluated the existing ELPBCs as a concentration-dependent macromolecule by (1) determining the critical micelle concentration (CMC) of ELPBCs with different segment ratios and (2) evaluating the rigidity of micelle constructs compared to aggregate form. Second, we selected peptide ligands, generated custom vectors and plasmids, and expressed a library of functionalized ELPBCs. Third, we analyzed these compounds with dynamic light scattering (DLS) to determine CMT, size, MW, and ligand density to determine if an ELPBC retained its self-assembly properties following functionalization. This specific aim is addressed in Chapters 2 and 3.

### **1.5.2.2 Specific Aim 2 – Identification of Conditions for Multivalent Interaction and Constructs Capable of Affinity-Modulation**

In Specific Aim 2 (SA2), we hypothesized that ligand-ELPBC promoted uptake by cells only in multivalent form by cells overexpressing an isolated cognate receptor. To address this, we evaluated the ability of the constructs developed in SA1 to specifically interact with cell receptors under a variety of conditions using a standardized *in vitro* assay compatible with ELPBC. First, we

engineered a cell line for expression of isolated receptors and compatible with current and future ELP constructs. This cell line also incorporated inducible receptor expression, combining the benefits of cell-based and surface-based binding assays. Second, we used these cells with ELPBCs to determine the effects of (1) self-assembly, (2) hyperthermia, (3) multivalency, (4) receptor expression, (5) ligand presentation, and (6) segment ratio on cellular uptake. The data was then used to identify the constructs most suitable for static and dynamic affinity targeting. This specific aim is addressed in chapters 4 and 5.

### **1.5.2.3 Specific Aim 3 – *In Vivo* Characterization of ELP Block Copolymers in Both Tumor and Normal tissues**



In Specific Aim 3 (SA3), we hypothesized that multivalent presentation of ligand (A) increases accumulation in the tumor region relative to the normal region, (B) reduces penetration distance versus non-ligand ELPBC, and (C) promotes specific interaction with tumor endothelial cells. To test this, we characterized the behavior of those constructs with the best interaction profiles identified in SA2. Since these constructs did not exhibit proper thermal profiles for DAM, we evaluated the effects of static multivalent targeting at normothermic conditions. First, we tested the ability for ligand-ELPBC to maintain self-assembly in serum. Second, we characterized behavior of these constructs in both tumor and normal vasculature using intravital microscopy and immunohistochemistry. These data were analyzed using custom MATLAB functions to quantitatively describe the effects of multivalent presentation on (1) tumor accumulation in both vascular and extravascular compartments, (2) penetration distance, and (3) binding location. Third, we evaluated the ability to monitor ELPBC conjugated to a therapeutic compound using the dorsal fold window chamber for future analysis of fluorescent ELP compounds.

### **1.5.3 Potential Difficulties**

The strategies of DAM and, to a lesser extent, static multivalent targeting represent major advancements in targeted drug delivery. However, full implementation of either requires overcoming several hurdles. First, controlled self-assembly using functionalized ELPBC for drug

delivery applications must occur under realistic conditions, and functionalized micelle formation must be retained in serum at concentrations to ensure self-assembly at concentrations throughout the time course of therapy for both dynamic and static multivalent targeting. Second, the constructs must be expressed from a genetic template and purified using non-chromatographic methods to fully exploit the precise composition and simple synthesis provided by ELP compared to synthetic polymers. Third, constructs intended for multivalent targeting must interact with a target receptor exclusively through multivalent presentation of its cognate receptor; ligand or thermal self-assembly cannot solely promote nonspecific cellular interaction as this leads to potential offsite binding. Fourth, strict thermal profiles are required for DAM application. Constructs that exhibit self-assembly with CMT = 39 °C – 42 °C are compatible with DAM, and constructs with CMT < 37 °C are compatible with static multivalent targeting. Fourth, ELPBCs for

**Table 1: Description of requirements for static and dynamic affinity modulation**

Requirements	Static 	Dynamic 
Interaction with receptor in multivalent form	●	●
No interaction with receptor in monovalent form		●
Exhibits a CMT between 39-42 °C		●
Exhibits a CMT below 37 °C	●	
Incorporates an inert thermal switch		●

either static or dynamic multivalent targeting must show greater accumulation in tumor regions relative to normal regions in an *in vivo* setting, as this setting provides a more accurate recreation of receptor expression and binding conditions. Fifth, the loading potential of thermosensitive ELPBC is lower than other thermally-insensitive nanoparticles, leading to a tradeoff between the advantages of controlled spatial distribution and therapeutic payload. Thus, static multivalent constructs that show increased relative accumulation will benefit more from higher payload than form DAM.



## **2 Fluorescence Characterization of Elastin-Like Polypeptide Block Copolymers**

### ***2.1 Introduction***

We have previously verified the formation of spherical micelles from elastin-like polypeptide block copolymer (ELPBC) in response to heat, but we did not evaluate all of the relevant parameters to micelle self-assembly. The goal of this study was to (1) determine the temperature-independent critical micelle concentration (CMC) for the self-assembling constructs and (2) identify structural differences between the hydrophilic unimer, amphiphilic micelle, and hydrophobic aggregate phases. The purpose of CMC identification was evaluation of micelle stability and feasibility of retaining self-assembly throughout the time course of therapy. The purpose of structure evaluation was observation of ELPBC physical changes through each of its phase transitions and identifications of physical differences between the micelle and aggregate forms. We used fluorescence-based spectroscopic techniques and novel algorithms to apply standard characterization methods in a fashion compatible with temperature- and concentration-dependent ELPBC. These data show that (A) all micelle-forming ELPBCs exhibit a CMC from 4 - 8  $\mu\text{M}$  in aqueous solution and (B) the micelle and aggregated homopolymer represent different material phases. Thus, thermosensitive ELPBC self-assembles into stable micelles at concentrations relevant for drug delivery when  $\text{CMT} < T < T_i$ , these micelles are physically distinct from micron-sized aggregates, and these analytical methods are applicable to study of other thermosensitive constructs.

#### **2.1.1 Critical Micelle Concentration**

A standard measure of micelle stability is the CMC. This value represents the minimum concentration of block copolymers required for stable particle formation. Micelle stability is defined by thermodynamic forces, and micelles with favorable phase separation in solution will develop intermolecular interactions at a lower minimum concentration. Thus, a low CMC is indicative of stable micelle formation, and, typically, block copolymer micelles are considered very

stable at a CMC < 10  $\mu$ M [90]. This value suggests the minimal dose required for retaining stable particle formation and ensuring drug sequestration within the micelle core throughout the course of therapy. The CMC is also important to thermally-sensitive ELPBCs because self-assembly must be retained for static targeting and dynamic affinity modulation (DAM). At concentrations significantly below the CMC, ELPBC will no longer exhibit thermosensitive micelle formation.

### **2.1.2 Micelle Core Viscosity**

As previously described, ELPBC exists in three phases. While both micelle and aggregate formation is triggered by collapse of one or both blocks, the persistence of two distinct structures suggests differences between the micelle core and aggregate form. The viscosity of the micelle core relates directly to water penetration within the core [208] and the fluidity of polymers within the structure [210]. This can affect several of the key parameters for using ELPBCs for drug delivery. First, a more viscous core will be more hydrophobic via water exclusion and therefore likely to entrap hydrophobic compounds. Second, a viscous core is also less likely to permit diffusion of drugs out of the core [109]. Third, core viscosity may affect ligand-receptor mobility and extension and thus the ability for specific interaction. Fourth, differences in the microstructure between micelle and aggregate forms suggest that each may behave differently for targeting applications. Fifth, significant changes in micelle viscosity between phases represents structure rearrangement, and further analysis of these transitions may provide additional insight into ELPBC behavior.

### **2.1.3 Fluorescence Probes**

#### **2.1.3.1 Pyrene**

Pyrene is a hydrophobic fluorescent probe used for studying the CMC of different block copolymers [211]. Pyrene consists of four interconnected aromatic rings, giving the compound both low solubility and a unique fluorescent emission spectrum (Fig. 7A). This low solubility causes pyrene to partition into hydrophobic environments. At low local concentrations, pyrene will exist as a monomer in solution and exhibit a fluorescent signal with four characteristic peaks. At

high local concentrations, pyrene will form excimers through intermolecular interactions which dramatically alter this spectrum [211]. The superposition of these two conditions will cause changes to the intensity ratio of peaks 1 and 3 ( $I_1/I_3$ ); greater monomer character (hydrophilic) will increase  $I_1/I_3$  while greater excimer character (hydrophobic) will decrease  $I_1/I_3$ . Studies have shown that this effect is absolute and can be used to evaluate the relative polarity of a given solution [212].

These two characteristics make pyrene a useful probe for detecting micelle formation [211]. As stable micelles form in solution, water is expelled from the core creating local hydrophobic microenvironments. Pyrene will partition in these regions, causing a reduction in the average  $I_1/I_3$  of the solution. At the concentration where stable micelles begin to form and the solution becomes less polar, the  $I_1/I_3$  value will drop sharply. The inflection point of this decrease is defined as the CMC. This technique is accepted as standard method for determining CMC values for a given block copolymer. It also confers advantages over other methods. Analysis of pyrene spectra generates continuous data rather than discrete data provided by dynamic light scattering (DLS) or cryo-transmission electron microscopy (TEM), and it can be performed independent of secondary structure formation. Additionally, pyrene data illustrates formation of stable micelles while other modalities identify formation of all particles within solution.

#### **2.1.3.2 PC<sub>3</sub>P**

1,3-*bis*(1-pyrenyl)propane (PC<sub>3</sub>P) is another fluorescent probe useful for investigating viscosity, the resistance to stress-induced deformation, within the micelle core. PC<sub>3</sub>P consists of two pyrene molecules connected by a propyl linker (Fig. 7B). PC<sub>3</sub>P can exist as either a monomer or excimer similar to pyrene. PC<sub>3</sub>P forms intramolecular excimers through flexible association of the pyrene groups in environments with high fluidity. However, local viscosity within the core will disrupt this association, increase the monomer population, and alter the fluorescence spectra [213]. Measurement of this spectra can be used to evaluate the relative viscosity of hydrophobic

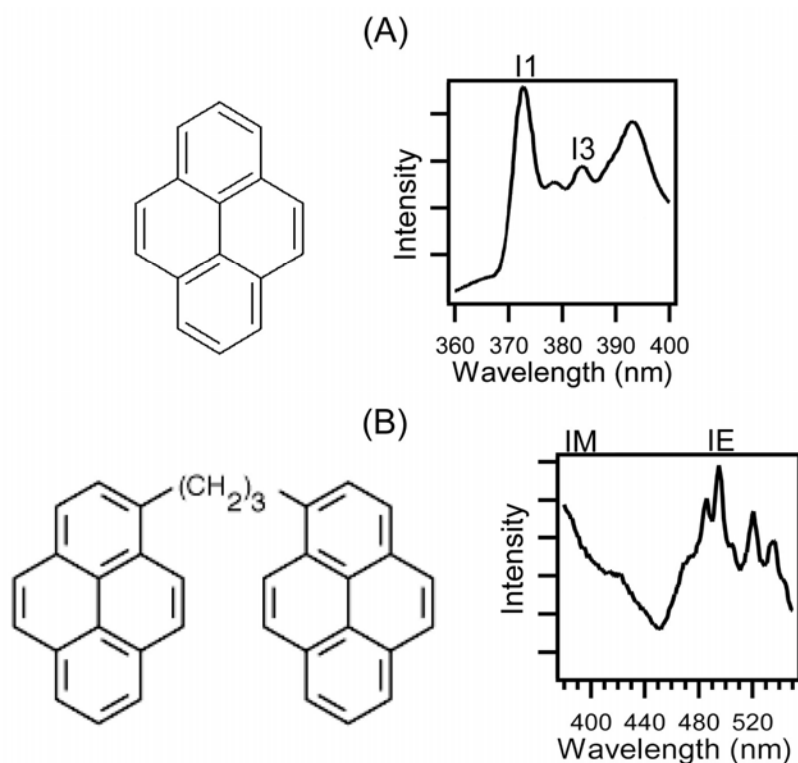


**Figure 7: Structures and spectra of pyrene and 1,3-bis(1-pyrenyl)propane. (A) Pyrene shows a characteristic spectra with four distinct peaks in monomer form. The intensity ratio between peaks  $I_1$  and  $I_3$  decreases with increased hydrophobicity of its environment. (B) 1,3-bis(1-pyrenyl)propane form excimers via stacking of aromatic rings producing unique fluorescent spectra. The intensity ratio of  $I_E/I_M$  increases in response to the hydrophobicity or rigidity of its environment.**

environments undergoing phase transition [111; 214]. This behavior is useful in analyzing the triphasic ELPBC as it allows for comparison of the viscosity between unimer, micelle, and aggregate states. Differences in viscosity of the hydrophobic regions in each phase identifies differences in nanostructure in a simple, high-throughput fashion, allowing PC<sub>3</sub>P analysis to serve as a screening method for nanoscale structural changes.

## **2.2 Materials and Methods**

### **2.2.1 Thermal Control of Fluorescence Spectrophotometer**

A custom script was written in ADL language to impart thermal ramping/scanning functionality to the Cary Eclipse Spectrofluorophotometer (Varian, Inc., Palo Alto, CA). The script uses a four-step algorithm to sequentially set temperature, scan active region, scan baseline, and

extract peak information based on information provided by the user. Input parameters corresponding to peak excitation, emission detection range, start temperature, step temperature, and end temperature were defined by the user using a graphical user interface (GUI). During each cycle, the temperature of a control sample was adjusted through a heating block to match the program-defined temperature and allowed to equilibrate for 2 minutes. Two scans were performed at each temperature, one active scan and one baseline scan, as defined by the fluorophore. Each spectra was analyzed for peak values within a specified 3 nm range to account for small spectral shifts. The corrected peak values were exported and the cycle was restarted at the next temperature. After the scanning was completed over the defined temperature range, the script exported a .txt file with the calculated peak values at each temperature for processing off-line. This method was used for all fluorescence data acquisition.

## **2.2.2 Determination of Critical Micelle Concentration of ELPBC**

### **2.2.2.1 Sample Preparation**

A pyrene probe (Sigma-Aldrich, St. Louis, MO) was used to determine the critical micelle concentration (CMC). Pyrene was dissolved in EtOH to make a 0.12 M stock solution, and Pyrene-PBS (*c.a.* .6  $\mu\text{M}$ ) solution was prepared by adding 1  $\mu\text{L}$  of stock solution to 20 mL of micro-filtered (0.02  $\mu\text{m}$ ) PBS. Solutions were sonicated prior to use to ensure fluorophore solubilization. Concentrated ELP was added to the pyrene-PBS solution immediately prior to the experiment and the ELP-fluorophore solution was transferred to a clean reduced-volume quartz cuvette (Starna Inc., Atascadero, CA).

### **2.2.2.2 Data Acquisition and Analysis**

All fluorescence measurements were made using a temperature-controlled Cary Eclipse Spectrofluorophotometer equipped with a Xenon flash lamp (Varian, Inc.). All temperature manipulation and data acquisition steps were automated using the previously described script. Pyrene emission spectra (exc. = 334 nm, em. = 360 - 400nm) were obtained from 20 - 32 °C at increments of 2 °C and 32 - 60 °C at increments of 1 °C. After each scan, location and intensity

of peaks falling within the predetermined range were identified (Pyrene: I<sub>1</sub>:370 – 373 nm, I<sub>3</sub>:381 – 384 nm) and used to calculate the I<sub>1</sub>/I<sub>3</sub> ratio at each temperature. A sigmoid curve was fit to the region surrounding T<sub>t1</sub> (30 °C - 45 °C) to obtain a function relating I<sub>1</sub>/I<sub>3</sub> to temperature. The CMC was then determined from this data first by plotting the I<sub>1</sub>/I<sub>3</sub> ratio obtained from each emission scan as a function of temperature. The minimum of each sigmoid fit applied from 35 °C - 45 °C was plotted as a function of ELPBC concentration and fit with a sigmoid curve. The inflection point was identified and defined as the CMC.

## **2.2.3. Evaluation of Microviscosity**

### **2.2.3.1 Sample Preparation**

1,3-*bis*(1-pyrenyl)propane ([PC<sub>3</sub>P], Invitrogen, Carlsbad, CA) was dissolved in acetone to make a 16 mM stock solution, and PC<sub>3</sub>P-PBS (*c.a.* .4 μM) solutions were prepared by adding 1 μL of stock solution to 20 mL of micron-filtered (0.02 μm) PBS. The solutions were sonicated prior to use to ensure solubility of the fluorophore in solution. Concentrated ELP solutions were added to the PC<sub>3</sub>P-PBS solution immediately prior to the experiment and the ELP-fluorophore solution was then transferred to a clean reduced-volume quartz cuvette (Starna Inc.).

### **2.2.3.2 Data Acquisition and Analysis**

All fluorescence measurements were made using the Cary Eclipse spectrofluorophotometer controlled using the custom thermal ramping script. PC<sub>3</sub>P emission spectra (exc. = 333 nm, em. = 380 - 500 nm) were obtained from 20 - 32 °C at increments of 2 °C and 32 - 60 °C at increments of 1 °C. The samples were allowed to equilibrate for two minutes prior to data acquisition after each temperature manipulation. After each scan, a peak finding algorithm was applied to the data to record the location and intensity of peaks falling within the predetermined range (PC<sub>3</sub>P: I<sub>M</sub>: 395 nm, I<sub>E</sub>: 495 nm). The I<sub>E</sub>/I<sub>M</sub> ratio is was calculated using a similar peak-finding algorithm as the pyrene study but with different bounds based on the peaks of PC<sub>3</sub>P fluorescence.

## 2.3. Results and Discussion

### 2.3.1 Thermally-Controlled Fluorescence Spectrophotometry

Fluorescence analysis of thermally-sensitive ELPBC requires independent spectral measurements at set temperature intervals. Available equipment provided two options, (1) manual ramping of temperature prior to each scan or (2) automated temperature ramping with continuous monitoring at a single emission wavelength. The first option yielded sufficient spectral data for analysis, but generation of a single I1/I3 curve at a given concentration required approximately 7 hours, leading to over 70 hours of manual operation required for one CMC

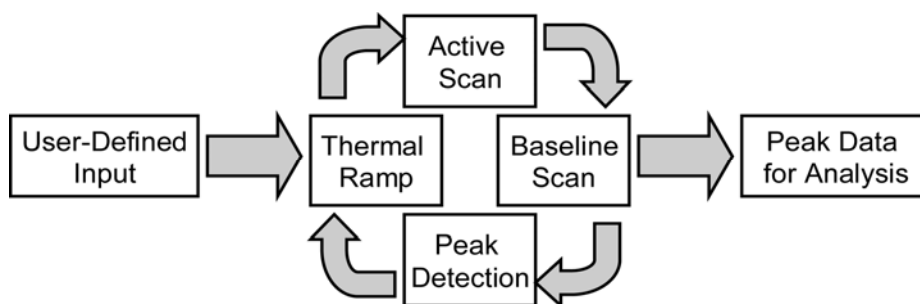


**Figure 8: Block diagram of fluorescence spectroscopy data acquisition. A custom program written in the ADL language ramps the temperature and obtains fluorescence spectra based on user-defined parameters. The resulting data set is then exported to peak detection and curve fitting macros for analysis.**

calculation. The second option provided more convenience, but small peak shifts throughout the scanning process created significant artifacts within the data given the close proximity of the four characteristic peaks. The solution thus was to create a custom scanning method that incorporated automated thermal ramping, full-spectral scanning, and peak identification to analyze different fluorophores in a high-throughput, yet precise, manner. This program conferred the advantages of (1) higher throughput with both smaller emission-scan intervals and higher sampling time, (2) more precise measurement of peak ratios, and (3) greater consistency through removal of user bias. This program was successfully implemented for pyrene and PC<sub>3</sub>P analysis and is expandable to other useful fluorophores for analysis.

### 2.3.2 Critical Micelle Concentration of Elastin-Like Polypeptide Block Copolymers

We used the pyrene method to determine the CMC of five different ELPBCs capable of forming micelles. The CMC is more difficult to obtain for these constructs as they exhibited both a CMC and critical micelle temperature (CMT). For simplicity, we will assume that ELPBC exhibits  $CMC_1$  at  $T < CMT$  and  $CMC_2$  at  $T > CMT$ . We will also assume that  $CMC_1 \gg CMC_2$  given that micelle formation is not observable at  $T < CMT$ . As the concentration of ELPBC increases, the CMT decreases, shifting the cutoff between  $CMC_1$  and  $CMC_2$  accordingly. Since we are interested in  $CMT_2$  as the relevant parameter for self-assembly, any measurements of  $CMC_2$  must be obtained above the CMT but below the region of aggregate formation. Thus, the best method to ensure proper CMC measurement was to monitor the  $I_1/I_3$  ratio over a range of temperatures for a range of concentration of each ELPBC.

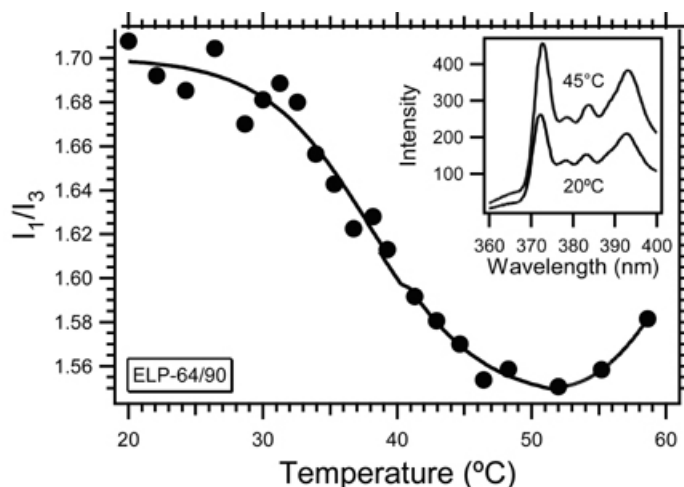


**Figure 9: Example of temperature-independent CMC calculation using pyrene spectra as a function of temperature. The  $I_1/I_3$  ratio of an ELPBC solution is measured over a range of temperatures from 20 – 60 °C. This ratio changed due to amplification of the spectra with micelle formation (inlay). The minimum  $I_1/I_3$  was plotted as a function of concentration.**

Reproduced with permission from Dreher, M.R. et al., *Temperature Triggered Self-Assembly of Polypeptides into Multivalent Spherical Micelles*. Journal of the American Chemical Society, 130(2): 687-694. Copyright 2007.

To accomplish this in a high-throughput manner, we monitored  $I_1$  and  $I_3$  values over a range of temperatures. An example of an  $I_1/I_3$  thermal scan illustrates the change in both pyrene spectra in the presence of micelle-forming ELPBC and the  $I_1/I_3$  ratio as a function of temperature



(Fig. 9). The pyrene spectra showed a more polar environment at low temperatures and a less polar environment at high temperatures.  $I_1/I_3$  decreased as the probe partitioned into a less polar region, presumably the micelle core.  $I_1/I_3$  remained relatively constant at temperatures below the CMT ( $T = 20\text{ }^\circ\text{C} - 35\text{ }^\circ\text{C}$ ). At temperatures between the CMT and  $T_t$ ,  $I_1/I_3$  monotonically

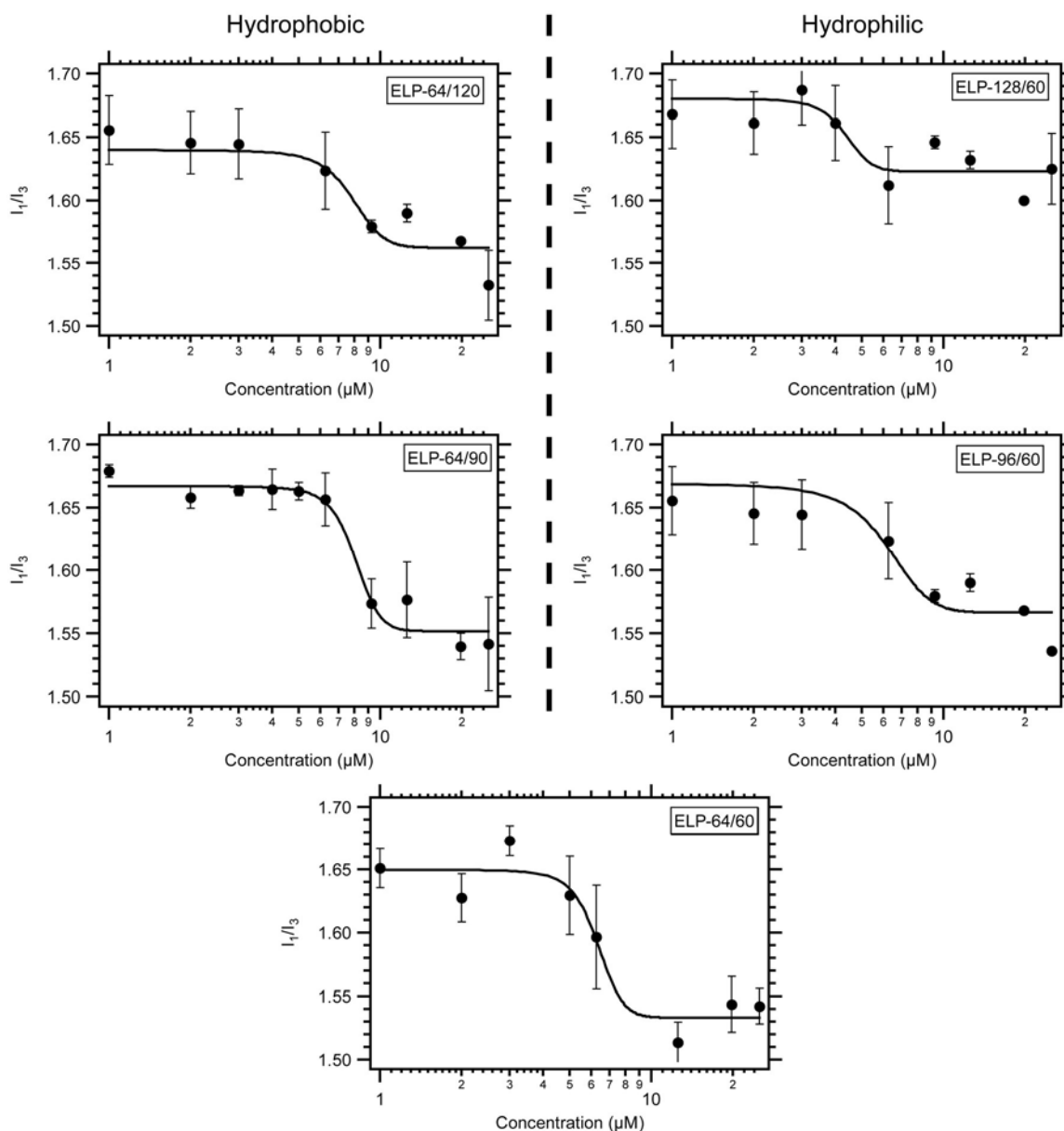


**Figure 10: Determination of CMC of ELPBCs using fluorescence spectroscopy. The minimum  $I_1/I_3$  ratio for each construct was plotted as a function of concentration. The inflection point of the resulting sigmoid curve was defined as the CMC ( $n = 3$ , bars = SE).**

decreased until it reached a minimum at  $T_t$  ( $T = 50\text{ }^\circ\text{C}$ ) indicating that the overall polarity of the micelle decreased throughout the micelle temperature range. The sharp decrease in I1/I3 as a function of temperature was evident in all ELPBC solutions. This suggests that the pyrene partitioned into the hydrophobic core of newly-formed micelles. Additionally, there was a slight increase of I1/I3 ratio following the micelle-to-aggregate transition. As the micelle goes through this phase transition, this increase in I1/I3 illustrates that the aggregate is either slightly more hydrophilic than the micelle core or leaking encapsulated pyrene. Similar findings by Chung *et al.* indicated release of the entrapped molecule from thermo-responsive micelles [109]. While this temperature region is outside of the range relevant to static or dynamic affinity targeting, it may have relevance of future uses of ELP aggregate as a localized drug delivery depot or a carrier for tumor ablation strategies.

The minimum I1/I3 value was extracted from each pyrene scan as a function of temperature for each ELPBC (Fig. 10). The data show that the minimum I1/I3 value for each construct remained constant at low concentrations for each ELPBC but decreased to a lower value as the concentration was increased. A sigmoid curve was then fit to the mean minimum I1/I3 values for each construct as a function of concentration, and the inflection point of this curve was identified as the CMC (Table 1). All of the nanoparticle-forming ELPBCs exhibited a CMC  $< 10\text{ }\mu\text{M}$  implying that ELPBC micelles are quite stable structures. In addition, the CMC slightly decreased with an increase in segment ratio of all tested constructs, showing that the hydrophilic segment also plays a supporting role in determining micelle stability. Most importantly, the low CMC value demonstrated that ELPBC will form stable structures at a concentrations relevant to systemic drug delivery applications.

The minimum I1/I3 ratio provides some insight as to the types of hydrophobic compounds that will partition into the hydrophobic core. At  $T > \text{CMT}$ , the core-forming block became hydrophobic and the overall polarity of the solution was similar to formamide or acetone according to the Winnik scale [212]. It follows that ELPBC without modification should be able to encapsulate drugs compatible with these solvents. Although work is required to calibrate this

scale to account for pyrene-based artifacts, the 11/13 ratio may be used to predict solubility of different drugs by different ELPBC constructs.

**Table 2: CMC of micelle-forming ELPBCs. There was a slight increase in CMC with increasing hydrophobic content of the ELPBC. All measured CMC < 10  $\mu$ M illustrating formation of stable micelles. Reproduced with permission from Dreher, M.R. et al., *Temperature Triggered Self-Assembly of Polypeptides into Multivalent Spherical Micelles*. Journal of the American Chemical Society, 130(2): 687-694. Copyright 2007.**

ELPBC Construct	Segment Ratio	CMC ( $\mu$ M)
ELP-128/60	2:1	4.4 $\pm$ .64
ELP-96/60	3:2	6.2 $\pm$ .95
ELP-64/60	1:1	6.3 $\pm$ .55
ELP-96/90	1:1	5.6 $\pm$ .97
ELP-64/90	2:3	8.1 $\pm$ .64
ELP-64/120	1:2	7.9 $\pm$ 1.2

While these data represent guidelines for stable micelle formation, the CMC is not an absolute determinant of either particle formation or stable micelles. CMC data based on pyrene is a representation of stability, not self-assembly. For example, a loose aggregate that does not promote pyrene partitioning may still appear during light scattering measurement. It is important to note this distinction as self-assembly may occur at concentrations below the CMC. Second, most pyrene will preferentially accumulate within hydrophobic regions but some will remain in solution. Based on our protocol and ELPBC's incompatibility with ultracentrifugation, we cannot remove the pyrene following micelle formation and, as a result, the observed minimum 11/13 values may be inflated due to the presence of free pyrene contributing to the bulk average. Due to this, stable micelles may still form at concentrations below the CMC. Even with this potential discrepancy, the calculated CMC will be higher than the actual value, not lower. Thus, it is possible for stable micelle formation at concentrations below the CMC. However, this does not change the overall conclusion that ELPBCs form stable micelles at concentrations above the CMC.

### **2.3.3 Evaluation of Microstructure of Micelle Core Versus Aggregate**

The microviscosity of the micelle core was qualitatively investigated with fluorescence spectroscopy using the previously-described fluorescent PC<sub>3</sub>P probe [210; 215]. We used the

custom thermal fluorospectroscopy method with different excitation and emission wavelengths to obtain the  $I_E/I_M$  spectra as a function of temperature for micelle-forming ELPBCs. The  $I_E/I_M$  ratio of ELPBC solutions was monitored and plotted as a function of temperature (Fig. 11).

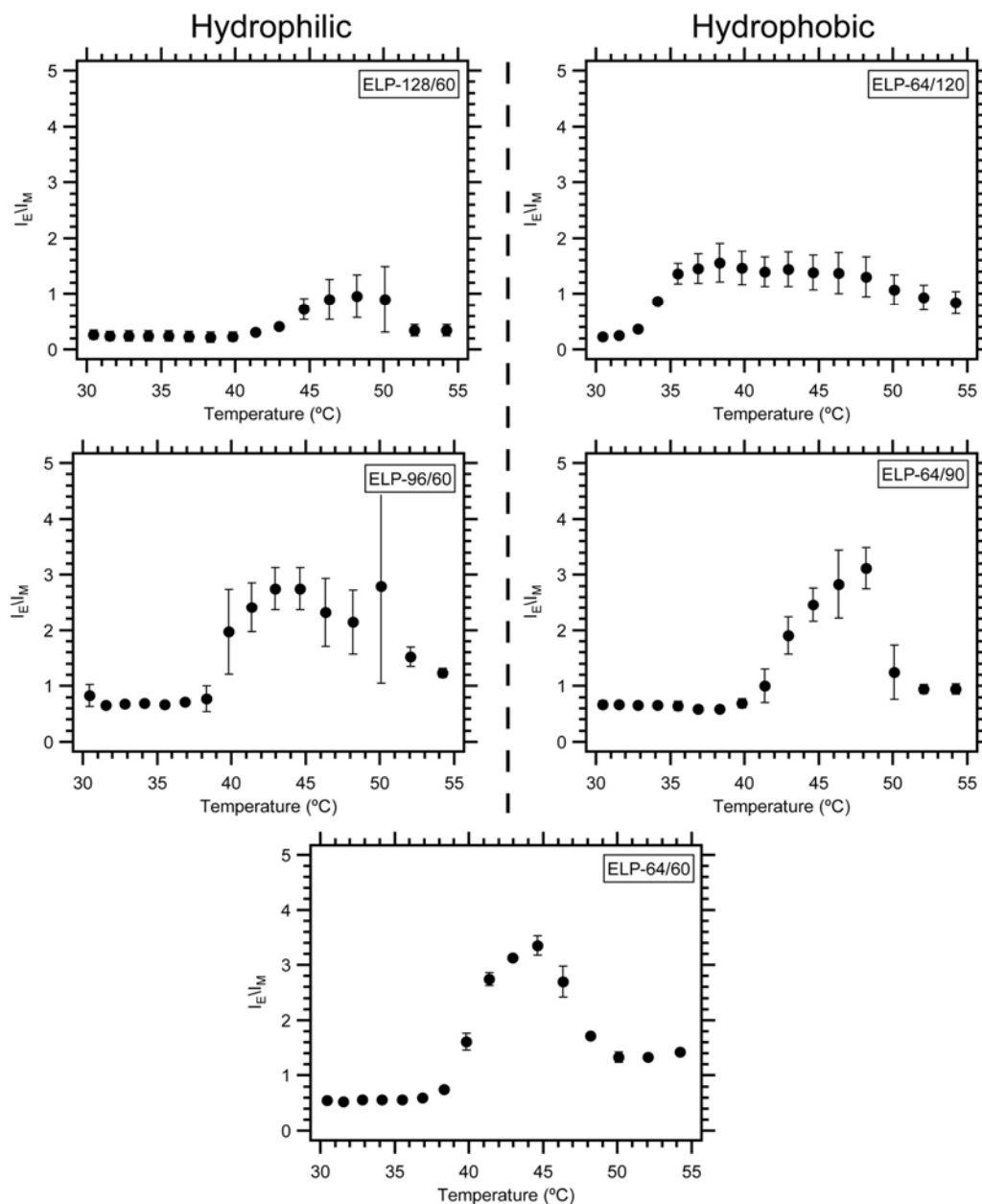


**Figure 11: Evaluation of ELPBC rigidity using fluorescence spectroscopy.** After measuring the  $I_E/I_M$  ratio over a range of temperatures, the maximum  $I_E/I_M$  ratio for each construct was plotted as a function of temperature. The viscosity of all ELPBC, with the exception of ELP-128/60, increased in rigidity with temperature until several degrees over CMT. The viscosity then decreased from the peak until  $T = T_t$  where viscosity remained constant following transition to micron-sized aggregate ( $n = 3$ , bars = SE).

Each construct showed three separate regions corresponding to the unimer, micelle, and aggregate regions.  $I_E/I_M$  was lowest in the unimer region corresponding to low rigidity. At the onset of micelle formation,  $I_E/I_M$  increased dramatically illustrating an increase in the rigidity within the micelle core. The greatest increase occurred in solutions containing ELPBC with a segment ratio closer to 1, illustrating a more viscous core in micelles with a segment ratio from .66 - 1.5. Additionally, the viscosity continued to increase after the onset of micelle formation. At the onset of aggregate formation,  $I_E/I_M$  decreased rapidly from its peak to a value between the unimer and micelle  $I_E/I_M$  values. This illustrates that the aggregate has more fluidity than the micelle but exhibits greater viscosity than the micelle form.

To further investigate the differences of the micelle form to aggregate form, we compared the  $I_E/I_M$  values of ELP-64/90 solution to homopolymeric ELP[V<sub>5</sub>A<sub>2</sub>G<sub>3</sub>-150] (ELP-150) solution (Fig. 12). At solution temperatures below the first  $T_t$ , the viscosity of an ELP-64/90 solution was similar to that of a control ELP-150 ( $T = 30 - 40$  °C). The viscosity increased within the micelle temperature range ( $T = 40 - 50$  °C) as indicated by the higher  $I_E/I_M$  of the ELP-64/90 solution. The control ELP-150 exhibited lower viscosity than the micelle after it underwent its inverse temperature phase transition ( $T_t = 42$  °C) into a bulk aggregate. Furthermore, the ELP-64/90 solution demonstrated a similar rigidity to the control ELP-150 after it underwent bulk aggregation at 50 °C. This showed with greater certainty that the ELPBC micelle has a different nanostructure than ELP aggregate in micelle form. It also reinforced the observation that the micelle disassembles and reassembles into an homopolymeric aggregate structure above its  $T_t$ .

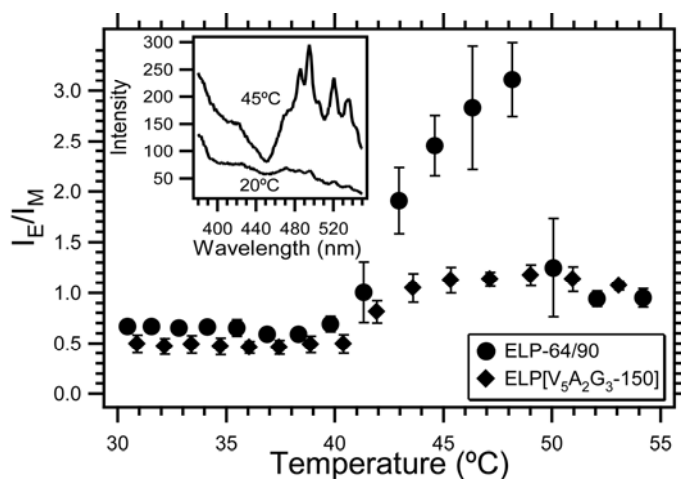


**Figure 12: Comparison of micelle viscosity to aggregate viscosity. Both ELP-64/90 and ELP-150 showed an increase in viscosity at CMT. ELP-64/90 in micelle form showed significantly higher rigidity than ELP-150 in aggregate form. When ELP-64/90 persisted in aggregate form, it exhibited similar viscosity to aggregate ELP-150 ( $n = 3$ , bars = SE). Reproduced with permission from Dreher, M.R. et al., *Temperature Triggered Self-Assembly of Polypeptides into Multivalent Spherical Micelles*. *Journal of the American Chemical Society*, 130(2): 687-694. Copyright 2007.**

These data suggest that the core of an ELPBC micelle is more viscous than either soluble ELP or ELP bulk aggregate. Also, the micelles appear to reorganize their entire structure during the transition to a bulk aggregate rather than form an cluster of micelle cores judging by the changes in viscosity between the micelle and aggregate form. While it is clear from this data that the micelle exists in a separate phase from both the unimer and aggregate forms, it is unclear how these potentially-conflicting effects affect receptor interaction. Lower viscosity may promote ligand accessibility as those associated with a less viscous structure may have a higher degree of freedom and better association with the cognate receptor. However, low viscosity also suggests less density and water exclusion, leading to interaction between the core and coronal segments and limited ligand-receptor accessibility. Conversely, the increase in viscosity is associated with water exclusion and denser coronal packing, generating greater repulsive forces between the hydrophilic and hydrophobic segments and thus greater ligand extension. This may also lead to less mobility in the corona and lower ligand accessibility. This difference justifies investigating both micelle- and aggregate-forming parent ELPs for both dynamic and static multivalent targeting.

## **2.4 Significance**

In the course of this study, we have developed software and corresponding protocol to analyze thermosensitive micelles using fluorescence characterization in a relatively high-throughput format. The flexibility of our approach allows for the characterization of both thermally-responsive and thermally-stable block copolymers. As seen in this study, both techniques are applicable to the study of block copolymers relying solely on hydrophobic interaction for self-assembly. While the CMC measurement technique is still untested with nanoparticles relying on chelation or crosslinking to stabilize the core, the microviscosity technique should be easily implemented for characterization of these constructs since excimer formation relies entirely intramolecular interaction. The user-friendly front end allows facile implementation of this software for those with limited computational experience.

We then used this protocol to analyze the CMC and structure of thermosensitive ELPBC. This data provides key information relating to thermosensitive micelles. First, the pyrene data establishes a CMC for these constructs between 4 - 8  $\mu\text{M}$ , verifying that these constructs are highly-stable at low concentrations and allowing further development for drug delivery applications. The CMC of the tested ELPBCs also show minimal variation in stability with changes in the segment ratio. This suggests that, despite the variation in growth patterns of the nanoparticle, the stability of the particle remains somewhat constant. Second, the microviscosity data illustrates that the micelle exists in a separate phase from both the unimer and aggregate forms. Also, the micelle appears to disassemble and reassemble into the aggregate form following bulk aggregate transition. The microviscosity data also shows that the micelle core exhibits rigidity independent of segment ratio within the .5 - 1.33 range, suggesting the ability to vary the segment ratio somewhat without significantly disrupting the micelle core. These findings justify further investigation of ELPBC with different segment ratios due to the unpredictable effects on ligand extension and mobility.

While this study focused primarily on the difference between the unimer to micelle phases, the unimer-to-micelle and micelle-to-aggregate transitions both show promise for future study and application. First, further experiments using differential scanning calorimetry have been performed to determine the potential for intermediate structure formation in both transitional states. Knowledge of these intermediates may explain subtle differences in observed ELPBC behavior and allow for rational selection of ELPBCs best suited for static or dynamic multivalent targeting. Second, observed disassembly of ELPBC between the micelle and aggregate forms may promote thermally-triggered release of hydrophobic compounds. The temperature at which the micelle disassembles is constant between ELPBCs of different segment ratio, and this bulk transition occurs at temperatures corresponding to thermal ablation strategies. This micelle-to-aggregate bulk transition therefore may have relevance for release of encapsulated drugs for high hyperthermia applications.



## **3 Generation and Evaluation of Ligand-Functionalized Elastin-like Polypeptide Block Copolymer**

### ***3.1 Introduction***

Dynamic affinity modulation (DAM) requires a material that transforms from a low-affinity monovalent state to a high-avidity polyvalent state through an external stimulus. While there are a number of constructs that have demonstrated improvement in tumor accumulation through low-affinity, passive accumulation [67; 72; 81; 88; 89; 202; 216] or high-avidity, active accumulation [75; 94; 169; 173; 181; 194; 195; 217], to the best of our knowledge, a material has not been generated with the capability to actively transition between these states. Elastin-like polypeptide block copolymer (ELPBC) allows us to generate this functionalized material featuring triggered self-assembly using single-step synthesis and chromatography-free purification. The genetic backbone allows for incorporation of peptide ligands at the hydrophilic terminus through modifying the gene template and precise control over composition. This ensures uniform and predictable micelle self-assembly as the hydrophilic block extends away from the core and presents hydrophilic ligands embedded at the coronal terminus [207]. Additionally, the thermal transition allows for single-step synthesis and chromatographic-free purification on the benchtop, providing both convenience and precise control over ligand conjugation ratios.

The goal of this section was to demonstrate the ability to ELPBC to act as a nanoscale scaffold for dynamic multivalent presentation of a targeting peptide ligand. First, we identified a set of ligands compatible with our system that exhibit low-affinity in monovalent form but high avidity in polyvalent form towards epitopes expressed in tumor vasculature. Second, we generated a set of modular vectors that incorporate a synthetic gene to encode three contiguous components: (1) a hydrophilic peptide ligand on the corona-forming segment of the ELPBC; (2) the gene for the ELPBC itself; and (3) a short peptide sequence – WPC – that provides a unique conjugation site within the hydrophobic core of the ELPBC. Different ELPBCs were selected to express a library of functionalized ELPBC constructs. Third, we characterized thermal self-

assembly of these new constructs to determine the effects of both ligand and conjugate on CMT, hydrodynamic radius, and ligand density. The results showed that the addition of the hydrophilic RGD or NGR ligand and synthetic conjugate did not disrupt self-assembly, and ELPBC self-assembly facilitated multivalent presentation of ligand. The attachment of ligand and conjugate did not disrupt thermal self-assembly, but it affected critical micelle temperature (CMT), molecular weight (MW), and coordination number (Z) while coronal density remained constant. While only the ELP-96/60 family exhibited the proper thermal profile for clinically-relevant dynamic multivalent targeting, all functionalized constructs demonstrated thermal self-assembly in an acceptable temperature range for short-term *in vitro* evaluation. These results showed ELPBC is applicable towards the strategy of DAM.

### 3.1.1 ELP Block Copolymer Modification

#### 3.1.1.1 Construct Design

The first step toward construct design was ligand and cysteine placement along the ELPBC. To ensure proper multivalent presentation, we placed the binding ligand with a flexible GGS linker [218] at the hydrophilic terminus and a unique cysteine residue at the hydrophobic terminus (Fig. 13). This design allowed for coexpression of both the ligand and binding site with

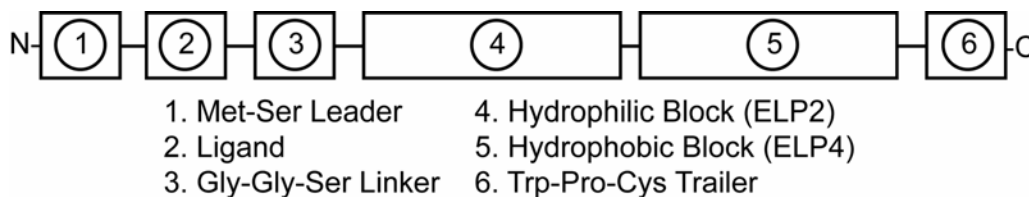


**Figure 13: Diagram of modified ELPBC. The existing ELPBC (4 and 5) is inserted into a custom vector encoding the start codon (1), the ligand (2), a gly-gly-ser linker (3), and cysteine trailer (6). All of these segments were continuously expressed on each ELPBC.**

ELPBC. Following expression, either an imaging agent such as fluorophore or therapeutic such as functionalized doxorubicin [219] can also be covalently conjugated to the cysteine residue through a maleimide linker. At  $T < CMT$ , the construct consists of a single hydrophilic chain with a

monovalent ligand and a single hydrophobic molecule. At  $T > \text{CMT}$ , the ELP[V<sub>5</sub>] block collapses, leading to micelle formation with multivalent ligand presentation on the corona and partitioning of hydrophobic conjugate in the core.

### 3.1.1.2 Ligand Selection

There are innumerable ligands used for targeting angiogenic tumor vasculature including small molecules [60; 220], antibodies/antibody fragments [221; 222], and peptides [181; 194; 223; 224]. However, we are limited to peptides to retain the maximum benefits of using ELPBC. First, a peptide ligand is required for incorporation at the gene level and single-step synthesis. Second, this peptide must be linear, short, and hydrophilic. Linear peptides will prevent incorrect intramolecular crosslinking and/or intermolecular covalent interactions, short peptides will minimize effects on ELP transition and the segment ratio, and hydrophilic peptides will promote extension of the coronal segment away from the core [207]. For greatest chance of translational impact, the ligands should also demonstrate proven binding efficacy but with difficulties stemming from “promiscuous” binding such as non-specific binding or accumulation in normal tissue. Most importantly, this ligand must exhibit a dramatic difference in affinity in monovalent and multivalent states. Ligands should exhibit monovalent affinity of  $K_D > 10^{-6}$  M and multivalent avidity of  $K_D < 10^{-8}$  M to ensure sufficient ligand-receptor interaction only in the multivalent state.

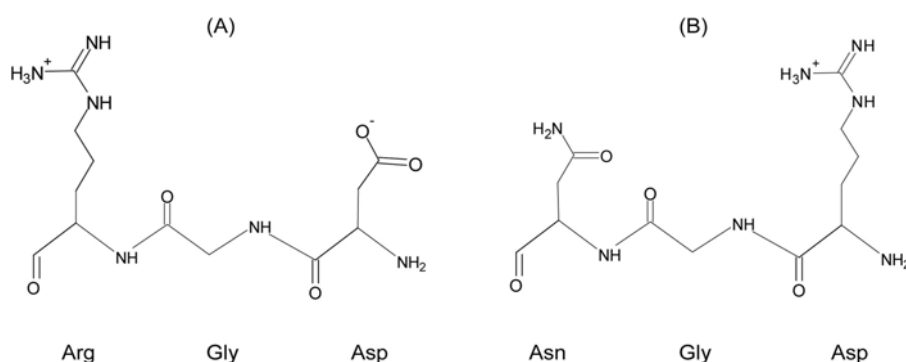


**Figure 14: Structure of RGD and NGR tripeptide ligands. (A) RGD is a zwitterion with formal charge = 0, but (B) NGR has a formal charge = +1 at pH = 7.4.**

Given these requirements, we focused our design on two distinct, short, distinct targeting peptides, GRGDS [165] and GNGRG [225] (Fig. 14). The GRGDS peptide is a linear, low-affinity RGD derivative with some specificity towards the  $\alpha v\beta 3$  integrin. GRGDS also is a zwitterion at pH = 7.4 and contains hydrophilic flanking residues, likely promoting some extension of this ligand away from the hydrophobic core. Similarly, the GNGRG peptide is a linear, low-affinity derivative of NGR, a tripeptide associated with aminopeptidase-N (CD13). GNGRG is charged at pH = 7.4 and also contains hydrophilic residues which should promote even greater extension away from the hydrophobic core. Both GRGDS and GNGRG exhibit  $K_d > 10^{-6} \text{ M}^{-1}$  in monovalent form, but both show increased specific interaction with their cognate receptor with multivalent presentation on other constructs. As previously described in section 1.1.3, both the RGD-based and NGR-based systems show affinity towards angiogenic vasculature but also potential off-site binding. Thus, both may benefit from spatial restriction of binding activity either through static multivalent targeting or DAM.

### **3.1.1.3 Vector Design**

Each ELPBC plasmid contains identical restriction sites flanking the gene compatible with the Sfi1 restriction site. Therefore, the most efficient method to functionalize the existing ELPBCs is to design a novel expression vector encoding both the ligand and cysteine residues. Each existing ELPBC gene can then be placed in this expression vector at the Sfi1 site. The encoded ligand will then be attached at the hydrophilic terminus and the cysteine residue will be attached at the hydrophobic terminus (Fig. 13). These attached groups will be coexpressed with ELPBC to efficiently create a library of RGD-, NGR-, and non-ligand ELPBC with varied segment ratios without repeating the recursive directional ligation cloning procedure [200; 201]. These vectors additionally are compatible with and allow for modification of other ELP genes.

### **3.1.1.4 ELPBC Expression, Purification, and Functionalization**

The unique properties of ELPBC greatly facilitate the synthesis of functionalized ELPBC constructs. Specifically, the genetic backbone and thermal purification allow for single-step

synthesis of ligand-ELPBC. Since the protein is coexpressed from the genetic template and the attachment of ligands is not stochastic, each ELPBC has exactly one attached ligand, conferring better control over conjugation compared to synthetic polymers. As expressed ligand-ELPBC can transition into aggregate form, it is purified using the inverse transition cycling (ITC) method allowing polymer retrieval without the use of organic solvents. Ligand-ELPBC also contains a unique cysteine residue for conjugation of maleimide-functionalized hydrophobic compounds for imaging [226] or therapeutics [102; 219] using established and compatible protocols. Beyond the advantages for drug delivery inherent to all polymers and peptides, ELPBC provides a robust platform for the generation of ligand-functionalized constructs with control, functionality, and ease not permitted with synthetic polymers.

### 3.1.2 Dynamic Light Scattering

Dynamic light scattering (DLS) is a technique for determining the size of particles in solution through analyzing diffusion coefficients [227]. In this technique, a beam of light is shined at a filtered dilute solution. The scattering pattern of this incident beam is measured at times  $t$  and  $t + \tau$  where  $\tau$  is a specific time interval. The overlap of these two signals over time interval  $\tau$  is then used to generate a correlation coefficient, and these coefficients are plotted as a function of  $\tau$  to generate an autocorrelation function. Decay of this correlation function is then fit with different sigmoid curves to determine the diffusion coefficient of each population in solution. This diffusion coefficient is then used to estimate the hydrodynamic radius ( $R_h$ ) of each mass population based on the equation:

$$R_h = \frac{RT}{6\pi N v D} \quad (3.1)$$

where  $R$  is the ideal gas constant,  $T$  is solution temperature,  $N$  is Avogadro's Constant,  $v$  is viscosity, and  $D$  is diffusion coefficient.  $R_h$  represents the radius of an ideal solid sphere with  $D$  equal to the measured value(s). The  $R_h$  and MW is also useful for estimating other parameters of spherical constructs such as coordination number ( $Z$ ), the number of molecules per construct, and coronal

density. While this technique is useful for estimating the size and MW of different constructs, it is best used for estimating size of spherical structures. This technique was previously used to identify micelle formation and determine CMT of ELP and unmodified ELPBCs [101; 200] [200]. We used this technique to (1) validate micelle formation, (2) determine effects of ligand and conjugate on CMT, and (3) identify changes in micelle physical parameters as compared to unmodified block copolymers.

## 3.2 Materials and Methods

### 3.2.1 Vector Design and Generation

Gene sequences for the peptide sequences Met-Ser-**Gly-Arg-Gly-Asp-Ser**-Gly-Gly-Pro-*Sfl1*-Trp-Pro-**Cys** (AS2), Met-Ser-**Gly-Asn-Gly-Arg-Gly**-Gly-Ser-Pro-*Sfl1*-Trp-Pro-**Cys** (AS6), and Met-Ser-Lys-Gly-Pro-*Sfl1*-Trp-Pro-**Cys** (SV2) were designed using codons with high transcription efficiency in *E. coli*. A unique *Sfl1* restriction site was inserted between the leader and trailer sequences compatible with the sticky ends of the existing ELP genes (Fig. 15).

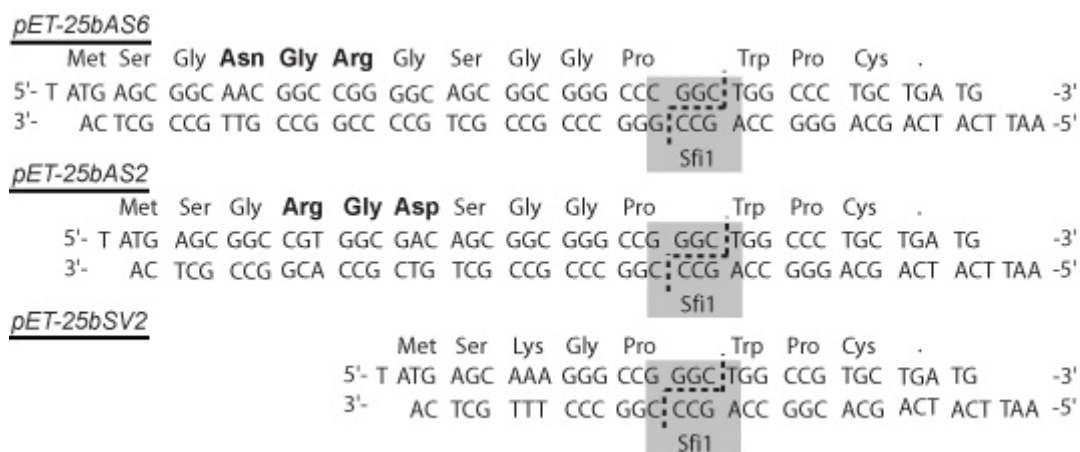


**Figure 15: Gene cassettes for creation of custom vectors for ELPBC library generation. pET-25bAS6 encodes the GNGRG ligand, pET-25AS2 encodes the GRGDS ligand, and pET-25bSV2 encodes the negative control. All cassettes contained a unique *Sfl1* restriction site for incorporation of ELPBC and cysteine for hydrophobic compounds. Reproduced in part with permission from ACS Nano, submitted for publication.**

Synthetic oligos of the forward and reverse sequences of each peptide (IDT, Coralville, IA) were obtained and annealed into a cassette by mixing 100 pmol of forward and reverse oligos, heating to 100°C, and cooling over two hours. Unmodified pET-25b expression plasmid

(Novagen, Madison, WI) was restricted with *Ava1* and *Nde1* (New England Biolabs, Ipswich, MA) and gel-purified. The annealed cassette was ligated into the restricted pET25b vector, transformed into Top10 competent *E. coli* cells (Agilent Technologies, Santa Clara, CA), and selected for ampicillin resistance. Individual clones were chosen, grown in 3 mL TB Dry (Mo Bio Laboratories, Carlsbad, CA), and subjected to diagnostic digest with *Sfi1* (New England Biolabs). Colonies corresponding to lanes with restricted plasmid were verified through direct sequencing.

### **3.2.2 Library Generation**

The genes corresponding to ELP2-96/4-60, ELP2-64/4-60, and ELP2-64/4-90 were excised from pUC19 through restriction at the *EcoR1* and *Bgl1* sites and isolated using gel purification. The modified pET-25b-SV2, -AS2, -AS6, and SV2-pET25b vectors were each restricted at the *Sfi1* site, yielding two sticky ends compatible with *EcoR1* and *Bgl1* restriction sites. The isolated gene inserts were then ligated to each modified vector at the *Sfi1* site. The resulting products were transformed into Top10 cells, selected for antibiotic resistance, and restricted with *Ava1* and *Nde1*. Clones containing an insert of the expected size were directly sequenced, and positive clones were transformed into BLR competent *E. coli* cells (Agilent Technologies) and stored as frozen stocks until further use.

### **3.2.3 ELPBC Purification**

Functionalized ELPBC were generated using a hyperexpression protocol and the previously-documented ITC purification method[201]. BLR *E. coli* containing the modified ELP plasmid were grown overnight in 50 mL TB Dry media (Mo Bio Laboratories, Inc.) spiked with 1 mg/mL ampicillin at 37 °C. The resulting cultures were centrifuged to remove media, and the resulting pellet was resuspended and grown overnight in 1 L ampicillin-spiked TB Dry media at 37 °C. The resulting culture was then purified using ITC. All heated centrifugations were performed without salt following the first round of ITC. Each ELP was purified from the soluble fraction of cell lysate by 5 rounds of centrifugation and resuspended in PBS. 5 µL of purified ELPBC was

heated at 95° C for 5 minutes and added to each well of a 4-15% gradient acrylamide gel (BioRad, Hercules, CA). The MW and qualitative purity was analyzed using SDS-PAGE.

### 3.2.4 Fluorophore Conjugation

AlexaFluor488-C5 maleimide (AF488; Invitrogen) was conjugated to the cysteine residue at the hydrophobic ELP terminus. 1 mL of 200 μM ELP was pelleted by centrifugation at 50 °C. The resulting pellet was resuspended in 900 μL conjugation buffer (0.1 M NaPO<sub>4</sub>, 3 mM tris(2-carboxyethyl) phosphine hydrochloride (Thermo Scientific, Waltham, MA) at room temperature. 1 mg of AF488 was then dissolved in 100 μL anhydrous di-methyl sulfoxide (Sigma-Aldrich), immediately mixed with ELP/binding buffer solution, and continuously rotated at RT. The reaction was quenched after 2 hours and excess fluorophore was removed by one round of ITC and desalting via a PD-10 desalting column (GE Healthcare, Waukesha, WI). The resulting ELP-AF488 concentration was determined with UV-Vis spectroscopy (Thermo Scientific) using:

$$C_{ELP-AF488} = \frac{Abs_{280} - .11 * Abs_{495}}{5690} \quad (3.2)$$

Since each ELP contains one conjugation site, the conjugation efficiency was determined as:

$$Eff = \frac{C_{AF488}}{C_{ELP}} \quad (3.3)$$

with  $C_{AF488}$  determined using extinction coefficients of 71000 cm<sup>-1</sup> M<sup>-1</sup> for AlexaFluor488 at 495 nm [102]. All samples were conjugated using this reaction and exhibited conjugation efficiency of > 70%.

### 3.2.5 Dynamic Light Scattering Measurements

100 μL of 10 μM ELP/PBS solution was filtered using a 0.02 μm syringe filter (GE Healthcare) and 35 μL of the filtered solution was added to individual wells of a 384-well plate (Corning, Corning, NY). Small drops of mineral oil were added to the top of each well to prevent evaporation. The well plate was analyzed using a thermally-controlled dynamic light scattering Wyatt Plate Reader (Wyatt Technology, Santa Barbara, CA). 18 acquisitions were obtained for



each well in 1 °C increments from 20 - 45 °C. The resulting data was analyzed using a Rayleigh sphere model and either a cumulant (1 population) or regularization (multiple populations) fit based on the sum-of-squares value. Populations comprising less than 2% of the total mass were excluded from the analysis. This data was used to directly determine the average hydrodynamic ratio ( $R_h$ ) and molecular weight (MW) of the particles in solution. The CMT was defined as the first temperature marking a step-increase in  $R_h$ . The number of unimers per micelle, coordination number, was estimated by equation:

$$Z = \frac{MW_{micelle}}{MW_{unimer}} \quad (3.4)$$

and ligand density was estimated by equation:

$$\rho_{ligand} = \frac{Z}{4\pi R_h^2} \quad (3.5)$$

### **3.3. Results and Discussion**

#### **3.3.1 Generation of RGD-, NGR-, and Non-Ligand ELPBC Gene Library**

We designed synthetic gene oligonucleotides to generate modified vectors for modification of existing micelle-forming ELPBC with either the GRGDS or GNGRG at the hydrophilic terminus and a unique cysteine at the hydrophobic terminus. These oligonucleotides encoded four contiguous segments: a hydrophilic ligand, a flexible linker, an Sfl1 restriction site, and a unique conjugation site. Gene cassettes consisting of these oligonucleotides were inserted into unmodified pET-25b vector to form the pET-25bAS2 and pET-25bAS6 vectors. Successful insertion of the gene cassette was confirmed first with restriction at the unique Sfl1 site and direct sequencing.

We selected three micelle-forming ELPBCs, ELP-96/60, ELP-64/60, and ELP-64/90 for modification. These ELPBCs were selected as they formed stable monodisperse micelles over the largest temperature range in non-functionalized form [101]. Additionally, these ELPBCs were closer to  $SR = 1$ , providing more tolerance for modification at either terminus given the required

SR of .5 – 2.0 for self-assembly [101] and .66 – 1.5 for stable micelle core formation. Gene inserts encoding ELP-96/60, ELP-64/60, or ELP-64/90 were inserted into the pET-25bAS2 or pET-25bAS6 vectors or the control pET-25bSV2 vector at the Sfi1 site. Restriction digests and sequencing of the 5' and 3' ends showed that the ELPBC genes were successfully inserted at the Sfi1 site of each vector and successful creation of the gene library described in Table 2.

**Table 3: Description of constructs developed for affinity targeting studies. The genes for each ELPBC were ligated into each of the custom expression vectors and expressed from BLR E. coli.**

		ELPBC Insert		
		ELP-96/60	ELP-64/60	ELP-64/90
Expression Vector	pET-25bSV2 (Cys)	✓	✓	✓
	pET-25bAS2 (RGD-Cys)	✓	✓	✓
	pET-25bAS6 (NGR-Cys)	✓	✓	✓

### 3.3.2 Expression of Functionalized ELPBCs

Clones encoding each of the candidate constructs were expressed and purified using the aforementioned ITC protocol. Each of the constructs led to successful protein expression with yields ranging from 30 mg/L at the low end to 200 mg/L at the high end. This variance was potentially caused by micelle formation versus aggregate formation at T = 37 – 50 °C and loss of ELPBC during cold centrifugation. While these yields were not as high as those obtained for homopolymeric ELP constructs, they were sufficient for the scale of the experiments performed in this course of study. SDS-PAGE results show that resulting ELPBC unimers are the expected MW as evidenced by the primary dark band at approximately 60 kDa for ELP2-96/4-60 and ELP2-64/90 and 50 kDa for ELP2-64/4-60 (Fig. 16). The faint secondary band observed in each lane represented twice the MW of the primary band. It was also the only other band on the gel, suggesting that it is a result of crosslinking between unblocked cysteine groups rather than extraneous protein from purification. This data demonstrated that the addition of a cationic ligand or a terminal cysteine did not disrupt protein expression or purification.

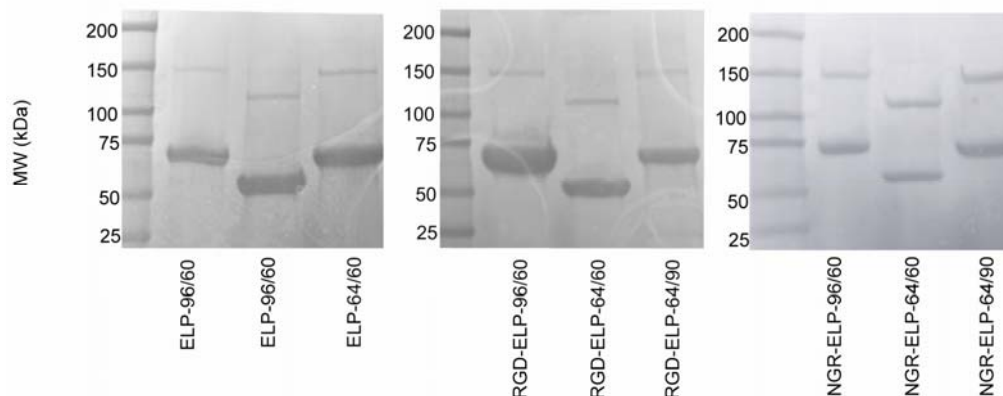


**Figure 16: SDS-PAGE of purified and modified ELPBC. Expressed ELPBC ran at the expected molecular weight and there was no impurity in the sample following five rounds of ITC. Reproduced in part with permission from ACS Nano, submitted for publication.**

Purified ELPBC was then conjugated to AlexaFluor488 at the unique cysteine residue. However, the conjugation protocol used for homopolymeric ELP constructs resulted in conjugation ratio of < 10% when applied to functionalized ELPBC. To remedy this, we reduced the concentration of TCEP, a reducing agent, from 3 mM to .3 mM. This dramatically increased the conjugation ratio of ELPBC to approximately 70% - 80%. These results suggest that TCEP provokes micelle formation which may obstruct the cysteine binding site and that different binding protocols are required for ELP homopolymer and diblock copolymer.

### 3.3.3 Evaluation of ELPBC Thermal Self-Assembly

We characterized the thermally triggered self-assembly of functionalized ELPBCs in aqueous solution by DLS. We monitored  $R_n$  and MW of a 10  $\mu$ M ELP solution as a function of temperature. This concentration was chosen as it is higher than the calculated CMC for all unmodified ELPBC, sufficiently dilute for DLS measurement, and practical for experimental reasons. These data indirectly yielded the CMT, Z, and terminal coronal density, all important parameters towards understanding effects of ligand on thermal self-assembly and suitability for static or dynamic multivalent targeting.

### 3.3.3.1 Effects of Ligand and Conjugate on Hydrodynamic Radius

$R_h$  was observed for all RGD-ELPBCs, NGR-ELPBCs and non-ligand ELP-64/90 ELPBCs from 20 °C – 45 °C (Fig. 17). All constructs exhibited two phases: (1) a soluble unimer phase with  $R_h = 5 - 8$  nm below the CMT and (2) a nanoparticle with a  $R_h = 25 - 30$  nm. In all cases, this pattern of self-assembly was similar to unmodified ELPBC with the presence of a region of stable micelle formation. Additionally, there was only one observable population in each ELPBC sample at most temperatures, illustrating clean self-assembly at  $T > \text{CMT}$ .

The addition of AlexaFluor488 affected the size of ELPBC compared to unmodified parent ELPBC [101], although the changes were subtle and different in each different ELPBC-AlexaFluor488. The  $R_h$  increased from 30.0 nm to 31.8 nm following conjugation of AlexaFluor488 to ELP-64/90, but the  $R_h$  decreased from 29.1 nm to 28.3 nm with ELP-64/60 and 32.0 nm to 26.7 nm with ELP-96/60. AlexaFluor488 affected size differently depending on segment ratio; size following conjugation increased with greater hydrophobic character and decreased with greater hydrophilic character.

The effects of ligand on micelle size were analyzed by comparing  $R_h$  of RGD- and NGR-ELPBC micelles to non-ligand ELPBC micelles (Table 3). The addition of neutral (RGD) and charged (NGR) ligand affected each of the constructs differently. The addition of RGD to ELP-96/60 led to a size decrease, but NGR did not. Conversely, NGR lowered the size of ELP-64/90 micelles more than RGD, and the size of ELP-64/60 micelles dropped with the addition of either ligand. Based on these results, both additional MW and charge affected the size of ELPBC micelles. Added charge affected hydrophilic ELPBC micelles more than added MW, but added MW affected hydrophobic ELPBC micelles more than added charge. Most notably, the addition of AlexaFluor488 and ligand did not prevent thermal self-assembly despite small changes in  $R_h$ , and functionalized ELPBC formed micelles in the desired size range for drug delivery [228]. Both of these observations suggested the suitability of ELPBC micelles for multivalent targeting.

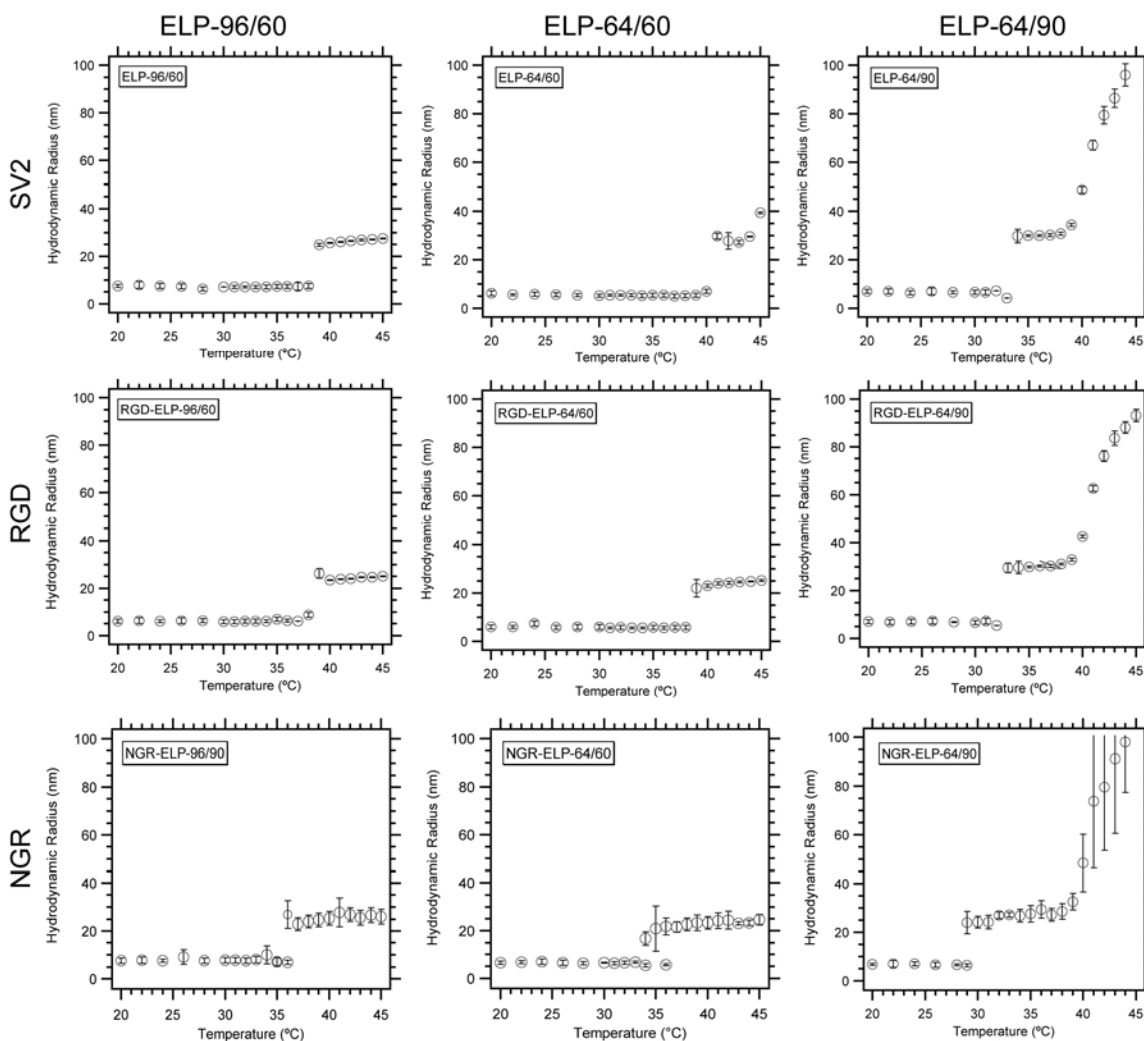


**Figure 17: Hydrodynamic radius ( $R_h$ ) of 10  $\mu$ M ELPBC-AlexaFluor488 solutions as a function of temperature. ELPBC, RGD-ELPBC, and NGR-ELPBC self-assembly consisted of two phases in the observed temperature range: soluble unimers ( $R_h$ ) at  $T < \text{CMT}$  and monodisperse nanoparticles at  $T > \text{CMT}$ . Slow nanoparticle growth was observed in the ELP-64/90 family of ELPBCs (bars = polydispersity).**

**Table 3: Hydrodynamic radius ( $R_h$ ), molecular weight (MW), coordination number (Z) and coronal terminus density of 10  $\mu$ M functionalized ELPBC. Reproduced in part with permission from ACS Nano, submitted for publication.**

ELP	Rh (nm)	MW (kDa)	Z	termini/nm <sup>2</sup>
ELP-96/60	26.7	7381	115	0.013
RGD-ELP-96/60	25	6292	98	0.012
NGR-ELP-96/60	26.7	7308	113	0.013

ELP	Rh (nm)	MW (kDa)	Z	termini/nm <sup>2</sup>
ELP-64/60	28.3	8391	167	0.017
RGD-ELP-64/60	24.3	5920	117	0.016
NGR-ELP-64/60	24.3	5922	117	0.016

ELP	Rh (nm)	MW (kDa)	Z	termini/nm <sup>2</sup>
ELP-64/90	31.8	10551	166	0.013
RGD-ELP-64/90	30.9	10348	161	0.013
NGR-ELP-64/90	27.7	8474	132	0.014

### 3.3.3.2 Effects of Ligand and Conjugate on Critical Micelle Temperature

The temperature at which an ELPBC population transformed from a bulk unimer to bulk micelle state was defined as the CMT. We used DLS results to observe this transition and defined a CMT for each construct at 10  $\mu$ M (Table 4). The CMT for ELP-96/60, ELP-64/60, and ELP-64/90 conjugated to AlexaFluor488 were 39 °C, 41 °C, and 34 °C, respectively. These corresponded relatively well to those observed with no modification with only a 1 - 2 °C decrease in CMT. This decrease suggested a slight increase in the hydrophobicity of the core-forming block relative to the hydrophilic block leading to phase separation at a lower temperature. While this effect may also be minimized given that AlexaFluor488 showed minimal effect on Tt of homopolymeric ELP, this data showed compatibility of micelle self-assembly with a synthetic conjugate.

**Table 4: transition temperatures of 10  $\mu$ M functionalized ELPBC in PBS.**

	ELP-96/60	ELP-64/60	ELP-64/90
<b>No Ligand</b>	39 °C	41 °C	34 °C
RGD	39 °C	39 °C	33 °C
NGR	36 °C	34 °C	29 °C

The addition of hydrophilic ligand to the coronal segment affected the CMT differently for each ELPBC relative to the non-ligand ELPBC. The addition of RGD to ELP-96/60 did

not affect the CMT, but the addition of RGD to ELP-64/60 and ELP-64/90 decreased the CMT by 2 °C and 1 °C, respectively. The addition of NGR significantly lowered the CMT of ELP-96/60 (3 °C), ELP-64/60 (7 °C), and ELP-64/90 (5 °C) as the effects of the charged NGR were more dramatic than uncharged RGD in all observed constructs. The effect was greatest on the ELPBC with SR = 1, and there was a greater effect on the ELP-64/90 than ELP-96/60. In all cases, incorporation of hydrophilic ligand stabilized the micelle as seen through the drop in CMT. The addition of a neutral hydrophilic ligand had a greater effect on ELPBCs with a smaller coronal segment but not a larger coronal segment. In all cases, addition of a charged ligand had a more pronounced effect on CMT than uncharged ligand, a consideration for future design.

The effects of ligand attachment on CMT set limits upon the utility of each construct. The strategy of DAM requires a construct with a CMT > 38 °C to test the effects of hyperthermia on multivalent targeting *in vivo*. Thus, these results show that of the functionalized constructs, only RGD-ELP-96/60 and RGD-ELP-64/60 exhibited the proper thermal characteristics for DAM. Additionally, these constructs exhibited a CMT very close to the thermal cutoff and thus have very low flexibility for effects due to serum and concentration, both of which are inversely proportional to  $T_t$  in homopolymeric ELP [101]. RGD-ELP-64/90 and all of the NGR-ELPBC constructs exhibited a CMT below the cutoff before serum effects. Thus, these constructs have thermal properties useful for static multivalent targeting but all except for RGD-ELP-64/90 and RGD-ELP-64/60 require redesign for DAM application.

**Table 5: Overview of the effects of modification on the CMT and Z of ELPBCs. The addition of hydrophobic construct decreased the CMT and increased the Z for all observed constructs. The addition of neutral and charged ligand following attachment of hydrophobic construct affected the CMT and Z differently based on the segment ratio, but neither increased with ligand addition with any condition.**

Modification	ELP	CMT			Z		
		96/60	64/60	64/90	96/60	64/60	64/90
Hydrophobic conjugate		↓	↓	↓	↑	↑	↑
Neutral ligand		---	↓	↓	↓	↓	---
Charged ligand		↓	↓	↓	---	↓	↓

### 3.3.3.3 Effects of Ligand and Conjugate on Coordination Number and Ligand Density

We next used micelle MW to determine the effects of conjugate and ligand on Z and estimated terminal density in the micelle corona. The addition of AlexaFluor488 to the parent ELPBC increased Z compared to the unmodified version, dramatically increasing Z in ELP-64/60 and ELP-64/90 and recruiting partially-collapsed ELPBC comprising the micelle core. The increased Z combined with the slight decrease in  $R_h$  demonstrates higher density in the corona as compared to unmodified ELPBC.

The effects of ligand on Z and terminal density in functionalized constructs were also examined. These effects varied with ELPBC segment ratio. First, the addition of RGD to ELP-96/60 or ELP-64/90 did not affect Z or coronal density. The addition to RGD to ELP-64/90 decreased Z, but the coronal density remained the same. Alternatively, NGR-ELP-96/60 showed an increased Z compared to both ELP-96/60 and RGD-ELP-96/60. NGR-ELP-64/60 showed a decreased Z compared to ELP-64/60 but similar to RGD-ELP-64/60. NGR-ELP-64/90 showed a significant decrease in Z as compared to both ELP-64/90 and RGD-ELP-64/90. These data showed that selection of ligand affected the ELPBCs recruited per micelle, causing changes in the number of conjugated moieties per micelle. Interestingly, the observed coronal density of each construct was unchanged by the addition of either ligand. Thus, the coronal density is dependent on segment ratio but independent of ligand composition, allowing control of ligand spacing through SR selection independent of ligand composition.

These data showed the addition of a neutral ligand such as RGD had a greater effect on self-assembly of ELPBC exhibiting a smaller hydrophobic block (ELP-96/60) as seen in the decrease in MW and Z, and the addition of a charged ligand such as NGR had a greater effect on self-assembly of ELPBC exhibiting a larger hydrophobic block. It also demonstrated that ligand density is controlled by the block copolymer SR rather than ligand composition, and the hydrophilic segment reaches optimal length without the incorporation of ligand. Since all of the ligand densities calculated in this study (.0124 - .0160 termini/nm<sup>2</sup>) corresponded well to the



minimum spacing needed to interact with clustered  $\alpha\beta 3$  integrin, it follows these may prove useful for multivalent targeting. While the density of CD13 expression is unknown, CD13 exhibits a 13.5 nm-wide head group [229]. Assuming maximum density without receptor deformation, the ligand density of all tested NGR-ELPBC should also allow multivalent interaction with multiple CD13 groups.

### **3.4 Significance**

The data presented in this section demonstrates several key requirements for the use of ELPBC for either dynamic or static affinity targeting. First, all functionalized active/control ELPBC constructs expressed and purified successfully. Despite incorporation of N-terminal charge, addition of RGD and NGR to the hydrophilic terminus did not prevent expression and purification and yielded clean samples and suitable yields. Second, addition of a zwitterion or charged hydrophilic ligand to the hydrophilic terminus did not disrupt self-assembly. As seen in the DLS data, both RGD and NGR addition and AlexaFluor488 conjugation still permitted thermally-triggered self-assembly. The inherent flexibility of ligands and synthetic conjugates showed that ELPBC is, based on preliminary results, a robust material that self-assembles predominantly through hydrophobic interaction. Third, both ligand and conjugate displayed an effect on self-assembly properties. The AlexaFluor488 conjugate promoted a significant increase in MW corresponding to higher Z and coronal density. Ligand size and charge both affected the CMT depending on segment ratio. The CMT was minimally affected by AlexaFluor488, and the terminal density was affected by the SR and hydrophobic conjugate, suggesting design flexibility in ligand and conjugate selection. The exact relation between ligand and conjugate is unclear, but any extractable trends would improve design of future constructs with more precise physical characteristics. Fourth, these constructs can all be tested for static and dynamic affinity targeting capabilities in short-term *in vitro* studies. However, further characterization must be performed in serum to identify the utility of these constructs for DAM from a material perspective.

## 4 Development of a Cell Line with Controllable Cell Receptor Expression for Cell-Binding Assay

### 4.1 Introduction

Numerous surface-based and cell-based assays are used for study of ligand-receptor interaction. Surface-based assays provide control over receptor density, while cell-based assays retain distinct functional behaviors. Both assay types promote benefits towards study of ligand-receptor interaction but also exhibit limitations. We required a versatile testing platform for evaluating ligand-ELPBC compatible with both the complexities of integrin behavior and reversible self-assembly, suggesting a cell-based assay. Additionally, we wanted to observe the effects of receptor expression in a systematic fashion, promoting the use of a surface-based assay. Thus, the goal of this study was to develop robust cell lines incorporating isolated and titratable receptor expression as a platform for *in vitro* cell based assays. We used retroviral vectors to introduce a doxycycline-sensitive promoter/reporter system for adjustable receptor expression on the surface of K562 human leukemia cells. The results demonstrated that K562 cells were susceptible to retroviral infection and antibiotic selection; K562 cells stably infected with a promoter gene showed external control over expression of a transfected control plasmid; and K562 cells containing both the promoter and monomeric receptor genes exhibited titratable expression on the cell surface. However, K562 cells did not incorporate a third transformed gene, preventing titratable expression of an exogenous dimeric receptor. Thus, K562 cells can serve as a platform for cell-based binding assays and titratable K562-Tet-On-CD13 cells are suitable for *in vitro* study, but further modification is needed to allow titratable dimeric receptor expression and precise control over receptor surface density.

### **4.1.1. Ligand-Receptor Binding Assays**

Ligand-receptor binding represents a large area of study, and different information regarding these interactions is required based on particular aims. As a result, a wide variety of strategies exist for detecting and evaluating ligand-receptor interaction. These approaches can be subdivided into thermodynamic, surface, and cell-based assays.

#### **4.1.1.1 Thermodynamic Assays**

Thermodynamic assays are based on the direct measurement of enthalpic changes in a closed solution following ligand-receptor interaction. Isothermal titration calorimetry (ITC) is a technique that measures the power needed to maintain temperature of a receptor solution with increasing ligand concentration [230]. In this method, free ligand is injected into the closed system, and the power needed to maintain constant solution temperature is monitored as a metric for change in heat. This technique can detect enthalpy changes associated with ligand binding and extract the binding affinity and stoichiometry of a given ligand-receptor interaction. Differential scanning calorimetry (DSC), a complementary technique, is used to evaluate the specific heat capacity as a function of temperature which is directly related to the change in entropy [231]. These complementary assays provide exquisite quantitative detail regarding thermodynamic changes through calculation of free energy [232]. However, these are typically very labor-intensive, time-intensive, and low-throughput strategies. Additionally, these assays are typically used with free receptors versus membrane-bound receptors. Therefore, thermodynamic assays are best applied when detailed information is needed regarding a known interaction between ligands and soluble receptors.

#### 4.1.1.2 Surface-Based Assays

Surface-based assays represent a strategy to detect ligand-receptor interaction with receptors attached to a fixed surface. These assays provide quantitative information regarding the kinetics of protein accumulation on a surface decorated with the target receptor [233]. Two well-known assays of this type are quartz-crystal microbalance (QCM) [234] and surface plasmon resonance (SPR) [235]. QCM is based on an oscillating quartz crystal with a thin surface coating. The quartz crystal, which has piezoelectric characteristics, is subjected to an alternating current at its resonance frequency. As material accumulates on the surface of the oscillating crystal, the change in the applied current is used to quantify the changes in mass and surface binding. This method can be used to detect interaction of soluble ligand with surface receptors. However, since this technique detects adhered mass, it is not capable of identifying differences between specific and non-specific binding, making it unsuitable for our needs. SPR is based on propagation of a plasmon, a surface electromagnetic wave that propagates parallel to a gold surface, following excitation by an incident beam. The amplitude of the plasmon is affected by thin films on the surface of the gold. If a solution is flowed over the surface of the chip, changes in the plasmon can be used to detect adherence of solution molecules to the chip to receptors adsorbed onto the gold surface [236; 237]. The change in the amplitude as a function of time can be used to quantify the binding kinetics for a given ligand-receptor interaction. This technique has proven very useful in detecting small bulk binding events and is very useful in detecting binding to immobilized receptors while minimizing non-specific accumulation due to constant solution flow. However, this technique is limited to ligand-receptor interactions independent of allosteric interaction or spatial receptor rearrangement. While techniques have been developed to incorporate lipid bilayers on SPR surfaces [238], the complex protocols still yield a surface that does not incorporate all the signaling processes necessary for some ligand-receptor binding events.

#### 4.1.1.3 Cell-Based Assays

Cell-based binding assays incorporate different cell lines, typically one receptor-positive and one receptor-negative, to evaluate specific ligand-receptor interactions. In these assays, a macromolecule presenting the ligand of interest is coincubated with each cell line in stationary or flow conditions. Following incubation, the cells are analyzed using a number of different strategies including competitive binding, flow cytometry, and fluorescence microscopy. The cell-based assay is the least regulated of the described techniques but also the most biologically-relevant. The cell will produce and present the receptor in the proper orientation, making cell-based assays typically cheaper and more efficient than physisorption for other surface-based assays, and behaviors affecting multivalent interaction are retained such as “inside-out”/“outside-in” signaling and clustering [239]. These both have contributed to the popularity of these assays for the study of integrin binding. Cell-based assays suffer from several important shortcomings. First, it is very challenging to analyze short-term binding kinetics as measurements are taken at a discrete time points rather than continuously over a single sample. Second, cells are dynamic scaffolds that will change their expression levels over time either through excessive passaging and/or repeated trypsinization [240]. Thus, wild-type cell lines will show expression dependence based on passage number, making it challenging to maintain consistency even within the same culture. Third, different cell lines will express different ancillary receptors, secrete different ECM components, present different accessible surface areas, and exhibit different metabolic rates. These differences decrease the signal-to-noise ratio when comparing data between active and control cell lines, further confounding binding data. Fourth, and most importantly, cell line contamination is a widespread issue with a large number of publicly available cell lines misidentified [241]. Therefore, a cell line characterized for one study may not be consistent when used for another given incorrect characterization of cell repository stocks.

All three types of assays have been utilized for the study of multivalent interaction between RGD- $\alpha\text{v}\beta\text{3}$  and NGR-CD13 [242], but the most pervasive method is the cell-based assay. A wide range of cell lines, healthy or pathogenic and wild-type or genetically modified,

have been used to identify constructs that exhibit specific cell targeting. A partial description of these active/control cell pairs are described in Table 6. While these studies all demonstrated a binding increase using multivalent constructs, there are complications with the use of separate cell lines. First, it is difficult to isolate a particular receptor if (A) the active control line is positive for multiple related receptors and/or (B) two different wild-type cells are used for active and control groups. A prime example is the HT-1080/MCF-7 pair as these cells have been previously used to determine specific binding to both  $\alpha v\beta 3$  and CD13. As the HT-1080 cell is positive for both receptors, it follows that this pair cannot be used to isolate binding to one of the receptors. Furthermore, conclusions regarding a specific binding mechanism are weakened by the use of unrelated cell lines. Second, receptor expression can vary greatly on non-immortalized cell lines. This is evident in human umbilical vein endothelial cells (HUVECs) as these exhibit large variance in their surface receptor expression at later passages [243]. Additionally, these cells express a wide variety of surface receptors, leading to similar difficulties with receptor isolation. Third, gene expression in transformed cell lines can decrease over time due to unstable transformation or

**Table 6: Examples of active/control cell lines for testing  $\alpha v\beta 3$  and CD13 ligand-receptor binding *in vitro*.**

Active Cell	Control Cell	Receptor Tested	References
M21	M21L	$\alpha v\beta 3$	[244-246]
U87-MG	MCF-7	$\alpha v\beta 3$	[247; 248]
K562- $\alpha v\beta 3$	K562	$\alpha v\beta 3$	[242]
BT-20	9L	$\alpha v\beta 3$	[168]
CD13/MOLT-4	MOLT-4	CD13	[128]
HUVEC	B16	$\alpha v\beta 3$	[249]
HUVEC	N/A	CD13	[189; 243; 250]
HT1080	MCF-7	CD13	[251; 252]
HT-1080	MCF-7	$\alpha v\beta 3$	[253]
HT-1080	SK-UT-1	CD13	[243]

different growth rates compared to untransformed cells. Repeated passaging can also alter the expression of different receptors on the cell surface, especially those associated with focal adhesions [240].

## **4.1.2 Universal Binding Assay Design**

Despite these challenges, the pervasive use of the cell-based assay, relative availability of reagents, and our interest in preserving native integrin geometry and clustering behavior led us to focus on cell-based assays as a testing platform. To minimize the negative effects and variability, we chose to develop a cell line with (1) isolated receptor presentation, (2) controlled gene expression, (3) potential for use as both an active and control group, and (4) compatibility with reversible self-assembly of ELP/ELPBC. The main challenges of incorporating reversible temperature- and concentration-dependent self-assembly and isolating individual receptor expression led us to focus our studies on the K562 cell line transformed with a tetracycline-sensitive promoter/reporter expression system.

### **4.1.2.1 K562 Erythroleukemia**

The K562 cell line is an immortalized erythroblastic leukemia cell line that is similar to undifferentiated granulocytes and erythrocytes. This cell line exhibits very low levels of adhesion receptors including  $\alpha\beta3$ ,  $\alpha\beta5$ , and CD13. This makes the cell line very useful as a negative control for cell-based binding assays. The K562 line grows in suspension, making it convenient for long-term passaging without use of trypsin. Additionally, this cell line grows in suspension and may reduce artifacts stemming from non-specific uptake of transitioned ELP by an adherent cell line [254]. Studies have also shown successful transformation of K562 cell lines to stably express either the  $\alpha\beta3$  integrin [255] or CD13 [256]. Thus, transformed K562 cells can serve as receptor-positive cell lines and wild-type K562 cells can serve as the negative control cell line to reduce artifacts. Therefore, the K562 cell line is ideal for evaluating interaction with a group of specific isolated receptors.

#### 4.1.2.2 Tetracycline-Responsive Plasmid System

A method for reliably controlling protein expression through a tetracycline-sensitive inducible promoter was previously developed [257]. This system allows for control over protein expression using small molecule drugs, leading to control over bulk protein expression. A commonly-used system incorporates two synthetic plasmids, one acting as a promoter gene and one acting as a reporter gene (Fig. 18). The promoter gene, Retro-X-Tet-On, encodes the CMV promoter sequence, the tetracycline-dependent transactivator in reverse (rtTA), and a region conferring antibiotic resistance. The reporter gene encodes for the tetracycline-response element (TRE), the gene of interest (GOI), and different antibiotic resistance.

In its normal configuration, tTA is constitutively expressed and will bind to the TRE segment flanking the gene of interest. When tetracycline binds to tTA, the complex is disabled and the GOI is not expressed. A fusion peptide combining tTA and the VP16 transcriptional activation region of the herpes simplex virus reverses the activity of the tTA complex and allowing

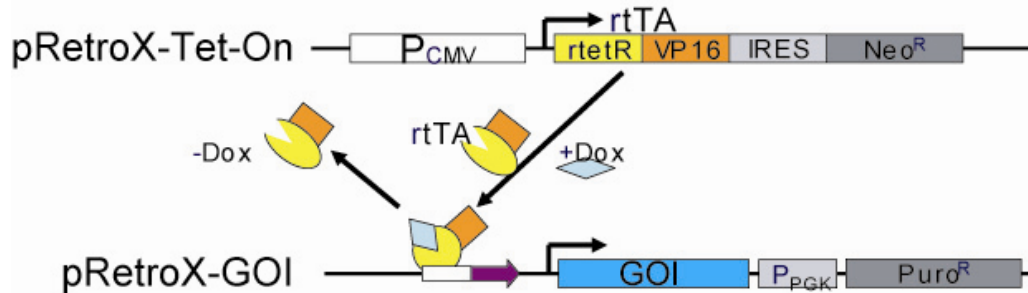


**Figure 18: Schematic of tetracycline-responsive expression system. The pRetro-X-Tet-On promoter gene ubiquitously expresses the tetracycline-sensitive transactivator (rtTA). This complex binds to the promoter region of the pRetroX-GOI containing the introduced gene of interest (GOI) in the presence of tetracycline, leading to expression of the GOI.**

expression of the GOI in the presence of tetracycline [258]. Thus, tetracycline can be used as a “switch” to activate gene expression on a per-cell basis. As tetracycline will bind with rtTA in a stochastic manner, greater concentrations of tetracycline will increase the number of cells with active gene translation, leading to titratable bulk protein expression. Doxycycline exerts a similar effect on rtTA as tetracycline but at lower concentrations, making it preferable due to a lower risk of cytotoxicity.



### **4.1.3 Flow Cytometry**

Flow cytometry is a common analytical technique used to quantify fluorescence intensity on a per-cell basis (Fig. 19A). A standard flow cytometer operates by passing a narrow band of cells suspended in isotonic sheath fluid through a series of light sources and corresponding detectors. The first set of detectors monitors forward- and side-scattering of visible light to determine cell size and nuclear fragmentation, respectively, to separate live cells from debris. The second set of detectors measures the intensity of fluorescence resulting from an incident laser at discrete excitation wavelength. This technique is also useful for sorting individual cells in real-time based on detector values by inducing charge on the stream and deflecting selected cells using electrostatic interaction.

Fluorescence intensity of each cell is recorded and processed to obtain a histogram describing the distribution of fluorescence intensities amongst the live cells (Fig. 19B). In a typical analysis, cells are sorted into different groups based on statistical differences compared to a control group. This sorting allows for identification of different cell populations based on size, nuclear fragmentation, or fluorescence signal. This technique is heavily used for cell phenotyping and sorting using fluorescently-labeled primary antibodies but can also be used to quantify binding/uptake of fluorescent compounds. While this technique does not provide data regarding intracellular localization, it represents a high-throughput method to quantifying membrane-based proteins and uptake of fluorescence compounds and is very useful for characterization of both cell characteristics and construct behavior.

### **4.1.4 Retroviral Infection Strategy**

Cell modification was achieved using a sequential transfection strategy. First, we infected K562 cells with retrovirus encoding the GFP plasmid to determine compatibility of K562 cells with retroviral transformation and the expected time for antibiotic selection. Second, we infected

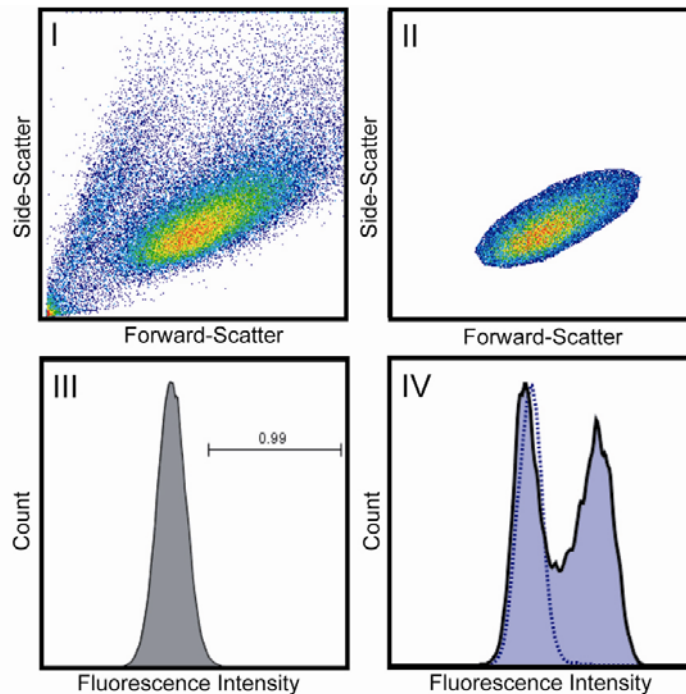


**Figure 19: Diagram of flow cytometry data acquisition and processing. An incident laser illuminates a flowing column of cells and the forward-scatter, side-scatter, and fluorescence spectra are measured on a series of detectors. (I) Raw data is obtained from a cell population. (II) Live cells are selected based on the forward- and side-scattered light. (III) A fluorescence histogram corresponding to unstained control cells is used to define a statistical population. (IV) All stained live cells are compared to the control population to identify fluorescence-positive cells.**

wild-type K562 cells with the pRetro-X-Tet-On promoter and selected a stable population. This population was then transiently transfected with a control expression gene to demonstrate (A) regulation of bulk expression of an exogenous gene and (B) the dynamic range of inducer molecule for titration. Third, stable K562-Retro-X-Tet-On was infected with retrovirus incorporating pRetro-CD13-Tight, the monomeric cell receptor with inducible control, to show the effects of induction on per-cell receptor expression, indicating if this cell line exhibits titrated receptor expression. Fourth, we then performed stepwise infection to introduce the dimeric  $\alpha\beta 3$  integrin into K562 cells. Cells were first infected with the tetracycline-sensitive pRetro- $\beta 3$ -Tight and second with the continuously-expressing pQC-Av-IH to generate a dual-stable K562-based cell line and evaluating the feasibility of titrating surface expression a dimeric receptor. Successful

completion of these steps followed by flow cytometric analysis determined if the K562 cell line serves a robust platform for testing specific binding of multivalent constructs.

## **4.2 Materials and methods**

### **4.2.1 Cell Culture**

GP-293 packaging cells (Clontech Laboratories Inc., Mountain View, CA) were cultured in DMEM (Gibco, Carlsbad, CA), 100 µg/mL amphotericin (Gibco), 100 µg/mL fungizone (Gibco), 100 units/mL penicillin (Gibco), and 10% fetal bovine serum ([FBS], Sigma-Aldrich, St. Louis, MO) in 75 cc flasks. Cells were trypsinized and split at a 1:3 ratio every 3 days. The K562 cell line (ATCC, Manassass, VA) was cultured in DMEM, 100 µg/mL amphotericin, 100 µg/mL fungizone, 100 units/mL penicillin, and 10% FBS in 75 cc flasks. During each passage, 3 mL cell suspension was pelleted and resuspended in 15 mL DMEM. Cells were split using a 1:5 ratio every 2-3 days. For antibiotic-resistant K562-based cell lines, the following concentrations of antibiotics were used for selection: 900 µg/mL G418 (Gibco), 5 µg/mL puromycin (Sigma-Aldrich), and 100 µg/mL hygromycin (Sigma-Aldrich).

### **4.2.2 Gene Construction**

Plasmids encoding the genes ITGAV, ITGB3, and ANPEP (Open Biosystems, Huntsville, AL) were obtained as frozen stocks and stored at -80°C. The plasmids pRetro-X-Tet-On, pRetro-X-Tight-Pur, pRetro-X-Tight-Luc, pQCXIH, pQC(GFP)IH, and pVSV-G (Clontech Laboratories, Inc.) were obtained, transformed into EBα competent *E. coli* cells (Stratagene, La Jolla, CA), and stored as frozen stocks for further amplification.

Cassettes encoding ANPEP or ITGB3 with sticky ends were generated with PCR from the template plasmid using synthetic primers (IDT, Coralville, IA). The forward and reverse synthetic oligos GGTATGATCAATGCGAGCGCG and GGATCAATTGTTAAGTGCCCCGGTACG were used to obtain the ITGB3 cassette, and CGTATGATCAATGGCCAAGGGCTTC and GCGCTCAATTGCTATTTGCTGTTTTCTG were used to obtain the ANPEP cassette. Each PCR reaction was cycled 35 times on a thermally-controlled heat block (Eppendorf, Hauppauge, NY)

and immediately purified using the gel extraction method (Qiagen, Valencia, CA). The gene cassette encoding ITGAV was obtained by cutting the ITGAV plasmid with AgeI and NotI restriction enzymes (New England Biolabs) and using gel extraction (Qiagen) to obtain the ITGAV cassette.

For ligation, the pRetro-X-Tight-Pur vector was restricted with BamHI and EcoRI enzymes (New England Biolabs) and purified using gel extraction. The restricted vector was then mixed with either ANPEP or ITGB3 insert at a 1:3 vector-insert ratio and incubated with T4 DNA ligase (Invitrogen, Carlsbad, CA) for 1 hour at 23 °C. The solution was transformed into competent EBα *E. coli* cells and plated for ampicillin selection. Resulting colonies were amplified and analyzed using restriction digest with EcoRI. Plasmids with the correct gel profile were verified with direct sequencing. A similar approach was used for ligation of pQCXIH and ITGAV except that pQCXIH was restricted with AgeI and NotI prior to gel extraction. All plasmids with the correct sequence following direct sequencing were stored as DMSO stocks at -80°C until further use.

### **4.2.3 Lipid-Based Transformation**

K562 cells were rinsed in antibiotic-free complete growth media at a concentration of  $2 \times 10^6$  cells/mL. For each transfection, 1 µg plasmid of interest was mixed with 4 µL Lipofectamine 2000 (Invitrogen) and incubated at RT for 30 min. This mixture was combined with 500 µL K562 cell suspension and incubated at 37 °C for 48 hrs. Following incubation, the cells were rinsed to remove lipofectamine complexes and resuspended in antibiotic-free media until use.

### **4.2.4 Retroviral Infection**

GP-293 packaging cells were split and grown in a 10 cm Petri dish (Corning, Corning, NY) until 60-70% confluent. Plasmid intended for retroviral infection (pI) and pVSV-G was amplified, purified, and measured using UV/Vis spectroscopy (NanoDrop, Wilmington, DE). For each infection, 6 µg of both pI and pVSV-G were mixed with 30 µL PLUS Reagent (Invitrogen) and 500 µL serum-free DMEM and incubated at RT for 15 minutes. 15 µL Lipofectamine

(Invitrogen) was then added to the mixture and incubated at RT for 30 minutes. The GP-293 cells were rinsed and incubated with 5 mL serum-free DMEM containing the plasmid mixture for 5 hours at 37 °C. After 5 hours, 5 mL DMEM/10% FBS was added to the culture and incubated for 2 days. Following transfection, the virus-conditioned media was removed, filtered with a .45 µm syringe filter, and stored at 4°C for use within 72 hr. For infection, 10<sup>6</sup> K562 cells were pelleted and resuspended in 4 mL virus-conditioned media, 4 mL DMEM/10% FBS, and 8 µg/mL polybrene solution. After 24 hr, cells were pelleted and resuspended in fresh 4 mL virus-conditioned media and 4 mL DMEM/10% FBS. After 24 hrs, K562 cells were rinsed twice in PBS and resuspended in antibiotic-free DMEM/10% FBS. Full media containing the selection antibiotic was added at least 18 hrs following infection. Starting at the day of plating, 10 µL of K562 cell suspension was removed from culture, mixed with 10 µL trypan blue stain (Sigma-Aldrich), and manually counted using a hemocytometer. The % live cells was calculated for each time point using the equation:

$$\%_{LiveCells} = 1 - \frac{n_{BlueCells}}{n_{TotalCells}} \quad (4.1)$$

Cells were passaged and counted every 2-3 days with fresh growth media containing antibiotics. Cultures were continually monitored until complete cell death or a noticeable increase in % live cells following antibiotic introduction.

#### 4.2.5 Luciferase Assay

K562 were stably transfected with pRetro-X-Tet-On (K562-Tet-On) using the protocol in 3.2.5. A subset of K562-Tet-On cells was then transiently transfected with pLuc using the protocol described in 4.2.3. Following transfection, 5 x 10<sup>4</sup> cells of K562-Tet-On-Luc, K562-Tet-On, and K562 were plated in triplicate in a 96-well plate at a total volume of 100 µL/well. Doxycycline (Clontech) was dissolved in serum-free DMEM below its solubility limit [259] and added to each well in a concentration gradient from 0 µg/mL – 100 µg/mL. Cells were incubated in presence of doxycycline for 48 hrs prior to assay. Each cell group was then analyzed for luminescence using

a Luciferase Assay Kit (Promega, Madison, WI). Briefly, cells were rinsed twice, lysed using a proprietary buffer, and combined with a luciferase substrate. Luminescence was then analyzed as a function of doxycycline in each cell line using a Wallac Victor3 96-well plate reader (Perkin Elmer, Waltham, MA).

#### **4.2.6 Semi-Quantitative RT-PCR**

K562-Tet-On cells were stably transfected with pRetro-ITGB3-Tight-Pur (K562-Tet-On- $\beta$ 3) using the protocol in section 3.2.5. K562 and K562-Tet-On- $\beta$ 3 Cells were rinsed, resuspended in antibiotic-free complete media at  $10^6$  cells/mL, and transferred to a 96-well plate at a volume of 100  $\mu$ L/well. K562-Tet-On- $\beta$ 3 cells were incubated in either 10  $\mu$ g/mL doxycycline or 0  $\mu$ g/mL doxycycline and K562 cells in 0  $\mu$ g/mL doxycycline for 48 hours. All cells were then lysed using RIPA buffer and centrifuged to remove cell debris. RNA was isolated from the supernatant and converted into DNA using reverse transcriptase. The gene solution was then analyzed using PCR (Bio-Rad, Hercules, CA) with the forward and reverse primers GCAATGGGACCTTTGAGTGT and TGGGACACTCTGGCTCTTCT flanking a 700 bp region of the  $\beta$ 3 gene. The resulting gene products were analyzed using gel electrophoresis.

#### **4.2.7 Antibody Staining**

K562-Tet-On cells were stably transfected with either pRetro-ANPEP-Tight-Pur (K562-Tet-On-APN) or pRetro-ITGB3-Tight-Pur (K562-Tet-On- $\beta$ 3), and K562-Tet-On- $\beta$ 3 cells were stably transfected with pQC-Av-IH (K562-Tet-On- $\alpha$ v $\beta$ 3) using the protocol in section 3.2.5. Cells were plated at  $10^5$  cells/well and incubated for 48 hrs in complete growth medium supplemented with 0-10  $\mu$ g/mL doxycycline. After 48 hrs, cells were rinsed twice and suspended in dPBS prior to analysis. Each well of K562-Tet-On-APN cells was stained with 10  $\mu$ g of FITC-WM15 Ab (eBioscience, Inc., San Diego, CA), and each well of K562-Tet-On- $\beta$ 3 cells was stained with FITC-Anti-CD61 ( $\beta$ 3) Ab (eBioscience, Inc.). Both cell types were incubated at 37 °C for 1 hr, rinsed twice, and fixed in 4% paraformaldehyde (Alfa Aesar, Ward Hill, MA) prior to analysis.

#### **4.2.8 Flow Cytometry Analysis**

Each stained cell group and an unstained control sample were analyzed using an LSR II flow cytometer (BD, Franklin Lakes, NJ). A gate corresponding to healthy cells was assigned based on the forward-scatter/side-scatter plot of the unlabeled control sample. The fluorescence histogram of the control sample was used to define receptor-positive and receptor-negative regions based on median fluorescence; cells with intensity  $> 2$  SD above mean fluorescence were defined as receptor-positive and cells with intensity below this value were defined as receptor-negative. A minimum of 15,000 live cells were analyzed per well. The percentage of receptor-positive cells and median intensity of the receptor-positive population were calculated using FlowJo analytical software (Tree Star, Inc., Ashland, OR). These data were plotted as a function of doxycycline concentration and fit with a sigmoid function to establish a dose-response curve using IgorPro (WaveMetrics, Inc., Lake Oswego, OR).

#### **4.2.9 Confocal Microscopy**

Cells were prepared using an identical protocol to those prepared for flow cytometry. Following fixation, the resulting cell suspension was concentrated to c.a. 5  $\mu$ L and transferred to a clean slide. Prolong anti-fade reagent (Invitrogen) was added to the cell droplet and sealed using a cover slip and clear nail polish. The slides were then imaged within 24 hours using a Leica SP5 upright confocal microscope (Leica Microsystems, Bannockburn, IL). Autofluorescence was corrected through spectral deconvolution, and resulting DIC and FITC images were processed using Adobe Photoshop (Adobe, Inc., San Jose, CA).

### ***4.3 Results and Discussion***

The ideal binding assay for soluble ligands and embedded receptors combines the control of surface-based assays such as SPR and QCM with the convenience and relevance of cell-based assays. The K562 cell line is useful for these assays due to low expression of surface receptors, growth in suspension eliminating the need for trypsin, and susceptibility to gene modification, and the tetracycline-responsive expression system allows for titration over bulk

protein expression through a dual-plasmid system and provides external control over cell behavior. By transforming the K562 cells with the dual-plasmid system, we intended to establish a cell line for titratable per-cell expression of different target receptors for use in cell-binding assays with ligand-ELPBC micelles.

### **4.3.1 Evaluation of Retroviral Infection**

Retroviral infection provides a greater chance of stable cell transformation than lipid-based transformation agents as the transformed plasmid is directly incorporated into the cell genome. While our protocol has been used for modification of endothelial cells, we have not previously used it to modify K562 cells. First, the retroviral vector may insert the plasmid at a location incompatible with the cell, resulting in cytotoxicity. Second, the suspension cell line makes monoclonal selection difficult. Third, the stability of K562 retroviral modification over time is unknown. Fourth, retroviral infection of K562 cells has proven challenging in past attempts with standard retrovirus. To evaluate the feasibility of the transformation method, a plasmid-borne GFP gene conferring puromycin resistance (pQ(GFP)I-Pur) was to introduced into the K562 cell line to establish compatibility of suspension K562 cells with retroviral infection and antibiotic selection.

We transfected the GP-293 cell line with both pQ(GFP)I-Pur and pVSV-G, a packaging signal for virus production. Wild-type K562 cells were then infected with the resulting pantropic retrovirus and monitored for GFP expression and antibiotic selection (Fig. 20). During the first passage, very few cells in culture showed green fluorescence. The cells in culture not expressing GFP were cretinated, a sign of cell death through antibiotic selection. The live cell count and GFP expression remained low for the first two weeks after which there was a notable increase in live cells. These cells also ubiquitously expressed GFP, albeit at visibly different levels. At three weeks, the K562-GFP cells showed exponential growth with nearly all viewed live cells expressing GFP. This data shows that K562 cells are susceptible to both retroviral infection and antibiotic selection. The population of live green cells eventually overtakes the dead cells,





**Figure 20: GFP expression in K562 cells infected with retrovirus and selected with puromycin. There was sporadic expression of GFP immediately following expression with widespread cell death. After two weeks, the population of GFP-expressing cells noticeably increased. The population reached exponential growth after three weeks with nearly ubiquitous GFP expression.**

illustrating that antibiotic selection is feasible. The resulting population was polyclonal, but this may not be a concern following introduction of the inducible cell line. These data together demonstrated that retroviral transfection is compatible with K562 cells.

#### **4.3.2 Regulation of Bulk Protein Expression**

We next used a retroviral vector to stably transform K562 cells with the tetracycline-sensitive promoter (K562-Tet-On). The plasmid encoding the tetracycline-responsive promoter (pRetro-X-Tet-On) and pVSV-G were co-transfected into GP-293 cells, and the resulting retrovirus was used to generate a stable K562-Tet-On cell line. Following infection, stable cells were selected with 900  $\mu\text{g}/\text{mL}$  G418 for 3 weeks. Once the cells reached exponential growth phase in antibiotic-containing media, we tested the promoter ability to regulate luciferase expression in response to doxycycline. K562-Tet-On cells were transiently transfected with pRetro-Luc-Tight (K562-Tet-On-Luc). K562, K562-Tet-On, and K562-Tet-On-Luc cells were then incubated with 0 – 10  $\mu\text{g}/\text{mL}$  doxycycline for 48 hours and analyzed for luciferase expression (Fig. 21).

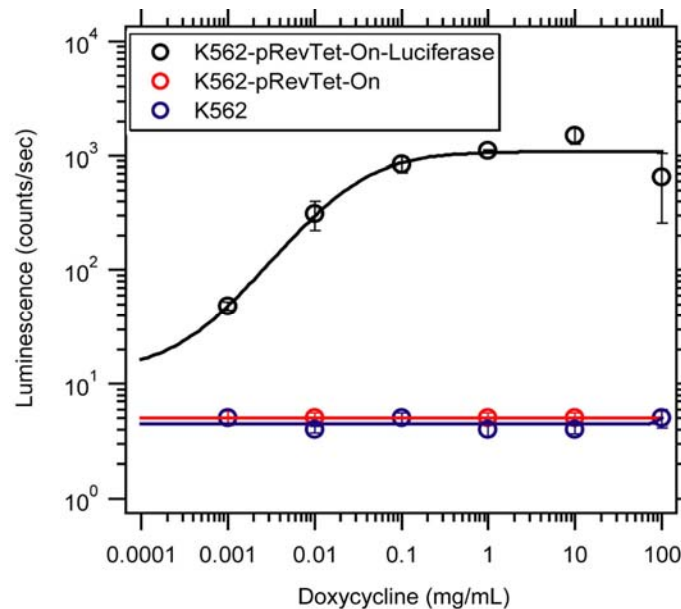


**Figure 21: Dose-response curves of luciferase expression in wild-type and modified K562 cells in response to doxycycline. Both wild-type K562 and K562-Tet-On cells without the luciferase plasmid showed no significant increase in luminescence with doxycycline concentration. K562-Tet-On transformed with luciferase showed a sigmoidal dose-response curve with a clear increase in luminescence with doxycycline up to a plateau at 1 mg/mL (n = 3, bars = SE).**

As expected, both wild-type K562 and K562-Tet-On cells showed no increase in luciferase production in response to doxycycline. K562-Tet-On-Luc, however, exhibited a dramatic response to doxycycline concentration. At 0  $\mu\text{g/mL}$ , there was a slight 2-fold increase in luminescence over both control cell lines, indicating minor leakiness of the promoter. As doxycycline concentration increased from .001 - 1  $\mu\text{g/mL}$ , luminescence also increased accordingly from 2-fold to 100-fold increase over control cells. Luminescence reached a plateau at 1  $\mu\text{g/mL}$  and expression became somewhat erratic at 10  $\mu\text{g/mL}$ , the toxicity limit for doxycycline in other cell lines [260]. The data clearly showed a dose-response effect of doxycycline and that the Retro-X-Tet-On promoter can regulate bulk expression of a target gene. This regulation was very tight given the relatively low levels of gene expression in the absence of doxycycline despite the presence of the target gene in the cell. Since the luciferase gene was transformed using a lipid-based vector rather than retrovirus, this upregulation was likely more pronounced with stable rather than transient transformation.

### 4.3.3 Plasmid Generation

We next generated a series of plasmid constructs with the genes ANPEP (CD13) and ITGB3 ( $\beta 3$  integrin subunit) for ligation into the tetracycline-sensitive pRetro-X-Tight-Pur reporter vector and ITGAV ( $\beta 3$  integrin subunit) for ligation into the ubiquitous pQCXIH vector. Since no available plasmids containing the ANPEP or ITGB3 genes were flanked by restriction sites compatible with the pRetro-X-Tight-Pur vector, we added compatible sticky ends using PCR. We designed two primer sets for ANPEP and ITGB3 to generate a cassette of each gene with Bcl1 and Mfe1 restriction sites for compatibility with Bam1 and EcoRI on pRetro-X-Tight-Pur (Fig. 22).

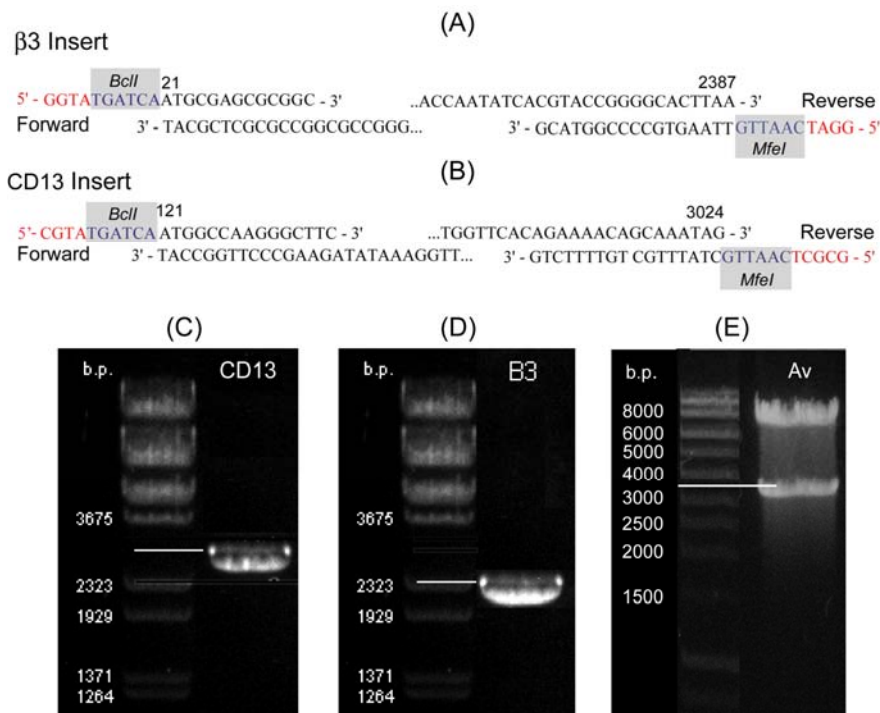


**Figure 22: Synthesis of genes for use with tetracycline-responsive system. (A/B) Forward and reverse primers were designed to add compatible, unique Bcl1 and Mfe1 restriction sites onto the human ANPEP and ITGB3. (C/D) The resulting PCR products exhibited the correct length and were ligated into the pRetroX expression plasmid. (E) The ITGAV gene was obtained directly from plasmid via restriction for insertion into pQCXIH.**

Each cassette was generated using PCR, restricted with these enzymes, and analyzed with gel electrophoresis. The resulting bands show that PCR resulted in a single gene product of the expected size (Fig. 22). These cassettes were then ligated into the pRetro-X-Tight-Pur vector and verified through restriction digests and direct sequencing. The ITGAV plasmid contained

unique restriction sites compatible with the MCS region on pQCXIH vector. Thus, the plasmid was restricted at the BamHI and NotI sites, and the resulting gene cassette was extracted and ligated into the pQCXIH vector. Restriction digests and sequencing confirmed the desired plasmid. These plasmids were stored as frozen stocks until use for transformation into K562 cells.

#### **4.3.4 Titration of a Monomeric Cell Surface Receptor**

We next evaluated the ability of stable K562-Tet-On cells to exhibit titratable gene expression through detection of CD13 on the cell surface. ANPEP was introduced into K562-Tet-On by first cotransfecting pRetro-ANPEP-Tight-Pur and pVSV-G in GP-293 cells to produce pantropic retrovirus with CD13. K562-Tet-On cells were then infected with retrovirus and selected with puromycin for 3 weeks to generate K562-Tet-On cells expressing CD13 (K562-Tet-On-CD13).

K562-Tet-On-CD13 were incubated in doxycycline from 0 – 10  $\mu\text{g}/\text{mL}$  for 48 hrs following by staining using primary-labeled WM15 anti-CD13 antibody, leading to a fluorescence signal proportional to the level of CD13 on the cell surface. The cells were analyzed for per-cell fluorescence intensity using flow cytometry. First, a negative control sample incubated with WM15 was measured to obtain mean fluorescence, and cells with fluorescence intensity 2 SDs higher than the control sample were defined as CD13+. Each subsequent cell population was analyzed for mean fluorescence over both the entire population and the CD13+ region.

The resulting histograms showed doxycycline-dependent effects. First, as doxycycline concentration increased, there was a simultaneous decrease in peak amplitude in the CD13- region and an increase in peak amplitude in the CD13+ region (Fig. 23A). Quantifying these changes, 5% of cells were CD13+ at 0  $\mu\text{g}/\text{mL}$  while increasing to 80% CD13+ at 10  $\mu\text{g}/\text{mL}$ . The %

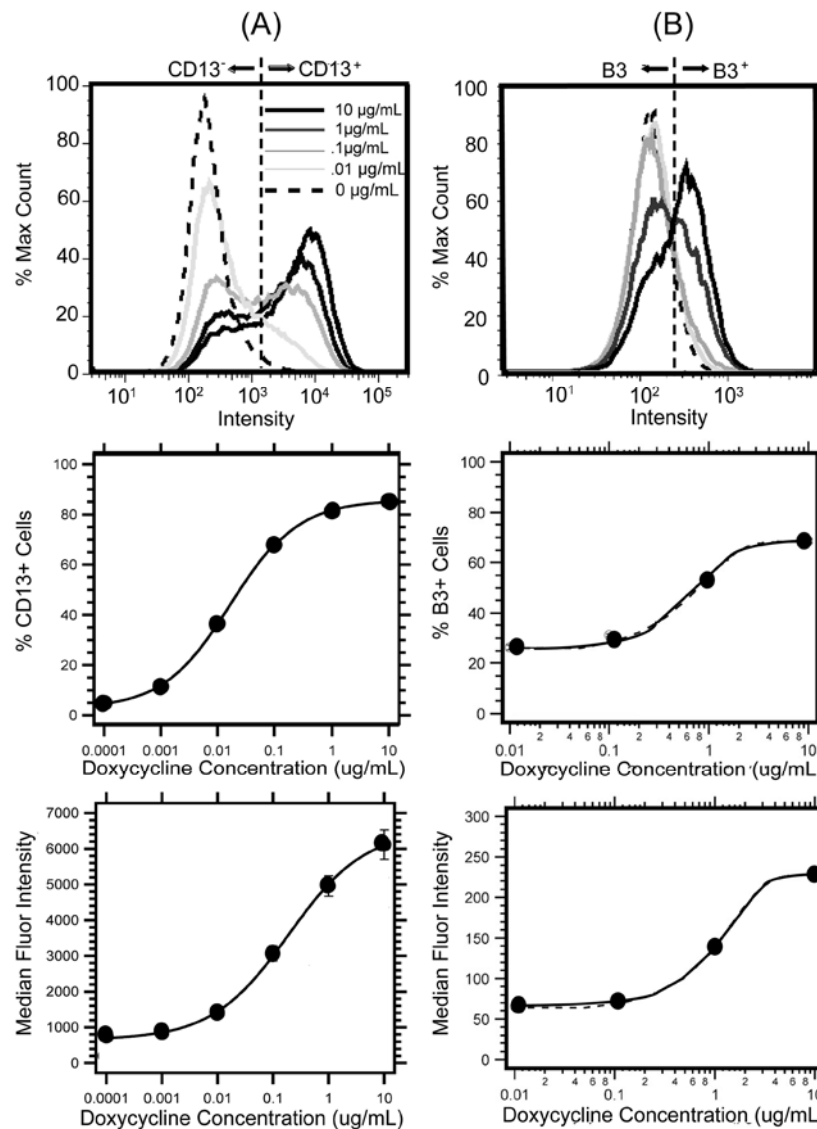


**Figure 23: (A) K562-Tet-On-APN and (B) K562-Tet-On-β3 response to increasing doxycycline concentration. (Top panel) The fluorescence histogram showed a gradual shift from a peak in the fluorescence-negative region to the fluorescence-positive region along with a right-shift of this second peak. This shift was more pronounced with K562-Tet-On-CD13 (A) than K562-Tet-On-β3 (B) (Center panel) There was an increase in the percentage of CD13+ and β3+ cells as a function of doxycycline. (Bottom panel) There was also an increase in the median fluorescence intensity of both K562-Tet-On-CD13+ and K562-Tet-On-β3+ cell populations (n = 3, bars = SE).**

CD13+ cells follows a similar dose response curve to that seen for the luciferase control, although the onset of gene expression occurred at a slightly higher doxycycline concentration. Second, there was a right peak shift in the CD13+ region with a corresponding increase in doxycycline

concentration. This shift represented a per-cell fluorescence increase and suggested that per-cell CD13 increased with increased doxycycline concentration. This shift showed an approximate 6-fold increase in median fluorescence of the CD13+ cell population in response to doxycycline concentration. Third, the positive staining with WM15 indicates that the CD13 isoform presented on these cells is the one with affinity for NGR [128]. These data together showed that while doxycycline increased discrete cell activation, it also increased per-cell receptor expression on each cell in the CD13+ region.

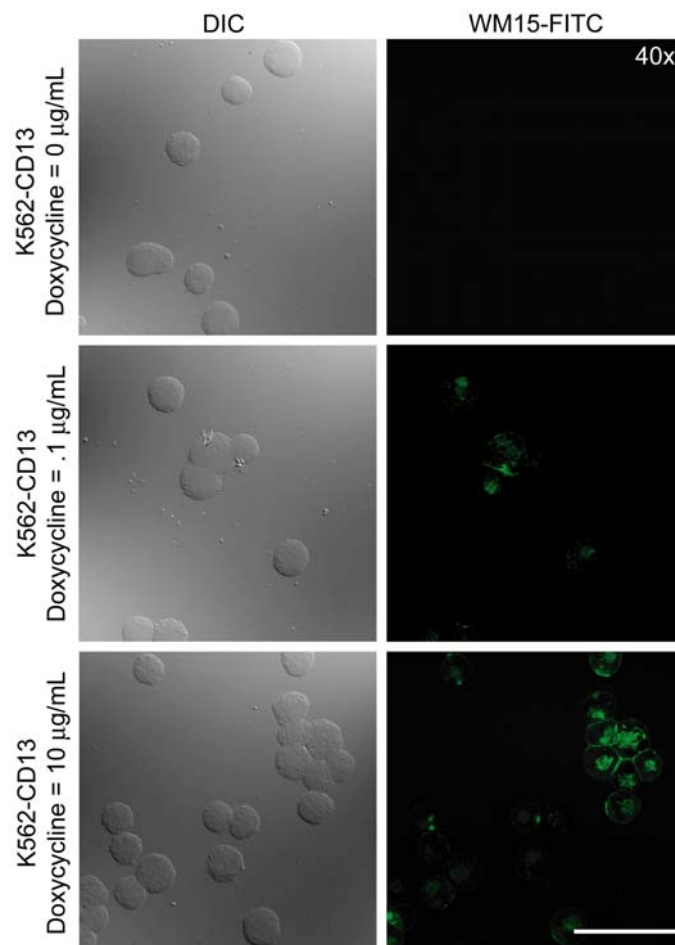


**Figure 24: Confocal microscopy images of K562-Tet-On-CD13 stained with FITC-WM15 Ab following incubation with doxycycline. There was an increase in both the percentage and intensity of fluorescent cells showing increased CD13 with doxycycline concentration. Size bar = 200 µM.**

This bimodal distribution of both CD13+ and CD13- K562-Tet-On-CD13 cells was verified using confocal microscopy. K562-Tet-On-CD13 cells were incubated at low (0 µg/mL), medium

(.1  $\mu\text{g}/\text{mL}$ ), and high (10  $\mu\text{g}/\text{mL}$ ) doxycycline concentrations and imaged for FITC emission (Fig. 24). There was no visible green fluorescence in cells incubated with WM15 at 0  $\mu\text{g}/\text{mL}$  doxycycline, showing little to no expression of CD13 without doxycycline. There were both fluorescent and non-fluorescent cells following incubation at .1  $\mu\text{g}/\text{mL}$  doxycycline and WM15, supporting the observed distribution between CD13+ and CD13- cells. There was also a distribution of fluorescent and non-fluorescent cells at high concentration of doxycycline, showing subpopulations of CD13+ and CD13- cells with positive cells showing greater fluorescence. The confocal images also show a range of fluorescence intensity on the imaged cells, reinforcing the wider secondary peak seen in the semi-log fluorescence histogram.

These results showed that a tetracycline-sensitive expression system controlled surface expression of CD13 in response to doxycycline. As seen in both the flow cytometry histograms and confocal microscopy images, there was no visible expression of CD13 in the absence of doxycycline similar to wild-type K562 cells. The two noticeable changes in the cell population with the addition of doxycycline were (1) a binary increase in cells in either the CD13- or CD13+ regions and (2) a right peak shift in the CD13+ region. The binary change likely represented a doxycycline threshold required for promoter activation. Although the solution may contain homogenous doxycycline, the intracellular concentration may be heterogeneous due to transport across the cell membrane. Those cells with a concentration above the threshold expressed the target gene, resulting in the discrete CD13- and CD13+ peaks. The peak shift in the second peak represented an increase in antibody binding per cell, presumably due to increased CD13 receptor expression. This was evident in the dose-response curve of the CD13+ median fluorescence and suggested that the expression per cell increases as a function of intracellular doxycycline concentration.

These two behaviors created a system in which doxycycline can increase presentation of a cell-based protein only following cell activation. Although this system led to bimodal distribution of receptor-positive and receptor-negative cells rather than homogenous expression, this distribution allows comparison between receptor-positive and receptor-negative cells in the same

population and. This distribution is a serendipitous asset for *in vitro* assays demonstrating specific targeting. The CD13+ cells also showed increasing median fluorescence with increasing doxycycline concentration, but the per-cell expression level was variable due to the wide peak width seen in FACS histograms. In its current state, the K562-Tet-On-CD13 is useful for altering the percentage of CD13+ and CD13- cells in a given population to indirectly prove specific binding with consistent median fluorescence of the CD13+ peak. Additionally, the level of expression shows rough titratability, but non-uniform expression even with the tightly-controlled median fluorescence, either due to intracellular transport differences or a polyclonal population, makes these cells less than ideal for studies regarding receptor density analysis in their current state.

#### **4.3.5 Titration of a Dimeric Cell Surface Receptor**

We next evaluated titration over expression of  $\alpha\beta3$  integrin, a dimeric receptor. Integrins are obligate heterodimers which require both subunits for cell expression [261]. Given that wild-type K562 cells do not express either the  $\alpha$  or  $\beta3$  subunits under normal conditions [262], both subunits must be transformed for the cell to express the assembled  $\alpha\beta3$  integrin on the surface. This also should allow for titratable control over the entire integrin complex  $\alpha\beta3$  by controlling expression of only one of the subunits. We chose to introduce the inducible expression of  $\beta3$  via the pRetro- $\beta3$ -Tight-Pur plasmid and continuous expression of  $\alpha$  via the pQC-Av-IH plasmid. First, wild-type K562 can upregulate the  $\beta3$  integrin in response to phorbol ester and other activating compounds, leading to potential upregulation of  $\beta3$  in the presence of doxycycline. Incorporation of  $\beta3$  on the inducible reporter ensures that  $\beta3$  will be upregulated at high doxycycline concentration independent of activation state. Second, wild-type K562 cells will also upregulate the gpIIb integrin subunit following activation [263], and this subunit forms a dimer with the  $\beta3$  subunit. In this case, introduction of ubiquitous  $\beta3$  expression could lead to continuous expression of gpIIb $\beta3$  and background interaction with RGD-based constructs. To avoid this potential scenario,  $\beta3$  cannot be incorporated using a continuously-expressed plasmid. Third,  $\alpha$



is not expressed by K562, and it is incompatible with integrin subunits expressed by K562 besides  $\beta 3$ . Thus, Av should only be presented on the cell surface with simultaneous upregulation of  $\beta 3$ .

We first transformed K562-Tet-On cells with pRetro-ITGB3-Tight using an established protocol for retroviral generation and infection. We then selected a stable population of cells (K562-Tet-On- $\beta 3$ ). Briefly, K562-Tet-On- $\beta 3$  was incubated with 10  $\mu\text{g}/\text{mL}$  and 0  $\mu\text{g}/\text{mL}$  doxycycline for 48 hours. Cells were then labeled with AlexaFluor488-labeled anti- $\beta 3$  Ab and analyzed for surface expression using semi-quantitative RT-PCR (Fig. 25) and surface expression using flow cytometry (Fig. 23B). RT-PCR revealed no visible expression of ITGB3 in the wild-type cells and low expression in K562-Tet-On- $\beta 3$  cells with no doxycycline. Alternatively, there was a significant increase in expression of ITGB3 in K562-Tet-On- $\beta 3$  cells incubated with 10  $\mu\text{g}/\text{mL}$  doxycycline. The resulting histograms corresponding to  $\beta 3$  surface expression showed similar trends of surface expression as CD13, albeit at a lower magnitude. First, a greater percentage of K562-Tet-On- $\beta 3$  cells exhibited fluorescence intensity in the  $\beta 3^+$  region with increased doxycycline from 0  $\mu\text{g}/\text{mL}$  - 10  $\mu\text{g}/\text{mL}$ . The percentage of  $\beta 3^+$  cells reached a maximum at approximately 70%, slightly lower but similar to K562-Tet-On-CD13. However, the minimum percentage at low values of doxycycline was approximately 25%, showing some leakiness in surface expression, likely due partial activation of wild-type cells in the presence of doxycycline. The change in median fluorescence of  $\beta 3^+$  cells with increasing doxycycline was a 3.5 - 4 fold increase compared to a 7.5 - 8 fold increase with CD13. Given that integrin subunit is only expressed on the cell surface in the presence of compatible subunits, the observed  $\beta 3$  on the cell surface likely corresponds to gpIIb $\beta 3$  expression. Since doxycycline increased expression of an integrin associated with offsite RGD binding, this may lead to potential complications with isolating  $\alpha v\beta 3$  from gpIIb $\beta 3$  for testing RGD-based constructs. However, it may also present a situation where the K562-Tet-On- $\beta 3$  could serve as a useful cell-based assay for testing RGD-gpIIb $\beta 3$  interaction for future study.

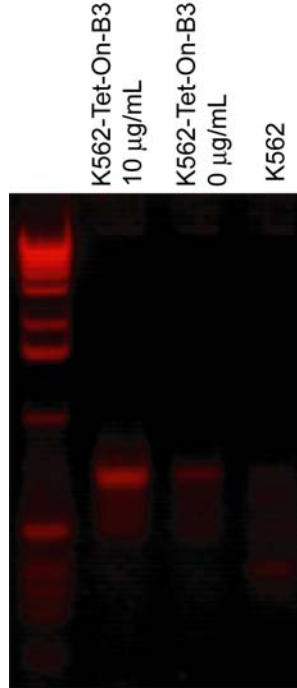


**Figure 25: Gel electrophoresis results following RT-PCR testing for  $\beta 3$  expression. There was an increase in the band corresponding to  $\beta 3$  expression with increased doxycycline. The gene was also expressed at a low level without doxycycline in K562-Tet-On- $\beta 3$  but at an undetectable level in wild-type K562 cells.**

Despite this potential uncertainty, we next attempted to transform K562-Tet-On- $\beta 3$  with pQC-Av-IH, the plasmid conferring continuous expression of the  $\alpha v$  integrin subunit and hygromycin resistance. We generated pantropic virus with sequence-verified pQC-Av-IH and VSV-G plasmid, infected the stable K562-Tet-On- $\beta 3$  cells, and selected using 100  $\mu\text{g}/\text{mL}$  hygromycin according to antibiotic resistance curves with untransformed cells. The percentage of live cells was then monitored for three weeks to determine successful infection. After three weeks, both K562-Tet-On- $\beta 3$  and K562-Tet-On- $\beta 3$ - $\alpha v$  cells showed nearly complete cell death for a prolonged period of time ( $< 5\%$  live cells) for 3 weeks. The transformation was repeated with fresh pQC-Av-IH and pVSV-G and yielded identical results with complete cell death within 2 weeks. Based on these results, K562 is compatible with double-stable transfection of the Tet-On promoter and  $\beta 3$  plasmids but may not be compatible with a third stable transformation. These difficulties show that the cloning strategy should be redesigned to generate a tri-stable K562 cell line expressing the  $\alpha v\beta 3$  integrin in a titratable fashion. However, the wide peak width in the

receptor-positive region with monomeric expression as well as potential complication with gp11b $\beta$ 3 expression shows that this still may not promote discrete, isolated receptor expression. Thus, stable transformation of  $\alpha$ v and  $\beta$ 3 plasmid without inducible control may promote benefits for cell-binding assays using a simpler approach.

#### **4.4 Significance**

The data generated in these studies has great relevance to the (1) development of a universal cell-binding assay for ligand-receptor interactions and (2) working towards production of controlled levels of both RNA and protein in mammalian cells. First, the advantages of using the K562 system versus other potential binding assays for study of transitioned ELPs are numerous, most notably the ease of culture, growth in suspension, and isolated expression of target cell receptors. In addition to upregulation, the binary activation also confers an advantage by splitting each cell group into receptor-positive and receptor-negative cells, allowing generation of active and control cells from the same culture.

This study establishes a standard protocol for developing and maintaining cell lines specific for each ligand-receptor pair. We have established a stable K562-Tet-On cell line, the desired monomeric gene can be easily inserted into the reporter gene following PCR modification, and the retroviral transformation protocol can lead to a stable cell line within 3 weeks of selection. Successful titration of receptor expression with both K562-Tet-On-CD13 and K562-Tet-On- $\beta$ 3 showed that K562-Tet-On represents a flexible platform for expressing proteins in a titratable fashion as on the cell surface and may prove useful for other monomeric receptors of interest to our group such as LHRH [223]. While future work is needed to establish a protocol for developing a cell line to control dimeric receptor expression, this protocol in its current state will both save time and reduce many of the uncontrollable barriers now associated with *in vitro* study.

Another ancillary benefit to this cell line is the potential for scalable RNA transcription and expression of protein. This, combined with the simple culturing routine, provides a platform for

generating expression gradients of RNA and/or soluble protein. Our data shows tight control over bulk protein expression in response to doxycycline concentration, suggesting that RNA expression is also under doxycycline control as well. The ability to specifically adjust expression of a target gene has great potential for studies requiring a protein or RNA concentration gradient and thus could have potential for studies calculating protein detection limit of a sensor or amplification of a target RNA/DNA sequence from a complex milieu.

## 5 Evaluation of Dynamic Affinity Modulation Using Elastin-Like Polypeptide Block Copolymers

### 5.1 Introduction

Ideally, dynamic affinity modulation (DAM) will limit the activity of vascular-targeted carriers to the tumor region while avoiding binding to healthy angiogenic vasculature using applied heat to control activity. For DAM to be successful using functionalized elastin-like polypeptide block copolymers (ELPBCs), several requirements must be met. First, ligand-ELPBC must exist in an “off” state below the CMT; it must not interact with cellular receptors in its hydrophilic, monovalent state. This ensures that ligand-ELPBC does not promote specific interaction outside of the selected region. Second, self-assembly of ELPBC into micelles must not promote cellular uptake independent of ligand presentation. This is important as the ELPBC must act as an inert scaffold and not directly enhance non-specific cellular uptake. Third, ligand-ELPBC must exist in an “on” state above the CMT; ligand-ELPBC micelles should lead to enhanced interaction with receptor-positive cells compared to receptor-negative cells. Meeting this last requirement would prove the ability for controlled multivalency to act as a trigger for receptor-specific cell uptake.

Thus, the primary goal of these studies was to verify the ability of ELPBC to act as a scaffold for dynamic affinity modulation (DAM). The most efficient method to demonstrate this was through a cell-based binding assay using the aforementioned K562 cell line expressing either the  $\alpha\beta3$  integrin or CD13. We showed that multivalent presentation of RGD ligand and  $\alpha\beta3$  overexpression are both required to promote specific interaction between RGD-ELPBC and K562- $\alpha\beta3$  cells. This interaction was dependent on ELPBC SR with improved uptake occurring with ELPBC with greater hydrophobic character. We repeated these experiments with NGR-ELPBC and K562-Tet-On-CD13. While there was no observed receptor-mediated uptake under all conditions, these results echo other data observed in the literature with other multivalent NGR constructs capable of binding to angiogenic vasculature. These results demonstrate that targeting

can be restricted through thermally-controlled multivalent presentation, demonstrating proof-of-principle of DAM. However, the CMT of the RGD-ELP-64/90 is too low and requires a slight increase before applying it for DAM under clinically-relevant conditions. Alternatively, further study is required to establish the benefits of multivalent NGR presentation *in vivo*.

### **5.1.1 K562 Binding Assay**

We used modified and wild-type K562 cells to perform the receptor-mediated cell uptake studies. Along with the advantages described in section 4.1.2.1, the K562 cell line provides several benefits specific to ELP and RGD/NGR multivalent interaction. First, past experiments have shown nonspecific uptake of transitioned ELP by adherent cell lines [254]. Since K562 grow in suspension, this nonspecific binding may be reduced. Second, integrins in adherent cell lines cluster at focal adhesions underneath the cell following activation [239]. The lack of focal adhesions in K562 cells suggests that integrins are fully accessible in suspension. Third, K562 cells can take up bound constructs when placed in a starved state. This improves retention of ELPBC following cell-binding and facilitates standard rinsing, staining, and fixation protocols without concern of ELPBC disassembly due to low concentration, thermal effects, or shear forces.

Since K562-Tet-On did not express  $\alpha\beta3$  integrin via the inducible promoter, we used a modified K562/ $\alpha\beta3$  cell line [242; 255]. This cell line was stably transformed using lipid-based vectors, but it also showed passage-dependent expression of  $\alpha\beta3$ . In characterization studies, expression of  $\alpha\beta3$  in at least 50% of cells lasts for several passages, permitting its use as an active cell line with K562 as the cognate negative control cell line (Fig. 26). It also shows a bimodal distribution of receptor-positive and receptor-negative cells, allowing for specificity evaluation in a single population. The K562-Tet-On-CD13 cell described in section 4.3.4 was used to evaluating the binding of NGR-ELPBC constructs to the CD13 receptor. K562-Tet-On-CD13 cells were incubated with 10  $\mu\text{g}/\mu\text{L}$  doxycycline to generate a bimodal CD13<sup>+</sup> active population and in the absence of doxycycline to generate a CD13<sup>-</sup> control population.

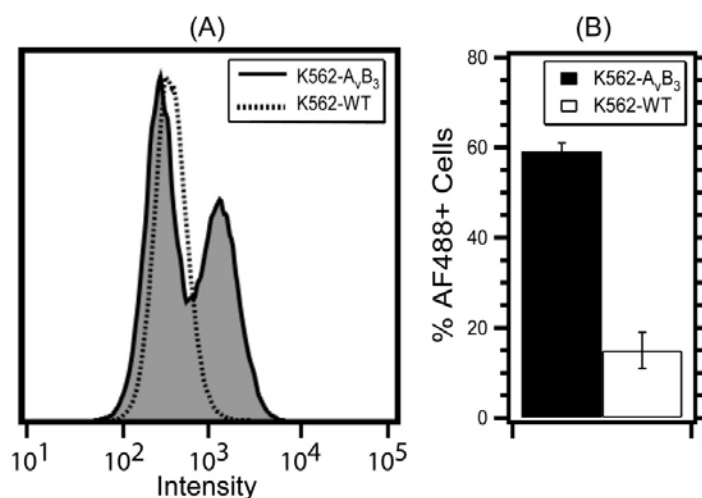


**Figure 26:  $\alpha_v\beta_3$  expression on K562- $\alpha_v\beta_3$  cells. (A) FACS histograms showed a bimodal distribution of intensities following incubation with LM609 Ab. (B) Approximately 60% of K562/ $\alpha_v\beta_3$  cells were  $\alpha_v\beta_3^+$  while < 15% K562-WT cells showed positive fluorescence, possibly due to non-specific uptake (n = 3, bars = SE). Reproduced in part with permission from ACS Nano, submitted for publication.**

We measured cellular uptake of ligand- and non-ligand ELPBCs by wild-type K562 human leukemia cells (receptor-negative control) and K562/ $\alpha_v\beta_3$  [255] or K562-Tet-On-CD13 (receptor-positive active group). Both cell lines were cultured at conditions that ensured maximum receptor presentation, and all constructs were incubated at temperatures ensuring monovalent or multivalent presentation. Cells were then analyzed for fluorescence intensity using flow cytometry as a marker for cellular uptake, and those exhibiting uptake were validated with confocal microscopy (section 6.1.2.1). These data were used to relate each construct to the three requirements for DAM and identify which, if any, constructs showed potential for DAM.

## **5.2 Materials and Methods**

### **5.2.1 Cell Culture**

Wild-type K562 cells were obtained from ATCC, K562/ $\alpha_v\beta_3$  were kindly provided by Dr. Rihe Liu in The Pharmacy School at University of North Carolina-Chapel Hill, and K562-Tet-On-CD13 cells were obtained using the procedures described in Chapter 4.2. Cell lines were maintained in DMEM supplemented with 10% FBS, 100  $\mu\text{g}/\text{mL}$  amphotericin, 100  $\mu\text{g}/\text{mL}$  fungizone, and 100 units/mL penicillin and maintained at 37  $^\circ\text{C}$  and 5%  $\text{CO}_2$ . K562/ $\alpha_v\beta_3$  media

also contained 500 µg/mL G418, and K562-Tet-On-CD13 media also contained 900 µg/mL of G418 and 5 µg/mL puromycin. Cultures were started from frozen cell stocks and split in a 1:5 ratio every 48 hours. Doxycycline was added from a frozen 100 µg/mL aliquot to 100 mL media 48 hours prior to experiments with K562-Tet-On-CD13 cells.

### **5.2.2 Cell Uptake**

500,000 K562, K562/ $\alpha\text{v}\beta\text{3}$  or K562-Tet-On-CD13 cells were plated in 6-well plates and allowed to incubate overnight. Cells were visually inspected, rinsed twice, and resuspended in 500 µL binding buffer (HBSS, 1 mM  $\text{CaCl}_2$ ) with 10 µM ELPBC. Each sample was rotated at either room temperature or 40 °C in normal atmosphere for 1 hr and rinsed in binding buffer 3 times. Cells for flow cytometry analysis were fixed in 4% PFA for 15 minutes and stored at 4 °C. Conditions showing successful uptake were independently repeated for confocal analysis.

### **5.2.3 Flow Cytometry Analysis**

An overview of flow cytometry is provided in section 4.1.4. Cell samples were analyzed using a LSRII Flow Cytometer within 18 hours of fixation. A minimum of 15,000 live cells were analyzed per sample, and FlowJo analytics software was used to quantify populations. Viable cells were gated using forward scatter and side scatter plots of an unstained control sample (Fig. 19). For Ab characterization, cells with intensity 2 SD over the median intensity of unlabeled control cells were defined as receptor-positive. Similarly, for uptake experiments, cells with intensity 2 SD over the median intensity of unheated cells were defined as fluorescence-positive. The median intensity of cells in the fluorescence-positive region was used to compare the fluorescence of heated fluorescence-positive cell populations to unheated control cells in this region to (A) overcome the bimodal distribution of receptor-positive and receptor-negative cells and (B) evaluate the effects of self-assembly and multivalent ligand presentation on cell uptake.

### **5.2.4 Confocal Imaging**

5 µL of unfixed cell sample was mixed with a small volume of Fluoromount-G (Electron Microscopy Sciences, Hatfield, PA) and placed on a glass slide. Samples were then mounted and



sealed using clear nail polish. Slides were then immediately imaged at 5x and 20x using an LSM5 Pascal confocal microscope (Zeiss, Oberkochen, Germany) with 2 channels for simultaneous imaging of DIC and AlexaFluor488. All images were obtained within 2 hours of slide mounting. Confocal images were not used for quantitative analysis.

## **5.3 Results and Discussion**

### **5.3.1 Evaluation of RGD-ELPBC Constructs with Constant Overexpression**

We used an *in vitro* cell assay based on the K562 cell line to test specific binding of RGD-ELPBC to cells upregulating  $\alpha\beta3$ . While this cell line does not exhibit precise control over  $\alpha\beta3$ , this cell line exhibits a bimodal distribution of receptor-positive and receptor-negative cells. This cell line was used as the active cell line and wild-type K562 was used as the negative control. Since the percentage of  $\alpha\beta3+$  cells drops with subsequent passages, all experiments performed within three passages following onset of exponential growth after thawing.

#### **5.3.1.1 Effects of Monovalent RGD Presentation on Cell Uptake**

We first evaluated the effects of monovalent presentation of RGD on cellular uptake by both K562 and K562/ $\alpha\beta3$  cells. 10  $\mu\text{M}$  RGD-ELPBC and ELPBC were incubated with K562 and K562/ $\alpha\beta3$  cells at  $T = 23^\circ\text{C}$  ( $T < \text{CMT}$ ) for one hour and analyzed using flow cytometry (FACS). This concentration was chosen as it showed self-assembly in all constructs, these temperatures were chosen to ensure monovalent presentation in all constructs, and the uptake conditions were chosen to promote uptake and accommodate technical limitations. Since each ELPBC was covalently labeled with AlexaFluor488, the measured fluorescence signal was proportional to cellular uptake of labeled ELPBC. The resulting FACS histograms showed that the resulting median fluorescence intensity was similar between RGD-ELPBCs and ELPBCs in either K562 or K562/ $\alpha\beta3$  cells (Fig. 27). These data show that monovalent, unimeric RGD-ELPBC is not capable of specifically interacting with the  $\alpha\beta3$  integrin at micromolar concentrations as compared to non-ligand ELPBC, creating an “off” state below the CMT.

### 5.3.1.2 Effects of Micelle Self-Assembly on Non-Specific Cell Uptake

We next evaluated the effect of thermal self-assembly on non-specific cellular uptake. We incubated non-ligand ELPBC at  $T = 40\text{ }^{\circ}\text{C}$  with K562 and K562/ $\alpha\text{v}\beta\text{3}$  cells. This temperature was chosen as it ensured self-assembly for all tested constructs but prevented cytotoxicity over the experimental time course. All samples were analyzed using FACS (Fig. 27). The histograms with each cell types at  $T < \text{CMT}$  were then used to identify a region 2 SD above the mean

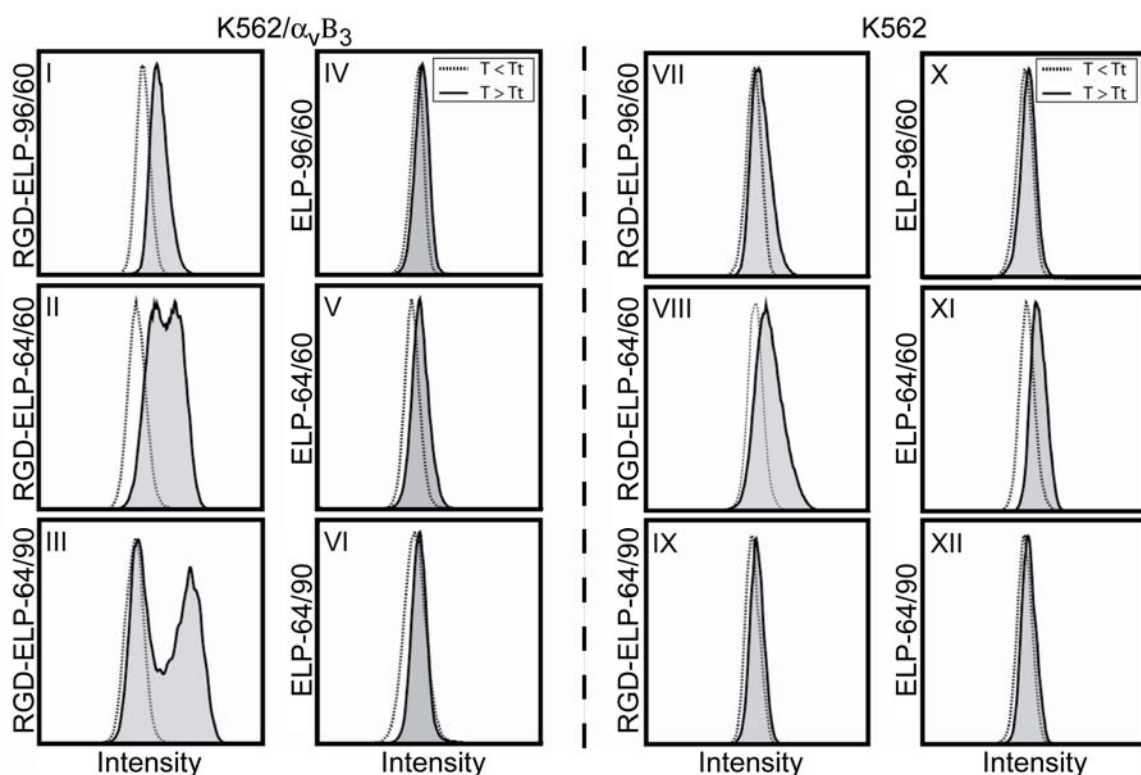


**Figure 27: Flow cytometry histograms of K562-WT and K562/ $\alpha\text{v}\beta\text{3}$  cells following incubation with ELPBC constructs at temperatures below and above the CMT. There was little difference between monovalent and multivalent presentation with any construct and K562 cells or non-ligand ELPBC and K562/ $\alpha\text{v}\beta\text{3}$  cells. There was increased uptake of RGD-ELPBC by K562/ $\alpha\text{v}\beta\text{3}$  cells with increasing hydrophobic character of RGD-ELPBC.**

Reproduced in part with permission from ACS Nano, submitted for publication.

fluorescence intensity, and cells within this region in cell populations at  $T > \text{CMT}$  were defined as AlexaFluor488+. The FACS histograms looked similar between all samples following incubation with non-ligand ELPBC. All samples had a low percentage of AlexaFluor488+ cells (2-8%) at  $T > \text{CMT}$ , possibly due to the temperature increase in combination with thermal self-assembly. There was also not a significant difference between % AlexaFluor488+ K562 and K562/ $\alpha\text{v}\beta\text{3}$  cells.

Cellular uptake following heating was further quantified by determining the median fluorescence increase of the AlexaFluor488+ region relative to the AlexaFluor488+ region of unheated cells (Fig. 28). There was minimal increase in uptake of any non-ligand construct following thermal self-assembly (~1-fold increase). These data showed that micelle formation is insufficient to promote significant cellular interaction and, thus, ELPBCs can act as inert thermosensitive scaffolds for multivalent ligand presentation.

### **5.3.1.3 Effects of Multivalent RGD Presentation on Specific Cell Uptake**

We next evaluated the effects of multivalent RGD presentation on specific cellular interaction. RGD-ELPBCs were incubated with K562 and K562/ $\alpha v \beta 3$  cells at  $T < CMT$  and  $T > CMT$  and analyzed using FACS. First, receptor-negative K562 cells incubated with RGD-ELPBCs yielded similar histograms to those incubated with non-ligand ELPBCs in either monovalent or multivalent form (Fig. 27). Using an identical grouping strategy to non-ligand ELPBCs, the percentage of AF488+ cells was not significantly different from either cell type incubated with non-ligand ELPBCs (Fig. 28). The increase in median fluorescence of the AF488+ region was minimal as compared to cells incubated with monovalent RGD-ELPBC. These results showed that RGD-ELPBCs will not promote significantly enhanced uptake in K562 cells lacking the cognate receptor. Second, histograms of K562/ $\alpha v \beta 3$  incubated with RGD-ELPBC at  $T > CMT$  varied from those incubated with control ELPBCs depending on the segment ratio (Fig. 27). There was not a noticeable increase in fluorescence in K562/ $\alpha v \beta 3$  cells incubated with RGD-ELP-96/60 at  $T > CMT$  compared to K562 cells. Alternatively, the histograms of cells incubated with RGD-ELP-64/60 and RGD-ELP-64/90 showed a bimodal distribution unlike K562 cells under

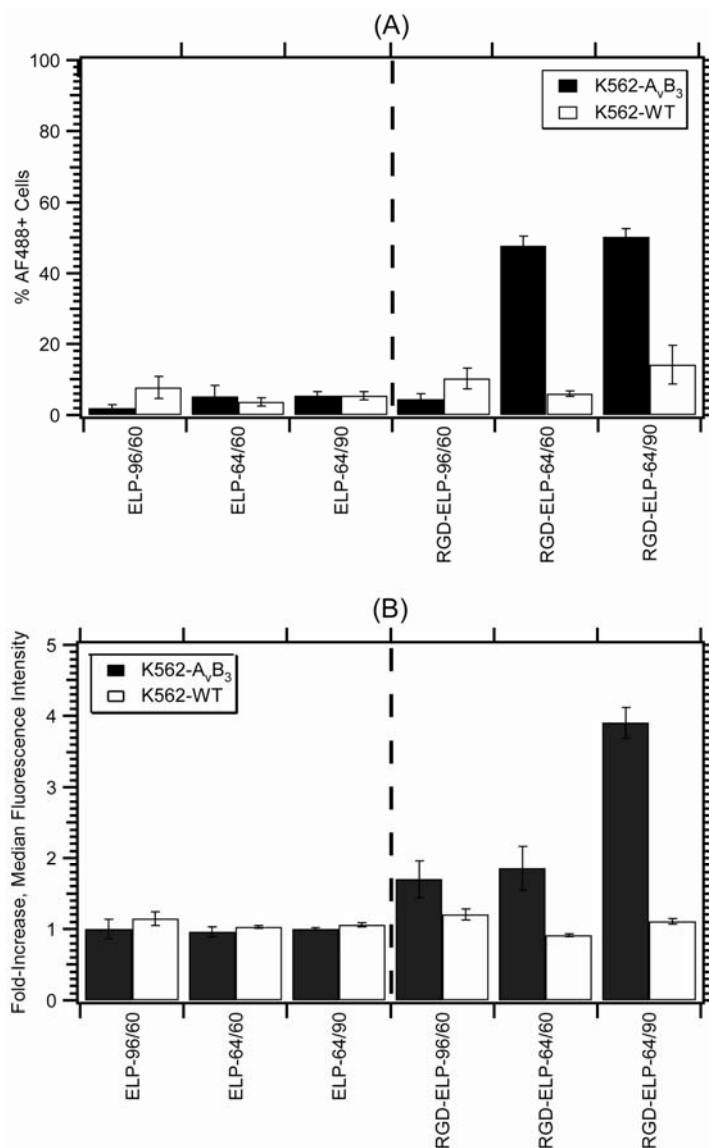


**Figure 28: Quantitative effects of multivalent RGD presentation on specific cellular uptake. (A) There was a significant increase in the percentage of fluorescence-positive cells when RGD-ELP-64/60 or RGD-ELP-64/90 was incubated with K562/ $\alpha\nu\beta$ 3 at T > CMT. (B) There was a significant increase in the median fluorescence of the second peak in both RGD-ELP-64/60 and RGD-ELP-64/90 with K562/ $\alpha\nu\beta$ 3 above the CMT (n = 3, bars = SE). Reproduced in part with permission from ACS Nano, submitted for publication.**

the same conditions. The first peak was similar in intensity to the single peak observed following incubation with non-ligand ELPBC, suggesting non-specific uptake as the origin of this peak. This second peak was not present in K562/ $\alpha\nu\beta$ 3 cells incubated with non-ligand ELPBC but present in K562/ $\alpha\nu\beta$ 3 cells stained with anti- $\alpha\nu\beta$ 3 Ab. The origin of the second peak was therefore likely increased uptake by  $\alpha\nu\beta$ 3+ cells. Further quantification of these histograms supported specific

interaction with  $\alpha v\beta 3$  in multivalent form (Fig. 28). The percentage of AlexaFluor488+ K562/ $\alpha v\beta 3$  cells increased significantly when incubated with RGD-ELP-64/60 and RGD-ELP-64/90 (48-50% AlexaFluor488+ cells) versus RGD-ELP-96/60 (4-5% AlexaFluor488+ cells). Interestingly, the second peak also shifted progressively further to the right with an increase in hydrophobic character as seen in the 2-fold and 4-fold increase in median fluorescence intensity in the AlexaFluor488+ region following incubation with RGD-ELP-64/60 and RGD-ELP-64/90, respectively.

Based on these positive results from FACS, we further validated these observations with confocal microscopy (Fig. 29). Images were taken of unfixed cells immediately following incubation with ELPBCs at the same conditions as the FACS experiments. First, K562/ $\alpha v\beta 3$  cells did not show significant green fluorescence when incubated with either RGD-ELPBC or ELPBC type below the CMT, corresponding to FACS histograms. Second, there was no significant visible fluorescence in either cell type incubated with ELPBC above the CMT or in K562 cells incubated with RGD-ELPBCs. Third, fluorescence intensities in K562/ $\alpha v\beta 3$  cells incubated with RGD-ELPBC varied with the hydrophilic-to-hydrophobic MW ratio. K562/ $\alpha v\beta 3$  cells incubated with RGD-ELP-96/60 did not produce significant visible fluorescence. However, the widefield images contained both labeled and non-labeled cells in the RGD-ELP-64/60 and RGD-ELP-64/90 populations, corresponding to the bimodal distribution seen in the FACS histogram. K562/ $\alpha v\beta 3$  cells incubated with RGD-ELP-64/90 also appeared brighter than with RGD-ELP-64/60 or RGD-ELP-96/60, echoing the FACS analysis. These results showed that multivalent presentation of RGD following ELPBC self-assembly promotes receptor-mediated uptake depending on the SR.

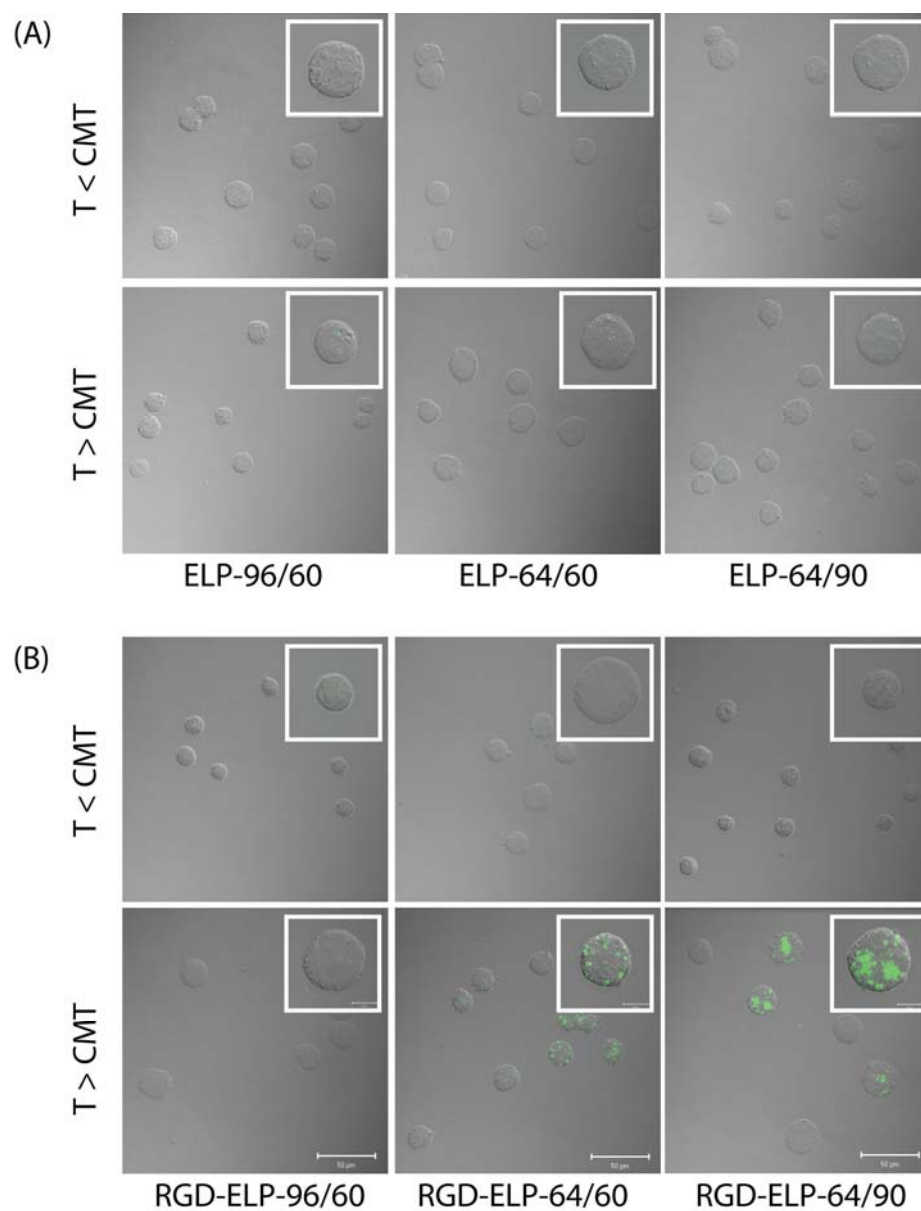


**Figure 29: Confocal fluorescence images of K562/ $\alpha\text{v}\beta\text{3}$  cells following incubation with 10  $\mu\text{M}$  of RGD-ELPBC (green). (A) There was no visible uptake of any of the ELPBC by K562/ $\alpha\text{v}\beta\text{3}$  cells below and above the CMT with the ligand-negative ELPBC controls. (B) There was minimal visible uptake of all three RGD-ELPBC below or above the CMT when incubated with K562 cells, showing that overexpression of the receptor is necessary for enhanced uptake. There was no visible uptake of RGD-ELP-64/60 or RGD-ELP-64/90 below the CMT by K562/ $\alpha\text{v}\beta\text{3}$  cells but significant uptake of RGD-ELP-64/60 or RGD-ELP-64/90 above their CMT. A binary population of highly fluorescent and non-fluorescent cells in the field of view was observed by fluorescence microscopy, corresponding to the bimodal distribution seen in the flow cytometry histogram in panels II/III in Fig. 3. Size bar = 50  $\mu\text{M}$ . Reproduced in part with permission from ACS Nano, submitted for publication.**

#### 5.3.1.4 Effects of Nanoscale RGD Presentation on Specific Cell Uptake

The improvement in multivalent targeting using RGD-ELPBCs with increased hydrophobicity prompted us to test if this improvement was due to nanoscale presentation or increased non-specific hydrophobic interaction. We first generated a MW-matched RGD-ELP-150 homopolymer using the techniques described in section 3.2.2. This polymer formed micron-sized aggregates at 37 °C following transition to a full hydrophobic state (Fig. 30). These aggregates also showed higher MW, Z,  $R_h$ , and did not show uniform self-assembly compared to micelles

RGD-ELP-150 was incubated above its  $T_t$  with both K562/ $\alpha\beta 3$  and K562 cells. The resulting uptake by K562/ $\alpha\beta 3$  cells was similar to RGD-ELP-96/60 and significantly lower than RGD-ELP-64/60 and RGD-ELP-64/90 (Fig. 31). The histograms were similar following incubation with RGD-ELP-150 at  $T < T_t$  and  $T > T_t$ , suggesting that aggregate formation does not promote multivalent interaction. Quantification of these histograms yielded similarly low percentages of AlexaFluor488+ K562 and K562/ $\alpha\beta 3$  cells as well as similar increases in median fluorescence

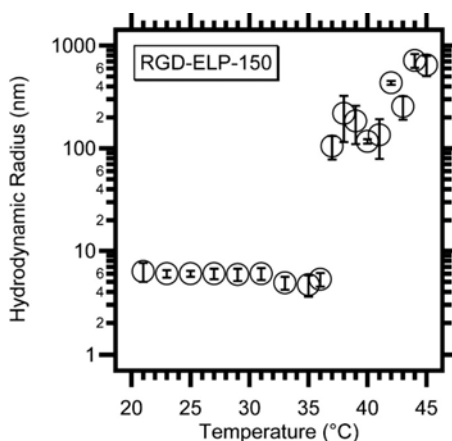


**Figure 30: Size of RGD-ELP-150 as a function of temperature. RGD-ELP-150 exists as a monovalent unimer at  $T < 37$  °C and a polydisperse aggregate at  $T > 37$  °C behaved similarly to other homopolymeric constructs (bars = polydispersity). Reproduced with permission from ACS Nano, submitted for publication.**

intensity. These data compared to enhanced uptake seen with RGD-ELP-64/90 showed that the smaller size and regulated multivalency of RGD-ELP-64/90 facilitated interaction with  $\alpha\beta 3$  on the cell surface rather than nonspecific uptake through increased hydrophobicity following ligand-receptor interaction as expected from RGD-ELP-150.

Together, these results showed that RGD-ELP-64/90 and, to a lesser extent, RGD-ELP-64/60 exhibited the proper characteristics for DAM. Neither monovalent ligand presentation nor micelle self-assembly promoted cellular interaction, but multivalent presentation of RGD via micelle self-assembly led to significant uptake of the polymer only by cells that overexpress the  $\alpha\beta3$  integrin. The degree of interaction was dependent on the ELPBC SR with increased hydrophobicity increased interaction. Additionally, data suggested micellar presentation of ligand through RGD-ELPBC provides greater specific interaction with  $\alpha\beta3$  than aggregate presentation through RGD-ELP, validating the use of ELPBC for DAM compared to ELP homopolymer. While these is a significant finding, RGD-ELP-64/90's CMT is below 37 °C making it unsuitable for preclinical investigation of DAM *in vivo*.

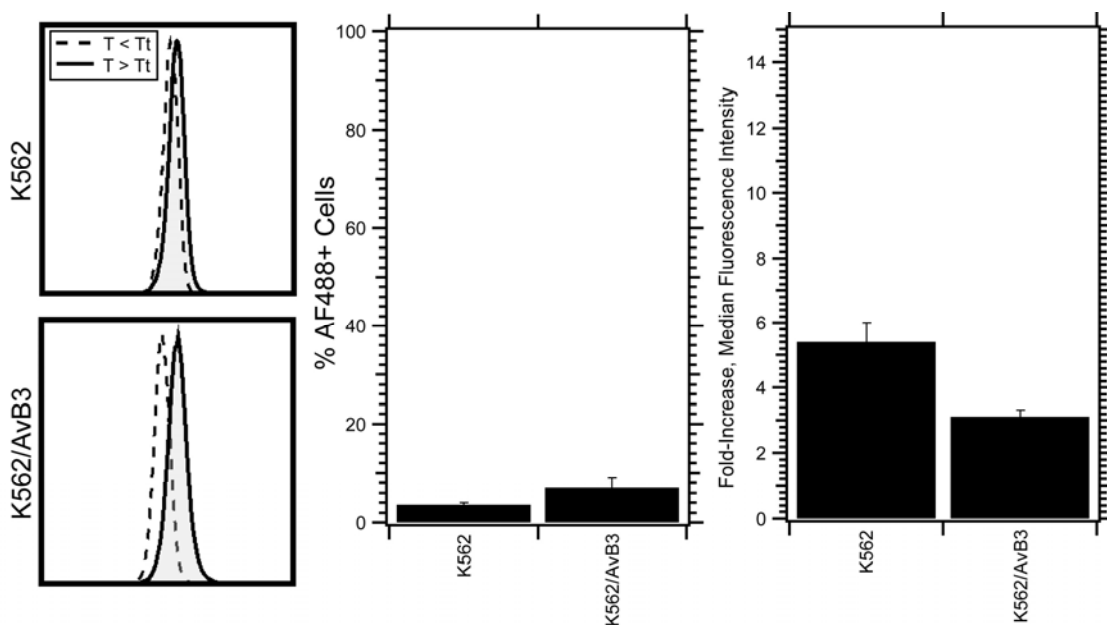


**Figure 31: Uptake of RGD-ELP-150 constructs by K562 and K562/ $\alpha\beta3$  cells. Histograms showed similar uptake in both cell lines below and above the  $T_t$  (left). There was also not a significant increase in the percentage of AlexaFluor488+ cells with heat (center). The median-fluorescence of AlexaFluor488+ cells also decreased with the addition of ligand, showing that aggregate formation did not facilitate multivalent interaction.**

### 5.3.2 Evaluation of NGR-ELPBC Constructs with Constant Overexpression

We used an *in vitro* assay based on the engineered K562-Tet-On-CD13 cell line to test specific binding of NGR-ELPBC. The K562-Tet-On-CD13 cell line was chosen for these studies



as it allows for control over CD13 expression levels. K562-Tet-On-CD13 with 1 µg/mL doxycycline was used as the CD13<sup>+</sup> active cell line, while K562-Tet-On-CD13 without doxycycline was used as the CD13<sup>-</sup> control cell line. CD13 surface expression on K562-Tet-On-CD13 can range from < 10% CD13<sup>+</sup> to 70 - 80% CD13<sup>+</sup> in response to doxycycline concentration (Fig. 23). All uptake experiments were performed and analyzed using identical strategies to those involving RGD-ELPBC uptake.

#### **5.3.2.1 Effects of Monovalent NGR Presentation on Cell Uptake**

We first evaluated the effects of monovalent presentation of NGR on cellular uptake by both CD13<sup>+</sup> and CD13<sup>-</sup> K562-Tet-On-CD13 cells. 10 µM NGR-ELPBC and ELPBC were incubated with K562-Tet-On-CD13 at T = 23 °C (T < CMT) and analyzed using FACS. The resulting FACS histograms showed that the resulting fluorescence intensities were similar between NGR-ELPBCs and ELPBCs in CD13<sup>+</sup> or CD13<sup>-</sup> K562-Tet-On-CD13 cells (Fig. 32). These data show that monovalent, unimeric NGR-ELPBC is not capable of binding to CD13 at micromolar concentrations, existing in an “off” state below the CMT similar to RGD-ELPBC at similar conditions.

#### **5.3.2.2 Effects of Micelle Self-Assembly on Nonspecific Uptake by Doxycycline-Responsive Cells**

We next evaluated the effect of thermal self-assembly on non-specific uptake by cells in the presence of doxycycline. We incubated non-ligand ELPBC at T = 40 °C with CD13<sup>+</sup> and CD13<sup>-</sup> K562-Tet-On-CD13 cells, and all samples were analyzed with FACS (Fig. 32). The resulting histograms showed minimal increase in fluorescence intensity following incubation with heat. These histograms were further quantified using identical procedures to those used for RGD-ELPBC analysis (Fig. 33). There was not a significant increase in the percentage of AlexaFluor488<sup>+</sup> cells incubated with non-ligand ELPBC with or without doxycycline. There was also a 1-fold increase in the median fluorescence of the AlexaFluor488<sup>+</sup> region in both cell conditions. This data shows that micelle self-assembly did not promote nonspecific uptake by modified K562 cells with or without doxycycline in solution.

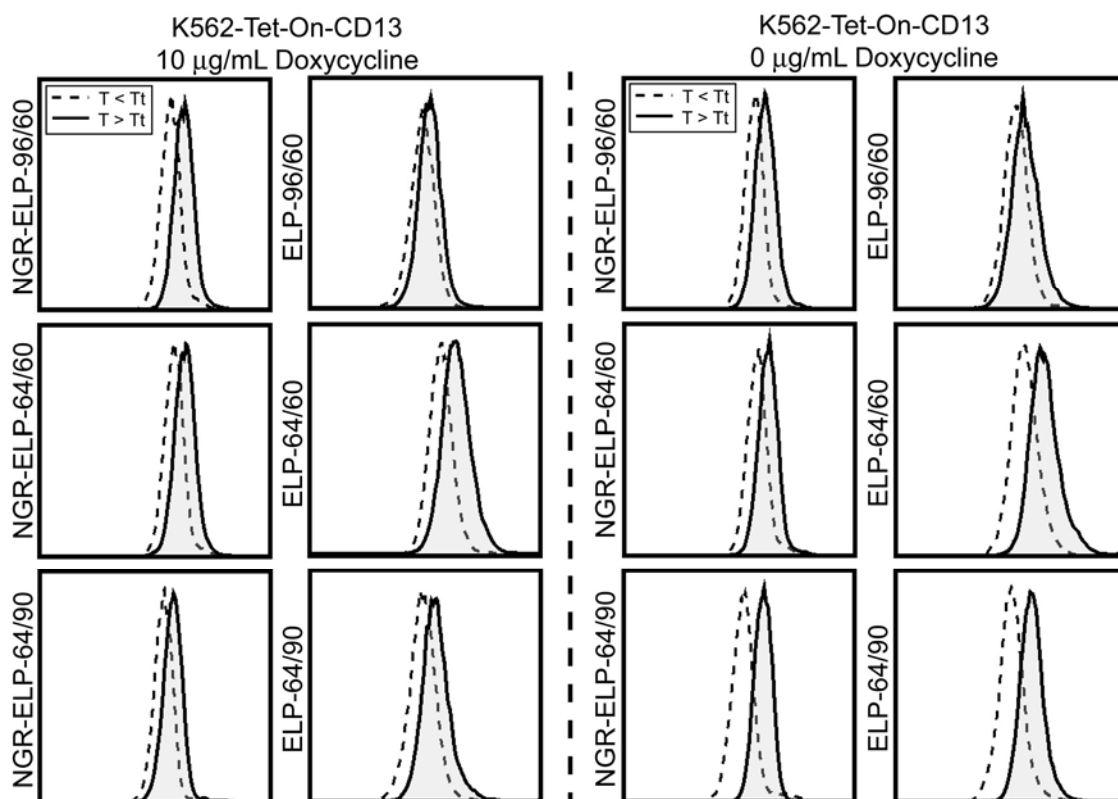


**Figure 32: Flow cytometry histograms of K562-Tet-On-CD13 cells incubated with ELPBC constructs at temperatures below and above the CMT. There was minimal effect of monovalent ligand presentation on cellular uptake. All cells also exhibited slightly increased uptake with heat. There was minimal difference in uptake of multivalent NGR-ELPBC or ELPBC micelles by CD13- or CD13+ cells.**

### 5.3.2.3 Effects of Micelle Self-Assembly on Nonspecific Uptake by Doxycycline-Responsive Cells

We then evaluated the effects of multivalent NGR presentation on specific cellular interaction. NGR-ELPBCs were incubated with CD13+ and CD13- K562-Tet-On-CD13 cells at  $T > \text{CMT}$  and analyzed using FACS. First, CD13- K562-Tet-On-CD13 cells incubated with NGR-ELPBCs yielded similar histograms to either CD13+ or CD13- cells incubated with non-ligand ELPBCs in micelle form (Fig. 32). The percentage of AlexaFluor488+ cells was not significantly different from non-ligand ELPBCs incubated with K562-Tet-On-CD13 in either condition (Fig. 33). Also, the increase in median fluorescence intensity of the AlexaFluor488+ region was minimal

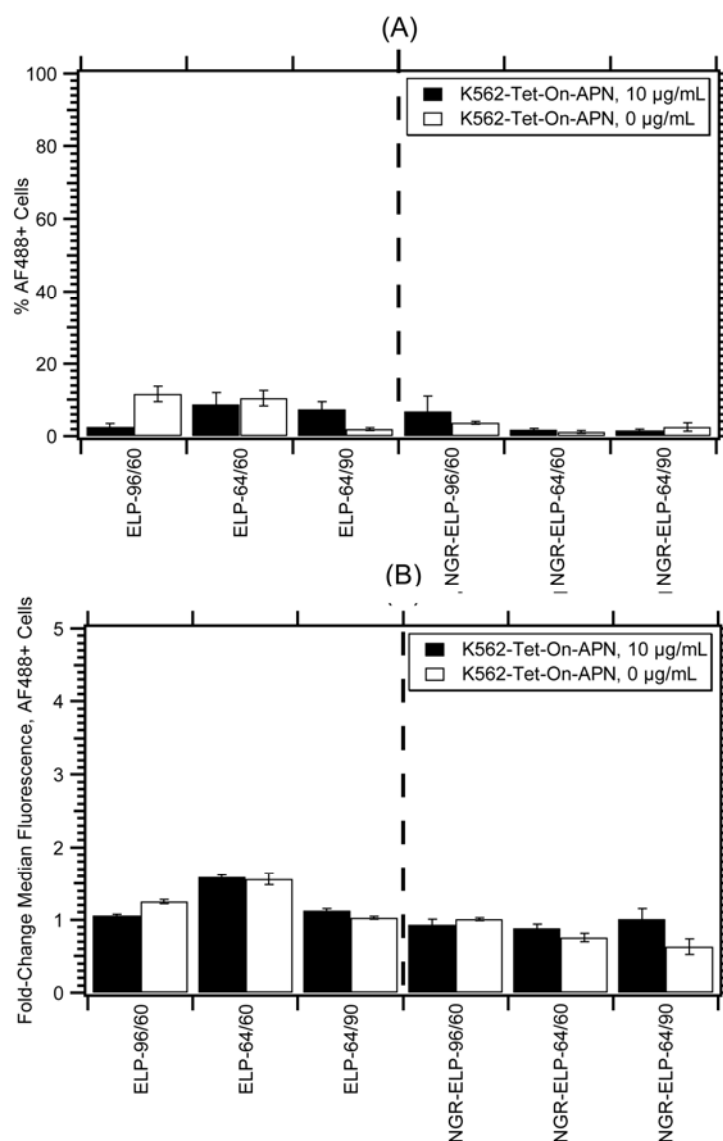


**Figure 33: Quantitative effects of multivalent NGR presentation on specific cellular uptake. (A) The percentage of fluorescence-positive cells was low (< 10%) with all constructs and both cell conditions, demonstrating that ligand presentation does not increase cell uptake. (B) There was only 1 - 1.5 fold increase in median fluorescence of receptor-positive cells with any of the tested constructs.**

compared to CD13- K562-Tet-On-CD13 cells incubated with monovalent NGR-ELPBC. These results showed that micellar NGR-ELPBC did promote significantly enhanced uptake in cells lacking the cognate receptor.

Second, histograms of CD13+ K562-Tet-On-CD13 incubated with NGR-ELPBC at T > CMT did not vary significantly from cells incubated with non-ligand ELPBCs (Fig. 32).

Interestingly, there was no noticeable change in the observed histograms following incubation of either cell type with NGR-ELPBC at T > CMT. Quantification of these histograms showed that the percentage of AlexaFluor488+ cells was slightly higher with non-ligand ELPBC than NGR-ELPBC in both cell types, but none of the constructs generated more than 15% AlexaFluor488+ cells, far lower than the receptor presentation on the CD13+ K562-Tet-On-CD13 cell line (Fig. 33). All NGR-ELPBC constructs also showed a .5 - 1-fold increase in median fluorescence of CD13+ K562-Tet-On-CD13 cells, similar to both non-ligand ELPBCs with either condition and NGR-ELPBCs with cells in the CD13- condition. These results show that multivalent presentation of NGR in micellar form does not facilitate cell binding or uptake regardless of CD13 expression on the cell surface.

Despite the lack of positive uptake results with the NGR-ELPBCs, the larger formal charge on the GNGRG peptide (+1) as compared to GRGDS ( $\pm 0$ ) suggests that the ligand will selectively partition to the outer edge of a scaffold with amorphous character. Thus, we repeated the uptake experiments using an NGR-ELP-150 construct as a homopolymeric control to test the ability of NGR-ELP to specifically target CD13 in micron-sized aggregate form. Briefly, a size-matched NGR-ELP-ELP-150 construct was cloned from the pET-25b-AS6 vector, purified, and conjugated to AlexaFluor488. NGR-ELP-150 was then incubated with K562-Tet-On-CD13 cells with and without doxycycline and analyzed using FACS (Fig. 34). The results showed a slight but insignificant increase in % AlexaFluor488+ cells and a slight decrease in median fluorescence in the AlexaFluor488+ region. This data showed that multivalent presentation of NGR via an aggregate scaffold does not sufficiently promote uptake by CD13+ cells.

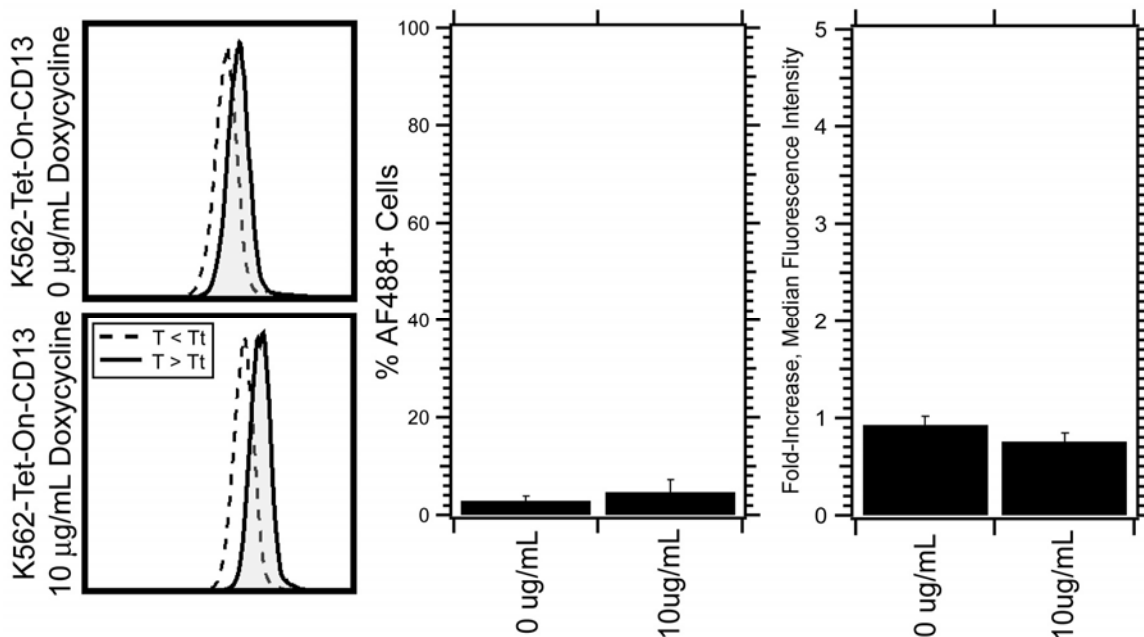


**Figure 34: Uptake of NGR-ELP-150 constructs by both CD13+ and CD13- K562-Tet-On-CD13 cells. Histograms showed similar uptake in both cell lines below and above the Tt (left). There was also not a significant increase in the percentage of AlexaFluor488+ cells with heat (center). The median-fluorescence of AlexaFluor488+ cells decreased with the addition of ligand, showing that aggregate formation did not facilitate multivalent interaction (right).**

#### 5.3.2.4 Receptor Codependence for *In Vitro* NGR Uptake

Our results surprisingly showed that neither monovalent nor multivalent presentation promoted receptor-specific uptake. While there was only a minimal increase with the addition of heat, the resulting histograms do not show a bimodal distribution of cells similar to that seen following WM15 Ab staining. Similarly, the dramatic uptake seen with RGD-ELP-64/90 was not seen with any of the NGR constructs in either monovalent or multivalent forms. Given the success with the RGD-ELPBC platform, this data showed that NGR-ELPBC does not promote cell uptake through interaction with CD13, similar to some *in vitro* studies and dissimilar to others demonstrating successful *in vivo* targeting of CD13.

To better understand low NGR-ELPBC binding to K562-Tet-On-CD13, we compared our *in vitro* uptake of NGR-based constructs with other published results. We identified three other CD13+ cells lines beyond K562 used in the literature for testing NGR binding: HT-1080 human fibrosarcoma, HUVEC, and CD13+ MOLT-4 human lymphoblastic leukemia. Each of these cell

lines were previously analyzed for uptake of NGR constructs using either flow cytometry or confocal microscopy. We crosschecked these and our results with expression of  $\alpha\beta3$  and  $\alpha\beta5$  (Table 7). Interestingly, both cell lines expressing CD13 and  $\alpha\beta$  integrins showed uptake in prior experiments, but cell lines only expressing CD13 did not show uptake of NGR-functionalized constructs *in vitro*.

This trend can be explained based on recent studies of CD13 function. CD13 assumes multiple roles due its ability to both enzymatically modify and non-enzymatically bind to NGR [250]. In cases of enzymatic activity, CD13 converts the NGR ligand to *iso*-DGR, a high-affinity ligand for  $\alpha\beta3$  integrin [197]. Additionally, many *in vitro* binding studies use cells that express many cell-surface receptors such as HT-1080 or HUVECs, not just CD13. Therefore, the NGR-ELPBCs may still interact with cellular CD13 following multivalent presentation, but this interaction may lead to enzymatic conversion and binding/uptake through the  $\alpha\beta3$  integrin. The trends of coexpression in cell lines showing successful *in vitro* uptake suggest this as the likely route of uptake. While further work is needed to further clarify the interplay between CD13 and  $\alpha\beta3$  for NGR binding, these observations demonstrate that the K562-based assay with isolated CD13 expression is insufficient to promote uptake. Considering that the lack of positive uptake is confounded by the potential mechanism and other successful NGR-based constructs for *in vivo* targeting showed similar results *in vitro*, *in vivo* testing of the NGR-ELPBCs will provide more direct evidence of the suitability of multivalent NGR targeting.

**Table 7: Results of NGR-mediated uptake studies with different cell lines. Uptake was only observed in cell lines expressing both CD13 and  $\alpha\beta3$ , suggesting a codependence between the two receptors for multivalent targeting.**

Cell Line	CD13	$\alpha\beta3$	In vitro Uptake?	<i>In vivo</i> Accumulation?	Reference
K562-Tet-On-APN	Yes	No	No	N/A	N/A
MOLT-4	Yes	No	No	Yes	[128]
HT-1080	Yes	Yes	Yes	Yes	[264; 265]
HUVEC	Yes	Yes	Yes	Yes	[243; 264; 265]

## 5.4 Significance

The results presented in this section clearly demonstrated proof-of-principle of DAM by promoting cell-specific targeting through thermally-triggered self-assembly of a ligand-functionalized ELPBC. RGD-ELPBC did not lead to cell uptake with monovalent ligand presentation, showing that ligand-ELPBC can persist in an “off” state. ELPBC also did not promote non-specific uptake following self-assembly, showing that ELPBC can serve as an “inert” scaffold for multivalent targeting. RGD-ELPBC specifically interacted with  $\alpha\beta3+$  cells following multivalent ligand presentation following micelle self-assembly, showing that RGD-ELPBC micelle persists in an “on” state and micelle self-assembly serves as a switch between the “on” and “off” state. The effect of DAM was most pronounced in the thermally-incompatible RGD-ELP-64/90 and not in the thermally-compatible RGD-ELP-96/60, suggesting a dependence of SR, and possibly terminal density, on multivalent ligand-receptor interaction. Based on its thermal and uptake properties, RGD-ELP-64/90 is compatible with static multivalent targeting but not dynamic multivalent targeting. To fully reap the benefits of RGD-ELPBC for DAM, changes must be made to raise the CMT to 39 – 42 °C while maintaining a SR = .66 to retain specific ligand-receptor interaction.

While the RGD uptake results clearly demonstrate the advantage of multivalent micellar presentation, NGR-ELPBC results are inconclusive. Binding studies with K562 expressing the proper CD13 isoform showed that multivalent presentation of NGR did not promote specific binding with cells overexpressing CD13. However, uncertainty surrounding the mechanism creates difficulties in the assay platform for testing NGR interaction. Given the results of other *in vitro* uptake assays using CD13+ cells with and without integrin expression, it follows that WM15-sensitive CD13 acts more as an enzyme than a binding site. Thus, these negative uptake results *in vitro* are insufficient to prove that NGR-ELPBC does not interact with CD13 following self-assembly, and further *in vivo* study is necessary for conclusively evaluating the benefits of static or dynamic multivalent targeting using NGR-ELPBCs.

## 6 Evaluation of *In Vivo* Multivalent Targeting Using ELP Block Copolymers

### 6.1 Introduction

Observation of nanoparticle behavior in an *in vitro* model provided proof-of-concept evidence of static and dynamic multivalent ligand targeting using ligand-ELPBC. However, the isolated receptor presentation and simplified experimental conditions limit the applicability of these findings in a preclinical setting. The *in vivo* environment presents transport barriers and heterogeneity found in solid tumors but not in cell culture, contains a complex milieu of proteins and lipids compared to aqueous solution, and more accurately represents overexpression, presentation, and behavior of antigens targeted for antivasular therapy. Data gathered from *in vivo* study better demonstrate ligand-ELPBC's ability to improve specific accumulation within the tumor region through multivalent ligand presentation.

Based on the findings of Chapter 5, none of the tested constructs showed the proper thermal and binding characteristics for improved binding through DAM. Additionally, the effects of mild to moderate hyperthermia on expression of vascular markers are not well documented. Given the lack of an ELPBC that exhibits the proper thermal and binding properties for DAM (CMT = 37 – 42 °C), the study in this Chapter was restricted to evaluation of the ability of static multivalent ligand presentation to improve tumor accumulation, specificity, and localization compared to normal tissue *in vivo*. This study complements the *in vitro* studies reported in Chapter 5, validate multivalent targeting using thermosensitive ELPBC, and set the stage for future *in vivo* studies of DAM using redesigned ELPBCs.

We employed two different methods to examine static multivalent targeting using ELPBCs, (1) intravital microscopy (IM) using the dorsal-fold window chamber model and (2) immunohistochemistry (IHC) using a subcutaneous tumor model. IM allowed real-time observation of compartmentalized ELP accumulation and extravasation in both tumor and normal tissue, while IHC permitted identification of binding to endothelial cells versus tumor cells



surrounding the vasculature. Based on our data, static multivalent ligand presentation affected the spatial distribution of fluorescence aggregation within the tumor with NGR promoting aggregation in the center of the tumor. Quantitatively, static multivalent presentation of NGR improved the specificity of tumor accumulation compared to non-ligand ELPBC, but static multivalent RGD presentation did not improve specificity compared to non-ligand ELPBC. The extravasation distance was greater for ligand-ELP-64/90 than non-ligand ELP-64/90, but both showed low penetration of 2-3 cell layers. IHC revealed greater colocalization of NGR-ELP-64/90 and RGD-ELP-64/90 on tumor endothelial cells compared ELP-64/90, greater colocalization of NGR-ELP-64/90 with individual tumor cells than RGD-ELP-64/90 or ELP-64/90, and non-specific interaction with muscle cells with all three constructs. These experiments were attempted with ELP-64/90-Doxorubicin constructs, but the technical limitations of the confocal microscope and the low loading capacity of ELPBC did not yield clearly defined images for analysis.

These results showed that static multivalent NGR presentation improved tumor specificity but RGD presentation did not. Additionally, the data suggested that ligand-ELPBC micelles are suitable for targeting tumor vasculature but not individual tumor cells distant from the vasculature in a mature tumor. Therefore, NGR-ELP-64/90 is a better construct for selectively targeting central tumor vasculature than RGD-ELP-64/90. Additionally, the non-specific interaction between transitioned ELPBC and the tumor periphery or muscle tissue showed that ELPBC micelles are not inert macromolecular carriers but may confer a unique ability to facilitate drug delivery to tumors independent from ligand presentation.

### **6.1.1 Intravital Microscopy**

IM describes a group of related optical imaging techniques used to visualize the behavior of different compounds within living tissue. While these imaging techniques are typically more complex than others involving fixed *ex vivo* samples, these techniques also provide a number of inherent advantages. The live sample allows for more accurate representation of particle behavior within tissue due to homeostatic maintenance of the *in vivo* environment. IM allows continuous

measurement rather than discrete sampling, more accurate quantification over shorter time scales, and clearer representation of kinetics. The use of a living sample permits imaging of complicated and dynamic systems. While IM is the best option for specific applications, there are disadvantages as well. Single-cell resolution is difficult using IM, making it inconvenient for monitoring cell activity. Additionally, IM is far more cost-, labor-, and equipment-intensive than other related techniques. The preparation used for IM may also disrupt the natural environment being observed, reducing data applicability.

#### **6.1.1.1 Laser-Scanning Confocal Microscopy**

There are also numerous imaging modalities and preparations used for IM, but this work focused on laser-scanning confocal microscopy (LSCM) and the transparent window chamber model based on our previous experience and available imaging equipment. LSCM is an optical technique that offers several advantages over conventional epifluorescence microscopy (Fig. 35) for observing biological tissues. This technique uses spatial filtering via pinholes on both the excitation source and the emission detector. These pinholes limit both the amount of light reaching the sample and scattered light outside the focal plane reaching the detector. This reduces photobleaching, increases contrast-to-noise ratio, and allows for 3D sectioning and recreation through isolation of individual focal planes [266].

Despite the advantages of LSCM, it has several disadvantages. It has limited usable penetration depth due to signal attenuation from both the pinhole on the incident laser and detector. It also is not a preferred technique for imaging weak fluorophores due to lower intensity coming from the tightly-defined focal plane. There have been recent advancements to improve these limitations. In some microscopes, discrete filter sets have been replaced with spectral deconvolution. This method allows for narrow definition of emission wavelengths, allowing for reduction of unwanted background fluorescence and stronger excitation intensity for a given fluorophore. Second, a strategy termed two-photon excitation has been developed to improve penetration distance. In this modality, two photons constructively interfere with each other,

leading to equal intensity at a lower frequency. Since signal attenuation in tissue is inversely proportional to light frequency, this method allows further penetration distance and higher signal from the sample. This technique permits imaging of subcutaneous tumors without invasive surgical preparation, a highly advantageous approach for imaging biological phenomena disrupted by wound healing. While both spectral deconvolution and two-photon microscopy are compatible with the window chamber model, we will use normal LCSM with the window chamber preparation for the following studies due to technological limitations.

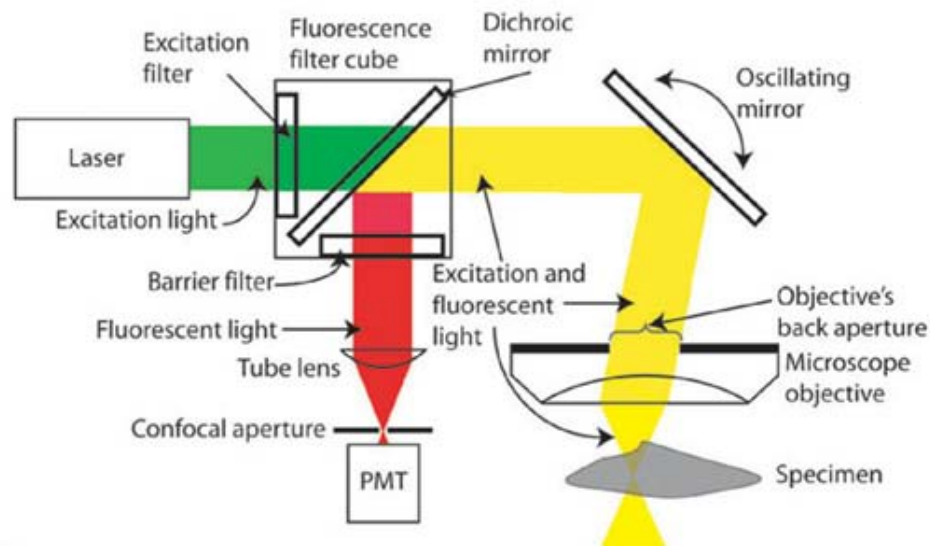


**Figure 35: Schematic of confocal microscopy. A monochromatic laser illuminates the sample through an adjustable pinhole and objective. Emission from the sample comes back through the objective and a pinhole to a PMT detector. The pinholes are calibrated to allow light from a narrowly defined depth of focus and block light scattered from other planes. This allows for higher contrast-to-noise ratio and sectioning of 3D tissues. Reprinted by permission from Macmillan Publishers Ltd: Nature Methods, Conchello, J.-A. and Lichtman, J.W., *Optical sectioning microscopy*. 2(12): 920-931. Copyright 2005.**

### 6.1.1.2 Dorsal Fold Window Chamber Model

The window chamber is a physical structure sealing an exposed tissue region and allowing observation through a transparent surface (Fig. 36). This fixture effectively converts the enclosed region into a complex flow chamber, and different window chamber preparations have been developed to observe biological structures *in vivo*. We used a dorsal fold window chamber that consists of two titanium plates sandwiching the dorsal skin fold on mice and an incision made on one side of the fold. Following the incision, a single-cell suspension of tumor cells was injected

subcutaneously into the intact skin and sealed with a glass cover slip. The resulting tumor provided a setting for evaluating behavior of different fluorescent compounds or labeling agents within the tumor microenvironment.

### 6.1.1.3 Imaging Fluorescence Compounds Within the Vasculature

A typical imaging routine using the window chamber model is described in Fig. 36. During imaging, the mouse is positioned recumbently on a custom translational stage. Compounds of interest are then administered systemically via tail-vein injection. The number of fluorescent markers for simultaneous imaging is limited by both by the excitation wavelengths and emission filters incorporated with the microscope. For our experiments, we first administered a high MW

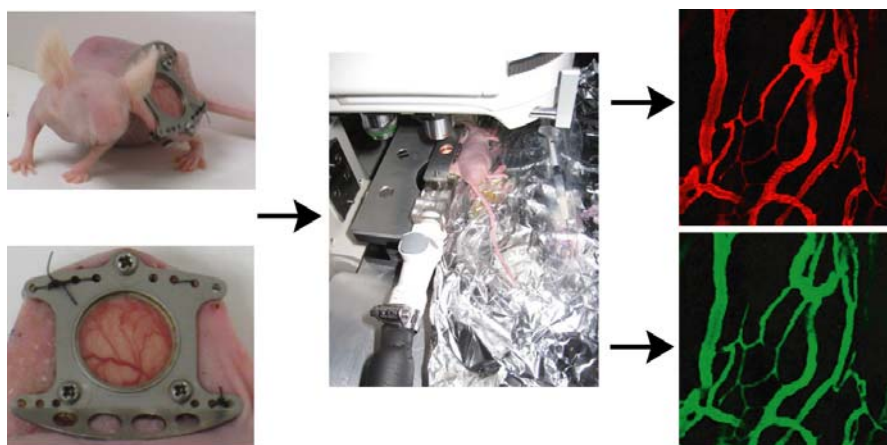


**Figure 36: Overview of intravital microscopy using the dorsal fold window chamber model. A nude mouse was surgically outfitted with a titanium chamber supporting the extended dorsal skin fold with or without an implanted tumor (left panel). The mouse was placed on a custom heated stage under a Zeiss LSM510 upright confocal microscope (center). Fluorescently-labeled contrast agent (red) and ELPBCs (green) were imaged simultaneously and analyzed using custom MATLAB functions (right).**

contrast agent to identify vessels and select a region of interest (ROI). We then administered the compound of interest. The entire volume within the ROI is imaged as a series of slices in the Z-direction, termed the z-stack. Sequential z-stacks are obtained for the time course of the experiment and analyzed using image processing software.

#### **6.1.1.4 Image Processing**

LCSM images provide sufficient resolution both in the lateral and axial directions to permit quantification of fluorescence intensity in the vascular and extravascular compartments as defined by the high MW contrast agent. Each z-stack image represents a 3D matrix of pixel intensity values. Thus, image processing is performed using MATLAB (The Mathworks, Natick, MA) due to its compatibility with multidimensional matrices, its library of available built-in and custom functions, and ease of programming in the MATLAB language. MATLAB is currently used to (1) apply motion correction to the data set, (2) automatically generate a binary mask separating the data into vascular and extravascular compartments and a distance map defining voxel coordinates relative to the vascular surface, (3) calculate accumulation in each compartment, and (4) determine penetration distance of fluorescence in extravascular region. These functions will be described further in section 6.2.6.

#### **6.1.2 Immunohistochemistry**

A more traditional alternative to IM is IHC using *ex vivo* tissue sections. IHC is compatible with a wide range of optical imaging techniques such as epifluorescence or confocal microscopy or non-optical methods such as scanning- or transmission-electron microscopy. Optical imaging techniques permit analysis at high or low magnification, allowing observation of single cells, tissue sections, or even whole animals [267]. IHC is compatible with different antibody labeling techniques and therefore useful for analyzing fluorescent ELPBC colocalization with different cell types in normal and tumor tissue. Following systemic administration of fluorescent ELP, excised tumor and normal tissue samples can be snap-frozen and sectioned to reveal spatial distribution within tissue cross-sections. Further immunostaining of these slices can reveal cell types present in regions of ELP accumulation, identifying ELPBC binding to endothelial cells or tumor cells in the perivascular region. These data complement quantitative IM data by allowing identification of binding sites and facilitate more complete analysis of ligand-ELPBC behavior in the tumor while bypassing the two-channel limit imposed by the current confocal microscope.

## **6.2 Materials and Methods**

### **6.2.1 CMT Measurement in Serum**

Functionalized RGD-, NGR-, and non-ligand ELP-64/90 were added to FBS to form 5  $\mu\text{M}$  and 10  $\mu\text{M}$  ELPBC solutions. 750  $\mu\text{L}$  of each solution was added to a reduced-volume quartz cuvette (Starna) and analyzed using a thermally-controlled Cary UV-Vis spectrophotometer (Varian, Inc.). The absorbance at 350 nm ( $\text{O.D.}_{350}$ ) was zeroed at 15  $^{\circ}\text{C}$  and monitored from 15 - 55  $^{\circ}\text{C}$  in .33  $^{\circ}\text{C}$  increments. The data was then corrected to separate effects of protein settling from thermal self-assembly using curve-fitting software. A linear fit was applied to the data from 15 - 25  $^{\circ}\text{C}$  and subtracted from the raw data to set a constant baseline. The point at which the corrected  $\text{O.D.}_{350}$  increased beyond the baseline was defined as the CMT.

### **6.2.2 ELPBC-Doxorubicin Conjugation**

Conjugation of Doxorubicin (Dox) to ELP-64/90, RGD-ELP-64/90, and NGR-ELP-64/90 was performed in two steps. Dox (Tecoland, Edison, NJ) was first functionalized with *n*- $\beta$ -maleimidopropionic acid hydrazide tri-fluoroacetic acid ([BMPH] Pierce Biotechnology, Rockford, IL) by dissolving 24.8 mg Dox and 11.3 mg BMPH in 11.3 mL anhydrous methanol and 11  $\mu\text{L}$  trifluoroacetic acid. The reactants were stirred for 16 hrs at 20  $^{\circ}\text{C}$  in the dark and concentrated by rotary evaporation. Prior to the conjugation with the functionalized Dox, 2 mL of 700  $\mu\text{L}$  ELP was reduced with 70  $\mu\text{L}$  of TCEP (100 mM, pH 7.0) at 5-fold molar excess of TCEP/thiol. The ELP phase transition was induced with 2.5 M NaCl, pelleted by centrifugation at 13200 g and 40  $^{\circ}\text{C}$ , and resuspended in 1.8 mL conjugation buffer (0.1 M  $\text{NaPO}_4$ , 1 mM EDTA, pH 7). Activated Dox (B-Dox) was resuspended in 2.25 mL anhydrous methanol and slowly transferred to the stirring ELP solution. 380  $\mu\text{L}$  TCEP (100 mM, pH 7.0) was added to the solution and stirred for 16 hours at 20  $^{\circ}\text{C}$  in the dark. Methanol was evaporated under nitrogen, and Dox precipitate was removed via 10 min centrifugation at 13200 g. The remaining unreacted Dox was removed by one round of ITC. The pellet was then resuspended in 1mL buffer (0.1 M  $\text{NaPO}_4$ , pH 7.0) and the resulting ELP-Dox concentration was obtained using:

$$C_{ELP-Dox} = \frac{Abs_{280} - .95 * Abs_{495}}{5690} \quad (6.1)$$

ELPBC-Dox solutions were stored at -20°C until use.

### 6.2.3 Dose Preparation

All ELP constructs were expressed, purified, and functionalized using techniques described in previous sections. Both 2MDa dextran-tetramethylrhodamine (Invitrogen) and dextran-FITC (Sigma-Aldrich) were purchased in conjugated form. Dextran was mixed with surgical-grade saline at 10 mg/mL concentration, heated at 37 °C for 1 hour, and sonicated for 10 min. The resulting suspension was centrifuged for 10 min at 11,000 g to remove insoluble aggregates. 1 mL ELPBC and dextran solutions were subjected to endotoxin removal via Detoxigel columns (Thermo Scientific) according to manufacturer specifications. The concentration of ELP was then measured using UV-Vis spectroscopy (Thermo Scientific) and resuspended in saline at a concentration of 141 µM. Dextran solutions were used at the concentration obtained following endotoxin removal. Both ELPBC and dextran solutions were stored in the dark at -20 °C until further use.

### 6.2.4 Dorsal Fold Window Chamber Surgery

5 - 6 week-old nude mice ([BALB/c nu/nu] Charles River Laboratories, Wilimington, MA) were housed in the Duke Main Vivarium according to Institutional Animal Care and Use Committee (IACUC) guidelines. For surgery, mice were anesthetized with *i.p.* injection of ketamine (100 mg/kg) and xylazine (10 mg/kg) and prepared for surgery in a sterile environment. The dorsal skin of the mouse was stretched and attached via suture to an immobilization rack. A circular incision of 1 cm in diameter was made in the skin fold and fitted with titanium chamber. For tumor imaging, a single-cell suspension of FaDu human squamous cell carcinoma cells was injected into the exposed skin in the window chamber ( $4 \times 10^4$  cells in 10 µL of DMEM without serum or phenol red). For normal tissue imaging, no tumor was implanted. The incision was sealed with a circular glass cover slip, and the mouse recovered in an environment slightly

warmer than room temperature (25 - 27°C). Imaging studies were performed 7 - 11 days after cell injection when tumors reached 2 - 3 mm in diameter.

## **6.2.5 Confocal Imaging Procedure**

The LSM510 upright laser-scanning confocal microscope (Zeiss) was used for all mouse imaging. This microscope was outfitted with two lasers and a filter set capable of excitation at 488 nm (green) and 546 nm (red). Mice implanted with a window chamber were anesthetized using *i.p.* injection of sodium pentobarbital (80 mg/kg). The tail vein was cannulated and the mouse was placed recumbently on a custom heated stage attached to the confocal microscope. The desired window chamber temperature, typically 37 °C, was selected using the programmable NESLAB RTE7 circulated water bath (Thermo Scientific). Low-magnification images were obtained using a Plan Fluor 5x objective (Zeiss) and higher magnification images were obtained with an LD Achromplan 20x objective (Zeiss). The tumor region was first identified at 5x using transmitted light through the eyepiece, and a suitable ROI was roughly selected at 20x. The protocol following this step was dependent on the conjugated fluorophore.

### **6.2.5.1 ELPBC-AlexaFluor488**

A dual color imaging routine consisting of line switching between green and red detection was used to obtain vessel images (red) and raw ELPBC data (green). The pinhole size corresponding to a slice thickness of 7.1 µm was selected for both channels, and the gain of each channel was raised until autofluorescence was detected from the tissue. A background image was then obtained prior to injection of any fluorescent compound. 100 µL of fluorescent dextran was then administered via the cannula and observed using a fast XY scan. The ROI was centered using the XY translational stage and the upper and lower limits of the tumor volume were set as bounds for the z-stack, and a single z-stack of the contrast agent was obtained to identify the plasma compartment. 100 µL of ELPBC was then administered via the cannula immediately followed by an imaging routine consisting of 20 z-stacks over 45 min. 40 µL of 80



mg/kg sodium pentobarbital was administered 40 min following the initial anesthesia dose and 20  $\mu$ L every subsequent 20 min. The mouse was sacrificed immediately after the imaging routine.

### **6.2.5.2 ELPBC-Dox**

Dox acts a weak fluorophore with peak excitation at 488 nm, similar to FITC, and peak emission at 595 nm, similar to rhodamine [268]. The protocol for imaging ELPBC-Dox consisted of similar steps, but the pattern of laser excitation was modified to account for this change in spectral characteristics. A dual-color line switching routine was used to simultaneously image both contrast agent and ELPBC-Dox. Each line was obtained using constant excitation at 488 nm, and the emission filter alternated between a band-pass filter from 545 - 595 nm and a low-pass filter at 595 nm. 100  $\mu$ L 2 MDa FITC-dextran solution was injected first to obtain a vessel mask. The gain on the red channel was maximized to the point of visible autofluorescence. 100  $\mu$ L ELPBC-Dox solution was then administered to reach a final serum concentration of 10 – 100  $\mu$ M/mouse. The ROI was excited at 488 nm (green) and detected at 595 nm (red), and, if necessary, the imaging parameters were then adjusted to obtain clear, separate images of FITC-Dextran and ELPBC-Dox. 40  $\mu$ L of 80 mg/kg sodium pentobarbital was administered 40 min after the initial anesthesia dose and 20  $\mu$ L every subsequent 20 min. The mouse was sacrificed following this imaging routine.

## **6.2.6 Image Analysis**

### **6.2.6.1 MATLAB Functions**

Table 8 describes the MATLAB functions and Table 9 describes the MATLAB scripts used for image analysis. The majority of the functions and scripts used to perform this analysis were previously written and documented [226] and were used to evaluate both the accumulation of homopolymeric ELP [160] and penetration distance of model macromolecular drug carriers [38]. The functions performed the necessary calculations for quantitative image analysis, while the scripts provided a front-end for user input and variable manipulation. The functions associated with mask generation were written specifically for this application.

**Table 8: MATLAB functions used for image analysis**

Function	Description
Loadlsm.m	Import '.tif' image files into MATLAB as a structure object
Showrs2.m	View images within structure
calcMotionCorrectParams.m	Evaluate coordinates for motion correction
applyMotionCorrectParams.m	Update structure using new coordinates
calcThresholdMask.m	Identify optimal threshold for binary mask
maskExpand.m	Replicate binary mask
processData3DlsmMask.m	Process accumulation data in each compartment based on binary mask and raw data
minDistMap3d.m	Convert binary mask to distance map
calcIntensityWithDistance.m	Process extravasation data in motion-corrected structure
plotDistanceAnalysisResults.m	Generate 3D contour plot describing extravasation distance

**Table 9: MATLAB scripts used for image analysis**

Script	Description
loadTimeSeriesVolumeScript.m	View and modify image sequence
ViewMotionCorrectedTsvScript.m	Review motion correction parameters
CalcThreshMaskScript.m	Generate binary mask from raw data
processData3DlsmMaskScript.m	Process and return accumulation data in each compartment based on binary mask and raw data
CalcMinDistMap3DScript.m	Generate distance map
calcIntensityWithDistanceScript.m	Calculates the intensity of each voxel over time with reference to the nearest vascular surface.
plotDistanceAnalysisDataScript.m	Creates 1D, 2D, and 3D plots from distance analysis.
findDistMapOffsetScript.m	Finds and corrects differences between raw data and binary mask in x,y and z

### 6.2.6.2 Data Processing Routine

Raw data from each imaging routine was exported offline to an image processing workstation containing both the LSM imaging software (Zeiss) and MATLAB equipped with the Image Processing toolbox. The flow chart shown in Fig. 37 illustrates the general procedure used to extract quantitative data regarding accumulation and extravasation from each data set. The image stack was separated into individual channels representing ELP and vessel contrast agent, and the image series from each channel were exported to MATLAB as a structure of '.tif' files. Images corresponding to vessel contrast agent were manually motion-corrected in the x, y, and z directions at three distinct features in the image and checked for accuracy. The z-stack of the

contrast agent at the initial time point was then used to generate a 3D binary mask separating the vascular and extravascular regions. The resulting binary mask was then used to generate a 3D map defining the distance of each voxel from the nearest vessel surface in the x, y, and z directions within the ROI. Motion-corrected data corresponding to ELPBC was then directly applied to the binary mask to obtain time-dependent accumulation data in the vascular and extravascular compartments and to the distance map to obtain time-dependent extravasation data. These operations were performed on the same data set, maximizing data production and minimizing the number of animals needed for each experiment.

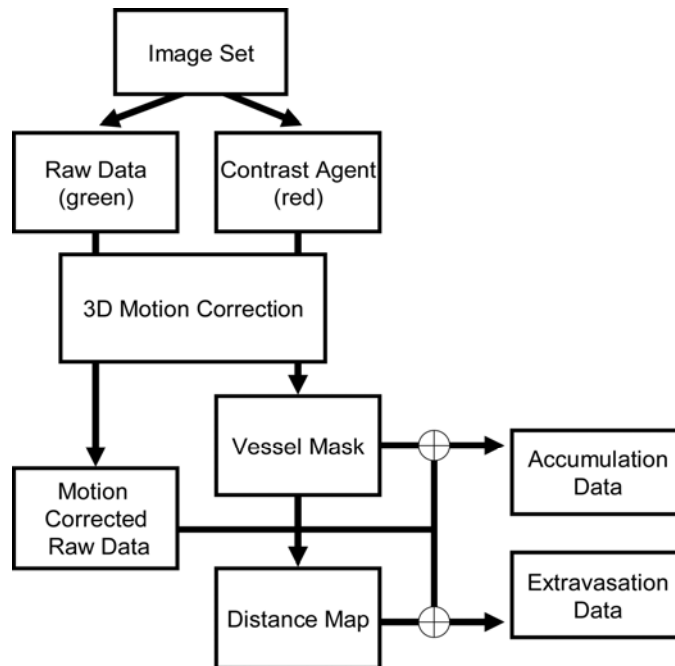


**Figure 37: Flow chart illustrating image processing routine for accumulation and extravasation analysis using the dorsal fold window chamber model.**

## 6.2.7 Immunohistochemistry

### 6.2.7.1 Dose administration

Nude mice were housed in at the Duke University Cancer Cell Isolation Facility according to IACUC guidelines. Tumor xenografts were induced on the hind leg following injection of  $10^6$  FaDu cells and allowed to grow for 7 - 10 days. Each tumor-borne mouse was given 100  $\mu$ L

ELPBC via tail-vein injection. 10 mg/kg Hoechst 33342 was then administered via tail-vein injection and the mouse was sacrificed after 1 minute. Both the tumor and thigh muscle on the opposite leg were quickly removed, embedded in tissue-freezing media (TBS, Durham, NC), and snap-frozen in liquid nitrogen. Each sample was sectioned into 15  $\mu\text{m}$  slices using a cryotome (Leica Microsystems), mounted on glass slides, and stored at  $-80\text{ }^{\circ}\text{C}$  until use.

#### **6.2.7.2 Imaging and Staining Protocol**

Tumor slices were first imaged for both green and blue fluorescence using a scanning-stage epifluorescence microscope (Nikon Instruments, Tokyo, Japan). All samples imaged for AlexaFluor488 and Hoechst 33342 were unfixed to preserve fluorescence, and slides were kept on dry ice at all times except during staining and imaging routines prior to fixing. Images of the entire tissue slice was obtained at 20x through a stitched matrix of 512 x 512 panels. Following the first imaging routine, slides were rinsed with blocking buffer (5% milk/TBST), labeled with anti-CD31 primary antibody (eBioscience), and stained with AlexaFluor546-anti-IgG secondary antibody (Invitrogen). Slides were reimaged for AlexaFluor546 and merged with the AlexaFluor488 and Hoechst 33342 images using ImageJ [269] and Photoshop.

#### **6.2.7.3 Colocalization Analysis**

Ten random 512 x 512 regions were selected in each merged image and exported as separate '.tif' files. Each file was then imported into a custom MATLAB script kindly provided by Dr. Nenad Bursac. These functions separated each image into red, green, and blue channels. Each channel was converted into a binary image based on the gray threshold. The binary images were then used to determine (1) the percentage of green pixels overlapping red pixels as a measure of ELPBC-endothelial cell colocalization and (2) the percentage of green pixel overlapping blue pixels as a measure of ELPBC-perivascular cell colocalization.

## **6.3 Results and Discussion**

### **6.3.1 Construct Selection**

In order to focus the *in vivo* studies on a manageable number of constructs, we analyzed ELP-64/90, RGD-ELP-64/90, and NGR-ELP-64/90 at a constant 37 °C. These conditions were chosen for several reasons. First, RGD-ELP-64/90 showed the most favorable interaction with overexpressed  $\alpha v\beta 3$  for *in vitro* studies, while NGR-ELP-64/90 performed equally to the other two constructs in CD13 targeting experiments. This allowed segment ratio (SR) consistency for comparison between RGD and NGR without sacrificing binding ability. Second, all ELP-64/90-based constructs formed micelles at a temperature below normothermic mouse body temperature. While this was not preferable for studying DAM, it was beneficial from an experimental standpoint as all imaging was performed at normothermic conditions, reducing potential variables from altered vessel permeability or receptor expression. While this strategy did not reveal advantages associated with DAM *in vivo*, it did identify constructs that exhibit avidity towards their cognate receptor *in vivo* and establish which constructs may benefit from optimization for DAM.

### **6.3.2 Self-Assembly in Serum**

As previously described, micelle self-assembly is governed by a number of thermodynamic properties. Self-assembly has been well studied and is predictable in aqueous solution. However, many polymeric micelles are irreversibly formed in aqueous solution and remain assembled in the protein-rich serum environment during systemic administration. ELPBCs, and especially those used for DAM, are unique in that self-assembly must occur reversibly in serum. ELPBCs have shown reliable and reversible self-assembly in aqueous solution but not serum [101]. If serum protein interferes with ELPBC either before or after self-assembly, this phenomenon may be disrupted. Thus, it was imperative to evaluate the effects of serum on micelle and aggregate formation.

We used UV-Vis spectroscopy to evaluate micelle formation in serum of the ELPBC constructs at both 5  $\mu$ L and 10  $\mu$ L. This method was chosen over DLS for previously-described compatibility reasons. While DLS provides more direct information regarding self-assembly, serum content overwhelms scattering and prevents accurate autocorrelation measurement. UV spectroscopy facilitated a method for subtracting out background signal and is preferred for indirectly obtaining self-assembly data for ELPBCs in serum.

Nanoparticle formation was monitored independent of miscellaneous serum protein by measuring the turbidity of ELPBC solutions in serum as a function of temperature. Each 5 and 10  $\mu$ M ELPBC sample was initially zeroed and monitored from 20 °C – 50 °C (Figs. 38 - 39). The raw data consisted of three regions similar to unmodified ELPBC turbidity profiles, presumably corresponding to unimer form, micelle form, and aggregate form. However, there was a linear decline in the signal in the unimer region not seen in turbidity profiles from aqueous solution due to protein settling in serum. A line was fit to this region and subtracted from the raw data to remove settling artifacts. The resulting curve was then used to verify nanoparticle formation through the presence of a foot region.

All tested constructs exhibited a foot region which extended from below to above 37 °C at both 5  $\mu$ M and 10  $\mu$ M. This suggests that ELPBC will remain in micelle form at normothermia to at least 50% clearance. The CMT was defined as the temperature at the first data point above the corrected baseline assuming that the foot region represented micelle formation. The CMT of these constructs was not significantly altered even in the serum environment, ranging from 30 – 33 °C at either concentration, and should remain in micelle form at normothermic conditions. These data support the use of ELP-64/90-based constructs for evaluation of static multivalent presentation within the tumor.

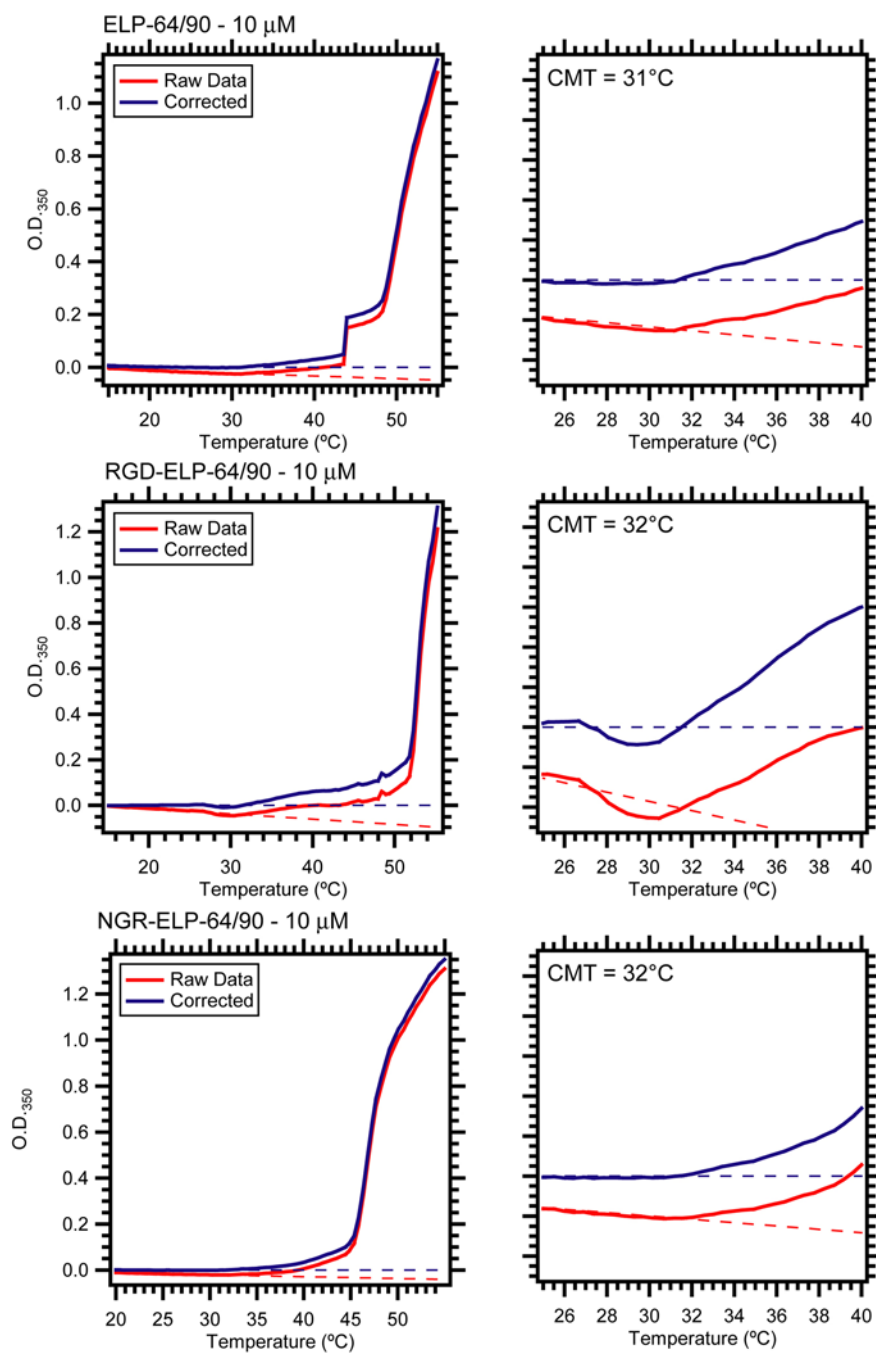


**Figure 38: Turbidity profiles of 10 μM ELPBC-AlexaFluor488 solutions in serum. All profiles were corrected for settling and examined for micelle formation. All three profiles exhibited a foot region, indicating micelle formation in serum at 10 μM.**

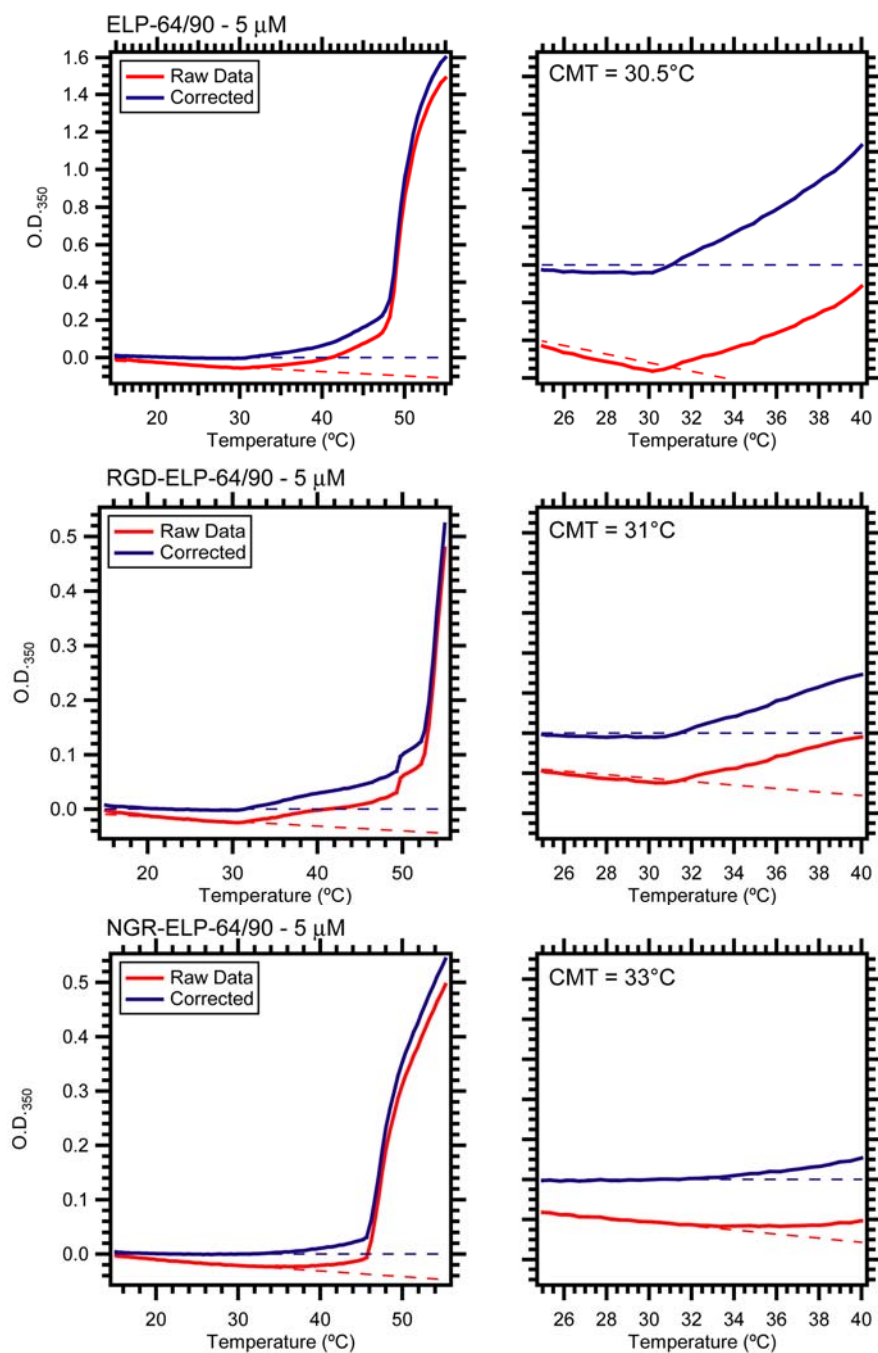


**Figure 39: Turbidity profiles of 5  $\mu\text{M}$  ELPBC-AlexaFluor488 solutions in serum. All profiles were corrected for settling and examined for micelle formation. All three profiles exhibited a foot region, indication micelle formation in serum at 5  $\mu\text{M}$ .**



### **6.3.3 Analysis of RGD-, NGR-, and Non-Ligand ELP-64/90 Accumulation Using the Dorsal Fold Window Chamber Model**

The window chamber model was used to determine the effects of multivalent ligand presentation on accumulation in both the vascular and extravascular compartments. Each of these data sets provide information regarding the effects of multivalent ligand presentation for tumor targeting. Changes in vascular accumulation over time represent reduction in plasma half-life either through clearance or offsite binding, and changes in extravascular accumulation represent the increase of drug carrier accumulating outside of the plasma compartment. Since active multivalent constructs should interact with endothelial cells or cells in the perivascular region, clear definition of the vascular and extravascular compartments is imperative to effectively use the window chamber model for quantification. Measuring these parameters over time illustrates the effects of multivalent ligand presentation on (1) plasma half-life, (2) accumulation in the perivascular/extravascular region, and (3) specificity for the tumor compared to normal tissue.

#### **6.3.3.1 Development of Automated Mask Generation**

As previously described, the initial z-stack prior to ELPBC administration was used to generate a binary mask defining the vascular and extravascular regions. Previously, this mask was created manually using the 3D-for-LSM software package (Zeiss) using a 5-step process as follows: (1) gaussian blur, (2) threshold, (3) scrap, (4) close, and (5) fill holes. While this method was useful in creating vessel masks, the reliance on arbitrary selection of a threshold value increased variability in edge definition from mouse to mouse. This variability was not a concern for detection of large aggregates in the vasculature or extravasation distance of inert macromolecules (< 100 kDa). Since our work focuses on constructs binding to the vessel wall and proximal tumor cells, incorrect definition of the plasma region may have a profound effect on the overall results. If the region is underdefined, then vascular fluorescence will be misinterpreted as extravasated ELPBC. If the region is overdefined, extravasation from the vasculature could be detected as vascular accumulation.

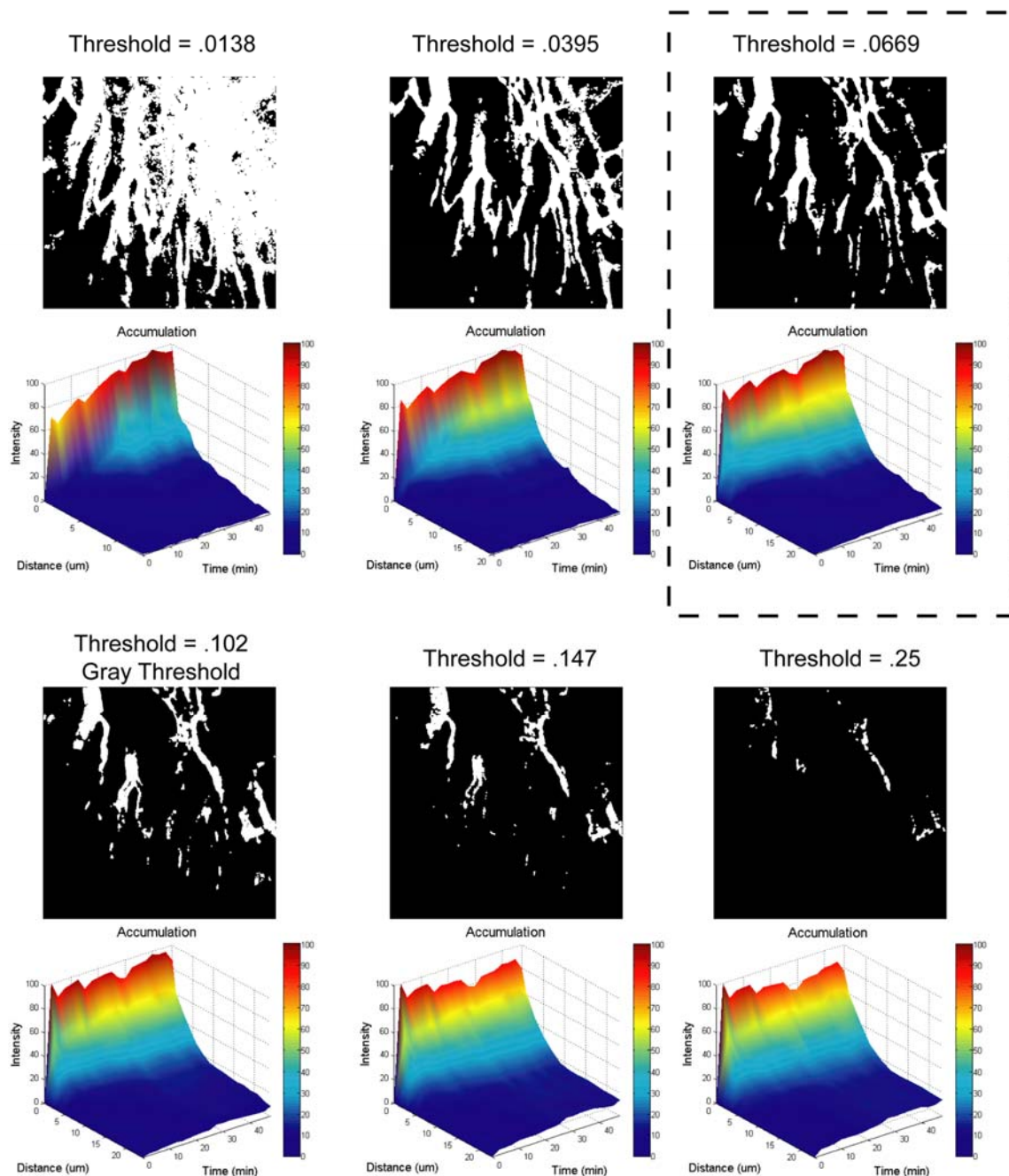


**Figure 40: Effects of threshold selection on mask generation and data calculation. As the threshold parameter increases, less pixels were associated with the vascular region as defined by the vessel mask image. Selection of this parameter affected accumulation data at the vessel wall due to ambiguity between the vascular and extravascular regions. The automated mask function yielded a threshold below the gray threshold (dashed box).**

This variability was demonstrated by generating extravasation profiles for an example ELP-64/90 data set using masks based on different arbitrary threshold values (Fig. 40). We

repeated the image analysis process for eight separate threshold values above and below the gray threshold. Lower threshold values represent a larger vascular region and higher threshold values represent a larger extravascular region. As seen in these images, the overall trends of accumulation versus clearance at the vessel wall changed as a function of threshold value and showed that an automated method to establish these bounds would improve the regularity of the calculated data.

MATLAB functions were written to automate the mask generation process based on the previous 5-step macro to limit effects from user bias (Fig. 41). This revised function was based on the assumption that the ideal mask encompasses the entire plasma region but no extravascular space. In order to identify the threshold best representing this condition, a large number of potential masks were generated using 200 arbitrary threshold values centered around the gray threshold value. Each mask was then compared to the contrast agent image at the initial time point using two cross-correlation functions. A region of the binary mask image was first compared to the whole raw data image, and a region of the raw data image was then compared to the whole binary mask image. Each of these comparisons yielded a correlation coefficient representing the degree of matching between the two images. The greatest non-zero threshold value which yielded the smallest difference between the correlation coefficients was identified as the mask value best representing the plasma compartment as defined by the contrast agent. This masking function typically returned a value slightly lower than the gray threshold which is consistent with masks generated with user-defined parameters. However, the algorithm allowed for consistent region definition between samples in a high-throughput, unbiased manner and was used to define the vascular and extravascular regions for all measurements.

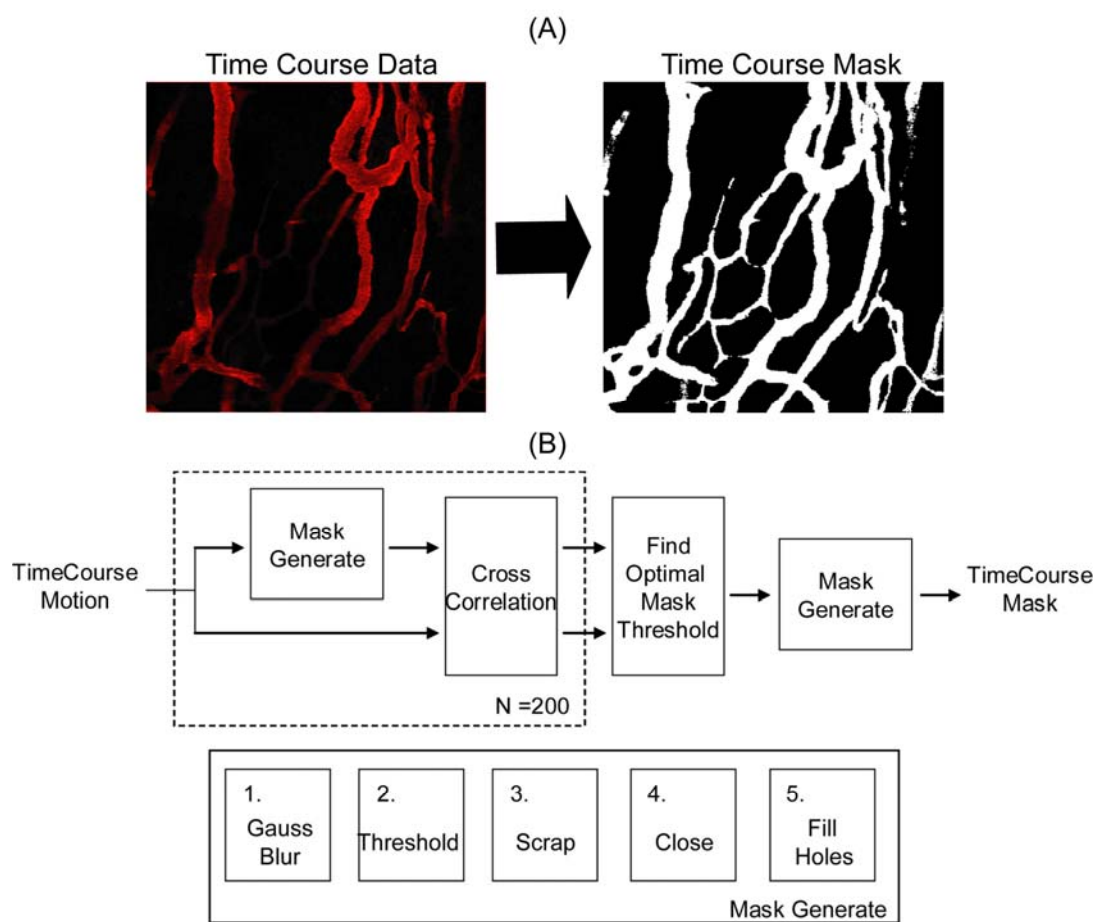


**Figure 41: Schematic of automated mask generation algorithm. A novel MATLAB algorithm was used to automate (A) binary mask generation form an initial Z-Stack. (B) A series of binary masks were generated with 200 different threshold values surrounding the gray threshold value of the initial vessel image from the plane of interest, and each resulting mask was cross-correlated with the initial raw data at that slice. The threshold value of this best-fit mask was used to generate a full 3D mask for the vascular volume.**

### 6.3.3.2 Effects of Multivalent Ligand Presentation on Tumor Spatial Distribution

The window chamber model allows observation of a whole tumor at low magnification. However, 3D quantification methods require selection of a specific ROI prior to administration of ligand-ELPBC. Additionally, we needed to select regions likely to contain angiogenic vessels in regions less susceptible to other macromolecules. We thus examined distribution of ligand-ELPBC and non-ligand ELPBC at lower magnification to best identify these regions in representative window chamber tumors. Mice bearing FaDu tumors in the window chamber were imaged at low magnification following initial administration of vessel contrast agent. Fluorescent

ELPBC constructs were then administered, and accumulation was viewed at different locations in the tumor to gather information from central vessels, peripheral mature vessels, and feeder vessels. The purpose of these experiments was to: (1) qualitatively examine the effects of vascular heterogeneity on ELPBC accumulation; and (2) identify which regions of the FaDu tumor serve as the best ROIs for quantitative analysis.

Figs. 42 - 44 show the accumulation patterns in different regions of representative tumor following administration of each construct. The central low-magnification image (5x) shows initial tumor vasculature prior to ELP administration (red), and the extracted high-magnification images (20x) show ELPBC accumulation 45 min after systemic administration (green). There were clear differences in the accumulation patterns of each construct. First, ELP-64/90 showed very little punctate fluorescence in any vessels. There was no visible accumulation in smaller or larger tumor vessels. However, there was binding to fibrous structures which were more pronounced at the tumor periphery, similar to previous experiments observing transitioned ELP homopolymer within the tumor. We hypothesized previously that these fibers were comprised of an ECM protein such as fibronectin or a structural protein such as actin, but the composition of these fibers is currently unknown. Second, RGD-ELP-64/90 showed a low level of accumulation in small, immature vessels in the center of the tumor. There was some punctate fluorescence in larger tumor vessels close to the tumor periphery, and this fluorescence was observed both inside and outside of the vessel region. Similar fibrous structures appeared at the peripheral regions similar to non-ligand ELP-64/90. Third, NGR-ELP-64/90 led to different accumulation patterns than ELP-64/90 or RGD-ELP-64/90. There was enhanced punctate fluorescence in the central immature vessels but low visible accumulation in either mature tumor vessels or feeder vessels. There was also enhanced extravasation at the tumor margin from the larger feeder vessels. Binding of NGR-ELP-64/90 to the fibrous structures was also observed, but it was not as well defined compared to the other two constructs at the tumor margin.

Based on these qualitative observations, multivalent ligand presentation clearly altered the spatial distribution of ELPBC following injection. While all constructs led to extravasation and

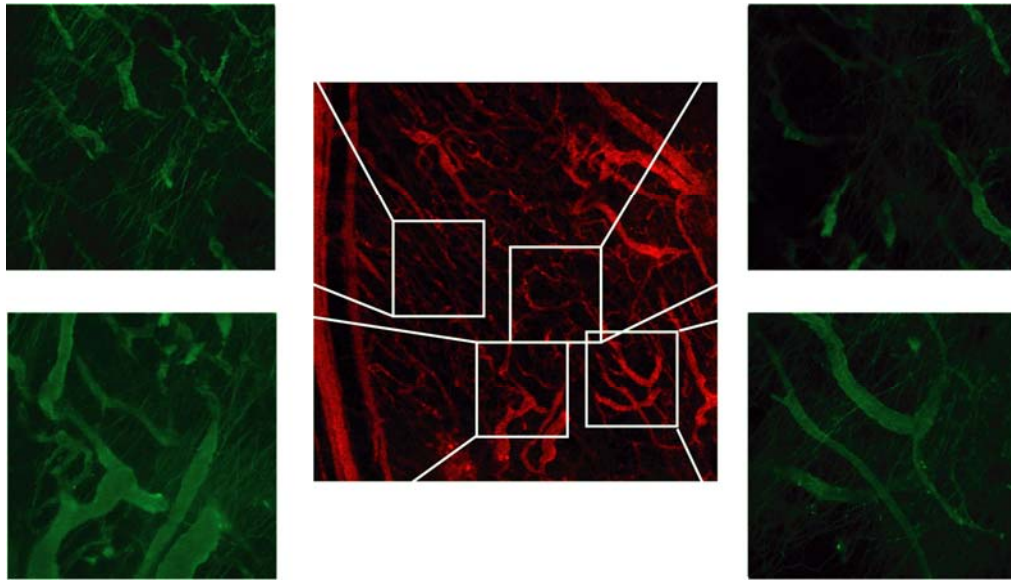


**Figure 42: Example spatial distribution of ELP-64/90 within the tumor 45 min following systemic administration. ELPBC showed low binding throughout the tumor regardless of vessel size. There was also ELPBC binding to thin fiber-like structures at the tumor periphery.**

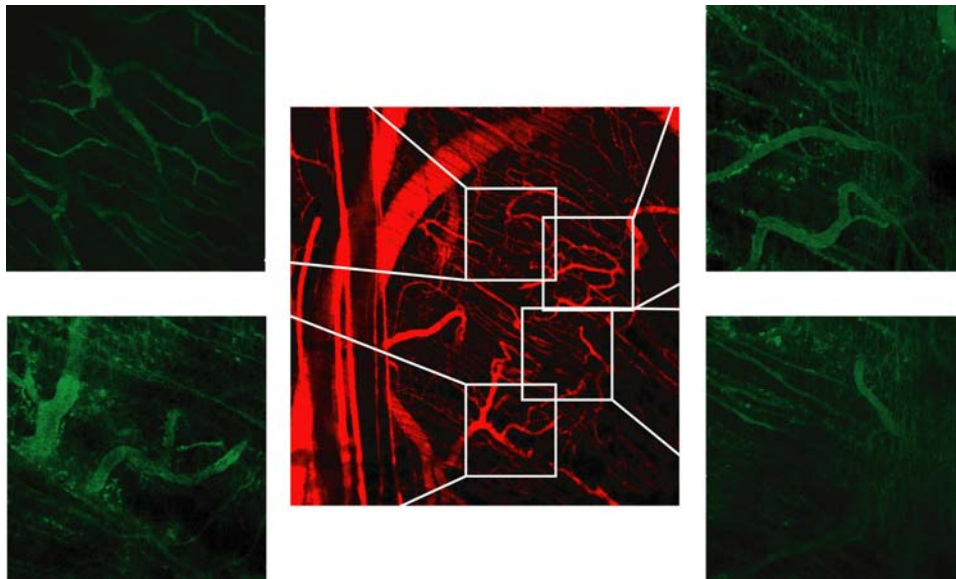


**Figure 43: Spatial distribution of RGD-ELP-64/90 within the tumor 45 min following systemic administration. RGD-ELP64/90 showed minimal punctate fluorescence in small vessels but disruption of larger peripheral vessels. RGD-ELP-64/90 also formed green fibers and punctate fluorescence at the tumor periphery.**

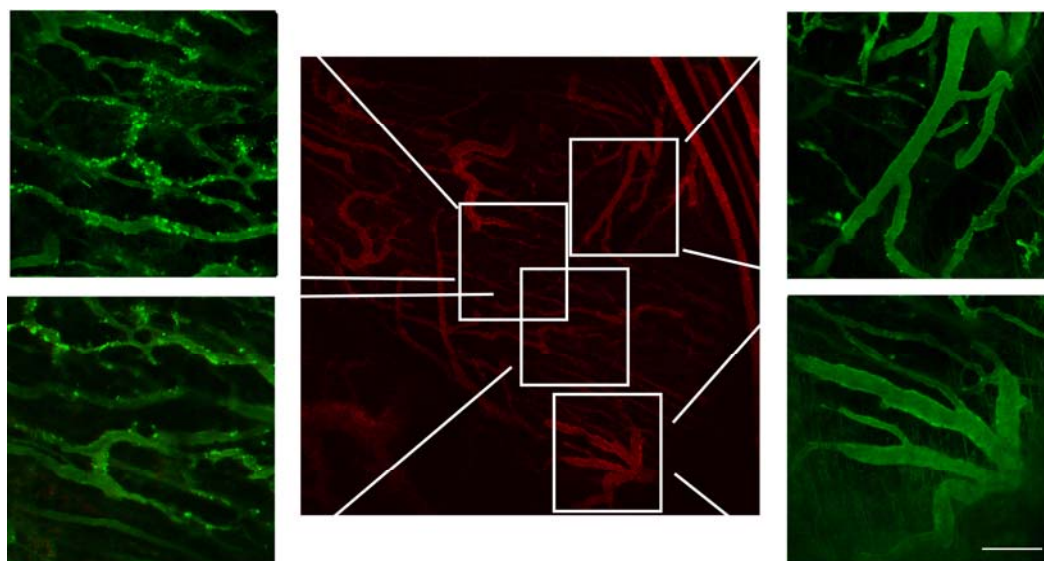


**Figure 44: Spatial distribution of NGR-ELP-64/90 within the tumor 45 min following systemic administration. NGR-ELPBC showed punctate fluorescence in small central vessels but less punctate fluorescence in larger vessels. There was also some NGR-ELP-64/90 binding to fibrous structures at the tumor periphery. Size bar = 100  $\mu\text{m}$ .**

accumulation at the periphery, RGD-ELP-64/90 showed punctate fluorescence in the extravascular tumor periphery while NGR-ELP-64/90 accumulated in smaller central vessels. These data also showed that ROI selection influences quantitative accumulation data. The initial purpose of multivalent ligand targeting was to promote ELPBC localization to angiogenic vessels in regions dominated by diffusive transport. Additionally, the window chamber provides a more accurate representation of the tumor in the central region due to artifacts resulting from wound healing at the tissue-cover slip boundary or low signal from deeper tissue. Thus, analysis of the small central vessels will provide more relevant information regarding the benefits of multivalent ligand presentation for vascular targeting, while other methods such as biodistribution would be more useful for quantifying effects of binding at the tumor margin.

### **6.3.3.3 Effects of Multivalent Ligand Presentation on Vascular Clearance**

Since ELPBC self-assembly is reversible and requires a minimum concentration for stable nanoparticle formation, the plasma concentration of ELPBC must remain at a level sufficient for multivalent presentation throughout the experimental time course. Additionally,

offsite binding to healthy tissues could alter the rate of clearance. The window chamber model provides a method for monitoring time-dependent concentration in the vascular component and estimating ELPBC plasma concentration. Thus, we used the window chamber to quantitatively evaluate the effects of ligand presentation on vascular clearance. The purpose of these experiments was to (A) determine the effects of multivalent ligand presentation on clearance and (B) estimate ELPBC plasma concentration over the imaging time course.

Following administration of contrast agent, an ROI was selected containing smaller vessels in the tumor center. Each of the constructs was administered and observed in either tumor or normal tissue by obtaining z-stacks for 45 min. The binary mask was used to define the vascular region, and the relative change in fluorescence intensity in the vascular region was calculated as a function of time (Fig. 45). The intensity of all constructs showed a decrease in the vascular compartment in both tumor and normal tissues. Both ELP-64/90 and RGD-ELP-64/90 showed more rapid clearance from tumor vasculature than normal vasculature in the first half of the time course, and the %ID reached similar levels after the entire time course. This reflects the expected results for passive carriers based on the EPR effect as macromolecules will extravasate more rapidly in the tumor tissue than the normal tissue. NGR-ELP-64/90 followed an opposite trend, showing less clearance in the tumor region than normal tissue. This is contrary to the EPR effect as NGR-ELP-64/90 constructs exited the vascular compartment more rapidly in normal tissue than tumor tissue. This observation suggests that NGR-ELP-64/90 interacts with a plasma-accessible component. Since the effects are seen only in tumor tissue, this component must be isolated to the tumor vasculature but not in normal vasculature. For this effect to occur as observed, the binding site must be immobilized in the tumor vasculature since blood flows in a closed loop. Regarding clearance, the fluorescence intensity stabilized at 40% - 50% I.D. or higher in all cases. Assuming that 100% represents an initial blood concentration of 10  $\mu\text{M}$ , the change in fluorescence intensity corresponded to a stable blood concentration of 4 - 5  $\mu\text{M}$ . These results showed that an initial dose of 10  $\mu\text{M}$  permits nanoparticle formation through the experimental time course based on *in vitro* self-assembly data for these ELPBCs in serum.



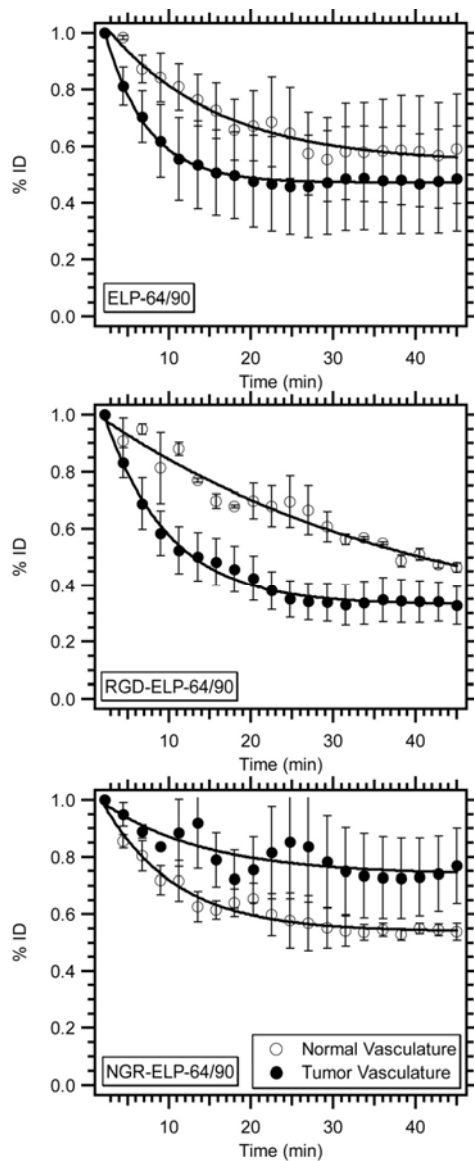


**Figure 45: Vascular concentration of ELPBC as a function of time in both tumor and normal vasculature. NGR-ELP-64/90 showed greater local clearance in normal vessels than tumor vessels, while ELP-64/90 and RGD-ELP-64/90 showed greater local clearance in tumor vessels than normal vessels ( $n = 3$ , bars = SE).**

#### **6.3.3.4 Effects of Multivalent Ligand Presentation on Tumor and Normal Tissue Accumulation**

We next used the window chamber images to determine the effects of ligand presentation on extravascular accumulation. The same image stacks used for measurements of vascular clearance were analyzed for extravascular accumulation in central vasculature, the

same binary mask was applied to the raw data to isolate the extravascular region, and slices were chosen near the center of the tumor to avoid artifacts. The average fluorescence intensity of the extravascular region in these slices was calculated at each time point and normalized to the value at  $t = 0$  min (Fig. 46). In each case, the extravascular fluorescence increased over the time course in both tumor and normal tissues. ELP-64/90 showed slightly greater accumulation in tumor tissues than normal tissues, leading to a ~2.75-fold increase in tumor tissue and a 2-fold increase in normal tissue. RGD-ELP-64/90 showed similar accumulation in normal tissue and tumor tissue with approximately a 2-fold increase in each and did not exhibit promote tumor specificity or enhanced accumulation. NGR-ELP-64/90, in contrast, showed a noticeable trend increase in tumor accumulation compared to normal tissue with static multivalent targeting. Tumor accumulation increased approximately 3.5-fold while normal tissue accumulation increased approximately 1.5-fold over the 45 min experimental time course.

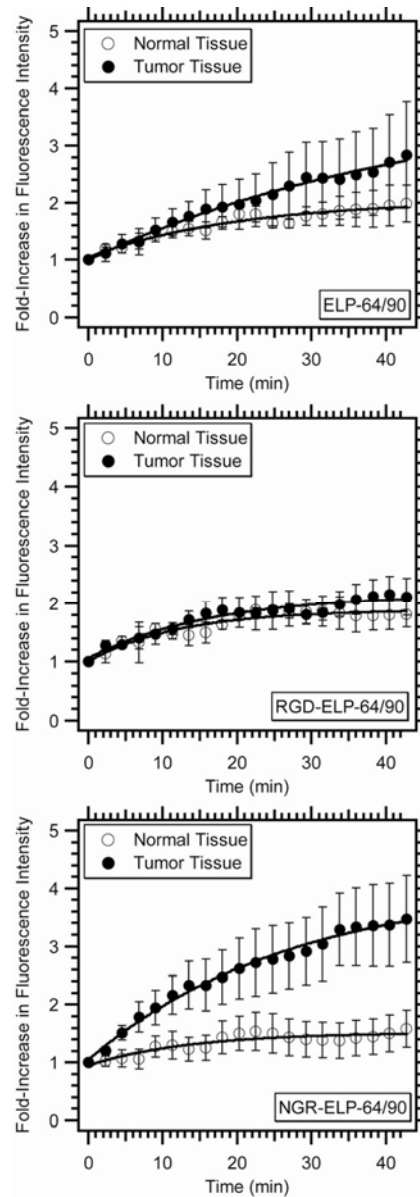


**Figure 46: Extravascular concentration of ELPBC as a function of time in both tumor and normal vasculature. In all cases, accumulation in normal tissue plateaued at 1.5 - 2-fold compared to initial extravascular intensity. NGR-ELPBC showed a 3.5-fold increase in tumor tissue, but RGD-ELPBC and ELPBC showed a 2 - 3 fold increase in tumor tissue over the time course. Additionally, NGR-ELPBC accumulation showed a trend greater specificity for the tumor compared to other constructs although this increase was not statistically significant (n = 3, bars = SE).**

These results showed ligand presentation affected accumulation in the extravascular space. The moderate increase seen with non-ligand ELPBC and RGD-ELPBC showed minimal benefits in uptake through the EPR effect, while the specific increase in accumulation with NGR-

ELP-64/90 showed interaction with either endothelial cells or other cells within the perivascular region. These findings showed a trend of specific tumor accumulation using NGR-ELP-64/90 compared to non-ligand ELP-64/90 and RGD-ELP-64/90, but these results were not statistically significant. Based on this increase in specificity without heat, NGR is preferable to RGD for static targeting construct using ELP-64/90 as the scaffold for multivalent presentation.

#### **6.3.3.5 Effects of Multivalent Ligand Presentation on Extravasation Distance**

Extravasation distance was measured using the dorsal fold window chamber model as a method to (A) evaluate penetration of the micelle into the tumor interstitium and (B) indirectly detect specific interaction between ligand-ELPBC and cells outside of the plasma compartment. In each data set, the binary mask was converted into a distance map defining the distance of each voxel from the nearest vessel surface. Each ELP image was then applied to this map. The intensity of each voxel throughout the time course was normalized to the maximum intensity observed throughout the time series, and an intensity matrix was generated for each mouse using bin definitions with  $\pm .2 \mu\text{m}$  precision. The matrices were averaged for each construct to observe the effects of ligand presentation on 3D penetration.

There was minimal extravasation of ELP-64/90 from the plasma region into the extravascular space (Fig. 47). Fluorescence intensity at the vessel wall followed a similar trend of exponential decay observed in vascular accumulation (Fig. 45). The extravascular concentration remained constant throughout the time course from 5 – 20  $\mu\text{m}$ , showing minimal accumulation in the extravascular space over time as expected through diffusive transport. RGD-ELP-64/90 and NGR-ELP-64/90 showed similar patterns of decay at the vessel wall, but each also exhibited an increase in extravascular accumulation as a function of time. RGD-ELP-64/90 showed an initial increase in the 5 – 10  $\mu\text{m}$  region following injection and reached a similar level throughout the observed region after 45 min. NGR-ELP-64/90 extravasated more slowly following injection compared to RGD-ELP-64/90, but there was a steady increase over the entire 20  $\mu\text{m}$  region over time. This onset of this increase was delayed in tissues further from the vessel wall, but the

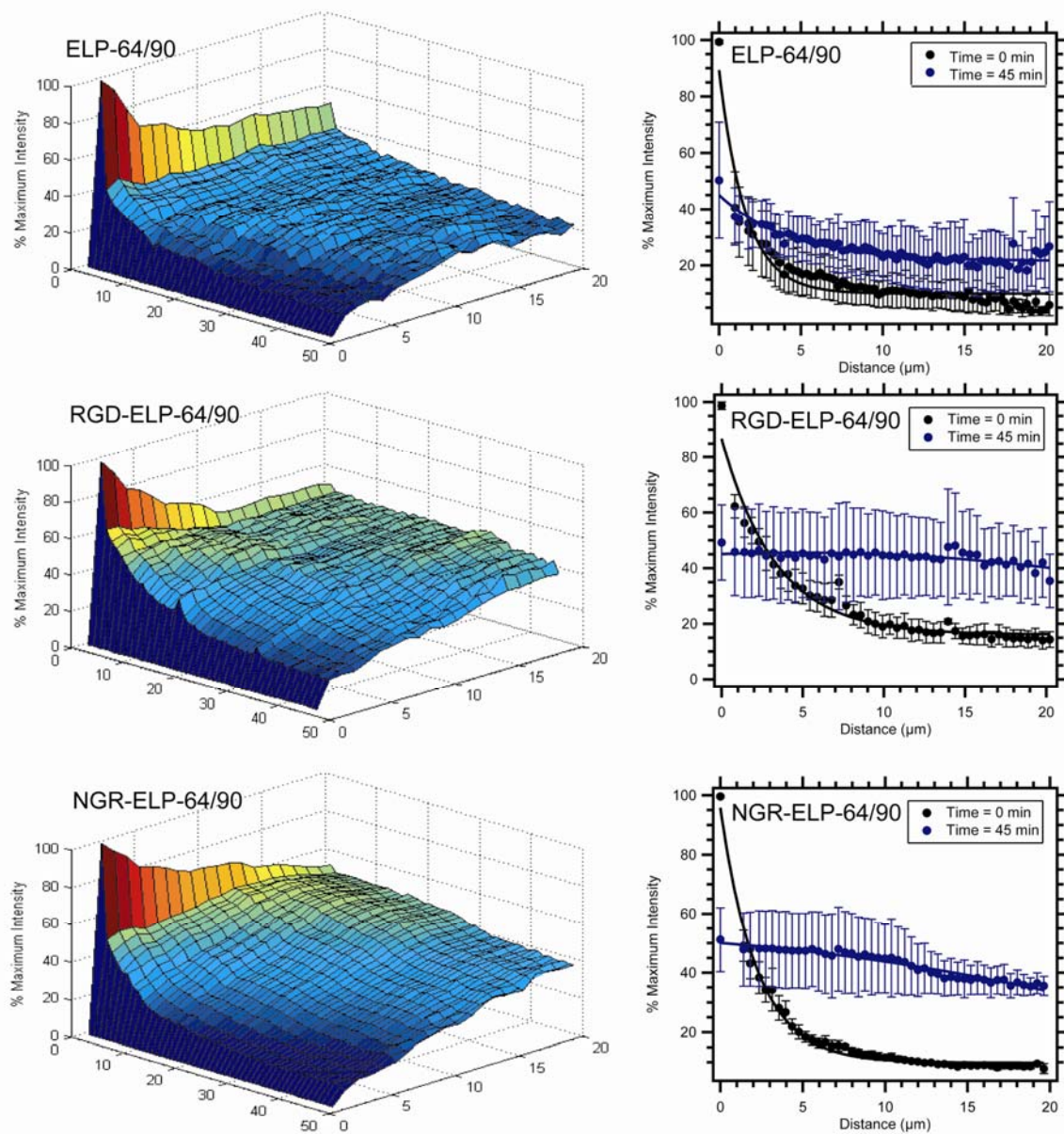


**Figure 47: Penetration distance of ELP-64/90, RGD-ELP-64/90, and NGR-ELP-64/90 micelles. Each contour plot represents the average penetration distance of each construct over the time course (left), and the histogram shows the intensity at at times = 0 min and 45 min. There was greater extravasation of ligand-ELPBC than non-ligand ELPBC. Extravasation was not expected beyond 20  $\mu\text{m}$  based on the micelle size ( $n = 3$ , bars = SE).**

increase was observed throughout the extravascular region. The highest accumulation occurred 0 – 10  $\mu\text{m}$  from the vessel wall, corresponding to 1 – 2 cell layers.

Given the large MW of the micelle (~6 MDA), we expected minimal extravasation based on previous studies involving penetration of macromolecular drug carriers and the dominance of diffusion over convection in the tumor center. Additionally, if the only method of transport in the observed regions was simple diffusion, the results should show greater penetration of the non-ligand ELP-64/90 compared to either ligand-ELP-64/90. However, these data showed that ligand-ELPBC penetrated the extravascular space more readily than non-ligand ELPBC, suggesting a form of active transport through interaction with antigens presented in the tumor vasculature. Interactions with binding sites could facilitate exit from the plasma compartment either through RGD-ELP-64/90 accumulation on endothelial cells or NGR-ELP-64/90 on endothelial cells or pericytes. These data suggest ligand presentation affects extravascular penetration, but more study is needed to identify cellular targets within the vasculature.

#### **6.3.4 Analysis of RGD-, NGR-, and Non-Ligand ELP-64/90 Cell Localization Using Immunohistochemistry**

While the dorsal fold window chamber model is a unique system allowing quantification of compartmentalized accumulation and extravasation, it is limited by several technical hurdles. First, the dorsal fold window chamber convolutes vessel receptor expression as it may introduce wound healing regions with similar angiogenic characteristics to developing tumors. Second, the cover slip replacing the skin may cause vessel disruption at the glass tissue interface, leading to accumulation artifacts. Third, the two-channel capability of the confocal microscope used for this study prevented the use of a third label in the window chamber. Fourth, confocal microscopy compatible with the window chamber does not provide sufficient resolution to isolate tumor endothelium from adjacent tumor cells, making it difficult to identify the binding site using the window chamber model.

Based on these limitations, we used a secondary method, IHC, to qualitatively evaluate (1) tumor and normal tissue accumulation and (2) binding sites within the endothelium and perivascular region. Subcutaneous FaDu tumor and thigh muscle were assayed in these studies; the thigh muscle was chosen as representative healthy tissue with significant vascularization. In

each experiment, an ELPBC construct was systemically administered and allowed to circulate for 1 hour followed by administration of Hoechst 33342. The tumor and muscle sections were removed, sectioned, and stained for endothelial cells to identify cellular interactions with ELPBC.

Fig. 48 illustrates both ligand and non-ligand ELPBCs in tumor tissue. In each tissue slice, CD31 represents endothelial cells (red) and perivascular nuclei represent functional vessels (blue). The spatial distribution of ELPBC-AlexaFluor488 (green) was then compared with the staining patterns of CD31 and the nuclear stain. First, there was a minimal increase in ELP-64/90 accumulation near endothelial cells and functional vessels. Second, there was also minimal visible green fluorescence in tumor slices following RGD-ELP-64/90 administration, although it was slightly more intense than non-ligand ELP-64/90 (ligand-negative control). Additionally, the limited visible RGD-ELP-64/90 fluorescence is highly localized to endothelial cells. Third, there was a noticeable increase in punctate fluorescence associated following administration of NGR-ELP-64/90. This fluorescence was associated with both functional vessels and endothelial cells.

These interactions were also observed in normal tissue following systemic administration (Fig. 49). Unlike tumor tissue, there was noticeable accumulation of all three constructs in functional vessels in normal tissue. Accumulation appeared strongest with RGD-ELP-64/90 and weakest with NGR-ELP-64/90. ELPBCs partially colocalized with CD31 stain but also accumulated in vessels between cells more noticeably than in tumor tissue. This could be a result of decreased permeability of normal vessels or interaction with a component distinct from endothelial cells.

We further quantified this colocalization of ELPBC with both endothelial cells and cells proximal to the plasma layer (endothelial cells, pericytes, etc.) using MATLAB image processing functions. Ten different regions were chosen in each tumor or normal tissue slice and separated into red, green, and blue channels. Each channel was converted into a binary image using the gray threshold as the cutoff intensity. Boolean functions were then used to calculate the percentage of ELP-64/90 colocalized with CD31 or Hoechst (Fig. 50). Non-ligand ELP-64/90 showed similar percentages of colocalization with endothelial cells in both normal and tumor

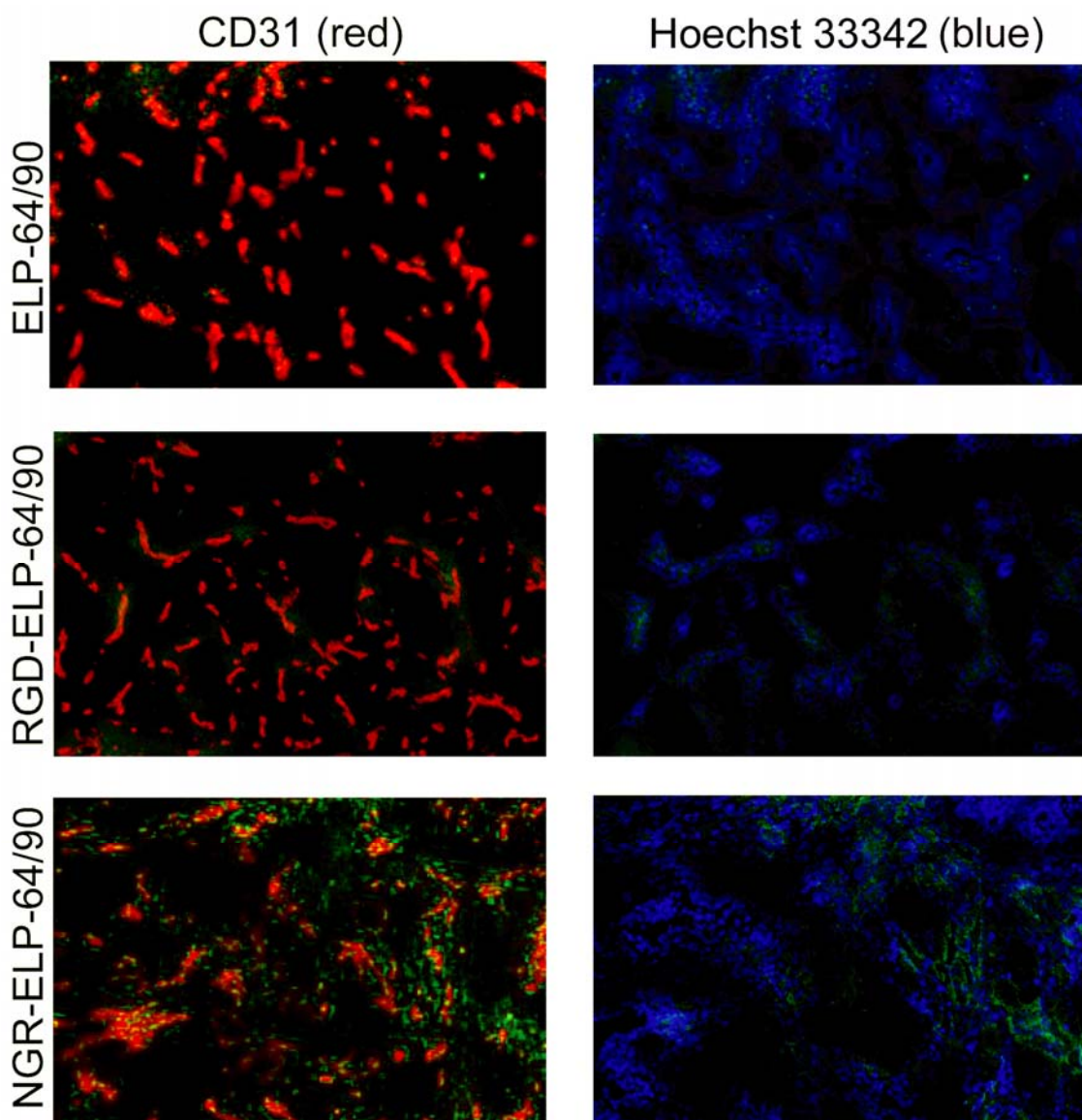


**Figure 48: Immunohistochemistry images of tumor tissue following administration of ELPBC (green). There was no visible accumulation of ELP-64/90 in the tumor, some accumulation of RGD-ELP-64/90 near the endothelial cells (red), and significant accumulation of NGR-ELP-64/90 near the endothelial cells and tumor cells (blue) surrounding the vessels.**



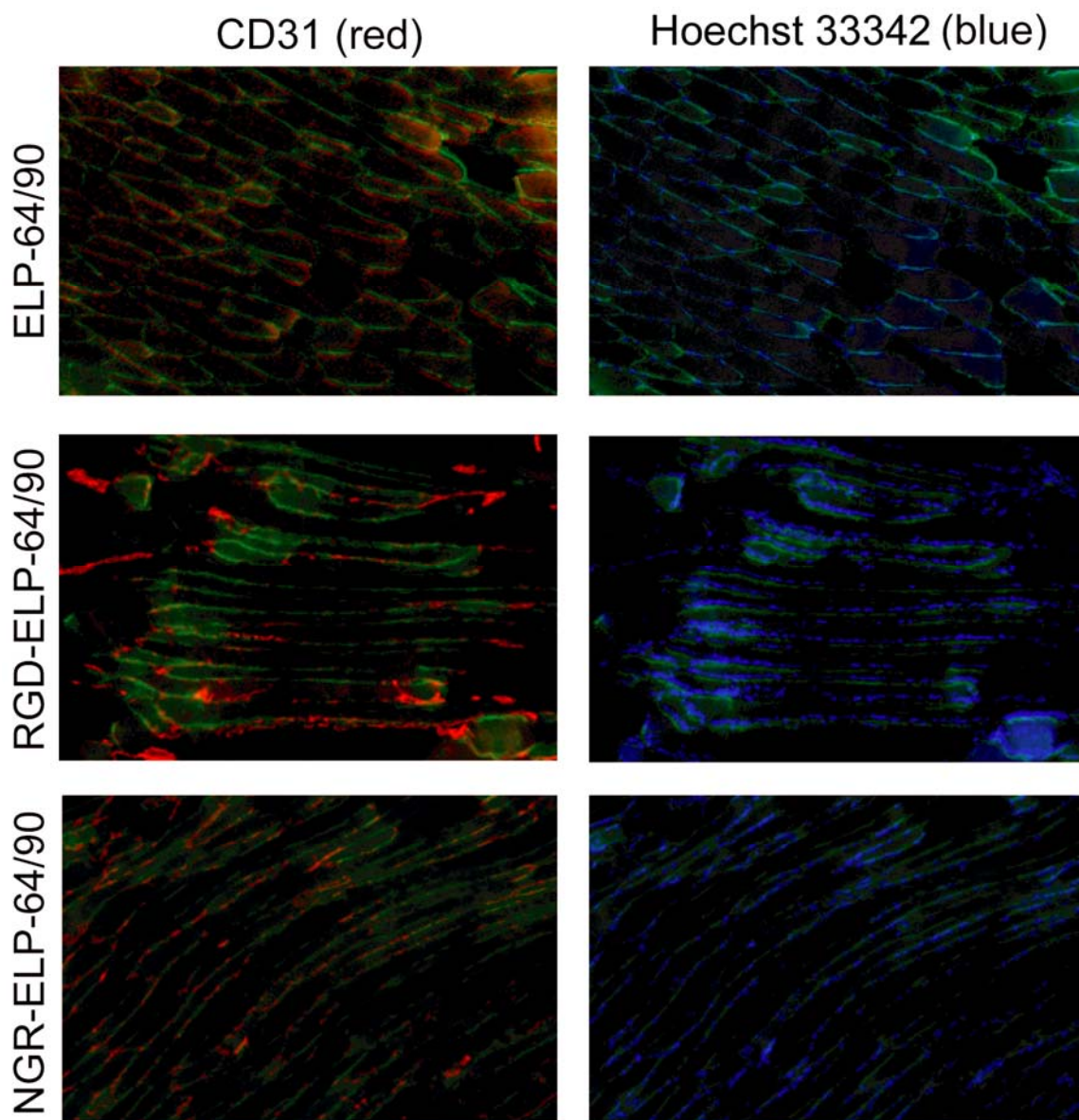


**Figure 49: Immunohistochemistry images of normal muscle tissue following administration of ELPBC. There was noticeable accumulation near the endothelial cells with all three constructs but the intensity of RGD-ELP-64/90 was stronger than the other two constructs.**

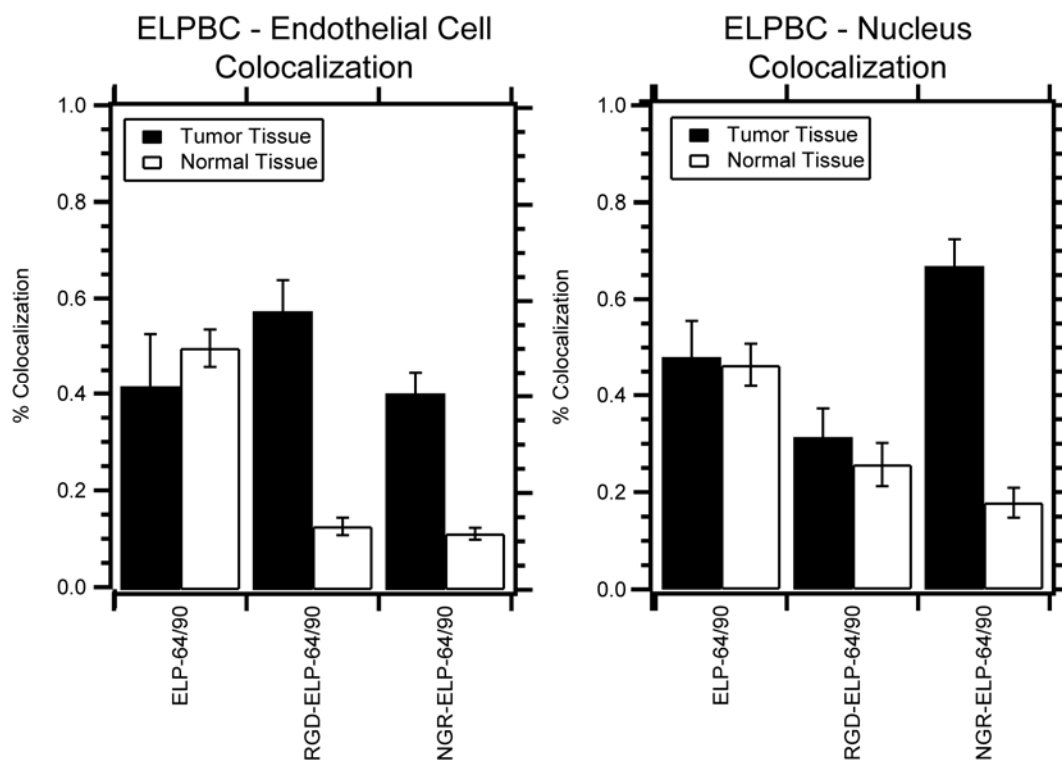


**Figure 50: Colocalization of ELPBC with endothelial cells and perivascular nuclei. The % green pixels overlapping with red (endothelial cells) and blue (nuclei) in each image were calculated using MATLAB. There was significant increase in tumor endothelium with multivalent ligand presentation compared to normal endothelium. There was more relative perivascular cell accumulation with multivalent NGR presentation compared to the other two constructs (bars = SE).**

tissues. Conversely, RGD-ELP-64/90 and NGR-ELP-64/90 showed higher colocalization with endothelial cells in tumor tissue than normal tissue. Both non-ligand ELP-64/90 and RGD-ELP-64/90 exhibited similar colocalization percentages to stained cell nuclei in both normal and tumor tissue. NGR-ELPBC, however, showed a significantly higher percentage of colocalization in tumor tissue than normal tissue. These results demonstrated that RGD-ELPBC and NGR-ELPBC interact with different types of cells following multivalent self-assembly. Our data showed that RGD-ELP-64/90 interacted preferentially with tumor endothelial cells, while NGR-ELP-64/90 interacted with tumor endothelium or distressed cells in the tumor perivascular region. This supports RGD binding to exposed integrins and NGR interacting with both CD13 and  $\alpha v \beta 3$ . While further study is needed to identify the exact receptors responsible for binding, there was a clear

dependence of ligand presentation on cell localization, suggesting that multivalent presentation can enhance interaction with endothelial cells and other cells proximal to the vasculature.

### **6.3.5 Evaluating Potential for Delivery of Doxorubicin Using ELPBC**

Both IM and IHC data supported the use of multivalent targeting to improve accumulation of an imaging agent or drug in a tumor. To better establish the utility of these drug carriers, we attempted to evaluate the potential of therapeutic delivery to the tumor to deliver Dox using the existing ELP-64/90-based constructs and novel imaging routines on the Zeiss LSM510 confocal microscope. The “activated” – cysteine-reactive Dox derivative, B-Dox was conjugated to the ELPBC through an acid-labile maleimide bond. Unfortunately, the current constructs only permitted an upper limit of one Dox molecule conjugated per ELPBC unimer. This created two constraints that we recognized at the outset of these experiments: (1) Dox loading in the micelles was low compared to other nanoparticles with preclinical success [202] and not suitable to evaluate the effect of ligand targeting on tumor regression; and (2) the low level of fluorescence imparted by a maximum of 1 Dox per ELP also impose a limitation on the IM analysis with our current microscope. Despite these constraints, we carried out an IM imaging study of Dox conjugated to the ELPBC constructs with the following aims: (1) to evaluate the effects of ELPBC-Dox on thermal self-assembly and (2) to determine if the currently available LSM510 confocal microscope permits intravital imaging of Dox at concentrations compatible with thermosensitive ELPBC.

#### **6.3.5.1 Effects of Doxorubicin Conjugation on ELPBC Self-Assembly**

RGD-, NGR-, and non-ligand ELP-64/90 were conjugated to B-Dox at the terminal cysteine residue with a conjugation ratio similar to AlexaFluor488 (~70%). Filtered 10  $\mu$ M solutions of ELPBC-Dox were then analyzed using DLS and the  $R_h$  and MW was monitored from 20°C – 45 °C (Fig. 51). The effects of Dox on CMT followed unexpected trends. First, the thermally driven self-assembly of ELP-64/90 was not dramatically affected by Dox conjugation as the CMT = 33 °C similar to the 35 °C CMT of unmodified ELP-64/90 [101]. We did however

observe two populations in solution from 33 °C – 35 °C, likely corresponding to both unimer and micelle form. RGD-ELP-64/90 was more affected by Dox conjugation as, interestingly, its CMT increased to 36 °C. There was a smaller range of stable micelle formation for RGD-ELP-64/90-Dox (36 °C – 39 °C) than RGD-ELP-64/90-AlexaFluor488. NGR-ELP-64/90 was dramatically affected by addition of Dox as the CMT increased to 38 °C, more than the other two constructs. Additionally, there was no temperature region that showed stable micelle formation as the nanoparticles that formed at 38 °C grew in size with increasing temperature (Fig. 51).

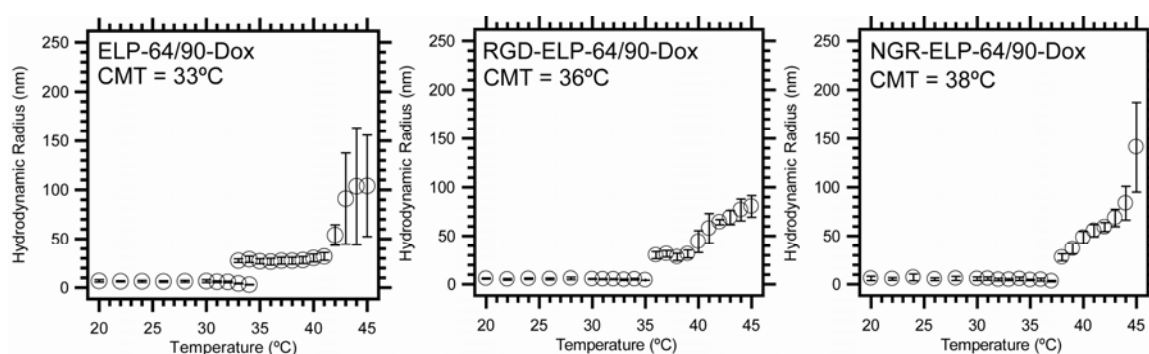


**Figure 51: Hydrodynamic radius of non-ligand-, RGD-, and NGR-ELP-64/90-Dox constructs as a function of temperature. Addition of Dox to ELP-64/90 did not significantly affect the transition temperature, but it raised the CMT of both RGD- and NGR-ELP-64/90. The range of stable micelle formation varied with the addition of binding ligand (bars = polydispersity).**

Unlike the CMT, the changes in size followed more predictable trends (Table 10). The size of each nanoparticle in the stable region ranged from ~28 – 31nm and did not change appreciably from the size of unmodified ELPBC. The MW and Z of RGD-ELP-64/90 and NGR-ELP-64/90 did not vary with addition of Dox, but the MW and Z of non-ligand ELP-64/90 decreased when conjugated to Dox. The coronal density was very similar between all tested constructs.

**Table 10: Self-assembly parameters of ELPBC-Dox constructs. There was a decrease in MW and Z with non-ligand ELP-64/90 but no change in the other parameters compared to constructs conjugated to AlexaFluor488.**

ELP	Rh (nm)	MW (kDa)	Z	termini/nm <sup>2</sup>
ELP-64/90-Dox	28	8189	129	0.013
RGD-ELP-64/90-Dox	30.4	9953	155	0.013
NGR-ELP-64/90-Dox	27.9	8111	126	0.013

While the addition of a single Dox molecule did not prevent triggered self-assembly, it did affect nanoparticle formation more than AlexaFluor488. These data illustrated that ELP-64/90 and RGD-ELP-64/90-Dox still formed thermosensitive micelles over a thermal range, but NGR-ELP-64/90-Dox did not. Dox also altered the physical parameters of non-ligand ELP-64/90 but not RGD- or NGR-ELP-64/90. Additionally, Dox changed the CMT of all three tested constructs, but the effect varied with ligand composition. Ligand and conjugate also affected CMT and physical parameters differently in ELPBC-Dox than ELPBC-AlexaFluor488, suggesting interplay between the hydrophobic conjugate and the attached ligand in nanoparticle self-assembly. In a broader sense, these data also showed that there is a limit to the types of terminal modification compatible with micellar self-assembly. However, identification of a predictive relationship between ligand, conjugate, and parent ELPBC represents a tremendous challenge given the wide selection space of potential ligand-conjugate pairs, a problem that will need to be solved to move these multivalent constructs into preclinical studies.

#### **6.3.5.2 Evaluation of Doxorubicin-Functionalized Constructs Using the Dorsal Fold Window Chamber**

We next evaluated the ability to observe ELP-64/90-Dox using the window chamber model. Dox is a weak fluorophore with an excitation peak at 488 nm and a broad emission from approximately 530 nm – 610 nm [268], both of which are compatible with available laser wavelengths and filter sets on the LSM510 used for IM. We simultaneously imaged Dox with a FITC vascular mask using a single excitation source and separate detectors for green and red fluorescence. The Dox-based construct was administered and imaged simultaneously with FITC-dextran using a line switching routine with each line on the raster-scanned image alternating between green and red fluorescence. This method was successfully implemented in the window chamber model to simultaneously image FITC-labeled liposomes loaded with Dox at a dose of 10 mg/kg and is directly applicable to other Dox-loaded macromolecules [202].

We used this routine to image 10  $\mu$ M ELP-64/90-Dox (.25 mg/kg) within the tumor using a FITC mask (Fig. 52). The intensity of the incident light and detector gain on both red (ELP-64/90-

Dox) and green (FITC-dextran) channels were increased to the highest power and gain that did not promote autofluorescence (Fig. 52A). ELP-64/90-Dox was then administered but was not visible in either channel (Fig. 52B). 2 MDa FITC-dextran was then administered to identify the vessels. The fluorescence from FITC-dextran was visible on the green detector but also bled through to the red detector (Fig. 52C). The imaging routine was then changed to the line switching routine used to simultaneously image AlexaFluor488 and rhodamine. As expected, the FITC contribution to the red channel was eliminated with this routine, but the ELP-64/90-Dox did not exhibit visible fluorescence (Fig. 52D). These results showed that .25 mg/kg Dox/dose did not produce the necessary signal for imaging with current microscopic capabilities.

We next increased the ELP-64/90-Dox dose to better enhance the visibility of Dox within the window chamber. While a MTD of ELP has not been established, we used a dose of ~100  $\mu$ M (2.5 mg/kg) assuming an average mouse body weight of 25 g as, given current protocols, this was the maximum dose resulting from a single conjugation reaction of ELP-64/90 with B-Dox. While this dose was an order of magnitude higher than the initial test, it was also still below the 10 mg/kg concentration previously visualized.

Each ELPBC-Dox construct and FITC-dextran was administered at ~100  $\mu$ M via tail-vein injection and z-stacks were obtained over the course of 1 hour (Fig. 53). There was still no visible red fluorescence with either the ELP-64/90-Dox or NGR-ELP-64/90-Dox, but there was faint, punctate red fluorescence with RGD-ELP-64/90-Dox outside of the vessel region. While the imaging routine reduced the potential for autofluorescence, this red pattern was similar to autofluorescence seen with high detector gain near the vessel/cover slip interface.

Given the limitation of one Dox molecule per ELP chain with thermosensitive ELPBC, the Dox dose at ELPBC concentration used for *in vitro* characterization did not produce a reliably strong signal for analysis. When using the highest Dox concentration possible with a single conjugation reaction, there was some faint visible fluorescence near smaller vessels. However, the high gain requirements for visualization increased the risk of autofluorescence. It is also unclear how the ELPBCs will behave structurally at a 100  $\mu$ M concentration. Thus, the weak

fluorescence and uncharacteristically high ELPBC concentration suggests that the window chamber model is more useful for imaging ELP-Dox constructs with higher loading per nanoparticle given the current microscope capabilities. However, additional modifications to the

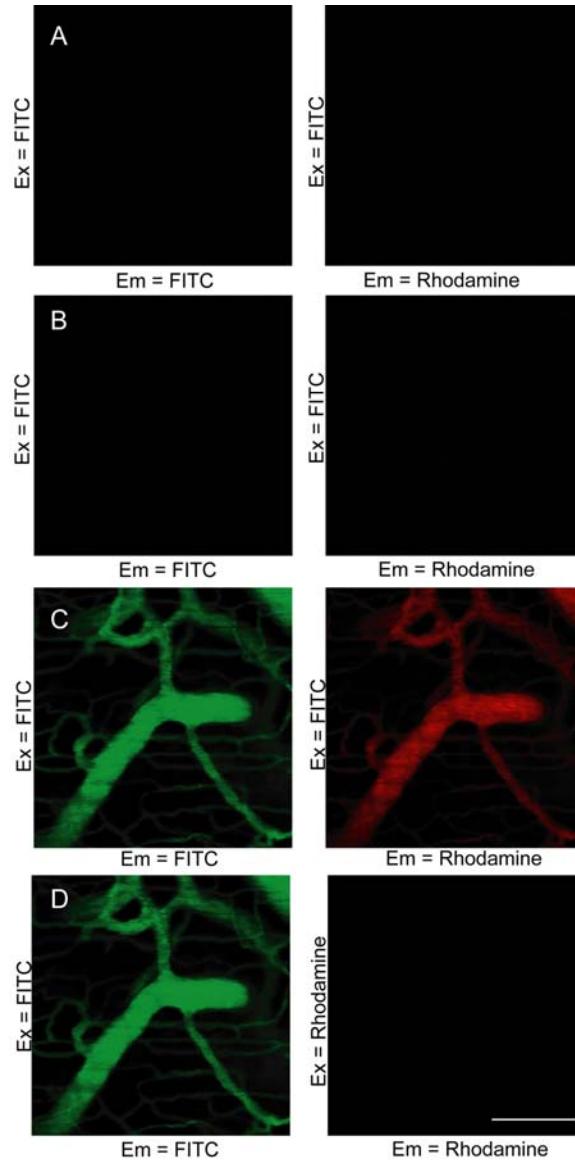


**Figure 52: Confocal images of ELP-64/90-Dox and FITC-Dextran in tumor vasculature. (A)** Laser power and gain on the green and red detectors were increased without autofluorescence. **(B)** 10  $\mu$ M ELP-64/90-Dox was not visible following injection. **(C)** FITC-Dextran was then administered and was visible in both the green and red channels. **(D)** The red/green imaging routine used for simultaneous imaging of AF488/rhodamine reduced bleedthrough, but did not permit imaging of ELP-64/90-Dox. Size bar = 150  $\mu$ m.

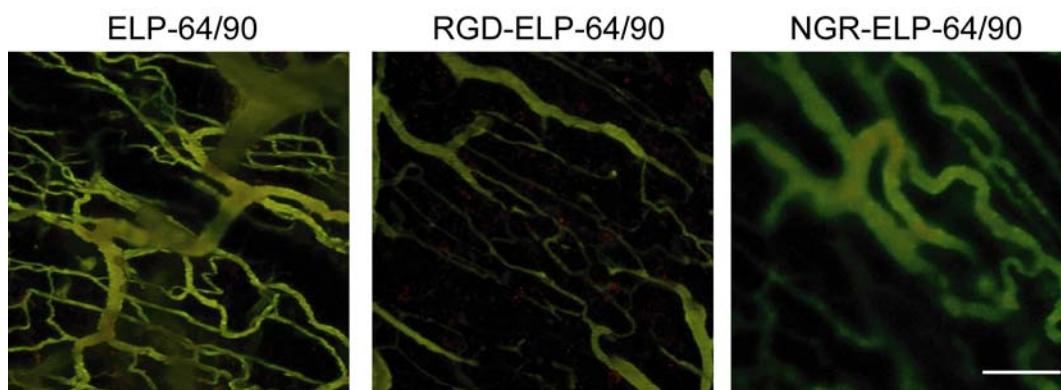


**Figure 53: Confocal images of 100  $\mu$ M non-ligand, RGD-, and NGR-ELP-64/90-Dox constructs in FaDu tumors using the dorsal fold window chamber. No punctate red fluorescence was observed with ELP-64/90-Dox or NGR-ELP-64/90-Dox. There was faint red punctate fluorescence observed with RGD-ELP-64/90-Dox although this fluorescence was similar to autofluorescence patterns. Size bar = 100  $\mu$ m.**

filter sets such as spectral deconvolution may allow for higher incident intensity and detector gain with lower risk of detected autofluorescence, permitting detection of these constructs.

## **6.4 Significance**

Our study of *in vivo* multivalent targeting using ELPBC showed that static multivalent presentation of NGR improved specific targeting of the tumor region, but static multivalent presentation of RGD did not. The window chamber images also showed pervasive non-specific interaction of micellar ELPBC with and without ligand with a component at the tumor margin. The low penetration distance and spatial distribution shown in histology slides both suggest that ligand-ELPBC micelles are best suited for targeting endothelial and perivascular cells. These findings, in conjunction with *in vitro* data, provide insight on the best routes to proceed for further development of each of the ELPBC constructs for unique applications in tumor targeting.

First, the NGR-ELP-64/90 construct showed improved tumor accumulation and specificity through static affinity targeting without hyperthermia. It also showed the ability to promote both endothelial cell and perivascular interaction, making it a useful construct for antivasular targeting. Since static multivalent NGR presentation promoted specific tumor accumulation and suffered from low Dox loading, it follows that the construct can be improved by improving the Dox loading while maintaining multivalent NGR presentation. Thus, NGR ligand functionality can be



applied to constructs with higher loading efficiency and demonstrated preclinical success to improve antitumor activity.

Second, the RGD-ELP-64/90 construct did not show enhanced tumor accumulation or specificity. However, RGD-ELP-64/90 did show successful interaction with the cognate receptor *in vitro* as well as specific colocalization with endothelial cells in histological analysis. Also, RGD has the potential to interact with blood-borne activated platelets through the gpIIb $\beta$ 3 integrin leading to offsite accumulation. For this reason, DAM may benefit RGD-ELP-64/90 by preventing off-site binding and improving interaction with tumor vasculature. For this to have an impact, however, the ELP-64/90 construct must be redesigned to exhibit a CMT from 39 – 42 °C in serum, a very small window given the uncertainty of binding benefits and the negative accumulation data with static multivalent expression.

Third, non-ligand ELP-64/90 did not promote specific tumor accumulation at the center of the tumor. However, this construct also did not behave like an inert nanoparticle as it adhered to fibers at the tumor margin, an area where convective transport dominates. If this micelle preferentially extravasates at the tumor periphery following systemic administration and remains in the tumor region through interaction with proteins in the margin, this interaction could promote a new strategy for margin targeting. The nanoscale size of the ELPBC micelle is advantageous compared over the larger homopolymeric ELP for targeting the tumor margin due to its smaller size and ability to circulate in a transitioned state. Further study of the interaction between ELPBC and protein components within the margin will further elucidate the potential of this strategy.

## 7 Affinity-Modulation Drug Delivery: Conclusions and Future Directions

### 7.1 Conclusions

The results of this work demonstrated that thermally-sensitive ELPBC can serve as a versatile material for dynamic or static multivalent targeting of tumor-associated antigens. All tested constructs showed sufficient stability and retention of thermosensitive behavior following modification with a peptide ligand at the hydrophilic ligand and a synthetic conjugate at the hydrophobic terminus. Given the proper physical characteristics, thermally-triggered self-assembly transformed RGD-ELPBC from an inert low-affinity monovalent unimer to an active high-avidity multivalent micelle as seen in uptake assays using a compatible engineered cell line. This proof-of-concept experiment is, to the best of our knowledge, the first demonstration of affinity modulation via an external thermal stimulus. Despite this success, the ELPBC constructs demonstrating specific multivalent interaction did not exhibit the proper thermal profile and require further modification to continue investigation of DAM *in vivo*.

Stable micelle formation at normothermic conditions allowed ELPBC micelles to serve as static multivalent nanoparticles for tumor targeting. Neither ELP-64/90 nor RGD-ELP-64/90 micelles promoted specific tumor accumulation, but NGR-ELP-64/90 increased specific tumor accumulation as demonstrated through window chamber analysis. Immunohistochemistry qualitatively showed this increase and also specific interaction of NGR-ELP-64/90 with tumor endothelial and perivascular cells. Although the exact site of cell binding beyond endothelial cells was unknown due to uncertainty surrounding the NGR-CD13 interaction, static multivalent ligand presentation conferred spatial restriction of binding activity without DAM. These results provided a clear strategy for future development of the three tested constructs, ELP-64/90, RGD-ELP-64/90, and NGR-ELP-64/90, to best exploit multivalent targeting for drug delivery applications. Additionally, many of the unique protocols developed throughout this study have direct benefits for further study of affinity targeting and indirect benefits for other applications within our group.

## **7.2 Future Directions**

### **7.2.1 Development of ELP2-ELP4 Block Copolymers for Targeted Drug Delivery**

The data obtained throughout the course of study illustrated separate development strategies for each of the non-ligand, RGD-, and NGR-ELP-64/90 block copolymers. To best develop these constructs for advancement to therapeutically-relevant preclinical models, the following steps should be taken: (1) NGR ligand should be applied to other constructs for static multivalent targeting of tumor vasculature; (2) RGD-ELP-64/90 should be redesigned for DAM through thermal optimization; and (3) the interaction between ELP-64/90 and components promoting accumulation at the tumor periphery and muscle cells should be further investigated as an alternative tumor margin targeting strategy.

#### **7.2.1.1 NGR-ELPBC**

DAM provides the ability to spatially-restrict binding as a method to improve antivasular targeting. However, ELPBCs compatible with thermal self-assembly have the tradeoff of low therapeutic payload. Since NGR-ELP-64/90 already demonstrates enhanced specificity and only requires static multivalent presentation to confer a benefit for specific targeting, the priority for this ligand-receptor pair can be shifted to increased payload rather than thermal optimization. Thus, the best next step to developing this construct is expanding NGR to a thermally-insensitive construct with better tolerance for therapeutic encapsulation.

We have recently demonstrated that thermally-insensitive nanoparticles will self-assemble in to large, polydisperse micelles following conjugation to 4 - 8 Dox molecules. These nanoparticles delivered substantial levels of Dox to the nucleus of cells in culture (Fig. 54) and promoted full regression of a C26 flank tumor with a single nanoparticle dose at 10 mg/kg [202]. However, a major concern with these nanoparticles is systemic toxicity as 10 mg/kg is close to the MTD of Dox. NGR-based multivalent targeting may promote greater accumulation in the

tumor region and lesser accumulation in normal tissue either allowing similar results at a lower systemic dose or lower toxicity at an equal systemic dose.

We hypothesize that these constructs will present static multivalent NGR following self-assembly through hydrophobic interaction between conjugated Dox. The larger micelle size should permit simultaneous ligand-receptor interaction at the cell surface, and the specificity seen with thermosensitive micelles should also translate to this larger construct. The increased Dox payload will increase the potential dose to a therapeutically-relevant level and allow for rapid translation to a preclinical model for repeating previous biodistribution and tumor regression studies. As an ancillary benefit, this larger concentration will permit direct analysis using the window chamber model. The results of this study would quickly establish any benefits of static multivalent presentation or curative effects.

#### **7.2.1.2 RGD-ELPBC**

DAM showed great potential in activating RGD-ELP-64/90 for specific interaction with the  $\alpha v\beta 3$  integrin *in vitro*. However, static presentation of RGD-ELPBC using the window chamber model showed no additional specificity for the tumor region compared to the normal region compared to non-ligand ELP-64/90. The observed fluorescence from histology was also minimal for RGD-ELP-64/90 compared to NGR-ELP-64/90. This could be a result of off-site binding to healthy angiogenic tissue or damaged tissue around the window chamber, ligand-blocking following binding to  $gpIIb\beta 3$  activated platelets blocking ligand accessibility, or simply improper proper ligand/receptor presentation for multivalent binding *in vivo*. In the case of off-site binding, thermally-appropriate DAM would reduce these interactions. However, DAM still cannot promote *in vivo* multivalent binding if the poor specificity is caused by poor multivalent interaction or if heat has negative effects on receptor expression. Given the small window for thermal optimization and unpredictable success even with optimized RGD-ELP-64/90, it follows that re-engineering ELP-64/90 for thermally-optimal DAM is only worthwhile if the strategy will be extended to candidate ligands beyond RGD. Otherwise, the time required to re-engineering the parent ELPBC is not

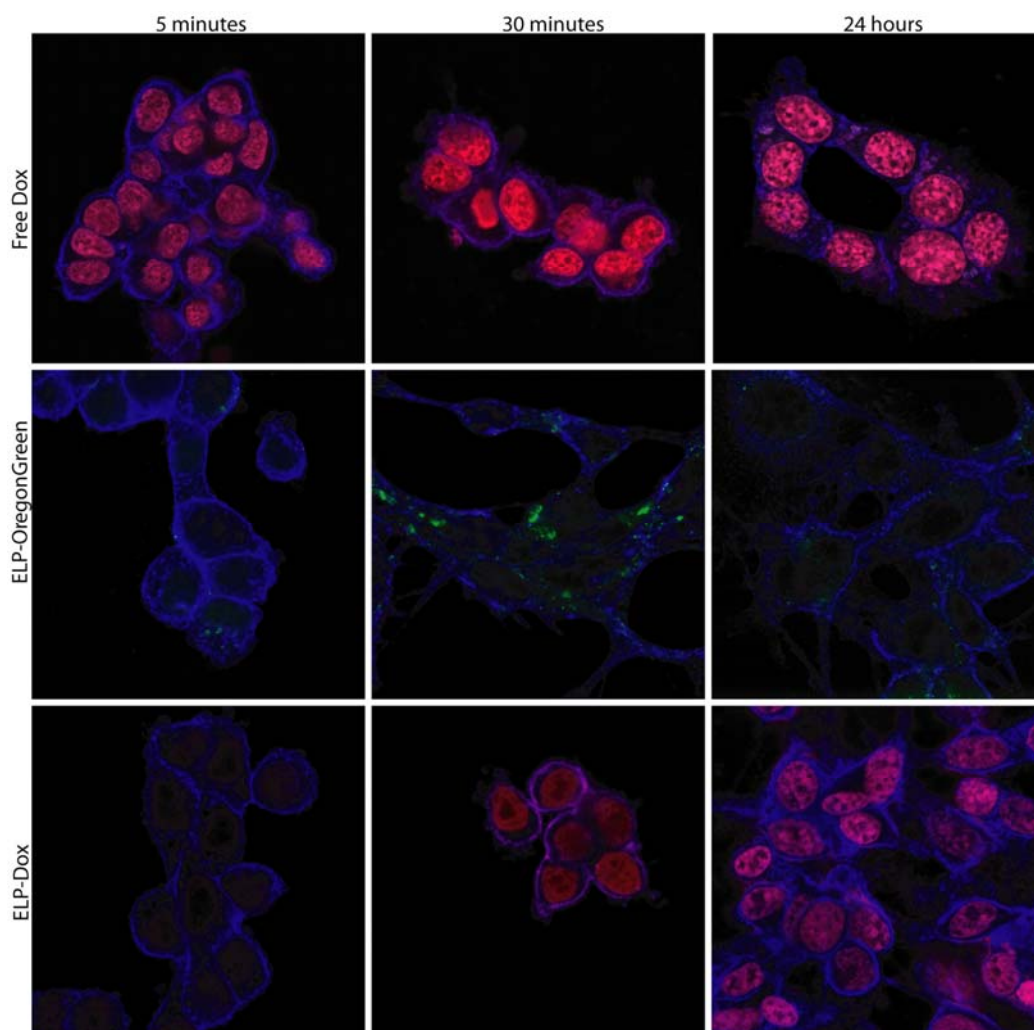


**Figure 54: Confocal images of C26 cells incubated with free Dox, ELP-OregonGreen, or ELP-Dox nanoparticles. Free Dox was trafficked to nucleus and ELP-OregonGreen was trafficked to lysosomes. ELP-Dox resulted in delayed nuclear accumulation of Dox, suggesting that ELP-Dox entered the lysosome followed Dox release. Reprinted by from Macmillan Publishers Ltd: Nature Materials, MacKay, J.A. et al., *Self-assembling chimeric polypeptide-doxorubicin conjugate nanoparticles that abolish tumours after a single injection*. 8(12): 993-9, copyright 2009.**

justified given the risk with the RGD tripeptide. Thus, the best strategy for improving the ELPBC system for *in vivo* DAM is to (A) redesign the carrier to exhibit the thermal properties of ELP-96/60 but the segment ratio of ELP-64/90 and (B) replace RGD with a ligand with more dramatic interaction upon self-assembly for *in vivo* use. Alternatively, RGD-ELPBC with its defined nanoscale architecture but poor *in vivo* performance is best used for characterization studies,

such as determining effects of receptor expression on interaction with current RGD-ELP-64/90 constructs.

First, according to the data, ELPBC for *in vivo* DAM must exhibit thermal properties similar to ELP-96/60 but with the segment ratio of ELP-64/90, exhibiting a CMT = 39 – 42 °C. This may be achieved by reducing the potential for intramolecular repulsion between the hydrophilic and hydrophobic blocks. It is possible to make the core-forming block slightly more hydrophilic, but making the coronal segment more hydrophobic may promote micelle instability, the aggregate transition, or poor ligand extension. Previous ELP design using the rules presented in work by Urry et al. [199] and Dreher et al. [101] has proven successful for generation of homopolymeric ELP and unmodified ELPBC and would likely be useful to alter this block.

DAM for thermally-optimized ELPBC would therefore provide the greatest benefit to ligands showing tremendous but cytotoxic effects following multivalent presentation. Thus, the RGD ligand should be replaced with a polyarginine ligand. Both monovalent constructs with 6 or more arginine residues [270] and nanoparticles functionalized with polyarginine show nonspecific cell penetration [96]. It follows that addition of a polyarginine ligand to ELPBC may allow for thermal control over surface charge density through micelle self-assembly cell penetration activity. Initial studies show that micelle self-assembly is retained following the addition of polyarginine to the hydrophilic terminus, and the ability to spatially restrict this activity would provide a much greater impact than restricting RGD interaction. Based on the effects seen in Chapters 3 and 6, modified ELPBC may exhibit a CMT outside of the desired range following modification at either terminus. Thus, a “living” predictive model based on previous self-assembly data would be useful for prioritizing the ligands and conjugates for modification and forming additional knowledge based on data already generated within the group. This proposed model is further described in section 7.3.1.1.

Second, uptake dependence on segment ratio was unexpected and difficult to fully understand. Based on the data, the difference is likely caused either by ligand spacing or ligand accessibility. An ancillary benefit of RGD-ELPBC is precise nanoscale architecture and ligand

density, allowing for testing of cell receptor expression using micelle ligand density as a dependent variable. Assuming that a modified cloning strategy allows for titratable  $\alpha\beta3$  expression on K562 cells, RGD-ELPBC and K562-Tet-On- $\alpha\beta3$  provides an elegant platform for testing the effects of receptor expression on multivalent interaction. If the results of this study show a expression threshold for multivalent interaction that varies with the ligand density of the parent ELPBC, then ligand spacing determines uptake. If variable cell expression yields the same results as these initial studies, then ligand accessibility and determines uptake. This study will provide widely-applicable information regarding multivalent interaction and allows us to reap further benefit from RGD-ELPBC constructs.

#### **7.2.1.3 Non-Ligand ELPBC**

Non-ligand ELPBC shows interesting behavior compared to both soluble and aggregate ELPBC observed in past studies. At the outset of these studies, we hypothesized that the ELPBC in micelle form would exhibit similar inert characteristics to other polymeric micelles used for improving plasma half-life. However, the ELPBC at  $T > CMT$  leads to accumulation along fibrous at the tumor periphery, and these structures are visible with both ligand- and non-ligand ELPBC at  $T > CMT$  and homopolymeric ELP at  $T < T_t$ . These data show that ELPBC are unique macromolecular drug carriers whose smaller size make them an alternative to homopolymeric ELP aggregates for targeting this tumor margin at normothermic conditions. Evaluation of non-ligand ELPBC requires two steps, (A) identification of ELPBC to components in the tumor margin and (B) standard biodistribution/PK studies with ELPBC for comparison to hydrophilic ELP-Dox nanoparticles.

The observation that ELPBC does not behave as an inert nanoparticle has both negative and positive consequences. Assembled ELPBC may exhibit excessive secondary interactions with components in the serum compartment or the vessel wall, negatively restricting multivalent interaction and promoting off-site accumulation. However, affinity towards these observed fibrous structures may also represent a tumor-specific interaction and provide a method for retaining

larger macromolecules at the tumor margin following convective extravasation. The best strategy for evaluating these factors is thus identifying the substrate with affinity for ELPBC. First, these fibers may consist of extracellular matrix (ECM) components or actin. Based on the appearance of the fluorescence, we can narrow the potential protein sites to those either forming fibers or associating with them (Table 11). This interaction can be tested in a relatively high-throughput manner using Surface Plasmon Resonance (SPR). Surface accumulation of ELPBC would then be tested to determine affinity to different ECM components at  $T > CMT$ . This high-throughput method would yield useful information in identifying this component. Additionally, the dorsal-fold window chamber model can be used for colocalization studies to identify the components of the fibers *in vivo*. No protocols have been developed to directly label these fibers, but it is possible that primary monoclonal antibodies or labeling agents can be applied either through systemic injection (section 7.2.2.4) or topical application following removal of the cover slip. Further understanding of tissue components with affinity for ELPBC will allow for better prediction of ELPBC accumulation patterns and evaluation of ELPBC micelles as macromolecules for tumor margin targeting. This knowledge may also lead to identification of other biomedical applications based on ELP-protein interaction.

**Table 11: List of proteins with potential affinity for transitioned ELPBC**

Protein	Description
Collagen	Long, fibrous structural protein found in ECM, connective tissue, fascia, and some cells
Elastin	Contractile load-bearing tissue present in larger vessels
Fibronectin	Ubiquitous ECM component in basement membrane and tumor interstitium
Laminin	Web-like component in basement membrane secreted by epithelial cells
Proteoglycans	Negatively-charged carbohydrates attached to proteins in ECM region
Actin	Contractile filaments found in eukaryotic cells

## 7.2.2 Protocols Applicable to Outside Study

### 7.2.2.1 Fluorescence-Based Characterization of Thermosensitive ELPBCs

The protocols designed for measuring CMC and microrigidity are expandable to other thermosensitive constructs. For example, the pyrene method has already been used to calculate the thermally-independent CMC of zinc-crosslinked nanoparticles. Measurement of the I1/I3 ratio



may also prove useful for future applications involving thermal encapsulation of hydrophobic compounds. By measuring the I1/I3 ratio of other ELPBC constructs, we can identify the effects of hydrophobic block composition on ability to solubilize hydrophobic compounds. The intuitive GUI interface and improved thermal ramping will also facilitate analysis of thermosensitive constructs using other environment-sensitive fluorescent probes.

### **7.2.2.2 K562 Cell Testing Platform**

The K562 cell platform was designed as an expandable platform from the universal K562-Tet-On cell. It lends itself well to continued study in three broad areas: (1) continued development of the K562-Tet-On- $\alpha\beta$ 3 cell line, (2) expansion for study of other ligand-receptor pairs, and (3) gradient generation for studies involving either protein or RNA detection. First, further work should be performed to resolve the difficulties with dimeric receptor expression. One option is to re-transform the K562-Tet-On cells with  $\alpha$  and  $\beta$ 3 plasmids in a different order to circumvent potential issues with antibiotic resistance. Another is to use a second inducible reporter plasmid, pRetro-X-Tight-Pur-Hyg, rather than the continuously expressing pQCXIH. While this may lead to difficulties with intracellular competition for doxycycline, it will regulate expression through a compatible promoter. Successful generation of this cell line would be beneficial to the study of existing constructs. Proper titratable expression of the  $\alpha\beta$ 3 integrin will provide a method for establishing expression thresholds required for multivalent targeting. Additionally, K562-Tet-On-  $\alpha\beta$ 3 cells could be used in coculture with K562-Tet-On-CD13 to evaluate the mechanism of NGR targeting. Interaction between NGR-ELP-64/90 and K562-Tet-On-  $\alpha\beta$ 3 cells can be monitored with and without K562-Tet-On-CD13 also in culture to determine the importance of CD13 enzymatic conversion in promoting specific accumulation.

Second, the K562 platform can be expanded to study other ligand-receptor interactions. Since there is low expression of membrane receptors on wild-type K562 cells, K562-Tet-On is a strong candidate for controlled expression of other surface receptors. Additionally, the most difficult technical hurdle of evaluating ELP ligand-receptor interaction for these studies was

reconciling staining and quantification protocols with reversible self-assembly. As this cell line can be triggered to promote cellular uptake in a starved state, it is useful for reversible ligand-receptor interactions and not just those associated with endocytosis. Some potential candidates for future study of ligand-receptor interactions include LHRH, matrix metalloprotease-9 (MMP9) [271] or  $\alpha_v\beta_5$  integrin. The flexibility of this cell line provides a compelling reason for its use as a standard platform for testing ELP-ligand-receptor interaction in the future.

Third, the gradient expression presented by these cells make them a practical, versatile, and cost-effective method for obtaining protein and RNA gradients for testing dose-response of different sensors. For protein detection assays, K562-Tet-On can be transformed with a target gene, activated, and harvested to quickly generate a gradient for applications that involve specific protein detection. Intact protein at known concentrations mixed with additional cell debris provides the advantage of simultaneously testing specificity with known quantities. This would be especially useful for (1) proteins that have limited commercial availability or have not yet been incorporated in ELP fusions and (2) testing biosensor detection limits in a more complex milieu than buffer. These advantages also extend to DNA and RNA detection. This cell line can generate a large RNA/DNA gradient based on a specific sequence. Given the current focus on developing sensors based on DNA/RNA binding and extension, this cell line provides a simple platform for testing the detection limit of different DNA/RNA segments. K562-Tet-On cells can be transformed with a target sequence under control of the inducible reporter and selected in 2-3 weeks. The cell line will produce a constant amount of background DNA/RNA but variable levels of a gene of interest based on doxycycline concentration. This will permit detection limit testing with typical background “noise” found within human cells, leading to results more closely representing real-world application.

### **7.2.2.3 Intravital Antibody Staining**

While the window chamber allows observation and quantification of punctate fluorescence within the vasculature, it is difficult to identify the exact binding sites of ELPBC in the

region of interest. To remedy this, we administered labeled primary antibodies via tail vein injection. The anti-gr1 antibody produced a strong fluorescence signal and illuminated monocytes and neutrophils within the tumor vasculature. While not all antibodies produced a suitable signal, all of those tested were nontoxic following removal of sodium azide via dialysis. The potential for advanced imaging studies using antibody staining is quite great, especially using a confocal microscope with > 3-channel functionality.

First, direct antibody labeling can be used to identify colocalization between different cell types and ligand-ELPBC within the vasculature. This is preferable to IHC as there will be no effects from ELPBC disassembly or washing out of fluorescence during the preparation. This technique would also generate time-dependent data rather than discrete data and permit kinetic analysis of a specific interaction using routine data analysis. While at least a third color is necessary to use this technique to its full benefit, it may provide a method for evaluating time-dependent colocalization.

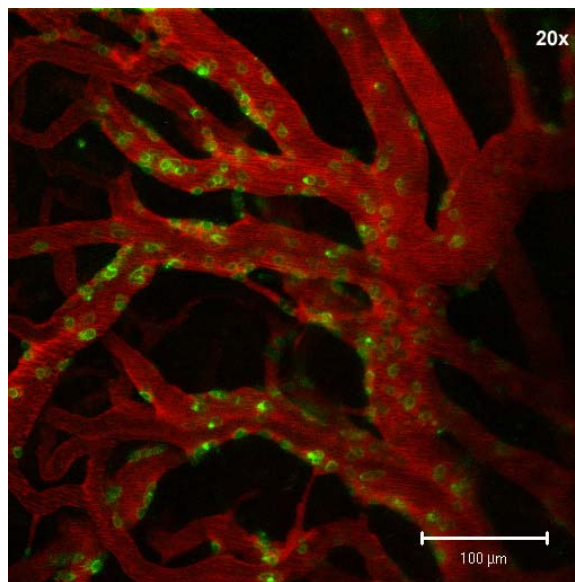


**Figure 55: Neutrophil localization in tumor vasculature. Tumor vessels were imaged following administration of vessel contrast agent (red) and anti-CD3 antibody (green) (size bar = 100 μm).**

Second, antibody labeling improves tumor characterization within the window chamber. For instance, the images generated of neutrophil behavior in both tumor and normal vasculature

show varied distribution of freely-mobile, rolling, and stationary cells. This technique could theoretically be expanded to monitor motion and accumulation of specific cell types using standard MATLAB functions, combining the authenticity provided by the *in vivo* environment and kinetic data provided by traditional flow chambers. Another example is analysis of vessel receptor expression at both normothermic and hyperthermic conditions. For example, antibodies specific for the mouse isoform of  $\alpha\beta3$  may be used to evaluate expression levels of these receptors in response to heat, important data for evaluating receptor expression. While further work is needed to identify or generate compatible fluorescent antibodies with this method, this has large implications for dynamic affinity modulation and also fills in a gap of knowledge within the field.

## **7.2.3 Additional Paths of Study**

### **7.2.3.1 “Living” Predictive Model for ELPBC generation**

ELPBC cloning and expression represents the greatest time investment relative to data generation, and the three variables of ELPBC, ligand, and conjugate complicate the design of ELPBC with a target CMT. Given that targeting applications require a specific and narrow CMT range, the ability to predict the effects of ligand and conjugate would greatly improve the applicability of these constructs. Our results showed both ligand and conjugate affect CMT in a codependent manner; thermal self-assembly is unchanged at some combinations of ELPBC segment ratio, ligand, and conjugate and dramatically changed with others. The increasing number of modified ELP2/ELP4 constructs and previous experience in forming predictive models for ELP fusion transitions based on hydrophobicity [272] may allow creation of a predictive model to estimate micelle self-assembly parameters.

Generation of this model requires two steps. First, all constructs based on the ELP2/ELP4 block copolymer platform should be analyzed with DLS following any terminal modification. Aside from the constructs analyzed in this work, prior studies include ELPBC with terminal biotin, polyarginine, polylysine, and control nonsense peptides. We can compile a robust and varied database containing the CMT and physical parameters of these and other future

ELP2/ELP4 constructs. Second, this pooled data should then be analyzed to identify mathematical trends to generate a “living” model for efficient combination of ligand, conjugate, and segment ratio. By relating ligand, conjugate characteristics, and segment ratio to physical parameters, it may be possible to predict different effects on CMT and self-assembly. Even a small improvement in predicting the effects of ligand and conjugate selection would confer very dramatic improvements to the design process. This model also would gain strength to constant refinement of the predicted trends. Most importantly, this strategy will allow for greater focus on *in vitro* and *in vivo* analysis which has greater scientific and translational impact.

#### **7.2.3.2 Evaluation of the Effects of Endotoxin on Multivalent Targeting**

While the samples used to quantify the *in vivo* effects of multivalent ligand presentation were all subjected to endotoxin removal, the samples used in initial window chamber experiments were performed without performing this step and led to dramatic results. Both RGD-ELPBC and NGR-ELPBC bound to different components in both tumor and normal vasculature in the presence of endotoxin but not following purification. RGD-ELPBC bound in a fibrous pattern in a region immediately adjacent to the plasma compartment, while NGR-ELPBC formed both small mobile aggregates and larger immobile aggregates. However, none of these distinctive patterns were visible after endotoxin removal.

Both RGD and NGR have been associated with targeting off-site receptors, and several of these receptors are upregulated on cells associated with immune response. For instance, RGD showed affinity towards  $\text{gpIIb}\beta 3$  on activated platelets. Additionally, platelets are associated with angiogenic vessels and wound healing, and platelet activation factor (PAF) is released following administration of endotoxin [273]. Staining patterns are similar to those obtained following direct staining of Von Willebrand Factor (VWF). VWF interacts with activated platelets to promote adherence of platelets to the vessel luminal wall. In the case of systemic immune response, the

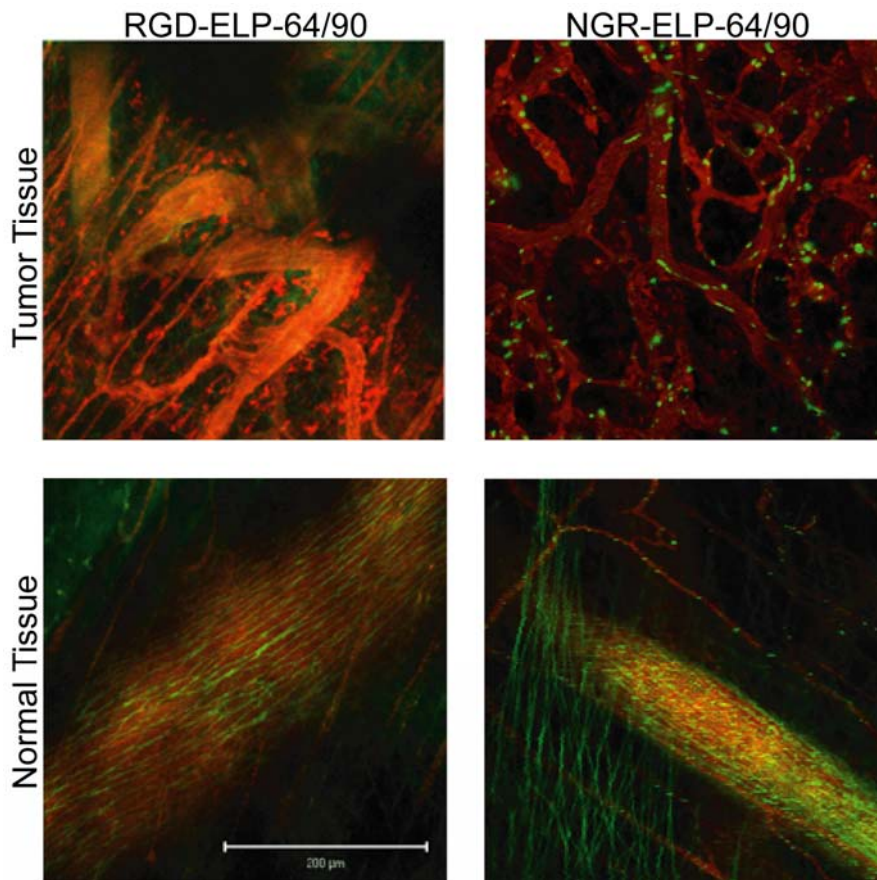


**Figure 56: Confocal images of RGD-ELP-64/90 and NGR-ELP-64/90 in presence of endotoxin. There was increased binding to fibrous structures in the perivascular region with both constructs and greatly increased punctate fluorescence in the vasculature with NGR-ELP-64/90. These images indirectly showed that ligand-ELP-64/90 interacts with components upregulated in immune response (size bar = 200  $\mu\text{m}$ ).**

increased number of activated platelets may interact with RGD-ELP-64/90 and act as a bridge connecting RGD-ELPBC to VWF within the vessel. Alternatively, the pattern seen with RGD-ELP-64/90 in normal vessels is similar to vessels with stained gap junctions. Since the addition of endotoxin leads to hypotension through dilated vessels, the RGD-ELP-64/90 patterns could be a result of increased access to endothelial gap junctions and interactions with integrins presented there. Similarly, CD13 is upregulated on monocytes [274] and secreted by neutrophils [275]. Given that mobile punctate fluorescence appears only with NGR-ELP-64/90, it follows that these aggregates represent specific interaction between NGR and soluble CD13 (small aggregates), circulating CD13+ monocytes (large mobile aggregates), or adherent CD13+ monocytes (large

stationary aggregates) within the tumor vasculature. These binding patterns provided a unique opportunity to observe the effects on accumulation patterns of multivalent constructs, serendipitous, indirect evidence of specific binding through ligand receptor interaction, and support that an endotoxin-mediated response was seen even in immune-compromised mice. While it seems imprudent to design a translational drug delivery system based on induced immune response, the ability to reversibly bind to receptors upregulated during an immune response could have beneficial effects for future applications.

## References

1. 2008. Cancer Facts and Figures. American Cancer Society.
2. Croce, C.M., *Oncogenes and Cancer*. New England Journal of Medicine, The, 2008. **358**(5): 502-511.
3. Greenblatt, M.S., Bennett, W.P., Hollstein, M. and Harris, C.C., *Mutations in the p53 Tumor Suppressor Gene: Clues to Cancer Etiology and Molecular Pathogenesis*. Cancer Research, 1994. **54**(18): 4855-4878.
4. Hollstein, M., *p53 mutations in human cancers*. Science, 1991. **253**(5015): 49.
5. Folkman, J., *Angiogenesis*. The Journal of biological chemistry, 1992. **267**(16): 10931.
6. Ferrara, N., *The biology of VEGF and its receptors*. Nature medicine, 2003. **9**(6): 669.
7. Neufeld, G., Cohen, T., Gengrinovitch, S. and Poltorak, Z., *Vascular endothelial growth factor (VEGF) and its receptors*. The FASEB Journal, 1999. **13**(1): 9-22.
8. Folkman, J. and Klagsbrun, M., *Angiogenic factors*. Science, 1987. **235**(4787): 442-447.
9. Folkman, J., *Clinical Applications of Research on Angiogenesis*. New England Journal of Medicine, The, 1995. **333**(26): 1757.
10. O'Reilly, M.S. et al., *Endostatin: An Endogenous Inhibitor of Angiogenesis and Tumor Growth*. Cell, 1997. **88**(2): 277-285.
11. Fukumura, D. et al., *Hypoxia and Acidosis Independently Up-Regulate Vascular Endothelial Growth Factor Transcription in Brain Tumors in Vivo*. Cancer Research, 2001. **61**(16): 6020-6024.
12. Shweiki, D., Itin, A., Soffer, D. and Keshet, E., *Vascular endothelial growth factor induced by hypoxia may mediate hypoxia-initiated angiogenesis*. Nature, 1992. **359**(6398): 843-845.
13. Hanahan, D., *The Hallmarks of Cancer*. Cell, 2000. **100**(1): 57.
14. Etoh, T. et al., *Angiopoietin-2 Is Related to Tumor Angiogenesis in Gastric Carcinoma: Possible in Vivo Regulation via Induction of Proteases*. Cancer Research, 2001. **61**(5): 2145-2153.
15. Yu, Q. and Stamenkovic, I., *Angiopoietin-2 Is Implicated in the Regulation of Tumor Angiogenesis*. American Journal of Pathology, 2001. **158**(2): 563-570.
16. Hanahan, D. and Folkman, J., *Patterns and emerging mechanisms of the angiogenic switch during tumorigenesis*. Cell, 1996. **86**(3): 353-64.
17. Ahmad, S.A. et al., *The Effects of Angiopoietin-1 and -2 on Tumor Growth and Angiogenesis in Human Colon Cancer*. Cancer Research, 2001. **61**(4): 1255-1259.



18. Peters, K.G. et al., *Functional Significance of Tie2 Signaling in the Adult Vasculature*. Recent Progress in Hormone Research, 2004. **59**(1): 51-71.
19. Cao, Y. et al., *Systemic Overexpression of Angiopoietin-2 Promotes Tumor Microvessel Regression and Inhibits Angiogenesis and Tumor Growth*. Cancer Research, 2007. **67**(8): 3835-3844.
20. Semenza, G.L., *Angiogenesis Ischemic and Neoplastic Disorders*. Annual Review of Medicine, 2003. **54**(1): 17-28.
21. Hashizume, H. et al., *Openings between Defective Endothelial Cells Explain Tumor Vessel Leakiness*. American Journal of Pathology, 2000. **156**(4): 1363-1380.
22. Eberhard, A. et al., *Heterogeneity of Angiogenesis and Blood Vessel Maturation in Human Tumors: Implications for Antiangiogenic Tumor Therapies*. Cancer Research, 2000. **60**(5): 1388-1393.
23. Warburg, O., *The Metabolism of Tumors*. 1930. Arnold Constable, London.
24. Swietach, P., Vaughan-Jones, R. and Harris, A., *Regulation of tumor pH and the role of carbonic anhydrase 9*. Cancer and Metastasis Reviews, 2007. **26**(2): 299-310.
25. Wykoff, C.C. et al., *Hypoxia-inducible Expression of Tumor-associated Carbonic Anhydrases*. Cancer Research, 2000. **60**(24): 7075-7083.
26. Wike-Hooley, J.L., Haveman, J. and Reinhold, H.S., *The relevance of tumour pH to the treatment of malignant disease*. Radiotherapy and Oncology, 1984. **2**(4): 343-66.
27. Helmlinger, G., Yuan, F., Dellian, M. and Jain, R.K., *Interstitial pH and pO<sub>2</sub> gradients in solid tumors in vivo: High-resolution measurements reveal a lack of correlation*. Nature Medicine, 1997. **3**(2): 177-182.
28. Tannock, I.F. and Rotin, D., *Acid pH in Tumors and Its Potential for Therapeutic Exploitation*. Cancer Research, 1989. **49**(16): 4373-4384.
29. Thiry, A., Dogné, J.-M., Masereel, B. and Supuran, C.T., *Targeting tumor-associated carbonic anhydrase IX in cancer therapy*. Trends in Pharmacological Sciences, 2006. **27**(11): 566-573.
30. Drummond, D.C., Zignani, M. and Leroux, J.-C., *Current status of pH-sensitive liposomes in drug delivery*. Progress in Lipid Research, 2000. **39**(5): 409-460.
31. Lee, E.S., Na, K. and Bae, Y.H., *Doxorubicin loaded pH-sensitive polymeric micelles for reversal of resistant MCF-7 tumor*. Journal of Controlled Release, 2005. **103**(2): 405-418.
32. Yuan, F., *Transvascular drug delivery in solid tumors*. Seminars in Radiation Oncology, 1998. **8**(3): 164-175.
33. Baxter, L.T. and Jain, R.K., *Transport of fluid and macromolecules in tumors. I. Role of interstitial pressure and convection*. Microvascular Research, 1989. **37**(1): 77-104.

34. Boucher, Y. and Jain, R.K., *Microvascular Pressure Is the Principal Driving Force for Interstitial Hypertension in Solid Tumors: Implications for Vascular Collapse*. Cancer Research, 1992. **52**(18): 5110-5114.
35. Jain, R.K., *Vascular and interstitial barriers to delivery of therapeutic agents in tumors*. Cancer and Metastasis Reviews, 1990. **9**(3): 253-266.
36. Matsumura, Y. and Maeda, H., *A New Concept for Macromolecular Therapeutics in Cancer Chemotherapy: Mechanism of Tumorotropic Accumulation of Proteins and the Antitumor Agent Smancs*. Cancer Research, 1986. **46**: 6387-6392.
37. Maeda, H., Wu, J., Sawa, T., Matsumura, Y. and Hori, K., *Tumor vascular permeability and the EPR effect in macromolecular therapeutics: a review*. Journal of Controlled Release, 2000. **65**(1-2): 271-284.
38. Dreher, M.R., Liu, W., Michelich, C.R., Dewhirst, M.W. and Chilkoti, A., *Tumor vascular permeability, accumulation, and penetration of macromolecular drug carriers*. Journal of the National Cancer Institute, 2006. **98**(5): 335-344.
39. Carmeliet, P., *Angiogenesis in health and disease*. Nature Medicine, 2003. **9**(6): 653-660.
40. Noboru, M. et al., *Angiopoietins and Tie-2 expression in angiogenesis and proliferation of human hepatocellular carcinoma*. Hepatology, 2003. **37**(5): 1105-1113.
41. Brooks, P.C., Clark, R.A. and Cheresh, D.A., *Requirement of vascular integrin alpha v beta 3 for angiogenesis*. Science, 1994. **264**(5158): 569-571.
42. Ruoslahti, E., *Targeting tumor vasculature with homing peptides from phage display*. Seminars in Cancer Biology, 2002. **10**(6): 435-442.
43. Ruoslahti, E., *Specialization of tumour vasculature*. Nature Reviews Cancer, 2002. **2**(2): 83-90.
44. Pasqualini, R. et al., *Aminopeptidase N Is a Receptor for Tumor-homing Peptides and a Target for Inhibiting Angiogenesis*. Cancer Research, 2000. **60**(3): 722-727.
45. Roberts, W.G. and Palade, G.E., *Increased microvascular permeability and endothelial fenestration induced by vascular endothelial growth factor*. Journal of Cell Science, 1995. **108**(6): 2369-2379.
46. Roberts, W.G. and Palade, G.E., *Neovasculature Induced by Vascular Endothelial Growth Factor Is Fenestrated*. Cancer Research, 1997. **57**(4): 765-772.
47. Tannock, I.F. and Hill, R.P., *The basic science of oncology*. 1998. McGraw-Hill, New York.
48. Giese, A., Bjerkvig, R., Berens, M.E. and Westphal, M., *Invasion of malignant gliomas and implications for treatment*. Journal of Clinical Oncology, 2003. **21**(8): 1624-1636.
49. Zelefsky, M. et al., *High dose radiation delivered by intensity modulated conformal radiotherapy improves the outcome of localized prostate cancer*. The Journal of Urology, 2001. **166**(3): 876-881.

50. Dupuy, D. and Goldberg, S., *Image-guided Radiofrequency Tumor Ablation: Challenges and Opportunities—Part II*. Journal of Vascular and Interventional Radiology, 2001. **12**(10): 1135-1148.
51. Jain, R.K., *Delivery of Novel Therapeutic Agents in Tumors: Physiological Barriers and Strategies*. Journal of the National Cancer Institute, 1989. **81**(8): 570-576.
52. Siddik, Z.H., *Cisplatin: mode of cytotoxic action and molecular basis of resistance*. Oncogene, 2003. **22**(47): 7265-7279.
53. Liu, L.F. et al., *Mechanism of action of camptothecin*. Ann N Y Acad Sci., 2000. **922**: 1-10.
54. Dark, G.G. et al., *Combretastatin A-4, an Agent That Displays Potent and Selective Toxicity toward Tumor Vasculature*. Cancer Research, 1997. **57**(10): 1829-1834.
55. Rowinsky, E.K. and Donehower, R.C., *Paclitaxel (Taxol)*. New England Journal of Medicine, 1995. **332**(15): 1004-1014.
56. Vermeulen, K., Van Bockstaele, D.R. and Berneman, Z.N., *The cell cycle: a review of regulation, deregulation and therapeutic targets in cancer*. Cell Proliferation, 2003. **36**: 131-149.
57. Gewitz, D.A., *A critical evaluation of the mechanisms of action proposed for the antitumor effects of the anthracycline antibiotics adriamycin and daunorubicin*. Biochemical Pharmacology, 1999. **57**(7): 727-741.
58. Binder, M. and Trepel, M., *Drugs targeting integrins for cancer therapy*. Expert Opinion in Drug Discovery, 2009. **4**(3): 229-241.
59. Nabors, L.B. et al., *Phase I and Correlative Biology Study of Cilengitide in Patients With Recurrent Malignant Glioma*. Journal of Clinical Investigation, 2007. **25**(13): 1651-1657.
60. Thorpe, P.E., *Vascular Targeting Agents as Cancer Therapeutics*. Clinical Cancer Research, 2004. **10**(2): 415-427.
61. Rowinsky, E.K., Eisenhauer, E.A., Chaudhry, V., Arbuck, S.G. and Donehower, R.C., *Clinical toxicities encountered with paclitaxel (Taxol)*. Semin Oncol, 1993. **20**(4 Suppl 3): 1-15.
62. Doroshow, J.H., *Doxorubicin-induced cardiac toxicity*. New England Journal of Medicine, 1991. **324**(12): 843-845.
63. Gottesman, M.M., *Multidrug resistance in cancer: role of ATP-dependent transporters*. Nature reviews. Cancer, 2002. **2**(1): 48.
64. El-Deiry, W.S., *The role of p53 in chemosensitivity and radiosensitivity*. Oncogene, **22**(47): 7486-7495.
65. Primeau, A.J., Rendon, A., Hedley, D., Lilge, L. and Tannock, I.F., *The Distribution of the Anticancer Drug Doxorubicin in Relation to Blood Vessels in Solid Tumors*. Clin Cancer Res, 2005. **11**(24): 8782-8788.

66. Heldin, C.H., Rubin, K., Pietras, K. and Ostman, A., *High interstitial fluid pressure - an obstacle in cancer therapy*. Nature Reviews Cancer, 2004. **4**(10): 806-13.
67. Duncan, R., *Drug-polymer conjugates: potential for improved chemotherapy*. Anti-Cancer Drugs, 1992. **3**(3): 175-210.
68. Duncan, R., *Polymer conjugates as anticancer nanomedicines*. Nature Reviews Cancer, 2006. **6**(9): 688-701.
69. Jain, R.K., *Delivery of molecular and cellular medicine to solid tumors*. Advanced Drug Delivery Reviews, 2001. **46**: 148-168.
70. Langer, R., *Drug delivery and targeting*. Nature, 1998. **392**(6679): 5-10.
71. Putnam, D. and Kopecek, J., *Polymer conjugates with anticancer activity*. In: Biopolymers II. 1995. pp. 55-123.
72. Kataoka, K., Harada, A. and Nagasaki, Y., *Block copolymer micelles for drug delivery: design, characterization and biological significance*. Advanced Drug Delivery Reviews, 2001. **47**(1): 113-131.
73. Allen, T.M. and Cullis, P.R., *Drug Delivery Systems: Entering the Mainstream*. Science, 2004. **303**(5665): 1818-1822.
74. Maeda, H., Sawa, T. and Konno, T., *Mechanism of tumor-targeted delivery of macromolecular drugs, including the EPR effect in solid tumor and clinical overview of the prototype polymeric drug SMANCS*. Journal of Controlled Release, 2001. **74**(1-3): 47-61.
75. Torchilin, V.P., Lukyanov, A.N., Gao, Z. and Papahadjopoulos-Sternberg, B., *Immunomicelles: Targeted pharmaceutical carriers for poorly soluble drugs*. Proceedings of the National Academy of Sciences, 2003. **100**(10): 6039-6044.
76. Lukyanov, A.N. and Torchilin, V.P., *Micelles from lipid derivatives of water-soluble polymers as delivery systems for poorly soluble drugs*. Advanced Drug Delivery Reviews, 2004. **56**(9): 1273-1289.
77. Kabanov, A.V., Batrakova, E.V. and Alakhov, V.Y., *Pluronic® block copolymers as novel polymer therapeutics for drug and gene delivery*. Journal of Controlled Release, 2002. **82**(2-3): 189-212.
78. Lee, C.C. et al., *A single dose of doxorubicin-functionalized bow-tie dendrimer cures mice bearing C-26 colon carcinomas*. Proceedings of the National Academy of Sciences, 2006. **103**(45): 16649-16654.
79. Israelachvili, J.N., Mitchell, D.J. and Ninham, B.W., *Theory of self-assembly of hydrocarbon amphiphiles into micelles and bilayers*. Journal of the Chemical Society, Faraday Transactions 2: Molecular and Chemical Physics, 1976. **72**(2): 1525 - 1568.
80. Whitesides, G.M., Mathias, J.P. and Seto, C.T., *Molecular self-assembly and nanochemistry: a chemical strategy for the synthesis of nanostructures*. Science, 1991. **254**(5036): 1312-1319.

81. Rösler, A., Vandermeulen, G.W.M. and Klok, H.-A., *Advanced drug delivery devices via self-assembly of amphiphilic block copolymers*. *Advanced Drug Delivery Reviews*, 2001. **53**(1): 95-108.
82. Förster, S., Abetz, V. and Müller, A.H.E., *Polyelectrolyte Block Copolymer Micelles*. In: *Polyelectrolytes with Defined Molecular Architecture II*. 2004. pp. 267-277.
83. Choucair, A. and Eisenberg, A., *Control of amphiphilic block copolymer morphologies using solution conditions*. *The European Physical Journal E: Soft Matter and Biological Physics*, 2003. **10**(1): 37-44.
84. Förster, S. and Plantenberg, T., *From Self-Organizing Polymers to Nanohybrid and Biomaterials*. *Angewandte Chemie*, 2002. **41**(5): 688-714.
85. Discher, D.E. and Eisenberg, A., *Polymer Vesicles*. *Science*, 2002. **297**(5583): 967-973.
86. Monica, L.A., Afsaneh, L. and Glen, S.K., *Amphiphilic block copolymers for drug delivery*. *Journal of Pharmaceutical Sciences*, 2003. **92**(7): 1343-1355.
87. Torchilin, V.P., *Block copolymer micelles as a solution for drug delivery problems*. *Expert Opinion on Therapeutic Patents*, 2005. **15**(1): 63.
88. Kwon, G.S. and Kataoka, K., *Block copolymer micelles as long-circulating drug vehicles*. *Advanced Drug Delivery Reviews*, 1995. **16**(2-3): 295-309.
89. Kakizawa, Y. and Kataoka, K., *Block copolymer micelles for delivery of gene and related compounds*. *Advanced Drug Delivery Reviews*, 2002. **54**(2): 203-222.
90. Torchilin, V.P., *Structure and design of polymeric surfactant-based drug delivery systems*. *Journal of Controlled Release*, 2001. **73**(2-3): 137-172.
91. Maeda, H., Wu, J., Sawa, T., Matsumura, Y. and Hori, K., *Tumor vascular permeability and the EPR effect in macromolecular therapeutics: a review* *Journal of Controlled Release*, 2000. **65**(1-2): 271-284.
92. Brannon-Peppas, L. and Blanchette, J.O., *Nanoparticle and targeted systems for cancer therapy*. *Advanced Drug Delivery Reviews*, 2004. **56**(11): 1649-1659.
93. Soga, O. et al., *Thermosensitive and biodegradable polymeric micelles for paclitaxel delivery*. *Journal of Controlled Release*, 2005. **103**(2): 341-353.
94. Lestini, B.J. et al., *Surface modification of liposomes for selective cell targeting in cardiovascular drug delivery*. *Journal of Controlled Release*, 2002. **78**(1-3): 235-247.
95. Bae, Y., Jang, W., Nishiyama, N., Fukushima, S. and Kataoka, K., *Multifunctional polymeric micelles with folate-mediated cancer cell targeting and pH-triggered drug releasing properties for active intracellular drug delivery*. *Molecular BioSystems*, 2005. **1**: 242-250.
96. Sethuraman, V.A. and Bae, Y.H., *TAT peptide-based micelle system for potential active targeting of anti-cancer agents to acidic solid tumors*. *Journal of Controlled Release*, 2007. **118**(2): 216-224.

97. Cappello, J., *The biological production of protein polymers and their use*. Trends in Biotechnology, 1990. **8**(11): 309-311.
98. Ghandehari, H. and Cappello, J., *Genetic Engineering of Protein-Based Polymers: Potential in Controlled Drug Delivery*. Pharmaceutical Research, 1998. **15**(6): 813-815.
99. Megeed, Z., Cappello, J. and Ghandehari, H., *Genetically engineered silk-elastinlike protein polymers for controlled drug delivery*. Advanced Drug Delivery Reviews, 2002. **54**(8): 1075-1091.
100. Nagarsekar, A. and Ghandehari, H., *Genetically Engineered Polymers for Drug Delivery*. Journal of Drug Targeting, 1999. **7**(1): 11-32.
101. Dreher, M.R. et al., *Temperature Triggered Self-Assembly of Polypeptides into Multivalent Spherical Micelles*. Journal of the American Chemical Society, 2007. **130**(2): 687-694.
102. Dreher, M.R. et al., *Evaluation of an elastin-like polypeptide-doxorubicin conjugate for cancer therapy*. Journal of Controlled Release, 2003. **91**(1-2): 31-43.
103. Wright, E.R. and Conticello, V.P., *Self-assembly of block copolymers derived from elastin-mimetic polypeptide sequences*. Advanced Drug Delivery Reviews, 2002. **54**(8): 1057-1073.
104. Holowka, E.P., Pochan, D.J. and Deming, T.J., *Charged Polypeptide Vesicles with Controllable Diameter*. Journal of the American Chemical Society, 2005. **127**(35): 12423-12428.
105. Chow, D., Nunalee, M.L., Lim, D.W., Simnick, A.J. and Chilkoti, A., *Peptide-based Biopolymers in Biomedicine and Biotechnology*. Materials Science and Engineering: Reports, 2008. **62**(4): 125-155.
106. Bae, Y., *Design of Environment-Sensitive Supramolecular Assemblies for Intracellular Drug Delivery: Polymeric Micelles that are Responsive to Intracellular pH Change*. Angewandte Chemie (International ed.), 2003. **42**(38): 4640.
107. Needham, D., Anyarambhatla, G., Kong, G. and Dewhirst, M.W., *A New Temperature-sensitive Liposome for Use with Mild Hyperthermia: Characterization and Testing in a Human Tumor Xenograft Model*. Cancer Research, 2000. **60**(5): 1197-1201.
108. Needham, D. and Dewhirst, M.W., *The development and testing of a new temperature-sensitive drug delivery system for the treatment of solid tumors*. Advanced Drug Delivery Reviews, 2001. **53**(3): 285-305.
109. Chung, J.E. et al., *Thermo-responsive drug delivery from polymeric micelles constructed using block copolymers of poly(N-isopropylacrylamide) and poly(butylmethacrylate)*. Journal of Controlled Release, 1999. **62**(1-2): 115-127.
110. Meyer, D.E., Kong, G.A., Dewhirst, M.W., Zalutsky, M.R. and Chilkoti, A., *Targeting a Genetically Engineered Elastin-like Polypeptide to Solid Tumors by Local Hyperthermia*. Cancer Research, 2001. **61**(4): 1548-1554.

111. Chung, J.E. et al., *Reversibly thermo-responsive alkyl-terminated poly(N-isopropylacrylamide) core-shell micellar structures*. Colloids and Surfaces B: Biointerfaces, 1997. **9**(1-2): 37-48.
112. Cheung, C.Y., Murthy, N., Stayton, P.S. and Hoffman, A.S., *A pH-Sensitive Polymer That Enhances Cationic Lipid-Mediated Gene Transfer*. Bioconjugate Chemistry, 2001. **12**(6): 906-910.
113. Park, S.Y. and Bae, Y.H., *Novel pH-sensitive polymers containing sulfonamide groups*. Macromolecular Rapid Communications, 1999. **20**(5): 269-273.
114. Urry, D.W. et al., *Temperature of polypeptide inverse temperature transition depends on mean residue hydrophobicity*. Journal of the American Chemical Society, 1991. **113**(11): 4346-4348.
115. Folkman, J., *Anti-angiogenesis: new concept for therapy of solid tumors*. Annals of Surgery, 1972. **175**(3): 409-416.
116. Folkman, J., *Angiogenesis in cancer, vascular, rheumatoid and other disease*. Nature Medicine, 1995. **1**: 27-30.
117. Jain, R.K., *Normalization of Tumor Vasculature: An Emerging Concept in Antiangiogenic Therapy*. Science, 2005. **307**(5706): 58-62.
118. Folkman, J., *Antiangiogenesis in cancer therapy--endostatin and its mechanisms of action*. Experimental Cell Research, 2006. **312**(5): 594-607.
119. Jain, R.K., *Molecular regulation of vessel maturation*. Nature medicine, 2003. **9**(6): 685.
120. Tozer, G.M., *Disrupting tumour blood vessels*. Nat Rev Cancer, 2005. **5**(6): 423.
121. Denekamp, J., *The tumour microcirculation as a target in cancer therapy: a clearer perspective*. European Journal of Clinical Investigation, 1999. **29**(9): 733-736.
122. Chaplin, D. and Dougherty, B., *Tumour vasculature as a target for cancer therapy*. British Journal of Cancer, 1999. **80**(1): 57-64.
123. Iyer, S., *Induction of apoptosis in proliferating human endothelial cells by the tumor-specific antiangiogenesis agent combretastatin A-4*. Cancer research, 1998. **58**(20): 4510.
124. Chaplin, D.J., Horsman, M.R. and Siemann, D.W., *Current development status of small-molecule vascular disrupting agents*. Curr Opin Investig Drugs, 2006. **7**(6): 522-8.
125. Jones, R.L. and Ewer, M.S., *Cardiac and cardiovascular toxicity of nonanthracycline anticancer drugs*. Expert Review of Anticancer Therapy, 2006. **6**(9): 1249-1269.
126. Gutheil, J.C. et al., *Targeted Antiangiogenic Therapy for Cancer Using Vitaxin: A Humanized Monoclonal Antibody to the Integrin  $\alpha_5\beta_3$* . Clinical Cancer Research, 2000. **6**(8): 3056-3061.
127. Arap, W., Pasqualini, R. and Ruoslahti, E., *Cancer Treatment by Targeted Drug Delivery to Tumor Vasculature in a Mouse Model*. Science, 1998. **279**(5349): 377-380.

128. Curnis, F. et al., *Differential Binding of Drugs Containing the NGR Motif to CD13 Isoforms in Tumor Vessels, Epithelia, and Myeloid Cells*. *Cancer Research*, 2002. **62**(3): 867-874.
129. Adams, G.P. et al., *High Affinity Restricts the Localization and Tumor Penetration of Single-Chain Fv Antibody Molecules*. *Cancer Research*, 2001. **61**(12): 4750-4755.
130. Dewey, W.C., *Arrhenius relationships from the molecule and cell to the clinic*. *International Journal of Hyperthermia*, 1994. **10**(4): 457-83.
131. Wust, P. et al., *Hyperthermia in combined treatment of cancer*. *The Lancet Oncology*, 2002. **3**(8): 487-497.
132. Urano, M., Kuroda, M. and Nishimura, Y., *For the clinical application of thermochemotherapy given at mild temperatures*. *Int J Hyperthermia*, 1999. **15**(2): 79-107.
133. Shen, R.N. et al., *Influence of elevated temperature on natural killer cell activity, lymphokine-activated killer cell activity and lectin-dependent cytotoxicity of human umbilical cord blood and adult blood cells*. *International Journal of Radiation Oncology Biology Physics*, 1994. **29**(4): 821-6.
134. Kong, G.A., Braun, R.D. and Dewhirst, M.W., *Hyperthermia enables tumor-specific nanoparticle delivery: effect of particle size*. *Cancer Research*, 2000. **60**: 4440-4445.
135. Repasky, E.A. and Issels, R., *Physiological consequences of hyperthermia: heat, heat shock proteins and the immune response*. *International Journal of Hyperthermia*, 2002. **18**(6): 486-489.
136. Song, C.W., *Effect of Local Hyperthermia on Blood Flow and Microenvironment*. *Cancer Research*, 1984. **44**: 4721-4730.
137. Song, C.W., Park, H. and Griffin, R.J., *Improvement of Tumor Oxygenation by Mild Hyperthermia*. *Radiation Research*, 2001. **155**: 515-528.
138. Dahl, O., *Interaction of heat and drugs in vitro and in vivo*. In: *Thermoradiotherapy and Thermochemotherapy*. 1995. Berlin, pp. 103-155.
139. 2004. *Hyperthermia in Cancer Treatment: Questions and Answers*. National Cancer Institute.
140. Dewhirst, M.W., Viglianti, B.L., Lora-Michiels, M., Hanson, M. and Hoopes, P.J., *Basic principles of thermal dosimetry and thermal thresholds for tissue damage from hyperthermia*. *International Journal of Hyperthermia*, 2003. **19**(3): 267-294.
141. Field, S. and Morris, C., *The relationship between heating time and temperature: its relevance to clinical hyperthermia*. *Radiotherapy and Oncology*, 1983. **1**(12): 179-186.
142. Stauffer, P.R., *Evolving technology for thermal therapy of cancer*. *International Journal of Hyperthermia*, 2005. **21**(8): 731-744.
143. Moffat, F.L., Falk, R.E., Laing, D. and Korbut, T.T., *Hyperthermia for cancer: A practical perspective*. *Seminars in Surgical Oncology*, 2006. **1**(4): 200-219.



144. Vujaskovic, Z. and Song, C.W., *Physiological mechanisms underlying heat-induced radiosensitization*. International Journal of Hyperthermia, 2004. **20**(2): 163-174.
145. Dieing, A. et al., The effect of induced hyperthermia on the immune system. In: Progress in Brain Research - The Neurobiology of Hyperthermia. 2007. pp. 137-152.
146. Wang, W.-C. et al., *Fever-Range Hyperthermia Enhances L-Selectin-Dependent Adhesion of Lymphocytes to Vascular Endothelium*. Journal of Immunology, 1998. **160**(2): 961-969.
147. Burd, R. et al., *Tumor cell apoptosis, lymphocyte recruitment and tumor vascular changes are induced by low temperature, long duration (fever-like) whole body hyperthermia*. Journal of Cellular Physiology, 1998. **177**(1): 137-147.
148. Russ, V. and Wagner, E., *Cell and Tissue Targeting of Nucleic Acids for Cancer Gene Therapy*. Pharmaceutical Research, 2007. **24**(6): 1047-1057.
149. Alan, T.L., Stefania, M. and Norman, B.A., *The effects of hyperthermia on vascular permeability in experimental liver metastasis*. Journal of Surgical Oncology, 1985. **28**(4): 297-300.
150. Kong, G., Braun, R.D. and Dewhirst, M.W., *Characterization of the Effect of Hyperthermia on Nanoparticle Extravasation from Tumor Vasculature*. Cancer Research, 2001. **61**(7): 3027-3032.
151. Hildebrandt, B. et al., *The cellular and molecular basis of hyperthermia*. Critical Reviews in Oncology/Hematology, 2002. **43**(1): 33-56.
152. Vertrees, R.A., Leeth, A., Girouard, M., Roach, J.D. and Zwischenberger, J.B., *Whole-body hyperthermia: a review of theory, design and application*. 2002. **17**(4): 279-290.
153. O'Neill, B.E. and Li, K.C.P., *Augmentation of targeted delivery with pulsed high intensity focused ultrasound*. International Journal of Hyperthermia, 2008. **24**(6): 506-520.
154. Gellermann, J. et al., *Methods and potentials of magnetic resonance imaging for monitoring radiofrequency hyperthermia in a hybrid system*. International Journal of Hyperthermia, 2009. **21**(6): 497-513.
155. Kuroda, K., *Non-invasive MR thermography using the water proton chemical shift*. International Journal of Hyperthermia, 2005. **21**(6): 547-560.
156. Lindner, L.H., Reinl, H.M., Schlemmer, M., Stahl, R. and Peller, M., *Paramagnetic thermosensitive liposomes for MR-thermometry*. International Journal of Hyperthermia, 2005. **21**(6): 575-588.
157. Kolios, M.C., Sherar, M.D. and Hunt, J.W., *Large blood vessel cooling in heated tissues: a numerical study*. Physics in Medicine and Biology, 1995. **40**(4): 477.
158. Ponce, A.M., Vujaskovic, Z., Yuan, F., Needham, D. and Dewhirst, M.W., *Hyperthermia mediated liposomal drug delivery*. International Journal of Hyperthermia, 2009. **22**(3): 205-213.

159. Meyer, D.E., Shin, B.C., Kong, G.A., Dewhirst, M.W. and Chilkoti, A., *Drug targeting using thermally responsive polymers and local hyperthermia*. Journal of Controlled Release, 2001. **74**(1-3): 213-224.
160. Dreher, M.R., Liu, W., Michelich, C.R., Dewhirst, M.W. and Chilkoti, A., *Thermal Cycling Enhances the Accumulation of a Temperature-Sensitive Biopolymer in Solid Tumors*. Cancer Research, 2007. **67**(9): 4418-4424.
161. Liu, W. et al., *Tumor accumulation, degradation and pharmacokinetics of elastin-like polypeptides in nude mice*. Journal of Controlled Release, 2006. **116**(2): 170-178.
162. Mammen, M., Choi, S. and Whitesides, G.M., *Polyvalent Interactions in Biological Systems: Implications for Design and Use of Multivalent Ligands and Inhibitors*. Angewandte Chemie, 1998. **37**(20): 2754-2794.
163. Friguet, B., Chaffotte, A.F., Djavadi-Ohanian, L. and Goldberg, M.E., *Measurements of the true affinity constant in solution of antigen-antibody complexes by enzyme-linked immunosorbent assay*. Journal of Immunological Methods, 1985. **77**(2): 305-319.
164. Hsu, S.M., Raine, L. and Fanger, H., *Use of avidin-biotin-peroxidase complex (ABC) in immunoperoxidase techniques: a comparison between ABC and unlabeled antibody (PAP) procedures*. Journal of Histochemistry & Cytochemistry, 1981. **29**(4): 577-580.
165. Koivunen, E., Wang, B. and Ruoslahti, E., *Phage Libraries Displaying Cyclic Peptides with Different Ring Sizes: Ligand Specificities of the RGD-Directed Integrins*. Nature Biotechnology, 1995. **13**(3): 265-270.
166. Kitov, P.I. and Bundle, D.R., *On the Nature of the Multivalency Effect: A Thermodynamic Model*. Journal of the American Chemical Society, 2003. **125**(52): 16271-16284.
167. Hong, S. et al., *The Binding Avidity of a Nanoparticle-Based Multivalent Targeted Drug Delivery Platform*. Chemistry & Biology, 2007. **14**(1): 107-115.
168. Montet, X., Funovics, M., Montet-Abou, K., Weissleder, R. and Josephson, L., *Multivalent Effects of RGD Peptides Obtained by Nanoparticle Display*. Journal of Medicinal Chemistry, 2006. **49**(20): 6087-6093.
169. Carlson, C.B., Mowery, P., Owen, R.M., Dykhuizen, E.C. and Kiessling, L.L., *Selective Tumor Cell Targeting Using Low-Affinity, Multivalent Interactions*. ACS Chemical Biology, 2007. **2**(2): 119-127.
170. Gestwicki, J.E., Cairo, C.W., Strong, L.E., Oetjen, K.A. and Kiessling, L.L., *Influencing Receptor-Ligand Binding Mechanisms with Multivalent Ligand Architecture*. Journal of the American Chemical Society, 2002. **124**(50): 14922-14933.
171. Kiessling, L.L., Strong, L.E. and Gestwicki, J.E., *Principles for multivalent ligand design*. Annual Reports in Medicinal Chemistry, 2000. **Volume 35**: 321-330.
172. Weissleder, R., Kelly, K., Sun, E.Y., Shtatland, T. and Josephson, L., *Cell-specific targeting of nanoparticles by multivalent attachment of small molecules*. Nature Biotechnology, 2005. **23**(11): 1418-1423.

173. Hood, J.D. et al., *Tumor Regression by Targeted Gene Delivery to the Neovasculature*. Science, 2002. **296**(5577): 2404-2407.
174. Xiong, J.-P. et al., *Crystal Structure of the Extracellular Segment of Integrin alpha Vbeta 3 in Complex with an Arg-Gly-Asp Ligand*. Science, 2002. **296**(5565): 151-155.
175. Xiong, J.-P. et al., *Crystal Structure of the Extracellular Segment of Integrin [Alpha]V[Beta]3*. Science, 2001. **294**(5541): 339.
176. Friedlander, M., *Definition of Two Angiogenic Pathways by Distinct alpha (v) Integrins*. Science, 1995. **270**(5241): 1500.
177. Reynolds, L.E. et al., *Enhanced pathological angiogenesis in mice lacking beta3 integrin or beta3 and beta5 integrins*. Nature medicine, 2002. **8**(1): 27-34.
178. Pasqualini, R., *av Integrins as receptors for tumor targeting by circulating ligands*. Nature biotechnology, 1997. **15**(6): 542.
179. Reichert, J., *Monoclonal antibodies market*. Nature reviews. Drug discovery, 2004. **3**(5): 383.
180. Ruoslahti, E., *RGD and other Recognition Sites for Integrins*. Annual Review of Cell and Developmental Biology, 2003. **12**(1): 697-715.
181. Nasongkla, N. et al., *cRGD-Functionalized Polymer Micelles for Targeted Doxorubicin Delivery*. Angewandte Chemie, 2004. **43**: 6323-6327.
182. Xiong, X.-B., Mahmud, A., Uludağ, H. and Lavasanifar, A., *Multifunctional Polymeric Micelles for Enhanced Intracellular Delivery of Doxorubicin to Metastatic Cancer Cells*. Pharmaceutical Research, 2008. **25**(11): 2555-2566.
183. Plow, E.F., Haas, T.A., Zhang, L., Loftus, J. and Smith, J.W., *Ligand Binding to Integrins*. Journal of Biological Chemistry, 2000. **275**(29): 21785-21788.
184. Stupp, R. and Ruegg, C., *Integrin Inhibitors Reaching the Clinic*. Journal of Clinical Oncology, 2007. **25**(13): 1637-1638.
185. Silva, R., D'Amico, G., Hovalva-Dilke, K.M. and Reynolds, L.E., *Integrins: The Keys to Unlocking Angiogenesis*. Arterioscler Thromb Vasc Biol, 2008. **28**(10): 1703-1713.
186. Ku, T.W. et al., *Direct design of a potent non-peptide fibrinogen receptor antagonist based on the structure and conformation of a highly constrained cyclic RGD peptide*. Journal of the American Chemical Society, 2002. **115**(19): 8861-8862.
187. Nabors, L.B. et al., 2007. Phase I and Correlative Biology Study of Cilengitide in Patients With Recurrent Malignant Glioma, pp. 1651-1657.
188. Look, A., Ashmun, R., Shapiro, L. and Peiper, S., *Human myeloid plasma membrane glycoprotein CD13 (gp150) is identical to aminopeptidase N*. Journal of Clinical Investigation, 1989. **83**(4): 1299-1307.
189. Mina-Osorio, P. et al., *CD13 is a novel mediator of monocytic/endothelial cell adhesion*. Journal of Leukocyte Biology, 2008. **84**(2): 448-59.

190. Riemann, D., *CD13—not just a marker in leukemia typing*. Immunology today, 1999. **20**(2): 83.
191. Bordessoule, D., Jones, M., Gatter, K.C. and Mason, D.Y., *Immunohistological patterns of myeloid antigens: tissue distribution of CD13, CD14, CD16, CD31, CD36, CD65, CD66 and CD67*. British Journal of Haematology, 1993. **83**(3): 370-383.
192. Favaloro, E.J., Browning, T. and Facey, D., *CD13 (GP150; aminopeptidase-N): predominant functional activity in blood is localized to plasma and is not cell-surface associated*. Experimental Hematology, 1993. **21**(13): 1695-701.
193. van Hensbergen, Y. et al., 2002. Soluble Aminopeptidase N/CD13 in Malignant and Nonmalignant Effusions and Intratumoral Fluid, pp. 3747-3754.
194. Buehler, A. et al., *cNGR: A Novel Homing Sequence for CD13/APN Targeted Molecular Imaging of Murine Cardiac Angiogenesis In Vivo*. Arteriosclerosis, Thrombosis, and Vascular Biology, 2006. **26**(12): 2681-2687.
195. Pastorino, F. et al., *Vascular Damage and Anti-angiogenic Effects of Tumor Vessel-Targeted Liposomal Chemotherapy*. Cancer Research, 2003. **63**(21): 7400-7409.
196. Mina-Osorio, P. and Minaosorio, *The moonlighting enzyme CD13: old and new functions to target*. Trends in molecular medicine, 2008. **14**(8): 361.
197. Corti, A., Curnis, F., Arap, W. and Pasqualini, R., *The neovasculature homing motif NGR: more than meets the eye*. Blood, 2008. **112**(7): 2628-2635.
198. Curnis, F. et al., *Enhancement of tumor necrosis factor alpha antitumor immunotherapeutic properties by targeted delivery to aminopeptidase N (CD13)*. Nature Biotechnology, 2000. **18**(1185-1190).
199. Urry, D.W., *Physical Chemistry of Biological Free Energy Transduction As Demonstrated by Elastic Protein-Based Polymers*—The Journal of Physical Chemistry B, 1997. **101**(51): 11007-11028.
200. Meyer, D.E. and Chilkoti, A., *Genetically Encoded Synthesis of Protein-Based Polymers with Precisely Specified Molecular Weight and Sequence by Recursive Directional Ligation: Examples from the Elastin-like Polypeptide System*. Biomacromolecules, 2002. **3**(2): 357-367.
201. Meyer, D.E. and Chilkoti, A., *Purification of recombinant proteins by fusion with thermally-responsive polypeptides*. Nature Biotechnology, 1999. **17**(11): 1112-1115.
202. MacKay, J.A. et al., *Self-assembling chimeric polypeptide-doxorubicin conjugate nanoparticles that abolish tumours after a single injection*. Nat Mater, 2009. **8**(12): 993-9.
203. Simnick, A.J., Lim, D.W., Chow, D.C. and Chilkoti, A., *Biomedical and Biotechnological Applications of Elastin-Like Polypeptides* Polymer Reviews, 2007. **47**(1).
204. Lee, T., Cooper, A., Apkarian, R.P. and Conticello, V.P., *Thermo-Reversible Self-Assembly of Nanoparticles Derived from Elastin-Mimetic Polypeptides*. Advanced Materials, 2000. **12**(15): 1105-1110.

205. Liu, S.Q., Tong, Y.W. and Yang, Y.Y., *Thermally sensitive micelles self-assembled from poly(N-isopropylacrylamide-co-N,N-dimethylacrylamide)-b-poly(D,L-lactide-co-glycolide) for controlled delivery of paclitaxel*. *Molecular BioSystems*, 2005. **1**(2): 158.
206. Kim, I.-S., Jeong, Y.-I., Cho, C.-S. and Kim, S.-H., *Thermo-responsive self-assembled polymeric micelles for drug delivery in vitro*. *International Journal of Pharmaceutics*, 2000. **205**(1-2): 165-172.
207. Dan, N. and Tirrell, M., *Self-assembly of block copolymers with a strongly charged and a hydrophobic block in a selective, polar solvent. Micelles and adsorbed layers*. *Macromolecules*, 2002. **26**(16): 4310-4315.
208. Chung, J.E., Yokoyama, M., Aoyagi, T., Sakurai, Y. and Okano, T., *Effect of molecular architecture of hydrophobically modified poly(N-isopropylacrylamide) on the formation of thermoresponsive core-shell micellar drug carriers*. *Journal of Controlled Release*, 1998. **53**(1-3): 119-130.
209. Trabbic-Carlson, K., Liu, L., Kim, B. and Chilkoti, A., *Expression and purification of recombinant proteins from Escherichia coli: Comparison of an elastin-like polypeptide fusion with an oligohistidine fusion*. *Protein Science*, 2004. **13**(12): 3274-3284.
210. Chung, J.E., Yokoyama, M. and Okano, T., *Inner core segment design for drug delivery control of thermo-responsive polymeric micelles*. *Journal of Controlled Release*, 2000. **65**(1-2): 93-103.
211. Kalyanasundaram, K. and Thomas, J.K., *Environmental effects on vibronic band intensities in pyrene monomer fluorescence and their application in studies of micellar systems*. *Journal of the American Chemical Society*, 2002. **99**(7): 2039-2044.
212. Dong, D.C. and Winnik, M.A., *The Py scale of solvent polarities*. *Canadian Journal of Chemistry*, 1984. **62**(11): 2560-2565.
213. Melnick, R.L., Haspel, H.C., Goldenberg, M., Greenbaum, L.M. and Weinstein, S., *Use of fluorescent probes that form intramolecular excimers to monitor structural changes in model and biological membranes*. *Biophysical Journal*, 1981. **34**(3): 499-515.
214. Emert, J., Behrens, C. and Goldenberg, M., *Intramolecular excimer-forming probes of aqueous micelles*. *Journal of the American Chemical Society*, 1979. **101**(3): 771-772.
215. Kwon, G.S. et al., *Micelles based on AB block copolymers of poly(ethylene oxide) and poly(beta-benzyl L aspartate)*. *Langmuir*, 1993. **9**(4): 945-949.
216. Lavasanifar, A., Samuel, J. and Kwon, G.S., *Poly(ethylene oxide)-block-poly(-amino acid) micelles for drug delivery*. *Advanced Drug Delivery Reviews*, 2002. **54**(2): 169-190.
217. Mitra, A. et al., *Targeting tumor angiogenic vasculature using polymer-RGD conjugates*. *Journal of Controlled Release*, 2005. **102**(1): 191-201.
218. Krishnamurthy, V.M., Semetey, V., Bracher, P.J., Shen, N. and Whitesides, G.M., *Dependence of Effective Molarity on Linker Length for an Intramolecular Protein-Ligand System*. *Journal of the American Chemical Society*, 2007. **129**(5): 1312-1320.

219. Furgeson, D.Y., Dreher, M.R. and Chilkoti, A., *Structural optimization of a "smart" doxorubicin-polypeptide conjugate for thermally targeted delivery to solid tumors*. Journal of Controlled Release, 2006. **110**(2): 362-369.
220. Siemann, D.W., Chaplin, D.J. and Horsman, M.R., *Vascular-targeting therapies for treatment of malignant disease*. Cancer, 2004. **100**(12): 2491-2499.
221. Gutheil, J.C. et al., *Targeted Antiangiogenic Therapy for Cancer Using Vitaxin: A Humanized Monoclonal Antibody to the Integrin AvB3*. Clinical Cancer Research, 2000. **6**(8): 3056-3061.
222. Neri, D. et al., *Targeting by affinity-matured recombinant antibody fragments of an angiogenesis associated fibronectin isoform*. Nature Biotechnology, 1997. **15**(12): 1271-1275.
223. Dharap, S.S. et al., *Tumor-specific targeting of an anticancer drug delivery system by LHRH peptide*. Proceedings of the National Academy of Sciences, 2005. **102**(36): 12962-12967.
224. Ellerby, H.M., Arap, W., Ellerby, L.M., Kain, R. and Pasqualini, R., *Anti-cancer activity of targeted pro-apoptotic peptides*. Nature Medicine, 1999. **5**(9): 1033.
225. Colombo, G. et al., *Structure-Activity Relationships of Linear and Cyclic Peptides Containing the NGR Tumor-homing Motif*. Journal of Biological Chemistry, 2002. **277**(49): 47891-47897.
226. Dreher, M.R., Drug Delivery to Solid Tumors with Elasin-Like-Polypeptide Drug Carriers. 2006. Duke University, Durham, NC.
227. Wyatt, P.J., *Light scattering and the absolute characterization of macromolecules*. Analytica Chimica Acta, 1993. **272**(1): 1-40.
228. Drummond, D.C., Meyer, O., Hong, K., Kirpotin, D.B. and Papahadjopoulos, D., *Optimizing Liposomes for Delivery of Chemotherapeutic Agents to Solid Tumors*. Pharmacological Reviews, 1999. **51**(4): 691-744.
229. Riemann, D., Kehlen, A. and Langner, J., *CD13 - Not Just a Marker in Leukemia Targeting*. Immunology Today, 1999. **20**(2): 82-88.
230. Leavitt, S. and Freire, E., *Direct measurement of protein binding energetics by isothermal titration calorimetry* Current Opinion in Structural Biology, 2001. **11**(5): 560-566.
231. Sturtevant, J.M., *Biochemical applications of differential scanning calorimetry*. Annual Review of Physical Chemistry, 1987. **38**(1): 463-88.
232. Jelesarov, I. and Bosshard, H.R., *Isothermal titration calorimetry and differential scanning calorimetry as complementary tools to investigate the energetics of biomolecular recognition*. Journal of Molecular Recognition, 1999. **12**(1): 3-18.
233. Myszka, D.G., *Kinetic analysis of macromolecular interactions using surface plasmon resonance biosensors*. Current Opinion in Biotechnology, 1997. **8**(1): 50-57.

234. O'Sullivan, C.K. and Guilbault, G.G., *Commercial quartz crystal microbalances - theory and applications*. Biosensors and Bioelectronics, 1999. **14**(8-9): 663-670.
235. Homola, J., Yee, S.S. and Gauglitz, G., *Surface plasmon resonance sensors*. Sensors and Actuators B: Chemical, 1999. **54**(1-2): 3-15.
236. Johnsson, B., Löfås, S. and Lindquist, G., *Immobilization of proteins to a carboxymethyl-dextran-modified gold surface for biospecific interaction analysis in surface plasmon resonance sensors*. Analytical Biochemistry, 1991. **198**(2): 268-277.
237. Johnsson, U. et al., *Real-time biospecific interaction analysis using surface plasmon resonance and a sensor chip technology*. Biotechniques, 1991. **11**(5): 620-627.
238. Salamon, Z., Wang, Y., Tollin, G. and Macleod, H.A., *Assembly and molecular organization of self-assembled lipid bilayers on solid substrates monitored by surface plasmon resonance spectroscopy*. Biochimica et Biophysica Acta, 1994. **1195**(2): 267-275.
239. Giancotti, F.G. and Ruoslahti, E., *Integrin Signaling*. Science, 1999. **285**(5430): 1028-1033.
240. Brown, M.A. et al., *The use of mild trypsinization conditions in the detachment of endothelial cells to promote subsequent endothelialization on synthetic surfaces*. Biomaterials, 2007. **28**(27): 3928-3935.
241. Roderick, A.F.M. et al., *Widespread intraspecies cross-contamination of human tumor cell lines arising at source*. International Journal of Cancer, 1999. **83**(4): 555-563.
242. Duan, J., Wu, J., Valencia, C.A. and Liu, R., *Fibronectin Type III Domain Based Monobody with High Avidity* Biochemistry, 2007. **46**(44): 12656-12664.
243. van Hensbergen, Y. et al., *A doxorubicin-CNGRC-peptide conjugate with prodrug properties*. Biochemical Pharmacology, 2002. **63**(5): 897-908.
244. Decristoforo, C. et al., *Comparison of in vitro and in vivo properties of [99mTc]cRGD peptides labeled using different novel Tc-cores*. Journal of Nuclear Medicine and Imaging, 2007. **2007**(51): 1.
245. Cressman, S. et al., *Binding and Uptake of RGD-Containing Ligands to Cellular  $\alpha v \beta 3$  Integrins*. International Journal of Peptide Research and Therapeutics, 2009. **15**(1): 49-59.
246. Almutairi, A. et al., *Biodegradable dendritic positron-emitting nanoprobe for the noninvasive imaging of angiogenesis*. Proceedings of the National Academy of Sciences, 2009. **106**(3): 685-90.
247. Cai, W. et al., *Peptide-Labeled Near-Infrared Quantum Dots for Imaging Tumor Vasculature in Living Subjects*. Nano Letters, 2006. **6**(4): 669-676.
248. Cai, W. and Chen, X., *Preparation of peptide-conjugated quantum dots for tumor vasculature-targeted imaging*. Nature Protocols, 2008. **3**(1): 89-96.

249. Park, K. et al., *Tumor Endothelial Cell Targeted Cyclic RGD-modified Heparin Derivative: Inhibition of Angiogenesis and Tumor Growth*. *Pharmaceutical Research*, 2008. **25**(12): 2786-2798.
250. Mina-Osorio, P. et al., 2008. CD13 is a novel mediator of monocytic/endothelial cell adhesion, pp. 448-459.
251. Moffatt, S., Wiehle, S. and Cristiano, R.J., *A multifunctional PEI-based cationic polyplex for enhanced systemic p53-mediated gene therapy*. *Gene Therapy*, 2006. **13**(21): 1512-23.
252. Moffatt, S., Wiehle, S. and Cristiano, R.J., *Tumor-specific gene delivery mediated by a novel peptide-polyethylenimine-DNA polyplex targeting aminopeptidase N/CD13*. *Human Gene Therapy*, 2005. **16**(1): 57-67.
253. von Wallbrunn, A. et al., *In vivo imaging of integrin  $\alpha v \beta 3$  expression using fluorescence-mediated tomography*. *European Journal of Nuclear Medicine and Molecular Imaging*, 2007. **34**(5): 745-754.
254. Raucher, D. and Chilkoti, A., *Enhanced Uptake of a Thermally Responsive Polypeptide by Tumor Cells in Response to Its Hyperthermia-mediated Phase Transition*. *Cancer Research*, 2001. **61**(19): 7163-7170.
255. Blystone, S.D., Lindberg, F.P., LaFlamme, S.E. and Brown, E.J., *Integrin beta 3 cytoplasmic tail is necessary and sufficient for regulation of alpha 5 beta 1 phagocytosis by alpha v beta 3 and integrin-associated protein*. *The Journal of Biological Chemistry*, 1995. **130**(3): 745-754.
256. Mishima, Y. et al., *Leukemic Cell-Surface CD13/Aminopeptidase N and Resistance to Apoptosis Mediated by Endothelial Cells*. *Journal of the National Cancer Institute*, 2002. **94**(13): 1020-1028.
257. Gossen, M. and Bujard, H., *Tight control of gene expression in mammalian cells by tetracycline-responsive promoters*. *Proceedings of the National Academy of Sciences*, 1992. **89**(12): 5547-5551.
258. Gossen, M. et al., *Transcriptional Activation by Tetracyclines in Mammalian Cells*. *Science*, 1995. **268**(5218): 1766-1769.
259. Bogardus, J.B. and Blackwood, R.K., Jr., *Solubility of doxycycline in aqueous solution*. *Journal of Pharmaceutical Sciences*, 1979. **68**(2): 188-94.
260. Ermak, G., Cancasci, V.J. and Davies, K.J.A., *Cytotoxic effect of doxycycline and its implications for tet-on gene expression systems*. *Analytical Biochemistry*, 2003. **318**(1): 152-154.
261. Hynes, R.O., *Integrins: Versatility, modulation, and signaling in cell adhesion*. *Cell*, 1992. **69**(1): 11-25.
262. Danen, E.H. et al., *Requirement for the synergy site for cell adhesion to fibronectin depends on the activation state of integrin alpha 5 beta 1*. *Journal of Biological Chemistry*, 1995. **270**(37): 21612-8.



263. Fong, A.M. and Santoro, S.A., *Transcriptional regulation of alpha IIb integrin gene expression during megakaryocytic differentiation of K562 cells. Role of a silencer element*. Journal of Biological Chemistry, 1994. **269**(28): 18441-18447.
264. Garde, S.V. et al., *Binding and internalization of NGR-peptide-targeted liposomal doxorubicin (TVT-DOX) in CD13-expressing cells and its antitumor effects*. Anti-Cancer Drugs, 2007. **18**(10): 1189-1200 10.1097/CAD.0b013e3282a213ce.
265. Wang, X. et al., *NGR-modified micelles enhance their interaction with CD13-overexpressing tumor and endothelial cells* Journal of Controlled Release, 2009. **139**(1): 56-62.
266. Conchello, J.-A. and Lichtman, J.W., *Optical sectioning microscopy*. Nature Methods, 2005. **2**(12): 920-931.
267. Wilson, D. et al., *Whole Mouse Cryo-Imaging*. Proc Soc Photo Opt Instrum Eng, 2008. **6916**: 69161I-69161I9.
268. Sarvazyan, N., *Visualization of doxorubicin-induced oxidative stress in isolated cardiac myocytes*. American Journal of Physiology - Heart, Circulation, and Physiology, 1996. **271**(5): 2079-2085.
269. Rasband, W.S., 1997-2009. ImageJ. In: U.S.N.I.o. Health (Editor), Bethesda, MD.
270. Wender, P.A. et al., *The design, synthesis, and evaluation of molecules that enable or enhance cellular uptake: Peptoid molecular transporters*. Proceedings of the National Academy of Sciences, 2000. **97**(24): 13003-13008.
271. Koivunen, E. et al., *Tumor targeting with a selective gelatinase inhibitor*. Nature Biotechnology, 1999. **17**(8): 768-774.
272. Trabbic-Carlson, K. et al., *Effect of protein fusion on the transition temperature of an environmentally responsive elastin-like polypeptide: a role for surface hydrophobicity?* Protein Engineering, Design and Selection, 2004. **17**(1): 57-66.
273. Hanahan, D.J., *Platelet Activating Factor: A Biologically Active Phosphoglyceride*. Annual Review of Biochemistry, 1986. **55**(1): 483-509.
274. Huschak, G., Zur Nieden, K., Stuttmann, R. and Riemann, D., *Changes in monocytic expression of aminopeptidase N/CD13 after major trauma*. Clinical & Experimental Immunology, 2003. **134**(3): 491-496.
275. Wagner, J.G. and Roth, R.A., *Neutrophil migration during endotoxemia*. Journal of Leukocyte Biology, 1999. **66**(1): 10-24.

## Biography

Andrew J. Simnick was born November 1, 1982 in Palos Heights, IL and grew up in the Chicagoland area with aspirations to play point guard at Duke University. At A.A. Stagg High School in Palos Hills, IL, he never made the basketball team but graduated as valedictorian and was named a National Merit Scholar. He pursued interests in engineering, science, and journalism at the University of Illinois-Urbana-Champaign. Andrew was awarded a Goldwater Fellowship in 2003 after undertaking research projects in both nuclear engineering under Dr. David Ruzic and electrical engineering under Dr. Kevin Kim. He graduated with University Honors in 2004 with a B.S. in electrical engineering and minors in both chemistry and bioengineering. He was then awarded an NSF IGERT Fellowship to pursue a Ph.D. in biomedical engineering at Duke University under Dr. Ashutosh Chilkoti building on his prior focus on drug delivery. In his time at Duke, he has been a co-author on eight publications and two successfully-funded R01 proposals. He also received the Biomedical Engineering Society Graduate Student Research Award in 2008. Outside of the lab, he remains an avid fan of Duke Basketball and greatly enjoyed being part of the community in Durham, NC.

## Publications

Simnick, A. J.; Valencia, C.A.; Liu, R.; Chilkoti, A., Morphing low affinity ligands into high avidity nanoparticles by thermally triggered self-assembly of a genetically encoded polymer, *ACS Nano* **2010**, (submitted).

Simnick, A. J.; Otvos, B.; Kontos, C. D.; Chilkoti, A., Engineered Cell Line with Titrated Receptor Expression for Multivalent Binding Assays, **2010**, (in preparation).

Simnick, A. J.; Liu, W.; Dreher, M. R.; Hanna, G.; Dewhirst, M. W.; Chilkoti, A., Multivalent NGR - Elastin-Like Polypeptide Micelles Improve Specificity of Tumor Targeting, **2010**, (in preparation).

Manzoor, A. A.; Lindner, L.; Simnick, A. J.; Park, J.; Dreher, M. R.; Da, S.; Needham, D. E.; Dewhirst, M. W., Thermally sensitive nanoparticles: the importance of triggered intravascular drug release, **2010**, (in preparation).

Liu, W.; MacKay, J. A.; Dreher, M. R.; Chen, M.; McDaniel, J. R.; Simnick, A. J.; Callahan, D. J.; Zalutsky, M. R.; Chilkoti, A., Injectable intratumoral depot of thermally responsive polypeptide–radionuclide conjugates delays tumor progression in a mouse model. *Journal of Controlled Release* **2010**, (in press).

MacKay, J. A.; Chen, M.; McDaniel, J. R.; Liu, W.; Simnick, A. J.; Chilkoti, A., Self-assembling chimeric polypeptide-doxorubicin conjugate nanoparticles that abolish tumours after a single injection. *Nature Materials* **2009**, 8, (12), 993-999.

Hucknall, A.; Simnick, A. J.; Hill, R. T.; Chilkoti, A.; Garcia, A.; Johannes, M. S.; Clark, R. L.; Zauscher, S.; Ratner, B. D., Versatile synthesis and micropatterning of nonfouling polymer brushes on the wafer scale. *Biointerphases* **2009**, 4, (2) 50-57.

Chow, D.; Nunalee, M. L.; Lim, D. W.; Simnick, A. J.; Chilkoti, A., Peptide-based biopolymers in biomedicine and biotechnology. *Materials Science and Engineering: R: Reports* **2008**, 62, (4), 125-155.

Dreher, M. R.; Simnick, A. J.; Fischer, K.; Smith, R. J.; Patel, A.; Schmidt, M.; Chilkoti, A., Temperature Triggered Self-Assembly of Polypeptides into Multivalent Spherical Micelles. *Journal of the American Chemical Society* **2007**, 130, (2), 687-694.

Simnick, A. J.; Lim, D. W.; Chow, D. C.; Chilkoti, A., Biomedical and Biotechnological Applications of Elastin-Like Polypeptides *Polymer Reviews* **2007**, 47, (1), 121.

Pyhtila, J.W.; Ma, H.; Simnick, A. J.; Chilkoti, A.; Wax, A., Analysis of long range correlations due to coherent light scattering from in-vitro cell arrays using angle-resolved low coherence interferometry. *Journal of Biomedical Optics*, **2006**, 11, (3).